

# LHCb 上粲夸克偶素产生和 $B_c$ 介子的实验研究

(申请清华大学理学博士学位论文)

培养单位: 工程物理系  
学 科: 物理学  
研 究 生: 安 刘 攀  
指 导 教 师: 高 原 宁 教 授

二〇一八年六月



# **Experimental studies of charmonium production and $B_c$ mesons at LHCb**

Dissertation Submitted to  
**Tsinghua University**  
in partial fulfillment of the requirement  
for the degree of  
**Doctor of Philosophy**  
in  
**Physics**  
by  
**AN Liupan**

Dissertation Supervisor : Professor GAO Yuanning

**June, 2018**



# 关于学位论文使用授权的说明

本人完全了解清华大学有关保留、使用学位论文的规定，即：

清华大学拥有在著作权法规定范围内学位论文的使用权，其中包括：（1）已获学位的研究生必须按学校规定提交学位论文，学校可以采用影印、缩印或其他复制手段保存研究生上交的学位论文；（2）为教学和科研目的，学校可以将公开的学位论文作为资料在图书馆、资料室等场所供校内师生阅读，或在校园网上供校内师生浏览部分内容；（3）根据《中华人民共和国学位条例暂行实施办法》，向国家图书馆报送可以公开的学位论文。

本人保证遵守上述规定。

（保密的论文在解密后应遵守此规定）

作者签名: 安刘攀

导师签名: 齐勇

日 期: 2018.06.01

日 期: 2018.06.01



## 摘要

量子色动力学 (QCD) 的低能标行为由非微扰效应主导, 以致我们对其理解远远不够。本论文利用大型强子对撞机上 LHCb 实验采集的质子-质子 ( $pp$ ) 对撞数据, 研究了粲夸克偶素的产生机制和  $B_c$  介子的性质, 以加深对 QCD 的理解。

高能  $pp$  对撞中粲夸克偶素的产生一般可以因子化为粲夸克对的产生和随后的强子化两个过程。前者可用微扰 QCD 计算, 后者为非微扰过程, 需要用非微扰方法处理, 依赖于实验结果作为输入。利用积分亮度  $3.05 \text{ pb}^{-1}$ 、质心能量  $13 \text{ TeV}$  的  $pp$  对撞数据, 在横动量  $p_T \in [0, 14] \text{ GeV}/c$  和快度  $y \in [2.0, 4.5]$  的运动学区间测量了瞬发  $J/\psi$  介子和来自底强子衰变的  $J/\psi$  介子的产生截面随  $p_T$  和  $y$  的变化关系, 结果分别与非相对论量子色动力学 (NRQCD) 和固定阶加次领头对数项 (FONLL) 计算相符。本分析还计算了质心系能量  $13 \text{ TeV}$  与  $8 \text{ TeV}$  的产生截面的比值随  $p_T$  和  $y$  的变化关系, 其理论和实验的不确定度均大幅降低, 有助于精确检验理论模型。结果表明, 瞬发  $J/\psi$  介子的实验测量与次领头阶 NRQCD 的计算结果相符, 来自底强子衰变的  $J/\psi$  介子的实验结果略高于 FONLL 的计算。

高能  $pp$  对撞中  $J/\psi$  介子对的产生有两种来源: 单部分子散射 (SPS) 过程和双部分子散射 (DPS) 过程。二者产生的  $J/\psi$  介子对的运动学特性存在明显区别, 前者可以利用理论计算, 后者可以通过  $J/\psi$  介子产生截面的测量结果得到。本论文利用积分亮度  $279 \text{ pb}^{-1}$ 、质心系能量  $13 \text{ TeV}$  的  $pp$  对撞数据测量了  $J/\psi$  介子对的产生截面随多个运动学变量的变化关系, 并针对不同理论模型对 SPS 和 DPS 贡献加以区分。结果表明: SPS 的贡献与领头阶  $k_T$  因子化模型的计算结果相符, 低于次领头阶色单态模型的计算; 在  $J/\psi$  介子对快度差较大的区域, DPS 贡献显著。

论文还研究了  $B_c$  介子的性质。利用积分亮度  $3 \text{ fb}^{-1}$ 、质心能量  $7 \text{ TeV}$  和  $8 \text{ TeV}$  的  $pp$  对撞数据, 测量了  $B_c^+$  介子的相对衰变分支比  $\mathcal{B}(B_c^+ \rightarrow \psi(2S)\pi^+)/\mathcal{B}(B_c^+ \rightarrow J/\psi\pi^+)$ , 与次领头阶 NRQCD 和  $k_T$  因子化的计算结果相符。利用积分亮度  $2 \text{ fb}^{-1}$ 、质心能量  $8 \text{ TeV}$  的  $pp$  对撞数据, 在  $B_c^+\pi^+\pi^-$  质量谱中对 ATLAS 实验观测到的  $B_c$  介子激发态  $B_c(2S)^+$  进行了寻找, 没有观测到信号。本分析在不同质量假设下对  $B_c(2S)^+$  和  $B_c^+$  产生截面的比值与  $B_c(2S)^+ \rightarrow B_c^+\pi^+\pi^-$  衰变分支比的乘积设置了上限。如果 ATLAS 实验从  $B_c^+$  介子出发重建  $B_c(2S)^+ \rightarrow B_c^+\pi^+\pi^-$  过程的效率非常高, 则两个实验的结果一致。

**关键词:** 量子色动力学; 重夸克偶素;  $B_c$  介子; LHCb 实验

## Abstract

Studies of the properties of heavy-flavour hadrons can help deepen the understanding of strong interactions, which are described by quantum chromodynamics (QCD). QCD processes at short distances are perturbative, while those at long distances are non-perturbative and remain less understood. This dissertation presents the experimental studies of charmonia and  $B_c$  mesons with data samples of proton-proton ( $pp$ ) collisions collected by the LHCb detector at the Large Hadron Collider.

In the production of quarkonium in  $pp$  collisions, the creation of heavy-quark pairs is expected to be perturbative, while the subsequent evolution of the heavy-quark pairs to quarkonia is non-perturbative, for which the calculations rely essentially on experimental inputs. The inclusive production cross-sections of prompt  $J/\psi$  mesons and those of  $J/\psi$  mesons from  $b$ -hadron decays in  $pp$  collisions at the centre-of-mass energy  $\sqrt{s} = 13$  TeV are measured using a data sample corresponding to an integrated luminosity of  $3.05 \text{ pb}^{-1}$  collected in early 2015. The kinematic range of the measured  $J/\psi$  mesons is  $p_T < 14 \text{ GeV}/c$  and  $2.0 < y < 4.5$ , where  $p_T$  and  $y$  indicate the transverse momentum and the rapidity of the  $J/\psi$  meson. The double differential cross-sections as functions of  $p_T$  and  $y$  of the  $J/\psi$  mesons are measured. The integrated cross-section of prompt  $J/\psi$  mesons is determined to be  $15.03 \pm 0.03 \text{ (stat)} \pm 0.91 \text{ (syst)} \mu\text{b}$ , and that of  $J/\psi$  mesons from  $b$ -hadron decays is  $2.25 \pm 0.01 \text{ (stat)} \pm 0.13 \text{ (syst)} \mu\text{b}$ . The results of prompt  $J/\psi$  mesons are consistent with the calculations of non-relativistic QCD (NRQCD) at the next-to-leading order (NLO), and those of  $J/\psi$  mesons from  $b$ -hadron decays are consistent with calculations of FONLL, the fixed order plus next-to-leading logarithms. The ratios of the production cross-sections at  $\sqrt{s} = 13$  TeV and those at  $\sqrt{s} = 8$  TeV are determined as functions of  $p_T$  and  $y$  to provide more precise comparisons with the theoretical models, since a large fraction of uncertainties cancel in the ratios from both the experimental and theoretical sides. The FONLL predictions tend to underestimate the cross-section ratios for  $J/\psi$  mesons from  $b$ -hadron decays.

Measurements of  $J/\psi$  pair production can provide additional information to test the QCD models. The  $J/\psi$  pair can be produced either through the process of single parton scattering (SPS), or through that of double parton scatterings (DPS). The SPS contribution can be calculated by QCD models, and the DPS contribution can be determined from

measurements of prompt  $J/\psi$  production cross-section. The production cross-sections of  $J/\psi$  pairs in  $pp$  collisions at  $\sqrt{s} = 13$  TeV are measured as functions of various kinematic variables with a data sample corresponding to an integrated luminosity of  $279 \text{ pb}^{-1}$ . The integrated production cross-section of  $J/\psi$  pair for  $J/\psi$  mesons in the kinematic range  $p_T < 10 \text{ GeV}/c$  and  $2.0 < y < 4.5$  is measured to be  $15.2 \pm 1.0 \text{ (stat)} \pm 0.9 \text{ (syst) nb}$ . The contributions of SPS and DPS are studied under various theoretical assumptions. Significant DPS contributions are observed in the high  $\Delta y$  range, where  $\Delta y$  is the difference of the rapidities between the two  $J/\psi$  mesons. The SPS contributions are consistent with the calculations of the leading-order (LO)  $k_T$  factorization, and are overestimated by the NLO colour-singlet model.

The decays and spectroscopy of  $B_c$  mesons are described by various QCD models, which can be tested through experimental studies of  $B_c$  mesons. The branching fraction ratio  $\mathcal{B}(B_c^+ \rightarrow \psi(2S)\pi^+)/\mathcal{B}(B_c^+ \rightarrow J/\psi\pi^+)$  is measured to be  $0.268 \pm 0.032 \text{ (stat)} \pm 0.007 \text{ (syst)} \pm 0.006(\mathcal{B})$  with the data samples collected in 2011 and 2012, corresponding to integrated luminosities of  $1 \text{ fb}^{-1}$  at  $\sqrt{s} = 7 \text{ TeV}$  and  $2 \text{ fb}^{-1}$  at  $\sqrt{s} = 8 \text{ TeV}$ , respectively. The last uncertainty is due to the uncertainties of the branching fractions of the  $J/\psi \rightarrow \mu^+\mu^-$  and  $\psi(2S) \rightarrow \mu^+\mu^-$  decays. The result agrees well with the calculations of the NRQCD approach at NLO and the  $k_T$  factorization method.

The  $B_c(2S)^+$  state, which was observed by the ATLAS experiment, is searched for in the  $B_c^+\pi^+\pi^-$  mass spectrum using the data sample collected in 2012. No signal is observed. Upper limits are set on the product of the relative production cross-section  $\sigma(B_c(2S)^+)/\sigma(B_c^+)$  and the branching fraction  $\mathcal{B}(B_c(2S)^+ \rightarrow B_c^+\pi^+\pi^-)$  under different assumptions of the  $B_c(2S)^+$  mass. The upper limits agree with the ATLAS result only if the unpublished efficiency of reconstructing the  $B_c(2S)^+$  state relative to that for the  $B_c^+$  meson is very large at ATLAS.

**Key words:** QCD; Heavy quarkonium;  $B_c$  meson; LHCb experiment

## Contents

Chapter 1	Introduction	1
1.1	The Standard Model	2
1.1.1	History	2
1.1.2	Overview	3
1.1.3	Formulation of the SM	3
1.2	QCD	4
1.2.1	QCD Lagrangian	4
1.2.2	QCD predictions on experimental observables	5
1.2.3	Quarkonia and $B_c$ mesons	8
1.3	Quarkonium production in proton-proton collisions	10
1.3.1	The NRQCD approach	11
1.3.2	Measurements on quarkonium production	19
1.3.3	Comparisons between predictions and measurements	20
1.4	Quarkonium pair production in $pp$ collisions	21
1.4.1	Quarkonium pair production in SPS	22
1.4.2	Quarkonium pair production in DPS	25
1.5	Decays of the $B_c^+$ meson	26
1.6	$B_c$ spectroscopy	29
Chapter 2	The LHCb experiment	30
2.1	The LHC	30
2.2	The LHCb detector	33
2.2.1	Tracking	35
2.2.2	Particle identification	44
2.2.3	Trigger	55
2.2.4	Data processing and simulation	59
Chapter 3	$J/\psi$ production in $pp$ collisions at $\sqrt{s} = 13$ TeV	61
3.1	Analysis strategy	61
3.2	Dataset	62
3.3	Candidate selection	63
3.4	Signal extraction	64

3.4.1	Determination of inclusive $J/\psi$ signal yield.....	65
3.4.2	Separation of prompt and detached $J/\psi$ candidates.....	65
3.5	Efficiency determination.....	69
3.5.1	Geometrical acceptance .....	69
3.5.2	Reconstruction and selection efficiency .....	70
3.5.3	Muon identification efficiency .....	73
3.5.4	Trigger efficiency .....	74
3.5.5	Total efficiency .....	75
3.6	Systematic uncertainties .....	76
3.6.1	Signal mass shape .....	76
3.6.2	Fit to $t_z$ .....	76
3.6.3	MuonID efficiency.....	77
3.6.4	Track reconstruction efficiency .....	77
3.6.5	Spectrum of $p_T$ and $y$ .....	78
3.6.6	Offline selection efficiency .....	78
3.6.7	Trigger efficiency .....	79
3.6.8	Polarisation scenarios .....	80
3.6.9	Other systematic uncertainties .....	82
3.6.10	Summary of systematic uncertainties.....	83
3.7	Results .....	83
3.7.1	$J/\psi$ production cross-sections.....	83
3.7.2	Fraction of $J/\psi$ from $b$ .....	85
3.7.3	$b\bar{b}$ production cross-section .....	86
3.7.4	Comparison with low energy cross-sections .....	86
3.7.5	Comparison with theoretical models .....	89
Chapter 4	$J/\psi$ pair production in $pp$ collisions at $\sqrt{s} = 13$ TeV .....	92
4.1	Analysis strategy .....	92
4.2	Dataset.....	93
4.3	Candidate selection .....	93
4.4	Signal extraction .....	96
4.5	Efficiency estimation.....	99
4.5.1	Acceptance efficiency .....	99
4.5.2	Global event cuts efficiency .....	99
4.5.3	Reconstruction and selection efficiency .....	100

4.5.4	Muon identification efficiency .....	102
4.5.5	Trigger efficiency .....	104
4.6	From- $b$ component determination .....	106
4.7	Cross-section determination .....	108
4.8	Systematic uncertainties .....	108
4.8.1	Signal mass shape .....	109
4.8.2	Global event cut efficiency .....	109
4.8.3	Statistical uncertainty of the simulation .....	110
4.8.4	Track detection efficiency .....	110
4.8.5	MuonID efficiency .....	110
4.8.6	Trigger efficiency .....	111
4.8.7	From- $b$ component .....	112
4.8.8	$\chi^2_{\text{DTF}}/\text{ndf}(J/\psi)$ cut efficiency .....	112
4.9	Polarisation scenario .....	112
4.9.1	Other systematic uncertainties .....	114
4.9.2	Summary .....	114
4.10	Results .....	115
4.10.1	Total production cross-section .....	115
4.10.2	Differential production cross-sections .....	117
4.10.3	Separation of the SPS and DPS components .....	119
Chapter 5	Measurement of the branching fraction ratio $\mathcal{B}(B_c^+ \rightarrow \psi(2S)\pi^+)/\mathcal{B}(B_c^+ \rightarrow J/\psi\pi^+)$ .....	127
5.1	Analysis strategy .....	127
5.2	Dataset .....	128
5.3	Candidate selection .....	130
5.3.1	Pre-selection .....	130
5.3.2	Multivariate analysis .....	130
5.4	Determination of signal yields .....	133
5.5	Efficiency estimation .....	137
5.6	Systematic uncertainties .....	139
5.6.1	Signal shape .....	139
5.6.2	Background shape .....	140
5.6.3	Simulation statistics .....	141
5.6.4	Lifetime of $B_c^+$ .....	141

5.6.5 Data and simulation discrepancy .....	141
5.6.6 Trigger efficiency .....	142
5.6.7 Summary .....	145
5.7 Results and comparison to theories .....	145
<b>Chapter 6 Search for excited <math>B_c^+</math> states</b> .....	<b>147</b>
6.1 Analysis strategy .....	147
6.2 Dataset .....	148
6.3 Candidate reconstruction and selection .....	148
6.3.1 Reconstruction and selection of $B_c^+ \rightarrow J/\psi \pi^+$ .....	148
6.3.2 Reconstruction and selection of $B_c^{(*)}(2S)^+ \rightarrow B_c^{(*)+} \pi^+ \pi^-$ .....	150
6.4 Upper limit .....	152
6.4.1 Efficiency calculation .....	156
6.4.2 Background estimation .....	157
6.4.3 Systematic uncertainties .....	158
6.4.4 Upper limit calculation .....	160
6.4.5 Result .....	162
<b>Chapter 7 Summary and prospects</b> .....	<b>164</b>
<b>References</b> .....	<b>167</b>
<b>Acknowledgments</b> .....	<b>176</b>
<b>Declaration</b> .....	<b>177</b>
<b>Appendix A Fits to the differential <math>J/\psi</math> pair production cross-sections with SPS and DPS predictions</b> .....	<b>178</b>
<b>Appendix B Comparison of the BDT input variable distributions for the <math>B_c^+ \rightarrow J/\psi \pi^+</math> and <math>B_c^+ \rightarrow \psi(2S) \pi^+</math> decays</b> .....	<b>186</b>
<b>Resume and Publications</b> .....	<b>195</b>

## Denotation

QCD	Quantum chromodynamics
SM	Standard Model
EW	Electroweak
PDF	Parton distribution function
LQCD	Lattice QCD
OPE	Operator product expansion
LHC	Large Hadron Collider
CSM	Colour-singlet model
NRQCD	Non-relativistic QCD
CO	Colour-octet
LDME	Long-distance matrix element
LO	Leading-order
NLO	Next-to-leading-order
NNLO	Next-to-next-leading-order
QGP	Quark-gluon plasma
LINAC	Linear Particle Accelerator
PSB	Proton Synchrotron Booster
PS	Proton Synchrotron
SPS	Super Proton Synchrotron
Run1	First run of the LHC
Run2	Second run of the LHC
VELO	Vertex locator
RICH	Ring-imaging Cherenkov detector
TT	Tracker turicensis
IT	Inner tracker
OT	Outer tracker
SPD	Scintillator pad detector
PSD	Preshower detector
ECAL	Electromagnetic calorimeter
HCAL	Hadronic calorimeter
PID	Particle identification

IP	Impact parameter
PV	Primary vertex
HPD	Hybrid photon detector
MWPC	Multi-wire proportional chamber
GEM	Gas electron multiplier
EFF	Event filter farm
FOI	Field of interest
DST	Data summary tape
CB	Crystal Ball
GEC	Global event cut
DSCB	Double-sided Crystal Ball
MagDown	Magnet pointing downwards
MagUp	Magnet pointing upwards

## Chapter 1 Introduction

Particle physics studies the basic elements of matter and the interactions between them. Up to now, the most widely accepted fundamental theory of particle physics is the Standard Model (SM). It classifies all the known elementary particles, as shown in Fig. 1.1, and describes the electromagnetic, the weak and the strong interactions among the four fundamental forces of nature, except the gravitation. Quantum chromodynamics (QCD), which describes the strong interaction, is a crucial component in the SM. It is not fully understood due to the non-perturbative nature at low energies. Various phenomenological QCD models, which rely on experimental results as inputs, are established to describe processes involving QCD. A large number of measurements have been performed over the years, leading to a significant development of the QCD theory. The measurements presented in this dissertation are part of the experimental efforts to promote the understanding of QCD.

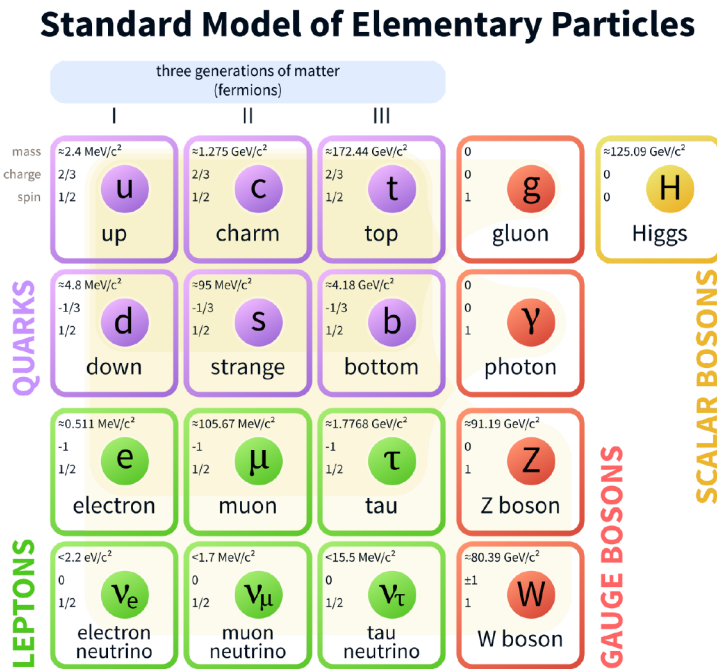


Figure 1.1 Summary of the elementary particles in the SM.

## 1.1 The Standard Model

### 1.1.1 History

Back to the mid-twentieth century, hadrons like protons, neutrons, pions, kaons and some hyperons have been observed. In 1964, the quark model was put forth by Murray Gell-Mann and George Zweig<sup>[1]</sup> to classify all hadrons in terms of quarks. Initially, only the up ( $u$ ), down ( $d$ ) and strange ( $s$ ) quarks were introduced. In the quark model, hadrons are divided into two categories: a) mesons, which consist of a quark and an antiquark, *e.g.* the  $\pi^+$  meson ( $u\bar{d}$ ); b) baryons, which consist of three quarks, *e.g.* the proton ( $uud$ ). In 1967, Steven Weinberg and Abdus Salam independently developed Sheldon Glashow's idea of unifying the electromagnetic and weak interactions into the electroweak (EW) interaction, and incorporated the Higgs mechanism into it as the electroweak symmetry breaking mechanism<sup>[2–4]</sup>. The EW theory predicted the existence of the  $W^\pm$  and  $Z^0$  bosons, which mediate the weak interaction, as well as the Higgs boson, which explains the non-zero masses of fermions and gauge bosons. In 1970, a fourth quark, known as the charm ( $c$ ) quark now, was proposed to explain the suppression of the  $K^+ \rightarrow \pi^+ \nu \bar{\nu}$  decay via the GIM mechanism<sup>[5]</sup>. In 1973, QCD, the gauge field theory defining the strong interaction between quarks and gluons, was formulated. In the same year, Makoto Kobayashi and Toshihide Maskawa introduced the third generation of quarks to the GIM mechanism to explain the observed CP violation in the kaon decay<sup>[6]</sup>. These persistent developments led to the formal establishment of the SM in 1974.

Since then, the world has witnessed the unprecedented success of the SM. In the famous “November Revolution” in 1974, the observation of the  $J/\psi$  meson by two independent experiments headed by Burton Richter and Samuel Ting confirmed the existence of the  $c$  quark<sup>[7,8]</sup>. Hereafter, the  $\tau$  lepton, the bottom ( $b$ ) quark, the  $W^\pm$  and  $Z^0$  bosons and the top ( $t$ ) quark were discovered one after another<sup>[9–14]</sup>, and the measurements proved that there are three and only three generations of fermions. The last missing block of the SM, the Higgs boson, was observed in 2012 at CERN<sup>[15,16]</sup>, showing a good agreement with the SM prediction. Despite the prosperous experimental confirmations, the SM is believed to be an incomplete theory. It doesn't incorporate the gravitation, includes no dark matter candidate, and can't explain some phenomena like baryon asymmetries in the universe. Driven by the desire to solve these problems, numerous efforts are ongoing in both the theoretical and experimental communities.

### 1.1.2 Overview

In the SM, matter is made of three generations of quarks ( $u$ ,  $d$ ,  $c$ ,  $s$ ,  $t$  and  $b$ ), three generations of leptons ( $e$ ,  $\nu_e$ ,  $\mu$ ,  $\nu_\mu$ ,  $\tau$ ,  $\nu_\tau$ ) and their antiparticles. The term “flavour” is used to indicate the species of the quarks and leptons. The  $c$ ,  $b$  and  $t$  quarks are called heavy quarks, as their masses are significantly larger than those of the  $u$ ,  $d$  and  $s$  quarks. The gluon, the photon and the  $W^\pm$  and  $Z^0$  bosons mediate the strong, the electromagnetic and the weak interactions, respectively. The Higgs boson generates masses for the massive fundamental particles. The electromagnetic force acts on particles with electric charge. All the elementary fermions experience the weak interaction, with which their flavours are changed. The strength of the weak force is around four orders of magnitude smaller than that of the electromagnetic force. The strong force occurs only between quarks and gluons, and has a strength of around 60 times that of the electromagnetic force at the femtometre scale. The gravitation force applies to all particles with masses, and has the smallest strength of approximately  $10^{-41}$  that of the electromagnetic force at the femtometre scale.

### 1.1.3 Formulation of the SM

The SM can be formulated in the mathematical framework of the quantum field theory. The construction of the SM is based on the gauge group  $SU(3) \times SU(2) \times U(1)$ , in which  $SU(3)$  is the gauge symmetry of the strong interaction, and the  $SU(2) \times U(1)$  component represents the EW interaction.

The  $U(1)$  and the  $SU(2)$  gauge groups conserve the weak hypercharge and the weak isospin, respectively, but their symmetries are broken by the interaction with the Higgs field. As a result, only a specific combination of the weak hypercharge and the weak isospin, *i.e.* the electric charge, is conserved. The Higgs mechanism creates masses for the three gauge bosons of the  $SU(2)$  group, *i.e.* the  $W^\pm$  and  $Z^0$  bosons, while the mediator of the  $U(1)$ , the photon, remains massless. The strength of the electromagnetic force is determined by the gauge coupling  $\alpha$ , which gets larger with increasing four-momentum transfer  $Q^2$  and is about  $1/137$  when  $Q^2 = 0$ . The small value of  $\alpha$  enables the application of perturbation theory. The strength of the weak force between leptons depends on the coupling constant  $\alpha_w$ , which is close to  $\alpha$  and the perturbation theory is also applicable. For quarks, the weak force strength also relies on the CKM matrix, in which there is a phase angle responsible for the CP violation. The  $\alpha$ ,  $\alpha_w$  and CKM matrix have been measured to a high precision.

Under the SU(3) symmetry of the strong interaction, the colour charge is conserved. The quarks experiencing the strong force have three types of colour charges: red, green and blue; while the antiquarks carry the three corresponding anticolours. The strong force is mediated by eight types of gluons in an octet, which carry simultaneously colour and anticolour. Unlike the EW force, the coupling constant of the strong force,  $\alpha_s$ , increases with decreasing  $Q^2$ . At low energy scale, it becomes so large that the perturbation theory is no longer applicable. This significantly complicates the predictions for QCD involved processes, as the calculation of non-perturbative QCD remains a puzzle today. An accurate understanding of QCD is necessary for both the validation of the SM and the search for new physics, thus is of high importance and has triggered a wide range of theoretical and experimental studies of QCD.

## 1.2 QCD

### 1.2.1 QCD Lagrangian

The Lagrangian of QCD is

$$\mathcal{L} = \sum_f \bar{q}_{f,i} \left( i \left( \gamma^\mu D_\mu \right)_{ij} - m_q \delta_{ij} \right) q_{f,j} - \frac{1}{4} G_{\mu\nu}^a G_a^{\mu\nu}, \quad (1-1)$$

in which the repeated indices are summed over<sup>[17]</sup>. The  $q_{f,i}$  is the space-time Dirac spinor field for the quark indexed by the flavour  $f$  and the colour  $i$ . The  $\gamma^\mu$  represent the Dirac  $\gamma$ -matrices. The  $D_\mu$  is the gauge-covariant derivative, equal to  $\partial_\mu + igA_\mu$ , where  $A_\mu = (\phi, \mathbf{A})$  is the SU(3) gauge field, and  $g$  is the QCD coupling constant related to  $\alpha_s$  according to  $\alpha_s \equiv g^2/4\pi$ . The  $m_q$  is the quark mass. The  $G_{\mu\nu}$  is the gluon field-strength tensor given by

$$G_{\mu\nu}^a = \partial_\mu A_\nu^a - \partial_\nu A_\mu^a + g f^{abc} A_\mu^b A_\nu^c, \quad (1-2)$$

where  $f^{abc}$  are the structure constants of the SU(3) group<sup>[17]</sup>. The fundamental parameters in QCD are the coupling constant  $\alpha_s$  and the quark masses.

As mentioned above, the coupling  $\alpha_s$  increases when the energy scale gets smaller. This behaviour can be revealed by two key properties of QCD: the colour confinement and the asymptotic freedom. The colour confinement is the phenomenon that particles carrying colour charge, including (anti)quarks, gluons, and (anti)quark pairs, can never

be isolated. It is due to the fact that the strong force between two colour charged particles approximates a constant as they are separated. The energy, which is proportional to the separation, continuously increases, and eventually produces a new quark-antiquark pair. The colour confinement has not yet been proved theoretically, but is validated by all the experiments so far. The asymptotic freedom is the property that the strong interaction becomes asymptotically weaker as the energy scale gets larger. The discovery of the asymptotic freedom is a relevant promotion in QCD. It makes the perturbative calculation possible in QCD processes at large energy scale.

The determination of  $\alpha_s$  is dependent on the QCD renormalisation, which is a technique used to treat the divergences arising in the calculations of physical observables, thus relies on the renormalisation scheme and scale. In the framework of perturbative QCD, when the renormalisation scale  $\mu_R$  is varied, the change of  $\alpha_s$  is given by the renormalisation group equation

$$\mu_R^2 \frac{d\alpha_s}{d\mu_R^2} = \beta(\alpha_s) = -(b_0\alpha_s^2 + b_1\alpha_s^3 + b_2\alpha_s^4 + \dots), \quad (1-3)$$

where  $b_0 = (33 - 2n_f)/(12\pi)$  and the coefficients for higher order terms of  $\alpha_s$  are dependent on the renormalisation scheme<sup>[17]</sup>. The value  $n_f$  is the number of quark flavours that can contribute to the vacuum fluctuation under the given energy scale. Considering only the  $b_0$  term in an energy range in which the value  $n_f$  is constant for simplicity, Eq. 1-3 gives  $\alpha_s(\mu_R^2) = (b_0 \ln(\mu_R^2/\Lambda_{\text{QCD}}^2))^{-1}$ . Here  $\Lambda_{\text{QCD}}$  inherits the dependence on the arbitrary starting renormalisation scale. The  $\Lambda_{\text{QCD}}$  parameter is the dividing scale of the perturbative and non-perturbative QCD, and can only be determined from experiments. For  $n_f = 3$  in the most widely used modified minimal subtraction ( $\overline{\text{MS}}$ ) scheme, measurements give  $\Lambda_{\text{QCD}} \approx 250 \text{ MeV}$ . For the energy region with  $|Q| \gg \Lambda_{\text{QCD}}$ ,  $\alpha_s$  tends to zero as indicated by the asymptotic freedom. For  $|Q| \leq \Lambda_{\text{QCD}}$ , QCD can no longer be treated perturbatively and Eq. 1-3 becomes invalid. A summary of the measured  $\alpha_s$  values at different energy scales,  $Q$ , is given in Fig. 1.2. The value of  $\alpha_s$  increases rapidly with  $Q$  when the energy goes down near  $\Lambda_{\text{QCD}}$ , and has been measured down to the energy scale of near 1 GeV.

### 1.2.2 QCD predictions on experimental observables

Theoretical predictions of QCD should be focused on observables measurable in experiments. The observables simplest to calculate are the fully inclusive cross-sections with no hadron in the initial state, *e.g.* the total cross-section of  $e^-e^+ \rightarrow \text{hadrons}$ . Energetic

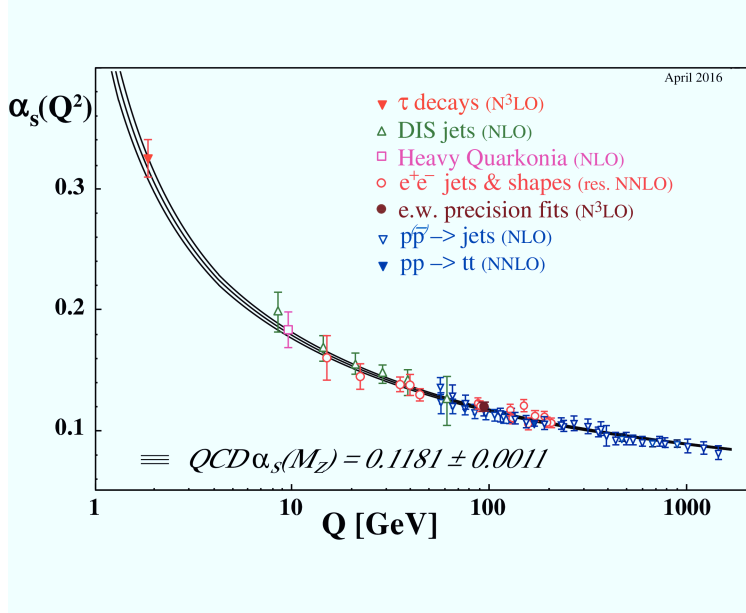


Figure 1.2 Summary of the measured  $\alpha_s$  values at different energy scales,  $Q$ . Figure taken from Ref. [17].

quarks are produced in the  $e^-e^+$  hard scattering, then undergo fragmentations into many subsequent quarks and gluons. The transition of the quarks and gluons into hadrons, *i.e.* the hadronisation process, only occurs on a later time scale. Substantially, it will not affect the features of the hard scattering. Since no knowledge of the details in the final state is required, the QCD prediction for the total cross-section can be dealt with the perturbation theory. The predictions for the inclusive cross-sections with no hadron in the initial state have been tested to a good precision.

The predictions for the fully inclusive cross-sections of processes with initial-state hadrons are more complicated, since they require the hadron structure functions as inputs. Deep-inelastic scattering (DIS) experiments exhibit that hadrons are composed of point-like constituents, named partons, which are indeed quarks and gluons. Parton distribution functions (PDFs) define the momentum distributions of the various kinds of partons within the hadron. They are usually determined within the collinear factorization framework. In such a frame, all the partons' momentum components transverse to the hadron momentum are considered to be negligible. The PDF of a certain parton  $a$  in the hadron  $h$  is defined as  $f_{a/h}(x)$ , in which  $x$  is the fraction of the longitudinal momentum of the hadron carried by the parton. The PDFs are not calculable in perturbative QCD, since the confinement of partons inside the hadron is a consequence of the non-perturbative nature of QCD. Theoretical extraction of PDFs using non-perturbative methods is very difficult, and such

attempts have just began in recent years. At present, the practical PDFs are all determined from experiments. The good thing is that PDFs are universal as long as the same factorization scheme is applied, which allows for the usage of PDFs determined from DIS in other processes. Apart from the PDFs, the predictions for the inclusive cross-sections with initial-state hadrons can also be managed perturbatively.

For observables other than the fully inclusive cross-sections, it is inevitable to encounter non-perturbative QCD due to the non-perturbative nature of hadron structures. The predictions for them can be carried out using non-perturbative methods, among which the most popular approaches are the lattice QCD (LQCD) and QCD sum rules. They both can be used to determine some fundamental QCD parameters, and have successfully reproduced a series of hadronic observables. However, their applications are still quite limited due to some intrinsic constraints. The most widely used method is to create phenomenological models based on the QCD factorization, which enables the application of rigorous perturbative calculation. An overview of LQCD, QCD sum rules and the QCD factorization is given in the following.

- **Lattice QCD**

LQCD is implemented on the basis of the Euclidean path integral formulation, in which expectation values of physical observables are obtained from the integrals of functions in the Euclidean space-time<sup>[17]</sup>. The QCD Lagrangian,  $\mathcal{L}_{\text{QCD}}$ , enters the functions in the form of  $\exp(\int d^4t \mathcal{L}_{\text{QCD}})$ . To calculate the integral numerically, the Euclidean space-time is discretized with a lattice spacing  $a$ . The quark and the gluon fields, contained in  $\mathcal{L}_{\text{QCD}}$ , are defined on the lattice sites and on the links between two adjacent sites, respectively. As the spacing  $a$  is suppressed to zero, the continuum QCD is recovered. There are many ways to perform the discretization. They should preserve the key properties of QCD, and should give the same results for the limit  $a \rightarrow 0$ . The uncertainties of the LQCD calculations mainly come from the numerical computation of the integral and the non-vanishing values of the spacing  $a$ . However, the decrease of the lattice spacing will lead to the increase of the consumption of computational resources.

- **QCD sum rules**

In QCD sum rules, hadrons are described by the interpolating currents of the constituent quarks. The correlator of the currents, based on the quark-level calculations, can be constructed. Through the operator product expansion (OPE), the short- and

long-distance components of the correlator are separately determined<sup>[18]</sup>. The short-distance terms can be calculated perturbatively, while the long-distance terms involving the universal quark and gluon condensates are parameterised in powers of the squared momentum. Via the dispersion relation, the quark-level correlator can be related to a counterpart calculated using physical hadronic parameters<sup>[18]</sup>. Usually, an ansatz for the hadronic spectrum is needed to separate different hadronic states, *e.g.* assuming the spectrum is composed of a first resonance and a continuum of the higher states. By matching the two expressions of the correlator, *i.e.* the one determined from the OPE and the counterpart obtained from the dispersion relation, a hadronic quantity can be extracted. Due to the cut-off in the OPE and the approximation in the ansatz for the hadronic spectrum, the method of QCD sum rules suffers an uncertainty as large as of 10-20%.

- **QCD factorization**

QCD processes at high energies almost unavoidably involve both partonic and hadronic level physics, thus cover multiple energy scales. The QCD factorization theorem assumes that the short- and long-distance processes can be factorized completely, with no interference that will affect the observables. The short-distance component can be determined using the perturbation theory, while the non-perturbative terms describing the long-distance process can be extracted from experimental measurements if they have a smaller number of freedom than the experiments. The long-distance terms are considered universal, thus can be used to predict other experiments.

### 1.2.3 Quarkonia and $B_c$ mesons

Heavy quarkonia, which are flavourless mesons made of a heavy quark and its antiquark, and the  $B_c$  mesons, which are composed of the  $\bar{b}$  and  $c$  quarks<sup>①</sup>, are ideal systems for the study of QCD. Both heavy quarkonia and the  $B_c$  mesons can be treated as non-relativistic systems, because the typical velocities of the heavy quarks inside them are small in the reference frame of the mesons. Due to the non-relativity, the calculations of the quarkonium (pair) production in proton-proton ( $pp$ ) collisions are significantly simplified, and the quark potential model is valid to describe the  $B_c$  mesons.

Quarkonium can be classified as charmonium and bottomonium, whose constituents

---

<sup>①</sup> The  $B_c$  meson refers to the whole  $B_c$  meson family, while the  $B_c^+$  meson represents the ground state of the  $B_c$  meson family. Charge conjugation is implied throughout the dissertation.

are  $c\bar{c}$  and  $b\bar{b}$ , respectively. There is no toponium since the lifetime of the  $t$  quark is too short to form a bound state. The spectroscopy of the charmonium system<sup>[17]</sup> is shown in Fig. 1.3. The states are defined by the spectroscopic notation  $n^{2S+1}L_J$ , where  $n = 1, 2, \dots$  is the radial quantum number,  $S = 0, 1, 2, \dots$  is the total spin,  $L = 0, 1, 2, \dots$  is the relative angular momentum (usually denoted as  $L = S, P, D, \dots$ ), and  $J$  denotes the total angular momentum<sup>[17]</sup>. The charge conjugation and parity quantum numbers of the states are determined according to  $C = (-1)^{L+S}$  and  $P = (-1)^{L+1}$ . The singlet states are named  $\eta_c$  and  $h_c$ , and the triplet states  $\psi$  and  $\chi_{cJ}$ . The quantum numbers, except the radial quantum number and the relative angular momentum, are omitted from the denotation. For example,  $\eta_c(2S)$  is the  $2^1S_0$  state with  $n = 2, S = 0, L = 0, J = 0, P = -1$  and  $C = +1$ . The lowest  $\psi$  state is denoted as  $J/\psi$  as a matter of convention. The bottomonium system is organised in a similar way. The singlet states are named  $\eta_b$  and  $h_b$ , and the triplet states  $\Upsilon$  and  $\chi_{bJ}$ . The  $B_c$  meson family is also predicted to have a rich spectroscopy, as shown in Fig. 1.4 according to the prediction in Ref. [19]. However, apart from the ground state  $B_c^+$ , only the  $B_c(2S)^+$  state is observed by the ATLAS experiment in 2014<sup>[20]</sup>.

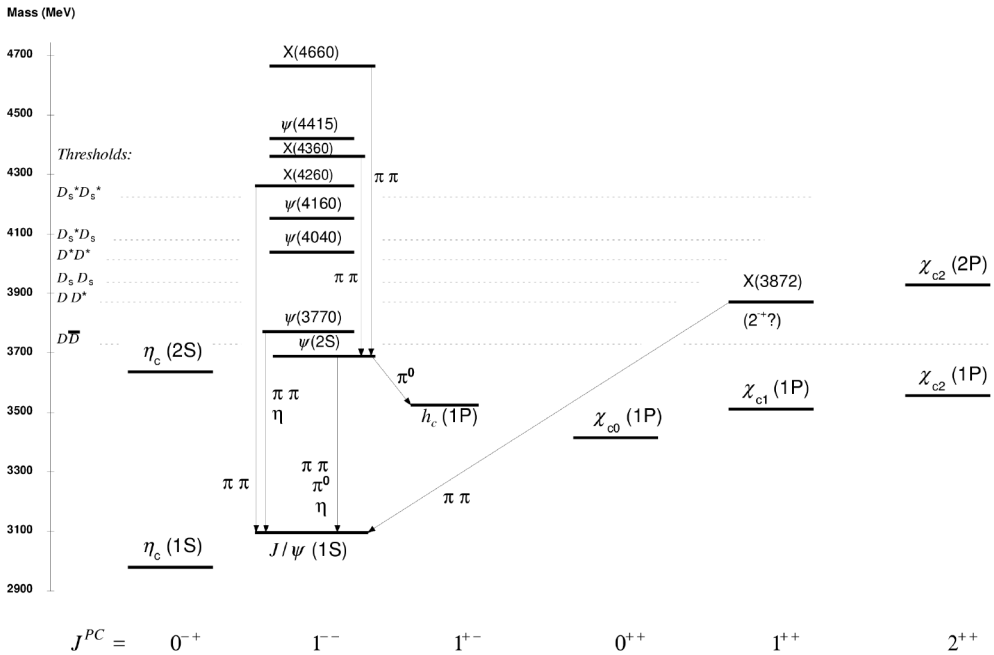


Figure 1.3 Spectroscopy of the charmonium system. The solid lines represent the observed states. Figure taken from Ref. [17].

This dissertation presents experimental studies of charmonia and  $B_c$  mesons with data samples of  $pp$  collisions collected by the LHCb detector at the Large Hadron Collider

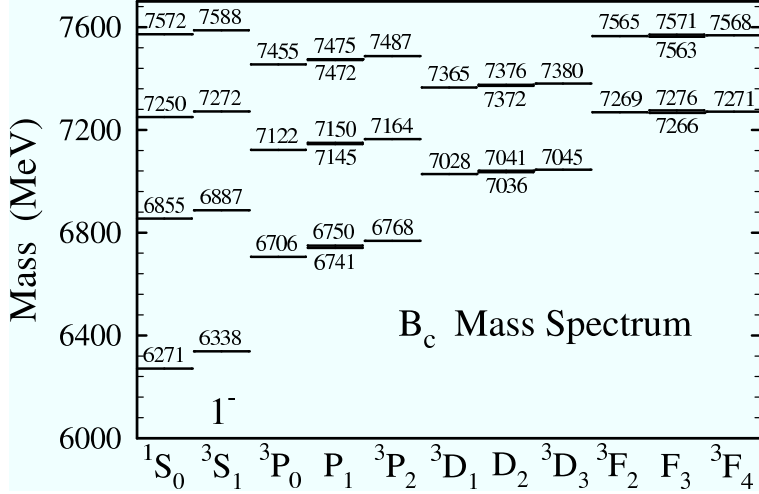


Figure 1.4 Prediction for the  $B_c$  mass spectrum according to Ref. [19].

(LHC): measurements of production cross-sections of  $J/\psi$  mesons and  $J/\psi$  pairs at the centre-of-mass energy of  $\sqrt{s} = 13$  TeV; the measurement of the branching fraction ratio  $\mathcal{B}(B_c^+ \rightarrow \psi(2S)\pi^+)/\mathcal{B}(B_c^+ \rightarrow J/\psi\pi^+)$ ; and the search for the excited  $B_c(2S)^+$  states in the  $B_c^+\pi^+\pi^-$  mass spectrum. They can provide valuable tests on the QCD models from both the perturbative and non-perturbative aspects.

### 1.3 Quarkonium production in proton-proton collisions

The mechanism of quarkonium production remains an intriguing puzzle after over forty years of theoretical and experimental researchs. There are four energy scales involved in the production of a quarkonium: the hard-scattering scale  $Q_{\text{hard}}$ , at which the quark-antiquark ( $Q\bar{Q}$ ) pair is produced; the masses of the heavy quarks  $m_Q$ , which set the scale of the kinematic threshold of the  $Q\bar{Q}$  production; the momentum of either heavy quark in the rest frame of the heavy quarkonium  $m_Q v$ , which is at the scale of the inverse of the quarkonium size; and the binding energy of the heavy quarkonium  $m_Q v^2$ . The quark masses are estimated to be  $m_c = 1.28 \pm 0.03 \text{ GeV}/c^2$  and  $m_b = 4.18_{-0.03}^{+0.04} \text{ GeV}/c^2$ <sup>[17]</sup>. The scale  $m_Q v^2$  is related to the mass splitting in the heavy quarkonium spectrum, which gives  $v^2 \simeq 0.3$  and  $v^2 \simeq 0.1$  for charmonium and bottomonium, respectively. The hierarchy of the multiple scales and the intrinsic QCD scale  $\Lambda_{\text{QCD}}$  is typically

$$Q_{\text{hard}} > m_Q \gg m_Q v > m_Q v^2 > \Lambda_{\text{QCD}}. \quad (1-4)$$

In consequence, the quarkonium production can be described in terms of two factorized stages: the short-distance production of the  $Q\bar{Q}$  pair at the  $Q_{\text{hard}}$  scale, which can be calculated perturbatively; and the long-distance hadronisation of the  $Q\bar{Q}$  pair into the heavy quarkonium state at the scales of  $m_Q v$  and  $m_Q v^2$ , which is a non-perturbative process. For a quarkonium with the transverse momentum  $p_T \gtrsim m_Q$ , the soft gluon exchanges between the two processes can be neglected. For a certain  $Q\bar{Q}$  pair, the shape of the  $p_T$  spectrum of the eventual quarkonium largely depends on the perturbative short-distance process, while its contribution to the quarkonium production cross-section significantly rests upon the the non-perturbative hadronisation process. The non-perturbative terms describing the hadronisation process have a number of freedom smaller than that of the quarkonium  $p_T$  spectrum in experiments. Therefore, measurements of the quarkonium  $p_T$  spectra can help fix the non-perturbative terms and test the perturbative calculations.

The colour-singlet model (CSM) under the non-relativistic QCD (NRQCD) framework was first proposed to describe quarkonium producion. In CSM, the initial  $Q\bar{Q}$  pair is assumed to be colourless and to have the same  $J^{PC}$  quantum numbers as the eventual quarkonium. Here  $J$ ,  $P$  and  $C$  stand for the total angular momentum, the parity and the charge conjugation, respectively. These quantum numbers are strictly conserved in strong interaction. The CSM was later extended to include the colour-octet (CO) contributions as well. When one refers to the NRQCD approach, it means both the colour-singlet and colour-octet contributions are included.

### 1.3.1 The NRQCD approach

#### 1.3.1.1 NRQCD Lagrangian

NRQCD is an effective field theory of QCD. In the NRQCD framework, contributions larger than the  $m_Q$  energy scale are integrated out. As given in Eq. 1-1, heavy quarks are described by space-time Dirac spinor fields in the full QCD. The integration for the higher energy scales of the QCD Lagrangian is very complicated in practice. As a result, the Lagrangian of NRQCD is usually obtained by writing down all interactions consistent with the QCD symmetries, including the SU(3) gauge symmetry, the rotational symmetry, and the CP symmetry. The procedure starts with an ultraviolet momentum cut-off  $\Lambda$  at the order of  $m_Q$ . It is valid for heavy quarkonium since the non-perturbative hadronisation process happens at the energy scale of  $m_Q v$  or less. The eliminated relativistic interactions happen at short distances, thus can be compensated by adding local interaction terms to the

Lagrangian. Under the non-relativistic assumption, the next step is to block-diagonalize the relativistic Dirac field theory, which leads to a non-relativistic Schrödinger field theory with two two-component Pauli spinor fields for the heavy quarks and antiquarks, respectively. The resulting Lagrangian of NRQCD is

$$\mathcal{L}_{\text{NRQCD}} = \mathcal{L}_{\text{light}} + \mathcal{L}_{\text{heavy}} + \delta\mathcal{L}, \quad (1-5)$$

where

$$\mathcal{L}_{\text{light}} = -\frac{1}{2}\text{tr}G_{\mu\nu}G^{\mu\nu} + \sum \bar{q}i\cancel{D}q \quad (1-6)$$

describes the gluons and light quarks,

$$\mathcal{L}_{\text{heavy}} = \psi^\dagger(iD_t + \frac{\mathbf{D}^2}{2m_Q})\psi + \chi^\dagger(iD_t - \frac{\mathbf{D}^2}{2m_Q})\chi \quad (1-7)$$

represents the non-relativistic heavy quarks and antiquarks, and  $\delta\mathcal{L}$  is the correction term to take into account the relativistic effects<sup>[21]</sup>. In Eq. 1-6,  $q$  is the Dirac spinor field for a certain light quark and is summed over all light flavours. In Eq. 1-7,  $D_t$  and  $\mathbf{D}$  are the time and space components of  $D^\mu$  respectively,  $\psi$  is the Pauli spinor field that annihilates a heavy quark, and  $\chi$  is the Pauli spinor field that creates a heavy antiquark. A two-fermion operator containing  $\psi^\dagger$  and  $\chi$  represents the creation of a  $Q\bar{Q}$  pair.

To recover the full QCD, an infinite number of interactions need to be included in  $\delta\mathcal{L}$ . *e.g.*

$$\begin{aligned} \delta\mathcal{L} = & \frac{c_1}{8m_Q^3}(\psi^\dagger(\mathbf{D}^2)^2\psi - \chi^\dagger(\mathbf{D}^2)^2\chi) \\ & + \frac{c_2}{8m_Q^2}(\psi^\dagger(\mathbf{D} \cdot g\mathbf{E} - g\mathbf{E} \cdot \mathbf{D})\psi + \chi^\dagger(\mathbf{D} \cdot g\mathbf{E} - g\mathbf{E} \cdot \mathbf{D})\chi) \\ & + \frac{c_3}{8m_Q^2}(\psi^\dagger(d\mathbf{D} \times g\mathbf{E} - g\mathbf{E} \times i\mathbf{D}) \cdot \sigma\psi + \chi^\dagger(d\mathbf{D} \times g\mathbf{E} - g\mathbf{E} \times i\mathbf{D}) \cdot \sigma\chi) \\ & + \frac{c_4}{2m_Q}(\psi^\dagger(g\mathbf{B} \cdot \sigma)\psi - \chi^\dagger(g\mathbf{B} \cdot \sigma)\chi) + \dots, \end{aligned} \quad (1-8)$$

where  $\mathbf{E}$  and  $\mathbf{B}$  are the electric and magnetic components of  $G^{\mu\nu}$  respectively<sup>[21]</sup>. The parameters  $c_i$  are the short-distance coefficients which can be calculated perturbatively as expansions of  $\alpha_s$  by matching the Lagrangian of QCD and NRQCD. The operators

Table 1.1 Velocity-scaling rules for the operators included in the NRQCD Lagrangian<sup>[21]</sup>.

Operator	Scaling estimate
$\alpha_s$	$v$
$\phi$	$(m_Q v)^{3/2}$
$\chi$	$(m_Q v)^{3/2}$
$D_t$	$m_Q v^2$
<b>D</b>	$m_Q v$
$g\mathbf{E}$	$m_Q^2 v^3$
$g\mathbf{B}$	$m_Q^2 v^4$
$g\phi$	$m_Q v^2$
$g\mathbf{A}$	$m_Q v^3$

are ordered according to the velocity-scaling rules, in which the importance of the terms is evaluated as powers of the quark velocity  $v$ . The  $v$  scalings are derived by requiring consistency of the equations of motion, and are summarised in Table. 1.1 for all the relevant operators, from which one can see the leading term in  $\delta\mathcal{L}$  is suppressed by  $v^2$  compared to  $\mathcal{L}_{\text{heavy}}$ . Practically, the Lagrangian is always truncated at a specific order.

### 1.3.1.2 Quarkonium production in NRQCD

Concerning quarkonium production in  $pp$  collisions, based on QCD factorization, the inclusive production cross-section of a heavy quarkonium  $H$  with certain  $J^{PC}$  quantum numbers can be expressed as

$$\sigma(H) = \sum_n \sigma(pp \rightarrow Q\bar{Q}[n] + X) \times \langle O^H(n) \rangle, \quad (1-9)$$

where  $\sigma(pp \rightarrow Q\bar{Q}[n] + X)$  is the cross-section to produce an  $Q\bar{Q}$  pair labelled by the quantum numbers  $J^{PC}$  and the colour from the  $pp$  collision, the indice  $n$  represents the possible  $^{2S+1}L_J^{[1,8]}$  structure of the  $Q\bar{Q}$  pair, and  $\langle O^H(n) \rangle$  represents the long-distance matrix elements (LDMEs) describing the hadronisation of a specific  $Q\bar{Q}$  state into  $H$ . The superscripts [1] and [8] represent colour-singlet and colour-octet, respectively. The production cross-section of the  $Q\bar{Q}$  state can be determined via

$$\sigma(pp \rightarrow Q\bar{Q}[n] + X) = \sum_{a,b} \int dx_1 dx_2 d\text{LIPS} f_{a/p}(x_1) f_{b/p}(x_2) |\mathcal{A}(ab \rightarrow Q\bar{Q}[n] + X)|^2, \quad (1-10)$$

in which  $a$  and  $b$  are two partons, each inside one proton, from whose interactions the  $Q\bar{Q}[n]$  state is produced,  $x_1$  and  $x_2$  are the longitudinal momentum fractions carried by  $a$  and  $b$ ,  $f_{a/p}(x_1)$  and  $f_{b/p}(x_2)$  are the PDFs for  $a$  and  $b$  in the proton, dLIPS indicates the lorentz-invariant phase space, and  $\mathcal{A}(ab \rightarrow Q\bar{Q}[n] + X)$  is the amplitude of the  $ab \rightarrow Q\bar{Q}[n] + X$  process<sup>[22]</sup>. The PDFs are non-perturbative but universal, thus can be determined from other kinds of experiments. The amplitude  $\mathcal{A}(ab \rightarrow Q\bar{Q}[n] + X)$  can be calculated perturbatively in powers of  $\alpha_s$ , as discussed below for the  $J/\psi$  production as an example.

In  $pp$  collisions at the LHC, heavy quarkonia are predominantly produced from gluon-gluon fusion since gluons take around half of the proton momentum<sup>[23]</sup>. In CSM, the  $Q\bar{Q}$  pair is colourless and has the quantum numbers of  $J^{PC} = 1^{--}$ , thus must couple to at least three gluons according to the Landau-Yang theorem<sup>[24]</sup> at tree-level. So the  $Q\bar{Q}$  state is produced through

$$g + g \rightarrow Q\bar{Q} + g \quad (1-11)$$

at leading-order (LO) in  $\alpha_s$ , as shown on the top left of Fig. 1.5. Its partonic differential cross-section  $d\hat{\sigma}/dp_T^2$  asymptotically scaling as  $\alpha_s^3 \cdot (2m_Q)^4/p_T^8$  when  $p_T \gg 2m_Q$ . The real-emission diagrams at next-to-leading-order (NLO) and next-to-next-to-leading-order (NNLO) are

$$g + g \rightarrow Q\bar{Q} + g + g \quad (1-12)$$

and

$$g + g \rightarrow Q\bar{Q} + g + g + g, \quad (1-13)$$

respectively, as displayed in Fig. 1.5 as well. Their asymptotic scalings are  $\alpha_s^4 \cdot (2m_Q)^2/p_T^6$  and  $\alpha_s^5/p_T^4$ , respectively. The power of  $p_T$  in the denominator decreases from the LO to NNLO, so the high order QCD corrections in CSM are substantial at the high  $p_T$  region.

In the CO model (COM), the  $Q\bar{Q}$  pair can have quantum numbers different from the

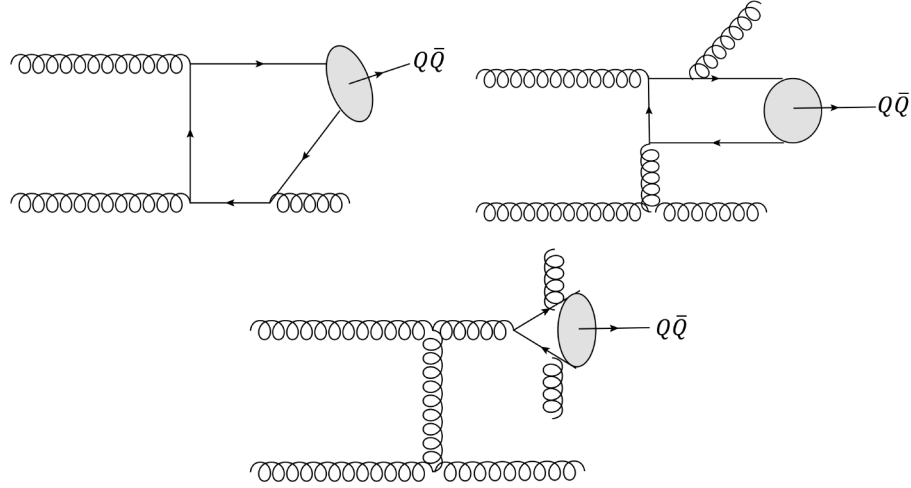


Figure 1.5 Feynman diagrams for the production of the  $Q\bar{Q}$  pair at (top left) LO, (top right) NLO and (bottom) NNLO in  $\alpha_s$  in CSM for the  $J/\psi$  production.

$J/\psi$  meson. At LO with  $p_T \neq 0$ <sup>①</sup>, the  $Q\bar{Q}$  state can be produced through either

$$g + g \rightarrow Q\bar{Q}({}^3S_1^{[8]}) + g \quad (1-14)$$

or

$$g + g \rightarrow Q\bar{Q}({}^3P_J^{[1,8]1}, {}^1S_0^{[8]}) + g, \quad (1-15)$$

in which the  $Q\bar{Q}$  state is coupled to one and two gluons respectively, as shown on the top of Fig. 1.6. The asymptotic scaling in  $p_T$  of  $d\hat{\sigma}/dp_T^2$  of the two processes are determined to be  $\alpha_s^3/p_T^4$  and  $\alpha_s^3 \cdot (2m_Q)^2/p_T^6$ , respectively. The production of the  $Q\bar{Q}$  state at NLO is via

$$g + g \rightarrow Q\bar{Q}({}^3P_J^{[1,8]1}, {}^1S_0^{[8]}) + g + g \quad (1-16)$$

as shown on the bottom of Fig. 1.6, which is scaling as  $\alpha_s^4/p_T^4$ .

In experiments, it is difficult to distinguish the quarkonia produced directly from the parton-parton collisions and from the excited quarkonium decays. As a result, the feed-downs from the  $\psi(2S)$  state and from the  $\chi_{cJ}$  state through the  $\chi_{cJ} \rightarrow J/\psi \gamma$  decays need

① In COM, the  $Q\bar{Q}$  pair can be produced through the processes  $g + g \rightarrow Q\bar{Q}({}^3S_1^{[8]}, {}^3P_J^{[1,8]}, {}^1S_0^{[8]})$ , but they will lead to  $p_T = 0$  under the collinear factorization. The NRQCD approach is not applicable when  $p_T = 0$ , therefore these processes are not taken into account in the calculations.

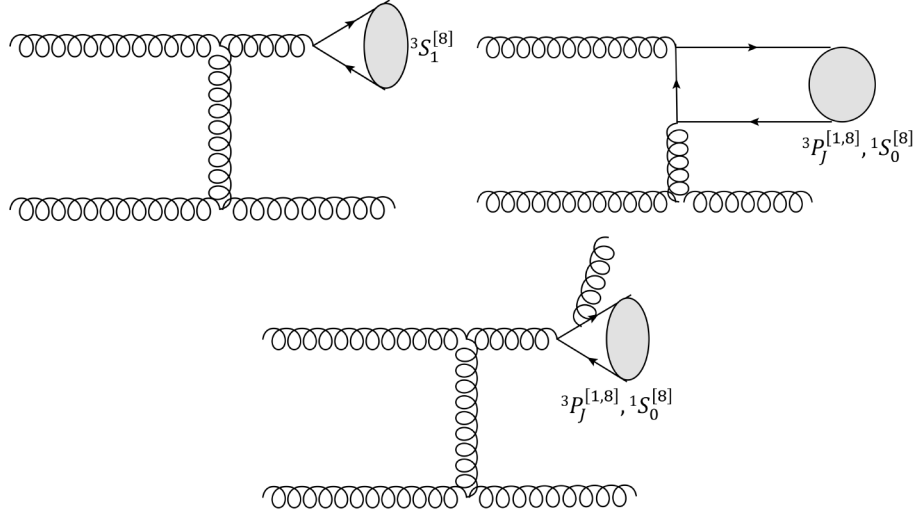


Figure 1.6 Feynman diagrams for the production of the  $Q\bar{Q}$  pair at (top) LO and (bottom) NLO in  $\alpha_s$  in COM for the  $J/\psi$  production.

to be considered in addition to the production from gluon-gluon fusion. The calculations of the  $J/\psi$  production is largely complicated due to the  $\psi(2S)$  and  $\chi_{cJ}$  contributions.

The LDMEs are given by the vacuum matrix elements of the production operators:

$$\langle O^H(n) \rangle = \langle 0 | O_n^H | 0 \rangle. \quad (1-17)$$

The production operators  $O_n^H$ , determined according to the NRQCD Lagrangian, have the generic form

$$O_n^H = \chi^\dagger \mathcal{K}_n \psi \left( \sum_X \sum_{m_J} |H + X\rangle \langle H + X| \right) \psi^\dagger \mathcal{K}'_n \chi, \quad (1-18)$$

where  $\mathcal{K}_n$  and  $\mathcal{K}'_n$  are products of a colour matrix, a spin matrix, a polynomial of  $\mathbf{D}$  and other fields. The colour matrix is determined by the colour of the  $Q\bar{Q}$  pair. For example, one has

$$O^H(1S_0^{[1]}) = \chi^\dagger \psi \left( \sum_X \sum_{m_J} |H + X\rangle \langle H + X| \right) \psi^\dagger \chi, \quad (1-19)$$

in which  $\mathcal{K}_n$  and  $\mathcal{K}'_n$  are both unity. The  $|H + X\rangle$  represents the Fock states, which are the intermediate states of the  $Q\bar{Q}$  pair and the quarkonium. The Fock states can be ranked in powers of  $v$ . Generally, the dominant Fock state is the  $|H\rangle$  state, in which  $H$  denotes the

colour-singlet quark pair with the same  $J^{PC}$  numbers as the quarkonium. For a given  $J^{PC}$ , a mixture between  ${}^3(J-1)_J$  and  ${}^3(J+1)_J$  is allowed. The second dominant component is the  $|H+g\rangle$  state with an extra gluon. Its probability is suppressed by  $\nu^2$ , and higher order states have even smaller probabilities of  $\nu^4$  or higher powers of  $\nu$ . For different  $Q\bar{Q}$  states, the possible Fock states are different.

When  $O_n^H$  is colour-singlet, according to vacuum-saturation approximation<sup>[21]</sup>, the predominant Fock state evolves into the quarkonium without emitting gluons. There is

$$\langle 0 | O_n^H | 0 \rangle \approx \langle 0 | \chi^\dagger \mathcal{K}_n \psi \left( \sum_{m_J} |H\rangle \langle H| \right) \psi^\dagger \mathcal{K}'_n \chi | 0 \rangle. \quad (1-20)$$

Considering that the matrix element is independent of the quantum number  $m_J$  since  $\psi^\dagger \mathcal{K}'_n \chi | 0 \rangle \langle 0 | \chi^\dagger \mathcal{K}_n \psi$  is rotationally invariant, one has

$$\begin{aligned} \langle 0 | \chi^\dagger \mathcal{K}_n \psi \left( \sum_{m_J} |H\rangle \langle H| \right) \psi^\dagger \mathcal{K}'_n \chi | 0 \rangle &= (2J+1) \langle H | \psi^\dagger \mathcal{K}'_n \chi | 0 \rangle \langle 0 | \chi^\dagger \mathcal{K}_n \psi | H \rangle \\ &\approx (2J+1) \langle H | O_n | H \rangle, \end{aligned} \quad (1-21)$$

where  $O_n = \psi^\dagger \mathcal{K}'_n \chi \chi^\dagger \mathcal{K}_n \psi$  are local four-fermion operators derived from  $\delta \mathcal{L}$ . According to the velocity-scaling rules, the operators  $O_n$  can be expanded as powers of  $\nu$ . When  $O_n^H$  is colour-octet, the  $Q\bar{Q}$  need to radiate gluons to form the quarkonium. The contribution at LO in  $\nu$  is given by

$$\langle 0 | O_n^H | 0 \rangle \approx \langle 0 | \chi^\dagger \mathcal{K}_n \psi \left( \sum_{m_J} |H+g\rangle \langle H+g| \right) \psi^\dagger \mathcal{K}'_n \chi | 0 \rangle, \quad (1-22)$$

in which there is one gluon emitted.

Altogether, each LDME is an expansion in powers of  $\nu$ . The predominant Fock states that contribute to the productions of various quarkonia are listed in Table 1.2. The CO contributions are suppressed by the LDMEs. By fitting to the measured quarkonium  $p_T$  spectrum, which have a larger number of freedom, the LDMEs can be determined. The LDMEs are universal for the production of a certain quarkonium, independent of the colliding particles and the collision energy. Thus they can be verified using different types of experiments. Besides, according to the spin symmetry of the heavy quarks, the LDMEs for the production of quarkonia that differ by a spin-flip transition, *e.g.*  $J/\psi$  and  $\eta_c$ , are related. It provides another constraint on the LDMEs.

Table 1.2 Predominant Fock states contributing to the productions of various quarkonia.

$v$ scaling	$\eta_c, \eta_b$	$J/\psi, \psi(2S), \Upsilon$	$h_c, h_b$	$\chi_{cJ}, \chi_{bJ}$
$v^3$	$^1S_0^{[1]}$	$^3S_1^{[1]}$	—	—
$v^5$	—	—	$^1P_1^{[1]}, ^1S_0^{[8]}$	$^3P_J^{[1]}, ^3S_1^{[8]}$
$v^7$	$^1S_0^{[8]}, ^3S_1^{[8]}, ^1P_1^{[8]}$	$^1S_0^{[8]}, ^3S_1^{[8]}, ^3P_J^{[8]}$	—	—

### 1.3.1.3 Relation to quark potential model

In CSM, the LDMEs can be estimated using quark potential model<sup>[22]</sup>, in which the potential between the quark and antiquark is assumed to be instantaneous. The validity of the quark potential model comes from the fact that the interaction time of the gluon exchange between the constituent quark and antiquark is much shorter than the time scale of the quark motion<sup>[21]</sup>. This fact is true only when the meson is non-relativistic.

With a certain potential model, the wave functions of the quarkonia can be calculated from the Schrödinger equation. With the Coulomb-gauge potential, the wave function of  $\eta_c$  is determined to be

$$\Psi_{\eta_c}(\mathbf{x}) = \frac{1}{\sqrt{2N_c}} \langle 0 | \chi^\dagger(-\mathbf{x}/2) \psi(\mathbf{x}/2) | \eta_c \rangle, \quad (1-23)$$

in which the factor  $N_c$  takes into account the sum over all possible spin and colour states<sup>[21]</sup>. According to Eqs. 1-17, 1-19, 1-20 and 1-21, there is

$$\langle O^{\eta_c} (^1S_0^{[1]}) \rangle = \langle 0 | O^{\eta_c} (^1S_0^{[1]}) | 0 \rangle = \langle \eta_c | \psi^\dagger \chi | 0 \rangle \langle 0 | \chi^\dagger \psi | \eta_c \rangle. \quad (1-24)$$

It gives

$$\langle O^{\eta_c} (^1S_0^{[1]}) \rangle = 2N_c \times \Psi_{\eta_c}^2(\mathbf{0}), \quad (1-25)$$

where  $\Psi_{\eta_c}(\mathbf{0})$  is the  $\eta_c$  wave function at origin. The relations between the wave functions and LDMEs for other quarkonia can be determined in similar ways.

### 1.3.1.4 Extension to the $k_T$ factorization method

The NRQCD approach can be extend to the  $k_T$  factorization method, in which the PDFs are determined assuming the  $k_T$  factorization other than the collinear factorization.

The  $k_T$  stands for the fraction of the total transverse momentum carried by a parton. In the  $k_T$  factorization framework, the PDFs depend on the fractions of both the transverse and longitudinal momentum carried by the parton. So far, considering the predictions for quarkonium production, the  $k_T$  factorization method is usually implemented based on CSM. By taking into account the dependence on the transverse momentum, this approach can include some higher-order contributions in  $\alpha_s$  even with the LO LDMEs. However, it suffers from a larger uncertainty since the PDFs are less constrained with one more free parameter.

### 1.3.2 Measurements on quarkonium production

The prosperous experimental studies of the quarkonium production started from the measurement of the  $J/\psi$  and  $\psi(2S)$  production cross-section in  $p\bar{p}$  collisions at  $\sqrt{s} = 1.8$  TeV by the CDF experiment at the Tevatron<sup>[25]</sup>. After that, the production and polarisation of the  $\psi$  and  $\Upsilon(nS)$  mesons were intensively studied at the Tevatron and RHIC. The operation of the LHC opened a new era for the quarkonium study. The centre-of-mass energy of  $pp$  collisions were largely enhanced to 7 TeV in 2010 and 2011, then to 8 TeV in 2012, and later to 13 TeV in 2015. The statistics are significantly increased, which are helpful to give rise to much more precise results. All the four large experiments at the LHC, *i.e.* ATLAS, CMS, LHCb and ALICE, make significant contributions to the quarkonium studies. With the different kinematic coverages and detector features, the measurements from the four experiments complement each other and exhibit a more comprehensive picture of the quarkonium production.

During the first run period of the LHC, the differential production cross-sections of the  $J/\psi$  meson as functions of its  $p_T$  and rapidity ( $y$ ) were measured by the LHCb experiment at the centre-of-mass energies of  $\sqrt{s} = 2.76$  TeV<sup>[26]</sup>, 7 TeV<sup>[27]</sup> and 8 TeV<sup>[28]</sup>. The measurements were performed in the kinematic range of  $p_T < 14$  GeV/ $c$  and  $2.0 < y < 4.5$ . The  $J/\psi$  polarisation was also measured at  $\sqrt{s} = 7$  TeV<sup>[29]</sup>. At ATLAS, the  $J/\psi$  production cross-sections were measured in the range of  $8 < p_T < 110$  GeV/ $c$  and  $|y| < 2.0$  at  $\sqrt{s} = 7$  TeV and 8 TeV<sup>[30]</sup>. At CMS, the production cross-sections were measured for  $J/\psi$  mesons with  $p_T < 50$  GeV/ $c$  and  $|y| < 2.4$  at  $\sqrt{s} = 7$  TeV<sup>[31,32]</sup>. The ALICE experiment measured the differential cross-sections for  $J/\psi$  mesons with  $p_T < 8$  TeV and  $2.5 < y < 4$  at  $\sqrt{s} = 2.76$  TeV<sup>[33]</sup> and 7 TeV<sup>[34]</sup>. All these measurements are consistent with each other in the overlapping kinematic regions. Besides the  $J/\psi$

meson, the production cross-sections and polarisations of the  $\psi(2S)$  and  $\Upsilon(nS)$  mesons are measured by these experiments in the kinematic ranges similar to the  $J/\psi$  meson. There are also measurements of the production cross-sections of the  $\chi_c$  or  $\chi_b$  mesons relative to the cross-sections of the  $\psi$  or  $\Upsilon$  mesons<sup>[35,36]</sup>. The  $\chi_c$  measurements can not only provide a new way to test the theoretical predictions, but also help understand the production and polarisation of the  $J/\psi$  meson, since the feed-down from  $\chi_c$  is a substantial source of the prompt  $J/\psi$  production and significantly affect the polarisation measurement of the  $J/\psi$  meson. In 2014, the production cross-section of the  $\eta_c(1S)$  meson in  $pp$  collisions relative to that of the  $J/\psi$  meson was measured for the first time by LHCb at  $\sqrt{s} = 7$  TeV and 8 TeV<sup>[37]</sup>. This measurement is highly important as the  $\eta_c$  production cross-section is related to that of the  $J/\psi$  meson according to the spin symmetry in the NRQCD approach.

The measurement of the  $J/\psi$  production cross-sections in the kinematic range of  $p_T < 14$  GeV/ $c$  and  $2.0 < y < 2.5$ , using the  $pp$  collision data collected in 2015 at  $\sqrt{s} = 13$  TeV, is presented in Chapter 3. At the CMS experiment, the  $J/\psi$  production cross-sections at  $\sqrt{s} = 13$  TeV were measured for the kinematic range of  $20 < p_T < 120$  GeV/ $c$  and  $|y| < 1.2$ <sup>[38]</sup>.

### 1.3.3 Comparisons between predictions and measurements

The measurements of the  $J/\psi$  and  $\psi(2S)$  productions by CDF showed that the CSM predictions at LO underestimated the cross-sections at high  $p_T$  by more than one order of magnitude<sup>[25]</sup>, as seen in Fig. 1.7. The NLO calculations of the CSM provide large corrections to the LO results, but still not satisfactory in describing neither the production cross-sections nor the polarisation. Nevertheless, the next-to-next-to-leading-order (NNLO) calculations of the CSM give a new lease of life to the CSM. The calculations at NNLO succeed in describing the  $\psi(2S)$  production cross-section from LHCb at  $\sqrt{s} = 7$  TeV<sup>[39]</sup>, as shown in Fig. 1.8. But there is still a long way to describe all the measurements of production and polarisation using the CSM.

In the NRQCD approach, the agreements between the calculations and the measurements are largely improved by including the CO contributions. As an example, the NLO NRQCD calculations from two groups<sup>[40?]</sup> agree well with the data, as shown in Fig. 1.8. However, problems arise when it comes to the polarisation. The NRQCD approach at LO predicts a large transverse polarisation for prompt  $J/\psi$  mesons, while all the measurements at the LHC indicate a polarisation consistent with zero<sup>[41–44]</sup>. Fig. 1.9

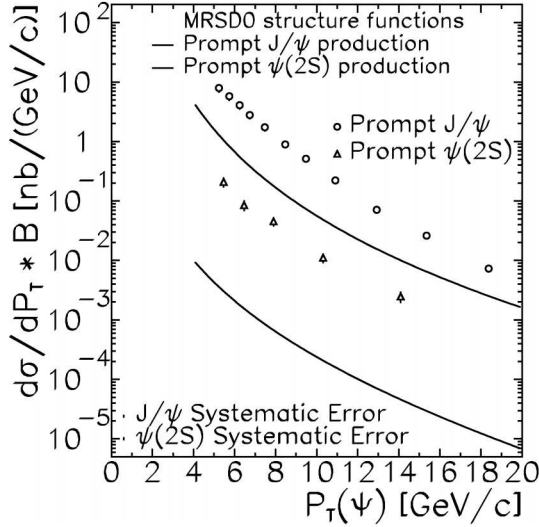


Figure 1.7 Differential production cross-sections of the  $J/\psi$  and  $\psi(2S)$  mesons as functions of  $p_T$  measured by CDF in proton-antiproton collisions at  $\sqrt{s} = 1.8$  TeV. The circles and triangles are the cross-sections of the  $J/\psi$  and  $\psi(2S)$  mesons, respectively. The solid lines are the predictions of the CSM at LO. Figure taken from Ref. [25].

shows as an example the result of the  $J/\psi$  polarisation in  $pp$  collisions at  $\sqrt{s} = 7$  TeV measured by LHCb. The polarisation puzzle remains not understood for years. Recently, a possible solution was proposed in Ref. [45]. As given in Table 1.2, contributions from the states  $^1S_0^{[8]}$ ,  $^3S_1^{[1,8]}$ , and  $^3P_J^{[8]}$  dominate the  $J/\psi$  production. The predicted transverse polarisation mainly comes from the  $^3S_1^{[8]}$  state. By including the NLO corrections of the  $^3P_J^{[8]}$  mode, which was not calculated in the previous predictions, the  $^3P_J^{[8]}$  channel contributes a positive longitudinal component and a negative transverse component to the  $J/\psi$  polarisation<sup>[45]</sup>. The cancellation of the transverse polarisation between the  $^3S_1^{[8]}$  and  $^3P_J^{[8]}$  channels can lead to the  $J/\psi$  mesons with almost zero polarisation (or with slight longitudinal polarisation).

#### 1.4 Quarkonium pair production in $pp$ collisions

In  $pp$  collisions, the quarkonium pair can be produced either from the process of single parton scattering (SPS) or through that of double parton scattering (DPS), as shown in Fig. 1.10. Quarkonium pairs produced from the SPS and DPS processes have distinct kinematic distributions, which allow for the discrimination of the SPS and DPS contributions in experiments.

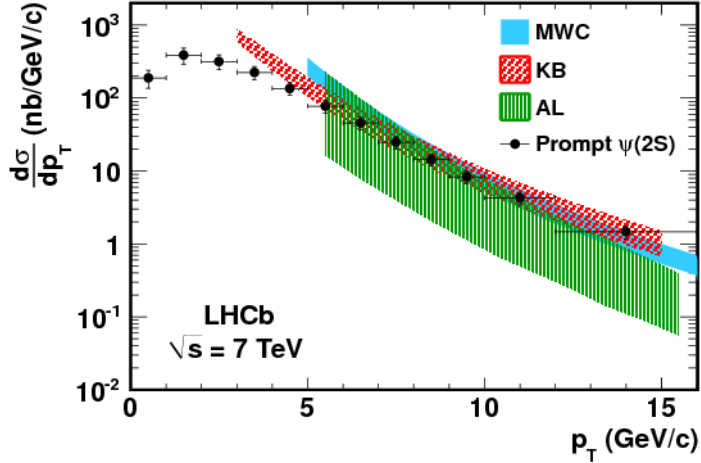


Figure 1.8 Differential  $\psi(2S)$  production cross-section in  $pp$  collisions at  $\sqrt{s} = 7$  TeV as a function of  $p_T$  measured by LHCb. The green hatched area shows the calculation of the CSM at NNLO. The red and blue hatched areas are the calculations of the NRQCD approach at NLO from two groups. Figure taken from Ref. [39].

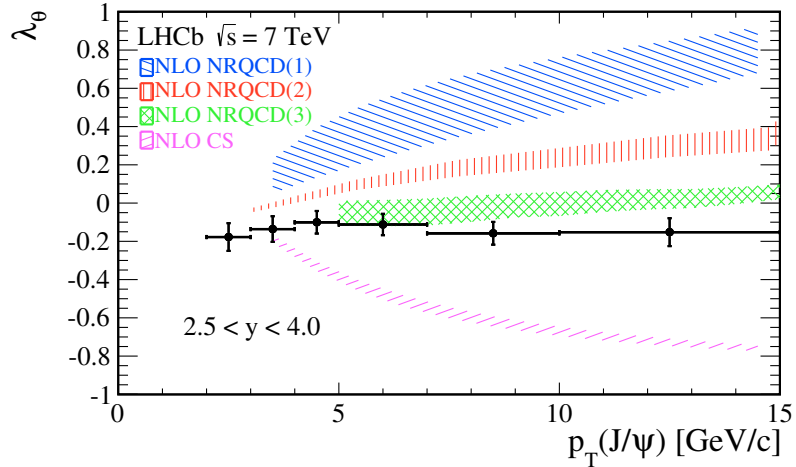


Figure 1.9 The  $J/\psi$  polarisation as a function of  $p_T$  measured by LHCb in  $pp$  collisions at  $\sqrt{s} = 7$  TeV. The hatched areas are the various theoretical predictions as indicated in the legend. Figure taken from Ref. [29].

#### 1.4.1 Quarkonium pair production in SPS

Quarkonium pair production through the SPS process can provide a new dimension for the test of the NRQCD calculations. To produce a pair of quarkonium in the SPS process of high-energy  $pp$  collisions, two sets of  $Q\bar{Q}$  states need to be produced from the gluon-gluon fusion. Similar to Eq. 1-9, the production cross-section of a heavy

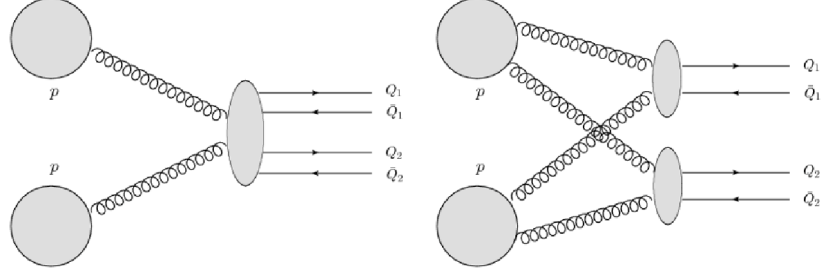


Figure 1.10 Diagrams for the quarkonium pair production in the (left) SPS and (right) DPS processes, respectively.  $Q_{1(2)}$  stands for a heavy quark, and  $\bar{Q}_{1(2)}$  stands for its antiquark.

quarkonium pair  $H_1 H_2$  can be given by

$$\sigma(H_1 H_2) = \sum_{n_1 n_2} \sigma(pp \rightarrow Q_1 \bar{Q}_1[n_1] Q_2 \bar{Q}_2[n_2] + X) \times \langle O^{H_1}(n_1) \rangle \langle O^{H_2}(n_2) \rangle, \quad (1-26)$$

in which the subscripts 1, 2 represent the corresponding parameters for the two quarkonia respectively. The production of the  $Q_1 \bar{Q}_1 Q_2 \bar{Q}_2$  pair is much more complicated than that in the single quarkonium production, while the hadronisation process is common between them. In CSM, at LO in  $\alpha_s$  ( $\mathcal{O}(\alpha_s^4)$ ), the  $Q_1 \bar{Q}_1 Q_2 \bar{Q}_2$  pair is produced through the process

$$g + g \rightarrow Q_1 \bar{Q}_1 Q_2 \bar{Q}_2, \quad (1-27)$$

as shown in Fig. 1.11. At NLO ( $\mathcal{O}(\alpha_s^5)$ ), in addition to the process

$$g + g \rightarrow Q_1 \bar{Q}_1 Q_2 \bar{Q}_2 + g, \quad (1-28)$$

the scattering of a gluon with a quark

$$g + q \rightarrow Q_1 \bar{Q}_1 Q_2 \bar{Q}_2 + q \quad (1-29)$$

also needs to be considered. The two processes are both shown in Fig. 1.11. At NNLO ( $\mathcal{O}(\alpha_s^6)$ ), there are much more diagrams that can produce two  $Q\bar{Q}$  pairs. A few typical diagrams for the process

$$g + g \rightarrow Q_1 \bar{Q}_1 Q_2 \bar{Q}_2 + g + g \quad (1-30)$$

and the process

$$g + g \rightarrow Q_1 \bar{Q}_1 Q_2 \bar{Q}_2 + c + \bar{c} \quad (1-31)$$

are shown in Fig. 1.12.

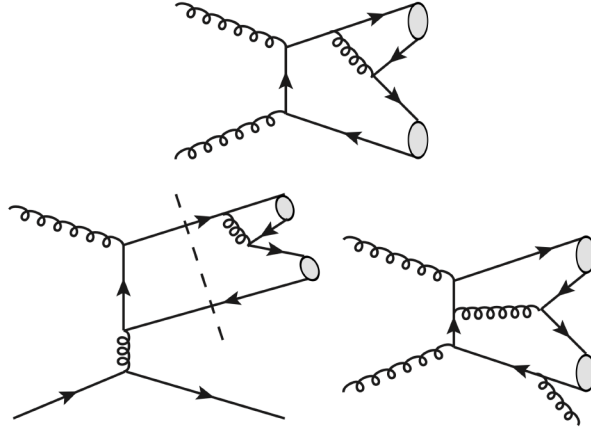


Figure 1.11 Feynman diagrams for the production of the  $Q_1 \bar{Q}_1 Q_2 \bar{Q}_2$  pairs at (top) LO ( $\mathcal{O}(\alpha_s^4)$ ) and (bottom) NLO ( $\mathcal{O}(\alpha_s^5)$ ) in  $\alpha_s$  in CSM for the  $J/\psi$  pair production. Figures taken from Ref. [46].

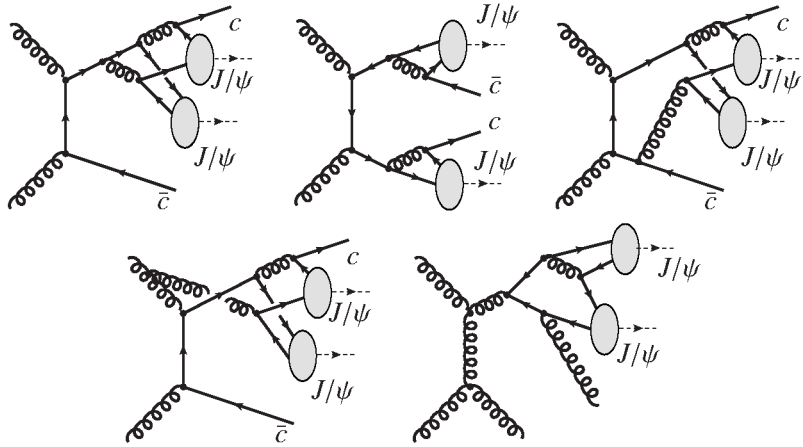


Figure 1.12 Feynman diagrams for the production of the  $Q_1 \bar{Q}_1 Q_2 \bar{Q}_2$  pairs at NNLO in  $\alpha_s$  ( $\mathcal{O}(\alpha_s^6)$ ) in CSM for the  $J/\psi$  pair production. Figures taken from Ref. [47].

The CO contributions to the quarkonium pair production are found to be small, as they are doubly suppressed by the LDMEs. Besides, in the colour-singlet processes at LO, the feed-down from some excited states is forbidden according to the selection rules. For

example in the  $J/\psi$  pair production, the initial state with two on-shell gluons ( $J^C = 1^-$ ) cannot result in the final state with  $J/\psi (J^C = 1^-) + \chi_c (J^C = 1^+)$  due to the conservation of  $C$ -parity. The exclusion of such feed-down, which plays an important role in the quarkonium production and is difficult to interpret, significantly simplifies the modelling of quarkonium pair production.

### 1.4.2 Quarkonium pair production in DPS

The DPS process has attracted great interest in the recent years. It can reveal the parton transverse profile inside the proton. In addition, some central backgrounds, *e.g.*  $Z + b\bar{b}$ ,  $W^+ + W^+$ , multi-jets *etc.*, present in the search for new physics beyond the SM are most probable to be produced through the DPS process. A good understanding of the DPS process can help identify their contributions. The mechanism of the DPS process is still opaque. Generally, the production cross-section of two quarkonia in the DPS process can be calculated as

$$\sigma_{\text{DPS}}(H_1 H_2) = \frac{1}{1 + \delta_{H_1 H_2}} \sum_{i,j,k,l} \int dx_1 dx_2 dx'_1 dx'_2 d^2 k_{T1} d^2 k_{T2} d^2 k'_{T1} d^2 k'_{T2} \\ \times \Gamma_{ij}(x_1, x_2, k_{T1}, k_{T2}) \times \sigma_{ik}^{H_1}(x_1, x'_1) \times \sigma_{jl}^{H_2}(x_2, x'_2) \times \Gamma_{kl}(x'_1, x'_2, k'_{T1}, k'_{T2}), \quad (1-32)$$

where  $H_1$  and  $H_2$  indicate the two quarkonia;  $\delta_{H_1 H_2}$  is the symmetry factor, which equals one only when  $H_1$  and  $H_2$  are identical and otherwise zero;  $\Gamma$  is the generalized double-parton distribution function with  $i, j, k, l$  representing a specific parton (quark, antiquark or gluon);  $\sigma$  is the parton-level quarkonium production cross-section in the SPS process;  $x$  represents the fraction of the proton longitudinal momentum taken by the interacting parton, and  $k_T$  represents such fraction of the proton transverse momentum. The most popular interpretation of the DPS process is based on the following two assumptions: a) the transverse and longitudinal components of the double parton distribution function can be factorized as

$$\Gamma_{ij}(x_1, x_2, k_{T1}, k_{T2}) = D_{ij}(x_1, x_2) T_{ij}(k_{T1}, k_{T2}), \quad (1-33)$$

where  $D$  and  $T$  stand for the longitudinal and transverse components, respectively; b) there is no correlation between the two partons from the same proton, which means

$$D_{ij}(x_1, x_2) = f_i(x_1) f_j(x_2) \quad (1-34)$$

and

$$T_{ij}(k_{T1}, k_{T2}) = T_i(k_{T1})T_j(k_{T2}). \quad (1-35)$$

The two assumptions are not strictly valid in QCD. However, currently the only demonstrated violation of the factorization is when the  $x$  is large. All the other factors that potentially break it turn out to have no visible effects. Under these two assumptions, the DPS contribution can be determined according to

$$\sigma_{\text{DPS}}(H_1 H_2) = \frac{1}{1 + \delta_{H_1 H_2}} \frac{\sigma(H_1)\sigma(H_2)}{\sigma_{\text{eff}}}, \quad (1-36)$$

where  $\sigma(H_1)$  and  $\sigma(H_2)$  are the inclusive prompt production cross-sections of the two quarkonia, and  $\sigma_{\text{eff}}$  is the effective cross-section. The effective cross-section  $\sigma_{\text{eff}}$  is determined from the transverse structure of the proton as

$$\sigma_{\text{eff}} = \int d^2 k_{T1} d^2 k_{T2} d^2 k_{T1'} d^2 k_{T2'} T_i(k_{T1}) T_k(k_{T2}) T_j(k_{T1'}) T_l(k_{T2'}), \quad (1-37)$$

thus should be independent of the processes and energy scales. A summary of the effective cross-sections measured by various experiments with different channels at different centre-of-mass energies<sup>[48]</sup> is shown in Fig. 1.13. The majority of the measured effective cross-sections are consistent and lie between 12 to 20 mb. However, the  $J/\psi$  pair productions of the ATLAS and D0 experiments indicate a much smaller value of  $\sigma_{\text{eff}}$ . The  $\sigma_{\text{eff}}$  value obtained from the  $J/\psi + \gamma$  process at the D0 experiment is even smaller. To measure the  $J/\psi$  pair production in the DPS process at the LHCb experiment, which will be described in Chapter 4, can provide important inputs to the study of the effective cross-section.

## 1.5 Decays of the $B_c^+$ meson

As the ground state of the  $B_c$  meson family, the  $B_c^+$  meson can only decay weakly since the flavours of the two constituent quarks are different. As shown in Fig. 1.14, it has rich decay modes, since the  $\bar{b}$  quark decays with the  $c$  quark as a spectator,  $\bar{b} \rightarrow \bar{c}(\bar{u}) + W^+$ ; the  $c$  quark decays with the  $\bar{b}$  quark as a spectator,  $c \rightarrow s(d) + W^+$ ; and the  $\bar{b}$  quark and the  $c$  quark annihilate into a virtual  $W^+$  boson,  $\bar{b} + c \rightarrow W^+$ . The processes in the weak decays are well understood, therefore the  $B_c^+$  meson decay is also an ideal laboratory for QCD studies.

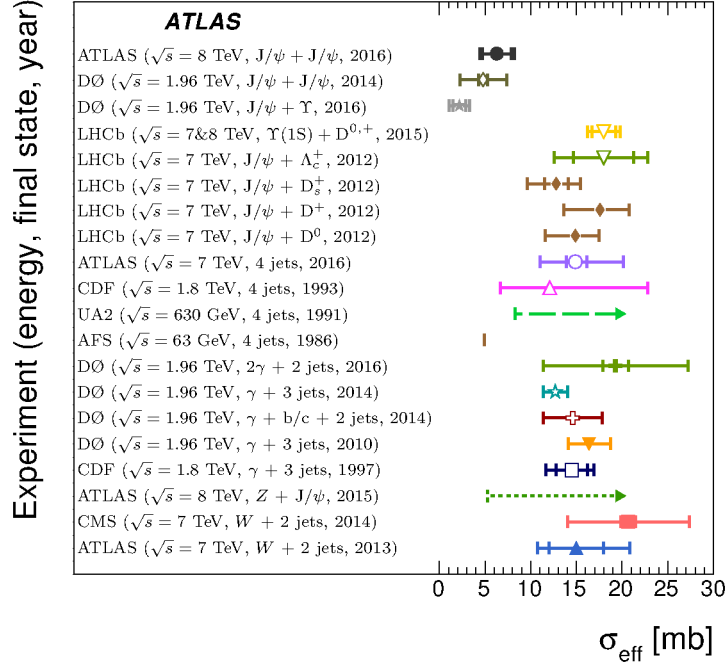


Figure 1.13 Summary of the effective cross-sections measured by various experiments using different channels at different centre-of-mass energies. Figure taken from Ref. [48].

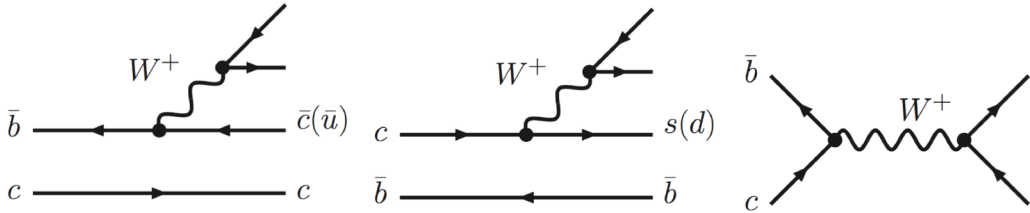


Figure 1.14 Feynman diagrams of (left) the  $\bar{b}$  decay mode, (middle) the  $c$  decay mode and (right) the annihilation mode for the  $B_c^+$  decay.

The first observation of the  $B_c^+$  meson was made by the CDF experiment at the Tevatron collider with the semi-leptonic  $B_c^+ \rightarrow J/\psi l^+ \nu$  decays<sup>[49,50]</sup>. The observation of the  $B_c^+ \rightarrow J/\psi \pi^+$  decay came after<sup>[51]</sup>. The study of the  $B_c^+$  meson is highly promoted at the LHC, since the production cross-section of the  $B_c^+$  mesons is one-order-of-magnitude higher at the LHC than that at the Tevatron. Many new channels have been observed by the LHCb experiment, such as  $B_c^+ \rightarrow J/\psi \pi^+ \pi^- \pi^+$ <sup>[52]</sup>,  $B_c^+ \rightarrow \psi(2S) \pi^+$ <sup>[53]</sup>,  $B_c^+ \rightarrow J/\psi D_s^{(*)+}$ <sup>[54]</sup>,  $B_c^+ \rightarrow J/\psi K^+$ <sup>[55]</sup>,  $B_c^+ \rightarrow B_s^0 \pi^+$ <sup>[56]</sup> and  $B_c^+ \rightarrow J/\psi K^+ K^- \pi^+$ <sup>[57]</sup>. The absolute branching fraction of any  $B_c^+$  decay channel has not been measured yet.

In this dissertation, the branching fraction of the  $B_c^+ \rightarrow \psi(2S) \pi^+$  decay is measured

relative to that of the  $B_c^+ \rightarrow J/\psi \pi^+$  decay. Various QCD models calculated these branching fractions<sup>[58–63]</sup>. The  $B_c^+ \rightarrow \psi(2S)\pi^+$  channel was first discovered using the  $pp$  collision data collected by LHCb at  $\sqrt{s} = 7$  TeV corresponding to an integrated luminosity of  $1 \text{ fb}^{-1}$ <sup>[53]</sup>. Limited by the sample size, the result is not precise enough to discriminate the theoretical calculations. In the analysis presented in this dissertation, the LHCb data of  $pp$  collisions corresponding to integrated luminosities of  $1 \text{ fb}^{-1}$  at  $\sqrt{s} = 7$  TeV and  $2 \text{ fb}^{-1}$  at  $\sqrt{s} = 8$  TeV are used. Owing to the larger sample size and improved analysis strategy, a more precise result is expected.

In the  $B_c^+ \rightarrow \psi\pi^+$  decay, where  $\psi$  represents both the  $J/\psi$  and  $\psi(2S)$  mesons, the weak decay process  $\bar{b} \rightarrow \bar{c} + W^+(\rightarrow u\bar{d})$  is well understood. To form a bound  $c\bar{c}$  state, the spectator  $c$  quark needs to have a large momentum transfer, typically around  $m_b m_c \approx 6 \text{ GeV}^2/c^2$ <sup>[58]</sup>, to catch the energetic  $\bar{c}$  quark from the  $b$  quark decay. The large momentum transfer makes it a short-distance process and enables the implementation of the perturbative QCD. What remain are the hadronisations of the  $\bar{b}c$  into the  $B_c^+$  meson, the  $c\bar{c}$  into the charmonium and the  $u\bar{d}$  into the  $\pi^+$  meson. In consequence, the decay amplitude of the  $B_c^+ \rightarrow \psi\pi^+$  decay can be factorized as

$$\mathcal{A}(B_c^+ \rightarrow \psi\pi^+) \approx \int dk_1 dk_2 dk_3 \Psi_{B_c^+}(k_1) \Psi_\psi(k_2) \Psi_{\pi^+}(k_3) H(k_1, k_2, k_3, t), \quad (1-38)$$

where  $k_i$ 's are the momenta of the quarks in the corresponding meson,  $t$  is the energy scale,  $H$  includes all the perturbatively calculable processes, and  $\Psi$  is the wave function for the indicated meson, which describes its hadronisation process. The  $u\bar{d}$  state produced from the  $b$  quark is typically energetic, thus not affected by the surrounding soft gluons. Its hadronisation process can be determined from other well-measured decays. The central components to be determined are the wave functions of the  $B_c^+$  and  $\psi$  mesons. They can be calculated from the non-relativistic potential equations<sup>[58–60]</sup>. There are also plenty of calculations based on the relativistic quark potential model<sup>[61–63]</sup>, in which relativistic corrections are included in the quasipotential equations. In NRQCD, the wave functions of the  $\psi$  mesons are closely related to the LDMEs of the colour-singlet components as explained in Sec. 1.3.1.3. The measurement of the relative branching fraction of the  $B_c^+ \rightarrow \psi(2S)\pi^+$  decay to the  $B_c^+ \rightarrow J/\psi \pi^+$  decay can provide a new way to verify NRQCD.

## 1.6 $B_c$ spectroscopy

A rich  $B_c$  spectroscopy is predicted by various potential models<sup>[19,64–73]</sup> and LQCD<sup>[74]</sup>, as shown in Fig. 1.4 according to the prediction in Ref. [19]. LQCD suffers from large uncertainty due to the limited computation power. In the potential models, the mass splittings of the  $B_c$  states are determined from their wave functions at the origin, which are calculated according to the assumed quark potential. The non-relativistic quark potential models are found to nicely describe the spectroscopies of the charmonium and bottomonium systems. They are expected to apply to the  $B_c$  mesons as well, in which the velocity of the quarks inside the meson is supposed to lie between those in charmonia and bottomonia. There are also many relativistic quark models, in which relativistic effects are taken into account in the quasipotential equation, used to predict the  $B_c$  spectroscopy. The study of the  $B_c$  spectroscopy can provide a powerful test of all these QCD models.

Apart from the ground state  $B_c^+$ , only the  $B_c(2S)^+$  state is observed by the ATLAS experiment in 2014<sup>[20]</sup> so far. The  $B_c(2S)^+$  state was discovered in the  $B_c^+\pi^+\pi^-$  spectrum at the mass  $6842 \pm 4$  (stat)  $\pm 5$  (syst) MeV/c<sup>2</sup>, as shown in Fig. 1.15. It can be the  $B_c(2^1S_0)^+$  state decaying via  $B_c(2^1S_0)^+ \rightarrow B_c^+\pi^+\pi^-$ , the  $B_c(2^3S_1)^+$  state decaying through  $B_c(2^3S_1)^+ \rightarrow B_c(1^3S_1)^+\pi^+\pi^-$  with  $B_c(1^3S_1)^+ \rightarrow B_c^+\gamma$ , where the low-energy  $\gamma$  is not reconstructed, or the mixture of the two states. The LHCb experiment has collected the world largest  $B_c^+$  sample so far, but in the lower momentum region compared to those at ATLAS. The mass resolution at LHCb is much better than that at ATLAS, which provides a larger chance to distinguish the  $B_c(2^1S_0)^+$  and  $B_c(2^3S_1)^+$  states. Therefore it is of high importance to perform the search for  $B_c(2S)^+$  and  $B_c^*(2S)^+$  states at LHCb, which is described in Chapter 6.

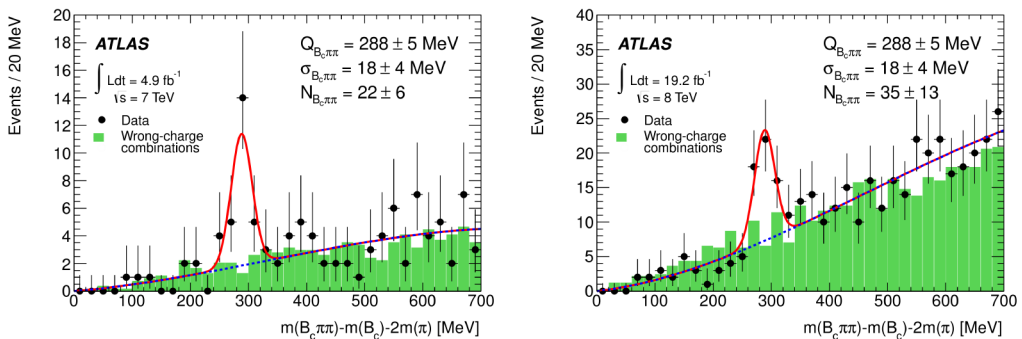


Figure 1.15 Observation of the  $B_c(2S)^+$  state in the  $B_c^+\pi^+\pi^-$  mass spectrum with the (left)  $\sqrt{s} = 7$  TeV and (right) 8 TeV data at ATLAS. Figures taken from Ref. [20].

## Chapter 2 The LHCb experiment

The LHCb experiment is one of the four large experiments at the LHC<sup>[75]</sup> at CERN. It is dedicated to precision studies of heavy flavour physics. The main objective of LHCb is to search for physics beyond the SM via precise measurements of CP violation and rare decays of bottom and charm hadrons<sup>[76]</sup>. Besides, the LHCb experiment covers a wide range of other physics programmes, *e.g.* hadron productions in both proton-proton and proton-nucleus collisions, hadron spectroscopy, lepton universality test and so on. The large production cross-sections of bottom and charm hadrons at the LHC establish LHCb as an excellent competitor in these areas, whereas the high event rate and background level in the LHC environment bring challenges to LHCb in the meantime. To accomplish the physics goals, the LHCb detector is designed to have: a) a high-bandwidth online data acquisition system with an efficient two-level trigger, to cope with the high event rate at the LHC; b) an excellent tracking system together with remarkable ability to identify final-state particles, which is essential to reconstruct and isolate the decays of heavy-flavour hadrons. In this chapter, the LHC is briefly introduced in Section 2.1. The LHCb detector, including the architecture and performance of the subsystems, the trigger, and the data processing, is described in Section 2.2.

### 2.1 The LHC

The LHC is the largest and most energetic tool ever built for particle physics studies. It is a two-ring superconducting accelerator and collider with a circumference of 26.7 km, and lies between 45 m and 170 m beneath the ground at the French-Swiss border near Geneva<sup>[75]</sup>. The LHC is a  $pp$  collider targeting a centre-of-mass energy of  $\sqrt{s} = 14$  TeV with two counter-rotating proton beams circulating in the two rings separately. With the unprecedented design energy, it aims at: a) testing the predictions of fundamental particles and forces in the SM, especially the origin of mass; b) probing the puzzle of matter and antimatter asymmetry in the universe; c) searching for dark matter and dark energy; d) answering other open questions concerning the supersymmetry, the unification of forces, the possible substructure of the elementary particles, the existence of extra dimensions and so on. The LHC is also designed to accelerate heavy ion beams up to the energy of 2.76 TeV per nucleon. The proton-nucleus and nucleus-nucleus collisions can create the

quark-gluon plasma (QGP) state, whose nature and properties are crucial to understand the evolution of the early universe.

The LHC injection complex<sup>[77]</sup> is shown in Fig. 2.1. Protons are produced from a bottle of hydrogen gas with the electrons of the hydrogen atoms stripped by an electric field. The Linear Particle Accelerator (LINAC2) accelerates the protons to an energy of 50 MeV, bunches the protons and focuses them transversely simultaneously. Then the protons are fed to the Proton Synchrotron Booster (PSB), where the proton energy is increased to 1.4 GeV. Two successive PSB pulses with 6 bunches are filled into the Proton Synchrotron (PS), in which the protons are accelerated to 25 GeV. The PS also splits the bunches longitudinally into twelve even fractions and suppresses the bunch length to fit into the buckets of the Super Proton Synchrotron (SPS). Three or four PS batches are injected to the SPS, which accelerates the protons to an energy of 450 GeV. Afterwards, twelve SPS injections are accumulated in each ring of the LHC, where the two beams are accelerated to the designed energy of 7 TeV. In the ultimate operating conditions, there are 2808 proton bunches per beam with a bunch spacing of 25 ns in the LHC, and each bunch is populated by around  $1.15 \times 10^{11}$  protons. This leads to a peak instantaneous luminosity of  $10^{34} \text{ cm}^{-2} \text{ s}^{-1}$  for  $pp$  collisions.

## The LHC injection complex

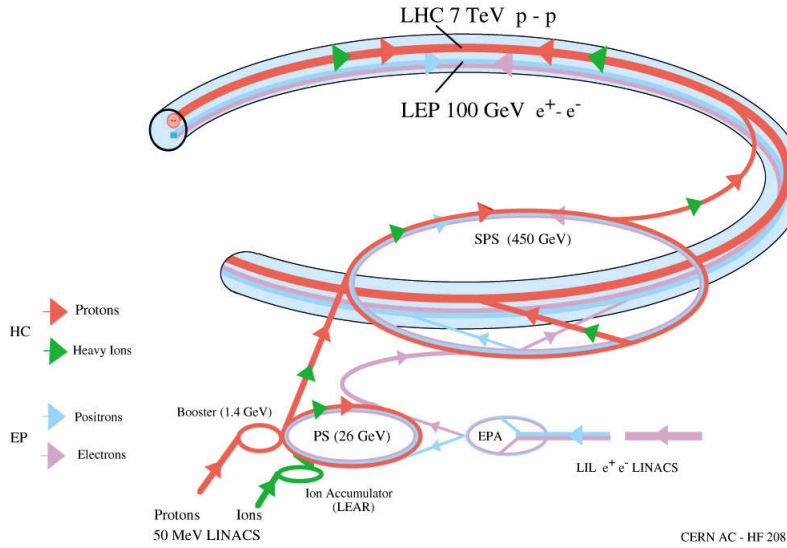


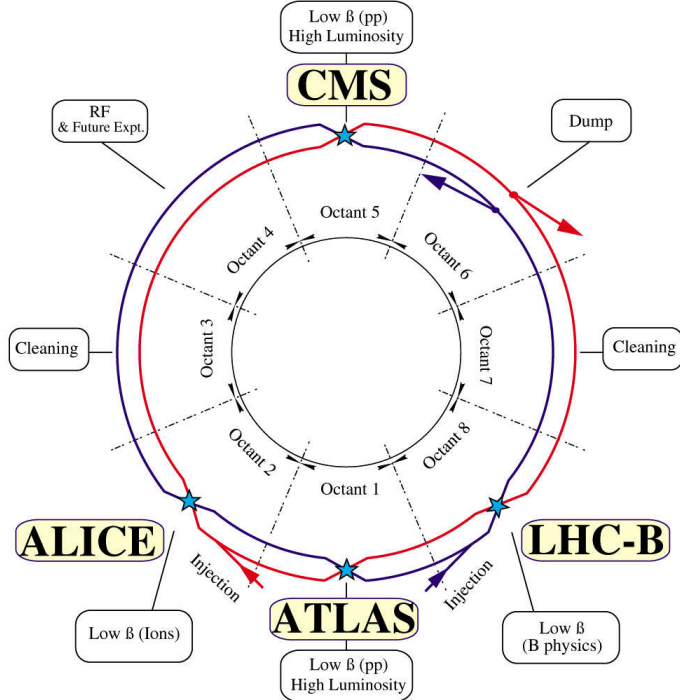
Figure 2.1 The LHC injection complex. Figure taken from Ref. [77].

Four large experiments are deployed along the LHC with distinctive scientific goals and characteristic detector designs, as shown in Fig. 2.2. The largest two are the ATLAS<sup>[78]</sup>

and CMS<sup>[79]</sup> experiments, which are two general-purpose detectors investigating broad physics topics, ranging from the search for the Higgs boson to the search for evidence of physics beyond the SM and dark matter candidates. Despite the same physics targets, they have different technical designs and performance. The designed peak luminosity for them is exactly  $10^{34} \text{ cm}^{-2} \text{ s}^{-1}$  as for the LHC. The LHCb experiment is designed for precision measurements in the forward region, and has a lower luminosity design of  $10^{32} \text{ cm}^{-2} \text{ s}^{-1}$ . The smaller luminosity at LHCb is achieved by adjusting the beam focus at the collision point. It gives the advantages of a smaller number of visible interactions for each beam-beam crossing, the low occupancy in the subdetectors, and the suppressed radiation damage. The ALICE experiment<sup>[80]</sup> is specialized to analyse heavy ion collisions, targeting at exploring the nature and properties of QGP. It aims at a peak luminosity of  $10^{27} \text{ cm}^{-2} \text{ s}^{-1}$  for lead-lead collisions. There are also three small experiments focusing on forward particles at the LHC: TOTEM<sup>[81]</sup>, LHCf<sup>[82]</sup> and MoEDAL<sup>[83]</sup>, which share the same collision points with the CMS, ATLAS and LHCb experiments, respectively. The TOTEM experiment measures the elastic scattering and diffraction dissociation in  $pp$  collisions. The LHCf experiment explores the origin of ultra-high-energy cosmic rays with  $pp$  collision data. The MoEDAL experiment is intended to search for the magnetic monopole.

After the successful first beam injection and collision in November 2009, the LHC commissioned the first run (Run1) from 2010 to 2013, during which the  $pp$  collision data were mainly recorded in 2011 and 2012. Protons collided at the centre-of-mass energies of 7 TeV and 8 TeV in 2011 and 2012 respectively, with a bunch spacing of 50 ns and a phased increase of bunch intensity. The peak instantaneous luminosity delivered by the LHC reached around  $8 \times 10^{33} \text{ cm}^{-2} \text{ s}^{-1}$  with 1380 bunches per beam. The first long shutdown took place afterwards from 2013 to 2014, when upgrades were made to allow for a larger centre-of-mass energy of 13 TeV and the ultimate bunch spacing of 25 ns. During the second run (Run2) started in 2015, the LHC has been operating at  $\sqrt{s} = 13 \text{ TeV}$  with the bunch spacing of 25 ns. A peak luminosity of  $2.05 \times 10^{34} \text{ cm}^{-2} \text{ s}^{-1}$ , more than twice the designed luminosity, was achieved in November 2017. The integrated luminosities recorded by the four large experiments during the commissioning years are illustrated in Fig. 2.3. So far, a total of around  $120 \text{ fb}^{-1}$  data is collected by the ATLAS and CMS experiments. The LHCb and ALICE experiments have taken data corresponding to around  $7 \text{ fb}^{-1}$  and  $50 \text{ pb}^{-1}$ , respectively. Stirring physics results made from these data marked the

## LHC LAYOUT



CERN AC\_EI2-4A\_V18/9/1997

Figure 2.2 Schematic layout of the LHC, where the four large experiments are shown. Figure taken from Ref. [84].

great success of the LHC and its experiments.

## 2.2 The LHCb detector

The LHCb detector is a single-arm forward spectrometer covering the angular range from approximately 10 mrad to 300 (250) mrad in the horizontal (vertical) plane, corresponding to the pseudorapidity range of  $2 < \eta < 5$  in the laboratory frame<sup>[76]</sup>. Such geometry is chosen due to the fact that, for  $pp$  collisions at the LHC energy scale, the  $b$ - and  $\bar{b}$ -hadrons are produced highly correlated, and are predominantly distributed in the forward and backward cones symmetrically, as shown in Fig. 2.4. The LHCb detector detects approximately 25% of the  $b\bar{b}$  quark pairs with a coverage of only around 2.4% of the  $4\pi$  solid angle. The schematic view of the LHCb detector is illustrated in Fig. 2.5. The right-handed coordinate system is applied, with the origin located at the collision

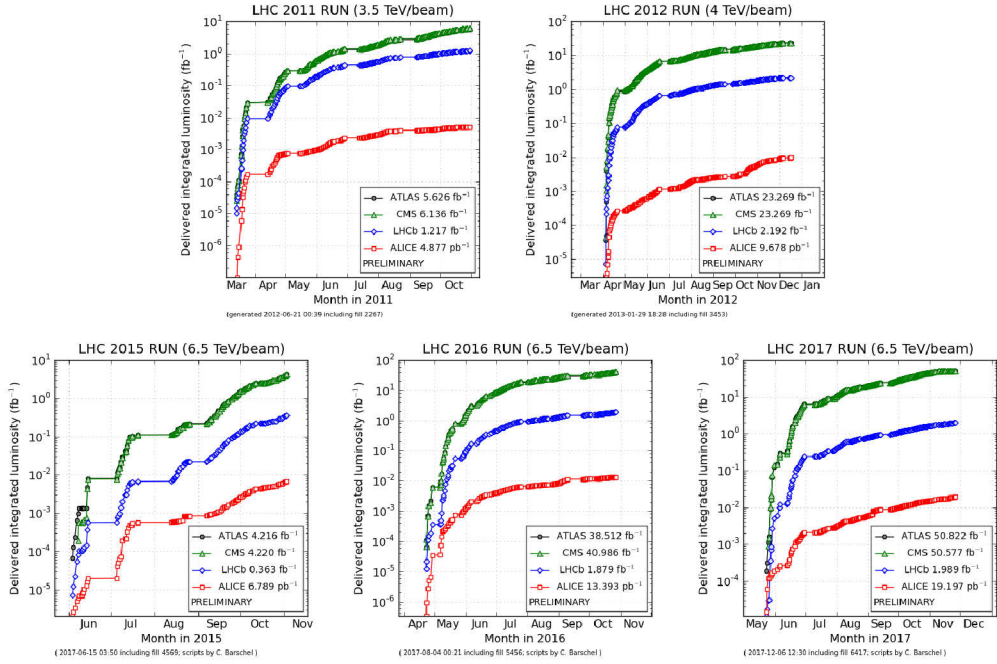


Figure 2.3 Evolution of the integrated luminosities in the four large experiments at the LHC for the years (top left) 2011, (top right) 2012, (bottom left) 2015, (bottom centre) 2016 and (bottom right) 2017.

point, the  $z$  axis pointing into the detector along the beam, the  $y$  axis pointing upwards along the vertical, and the  $x$  axis completing the system. Most of the detector components are assembled in two halves, which can be shifted out horizontally to allow for assembly, maintenance and access to the beam pipe.

Encompassing the  $pp$  collision region is the vertex locator (VELO), which is a high-precision silicon-strip detector. It is followed by the first ring-imaging Cherenkov detector (RICH1), which provides identification of charged hadrons in the momentum range of  $1 - 60 \text{ GeV}/c$ . Behind the RICH1 is the tracker turicensis (TT) made of silicon microstrips. After that there is a warm dipole magnet which enables the measurement of the momenta of charged particles. There are three planar tracking stations T1-T3 downstream of the magnet, where silicon microstrips are employed in the inner parts (IT), and straw tubes are adopted in the outer parts (OT). The second ring-imaging Cherenkov detector (RICH2) sits afterwards, responsible for the discrimination of charged hadrons with momenta of  $15 \text{ GeV}/c$  up to larger than  $100 \text{ GeV}/c$ . The following calorimeter system consists of a scintillator pad detector (SPD), a preshower detector (PSD), an electromagnetic calorimeter (ECAL) and a hadronic calorimeter (HCAL) located one by one. It identifies electrons, photons and hadrons, and measures the energy deposits and

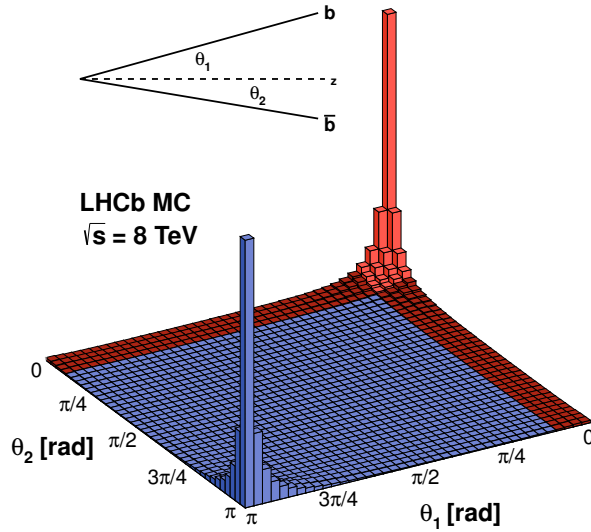


Figure 2.4 Simulation of the production angles of the  $b$ - and  $\bar{b}$ -hadrons in  $pp$  collisions at  $\sqrt{s} = 8$  TeV. Similar results apply for  $pp$  collisions with the centre-of-mass energy ranging from 7 TeV to 14 TeV.

the coordinates of them. The last part is the muon detection system made of multi-wire proportional chambers (MWPC), with one chamber placed upstream of the calorimeter system, and the other four downstream of it. The components can be categorized into the tracking and the particle identification (PID) systems according to their facilities. The concrete design and the performance of each subdetector are presented below. The trigger and data processing systems are also discussed.

### 2.2.1 Tracking

The tracking system is composed of the VELO, the TT and the tracking stations T1-T3. The magnet can also be considered as part of the tracking system.

#### 2.2.1.1 Magnet

Magnet deflects charged particles, allowing the measurement of the particle momentum. The magnet used in the LHCb detector is a dipole magnet made of saddle-shaped coils<sup>[76]</sup>, as shown in Fig. 2.6. Two symmetrical parts are placed horizontally on the top and bottom of the beam pipe, respectively. The magnetic field is mainly along the  $y$  axis pointing either downwards or upwards, deflecting the charged particles horizon-

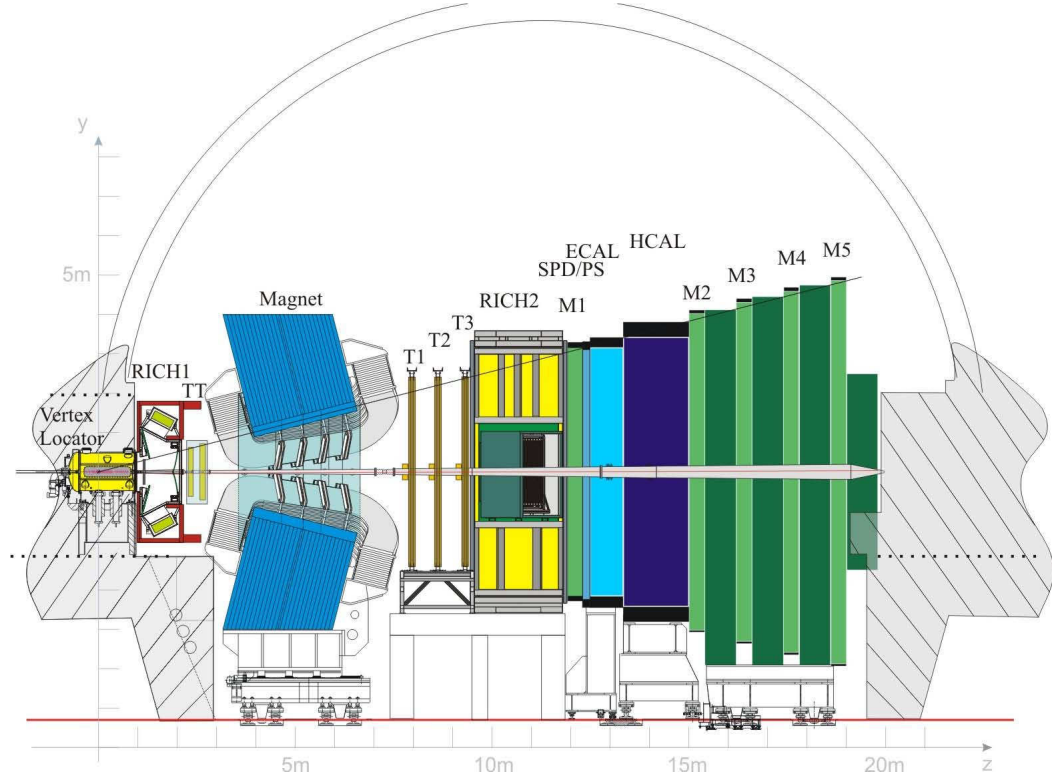


Figure 2.5 Layout of the LHCb detector. Figure taken from Ref. [76].

tally. During the operation, the polarity of the magnetic field is changed periodically to control asymmetry effects introduced by the detector, which is crucial to CP violation measurements. The magnet is required to cover the full angular acceptance of LHCb, and to be high in the TT and the tracking stations T1-T3 but low in the RICHs. Driven by these constraints, the magnet is designed to have a bending power of 4 Tm for 10 m long tracks<sup>[76]</sup>. An accurate mapping of the magnetic field is essential for a precise momentum measurement. At LHCb, the magnetic field is measured using a well aligned Hall probe array to the precision of about  $4 \times 10^{-4}$ . The measured component of the magnetic field in the  $y$  direction is shown in Fig. 2.7 for the coordinates with  $x = 0$  and  $y = 0$  along the  $z$  axis for both polarities.

### 2.2.1.2 Vertex locator

The VELO measures the track positions close to the colliding region, and is responsible for recognising the isolated decay vertices which are unique for the  $b$ - and  $c$ -hadrons. It is crucial to the lifetime measurements and to the measurements of impact parameter (IP), which is the closest distance between a track and the primary vertex (PV), and is used to distinguish particles produced promptly from  $pp$  collisions and from the decays

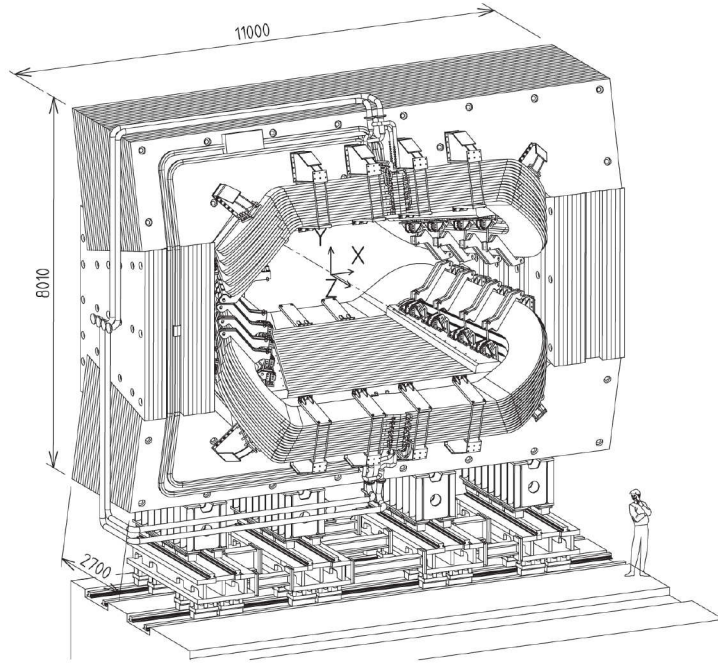


Figure 2.6 Schematic view of the dipole magnet. Figure taken from Ref. [76].

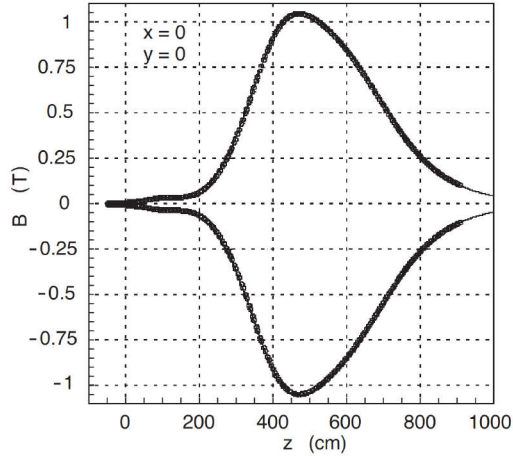


Figure 2.7 The  $y$  component of the magnetic field for positions with  $x = 0$  and  $y = 0$  along the  $z$  axis for both polarities. Figure taken from Ref. [76].

of  $b$ - and  $c$ -hadrons. Generally, the VELO is required to have a large track detection efficiency and an excellent IP resolution, and to accept particles produced in the region with  $|z| < 10.6$  cm and having pseudorapidity in the range of  $1.6 < \eta < 4.9$ .

The VELO is composed of a series of microstrip silicon modules with a cylindrical geometry placed along the beam pipe<sup>[76]</sup>, as shown in Fig. 2.8. The modules are retractable along the  $x$  axis to provide an approach as close as 8 mm to the beam centre during physics

runs, and to shift out by 30 mm from the interaction region during beam injection for safety. Each of the VELO modules consists of an R-sensor and a  $\phi$ -sensor, providing measures of the  $r$  and  $\phi$  coordinates respectively, while the  $z$  coordinate is given by the known position of the module. The  $r\phi$  scheme is chosen instead of a rectilinear geometry to allow for a fast reconstruction of tracks and vertices. A conceptual representation of the R- and  $\phi$ -sensor is shown in Fig. 2.9. The R-sensors consists of semicircular concentric silicon strips with the centre at the beam position. The strips are segmented into quarters to reduce occupancy and capacitance. The innermost strips have the minimal pitch of 38  $\mu\text{m}$ , which increases linearly to 102  $\mu\text{m}$  at the outer edge with  $r = 41.9$  mm. Under such arrangement, each strip contributes approximately equally to the precision of IP. The  $\phi$ -sensors are subdivided into two parts to avoid extremely high strip occupancy and to prevent the pitch from going too large with increasing radius. In the inner region with the outer boundary at the radius of 17.25 mm, the pitch varies from 38  $\mu\text{m}$  to 78  $\mu\text{m}$ . The outer region starts with a pitch of 39  $\mu\text{m}$  and ends with a 97  $\mu\text{m}$  pitch at the largest radius. The inner and outer strips are skewed in opposite directions with angles of 20° and 10° respectively to optimise pattern recognition. The skew is reversed for neighbouring  $\phi$ -sensors to better distinguish noise hits from signal hits. All the R- and  $\phi$ -sensors are 300  $\mu\text{m}$  thick. The geometrical setup of the modules, as shown in Fig. 2.8, is mainly driven by the requirement of angular acceptance and by the fact that clusters from at least three VELO stations are needed for the pattern recognition algorithm to reconstruct a track.

The track detection efficiency of the VELO for tracks also passing the downstream tracking stations is generally around or above 98%<sup>[85]</sup>, as illustrated in Fig. 2.10. The individual hit resolution is strongly dependent on the strip pitch and the projected angle, which is the angle perpendicular to the sensor plane<sup>[86]</sup>, as shown in Fig. 2.11. The best hit resolution is determined to be around 4  $\mu\text{m}$  with a minimal pitch of 40  $\mu\text{m}$  and an optimal projected angle of 8°. It leads to the excellent PV resolution, which is better than 35  $\mu\text{m}$  and 280  $\mu\text{m}$  and can reach 10  $\mu\text{m}$  and 60  $\mu\text{m}$  in the  $x/y$  and  $z$  directions, respectively<sup>[85]</sup>, as shown in Fig. 2.12. With the tracks and PVs in place, the IP resolution is determined as a function of the track momentum as displayed in Fig. 2.13.

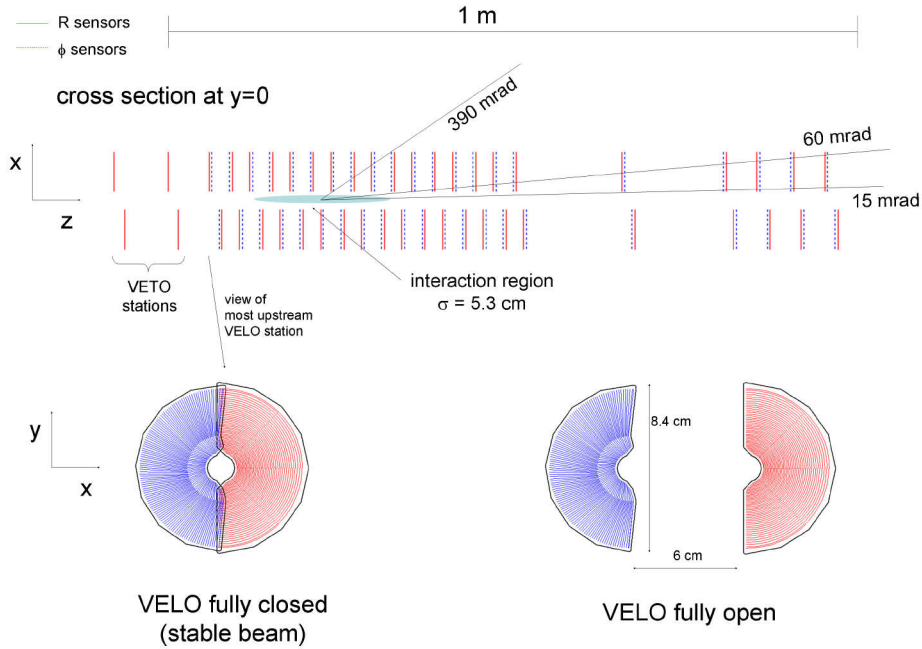


Figure 2.8 Arrangement of the VELO sensors shown in the  $(x, z)$  plane at  $y = 0$ . The view of the most upstream VELO station in the  $(x, y)$  plane is also displayed in both the closed and open positions. The two veto stations left of the VELO sensors are used to suppress events with multiple interactions. Figure taken from Ref. [76].

### 2.2.1.3 Tracker turicensis

The TT is a silicon microstrip tracker placed upstream of the dipole magnet. It is a planar tracking detector covering a 150 cm wide and 130 cm high region centred at the beam pipe. The TT comprises four detection layers called  $x-u-v-x$  with an increasing  $z$  coordinate. The strips are vertical in the  $x$  layers, and are tilted by  $-5^\circ$  and  $5^\circ$  in the  $(x, y)$  plane in the  $u$  and  $v$  layers, respectively. To optimise the track reconstruction, the layers are arranged in two sets,  $x-u$  and  $v-x$ , with a spacing of around 27 cm along the  $z$  axis. Each set provides a measure of one position, then two sets together determine one trajectory. The schematic view of the  $v$  layer is shown in Fig. 2.14. The detection layers are built of rectangular silicon sensors. One, two, three or four sensors are bonded together as a sector and share one readout hybrid. The arrangement is such that sectors closer to the beam pipe have a smaller number of sensors to balance the occupancy. The silicon sensors are 9.64 cm wide, 9.44 cm long and 500  $\mu\text{m}$  thick. Each sensor has 512 silicon strips with a pitch of 183  $\mu\text{m}$ , which is adequate to meet the requirement of single-hit resolution. The hit detection efficiency of the TT is measured to be larger than 99.7%. The single-hit

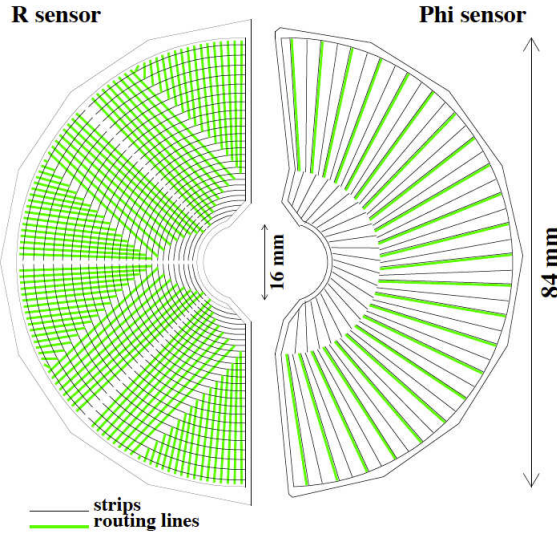


Figure 2.9 Schematic layout of the  $r\phi$  geometry of the VELO sensors. The green routing lines indicate read out of the strips. Figure taken from Ref. [85].

resolutions for all modules are typically between  $40\text{ }\mu\text{m}$  and  $60\text{ }\mu\text{m}$ , and are better in the outer regions<sup>[86]</sup>, as shown in Fig. 2.15.

#### 2.2.1.4 Tracking stations

The tracking stations T1-T3 are located downstream of the magnet, with an identical design for all the three stations. Each station is made up of four layers in an  $x-u-v-x$  geometry the same as the TT. The IT covers the region with  $|y| < 10.9(20.7)\text{ cm}$  for  $|x| < 62.8(26.5)\text{ cm}$ , while the OT corresponds to the outer region extending to the full acceptance of the LHCb detector. The boundary is chosen to guarantee an occupancy below 10% for the OT modules.

The IT is equipped with silicon strip sensors, as shown in Fig. 2.16. The modules with one sensor are placed above and below the beam pipe. The modules on the left and right of the beam pipe are made of two sensors. The silicon sensors are 7.6 cm wide and 11 cm long, carrying 384 strips with a pitch of  $198\text{ }\mu\text{m}$ . The sensors in the one-sensor and two-sensor modules are  $320\text{ }\mu\text{m}$  and  $410\text{ }\mu\text{m}$  thick, respectively, to guarantee an optimised signal-to-noise ratio and a minimised material budget at the same time. The IT provides hit detection efficiencies larger than 99.8%. The single-hit resolutions for all modules are around  $50\text{ }\mu\text{m}$  as shown in Fig. 2.17.

The OT is instrumented with gaseous straw tubes. The arrangement of the straw-tube modules in the OT is shown in Fig. 2.18. Each module consists of two staggered layers

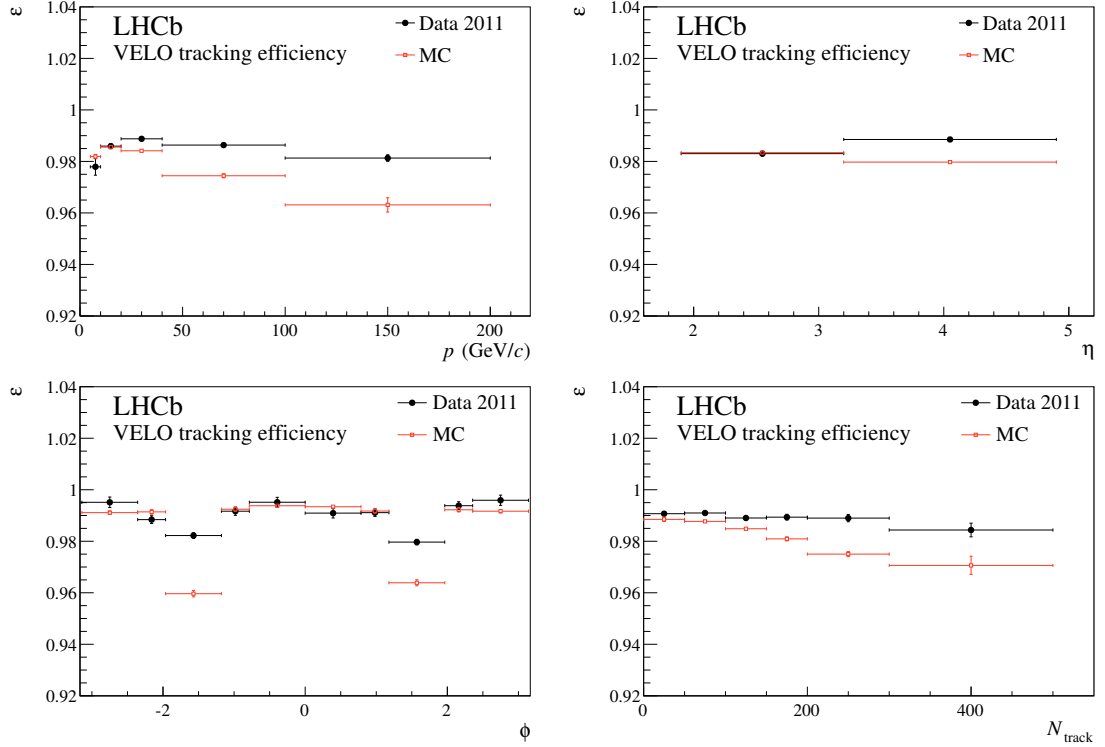


Figure 2.10 Track detection efficiency of the VELO as functions of (top left) the momentum, (top right) the pseudorapidity, (bottom left) the azimuthal angle and (bottom right) the number of tracks in the events. Figures taken from Ref. [85].

of straw tubes, as shown in Fig. 2.19. The straw tubes are 2.4 m long and have an inner diameter of 4.9 mm with an anode wire placed at the centre. A mixture of Argon (70%), CO<sub>2</sub> (28.5%) and O<sub>2</sub> (1.5%) is filled in the tubes to obtain a fast drift time. The average hit detection efficiency of each OT module for tracks crossing the centre of the tube with  $|r| < 1.25$  mm is determined to be around 99.2%. The single-hit resolution is determined from the fit to the hit distance residual distribution, as shown in Fig. 2.20. It can reach 180  $\mu\text{m}$  if the staggered layers are allowed to shift independently in the alignment<sup>[87]</sup>.

### 2.2.1.5 Performance

Tracks are reconstructed using the hits detected by the VELO, the TT, the IT and the OT together. The reconstructed tracks can be categorized into the following classes as indicated in Fig. 2.21:

- **Long tracks:** tracks crossing all the way through the VELO, the TT and T1-T3. These tracks are most precisely measured and most widely used in physics analyses.

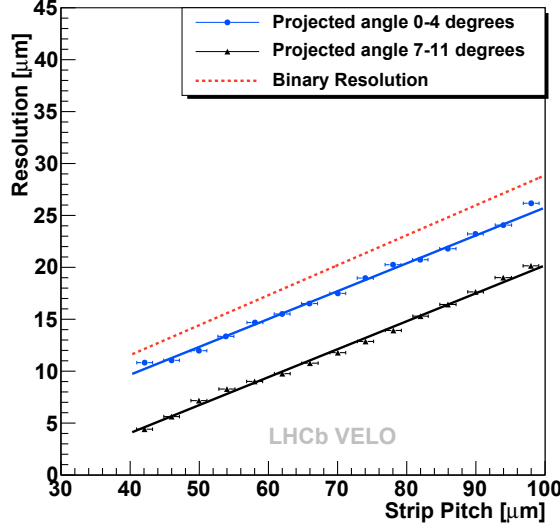


Figure 2.11 Hit resolution of the VELO R-sensors as a function of the strip pitch in two projected angle bins are shown in solid lines. The red dashed line is the resolution for binary readout. Figure taken from Ref. [86].

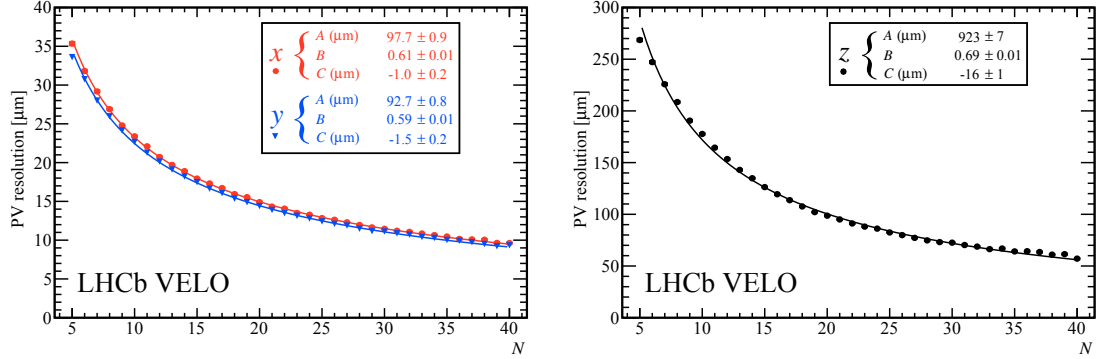


Figure 2.12 PV resolution of the VELO in the (left)  $x/y$  and (right)  $z$  directions for events with one PV as a function of the number of tracks. Figures taken from Ref. [85].

- **VELO tracks:** tracks with large angles or going backwards thus only passing the VELO. These tracks are mainly used to reconstruct the PV and/or to reject events with multiple interactions.
- **Upstream tracks:** tracks detected only by the VELO and the TT. These tracks tend to have smaller momenta and are bent outside the LHCb acceptance by the magnet. They are in particular useful for the PID in RICH1.
- **Downstream tracks:** tracks passing through the TT and T1-T3. They are mainly decay products of particles with a long lifetime, *e.g.*  $K_s^0$  and  $\Lambda$ .

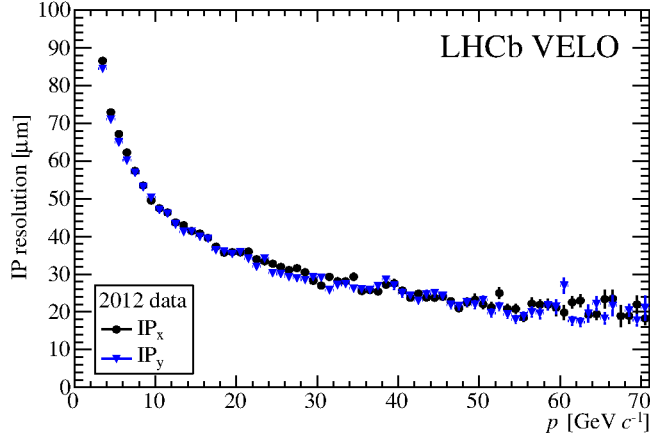


Figure 2.13 IP resolution of the VELO resolved in the  $x$  and  $y$  directions as a function of the track momentum. The  $z$  component is negligible. Figure taken from Ref. [85].

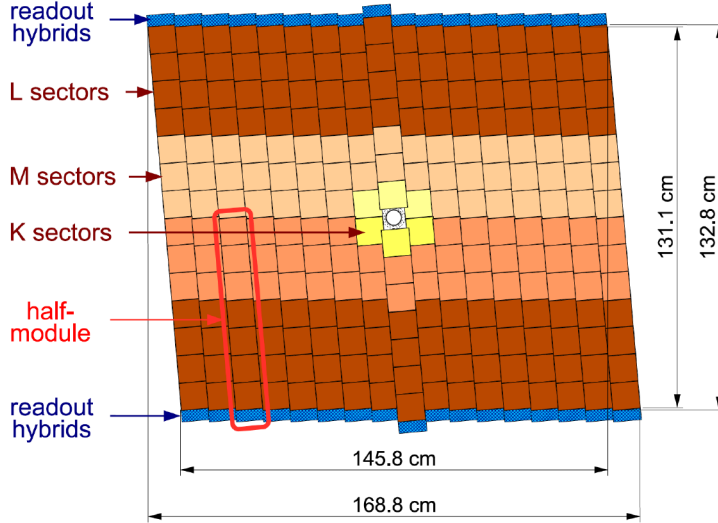


Figure 2.14 Layout of the  $\nu$  layer in the TT. Figure taken from Ref. [76].

- **T tracks:** tracks only traversing T1-T3 which can aid the pattern recognition in RICH2.

The track detection efficiencies for long tracks as functions of the momentum, the pseudorapidity, the number of tracks and the number of PVs are illustrated in Fig. 2.22. The average track detection efficiency is greater than 96% for the tracks with  $p < 200 \text{ GeV}/c$ ,  $1.9 < \eta < 4.9$ , number of tracks  $< 300$  and number of PVs  $< 6$ . Only when the number of tracks is above 300, it is slightly smaller than 96%<sup>[86]</sup>. The relative momentum resolution,  $\delta p/p$ , is determined as a function of the momentum of the particle, as shown in Fig. 2.23. It ranges approximately from 0.5% to 1.1% with an increasing momentum

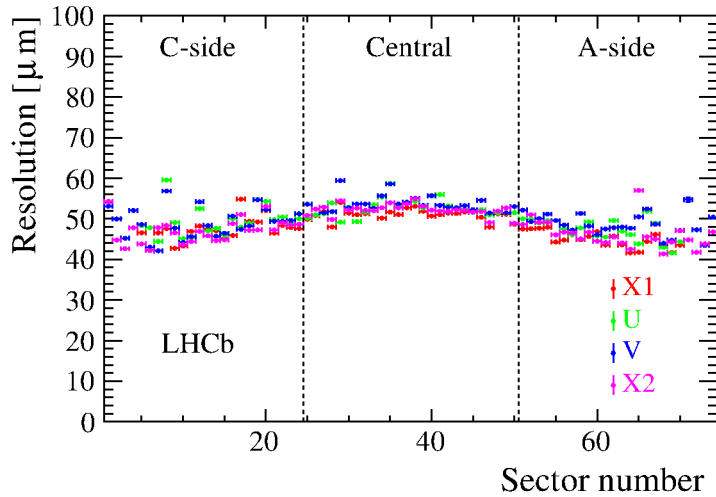


Figure 2.15 Single-hit resolutions for all modules in the TT. The sector numbers are positively correlated to the  $x$  coordinates. Figure taken from Ref. [86].

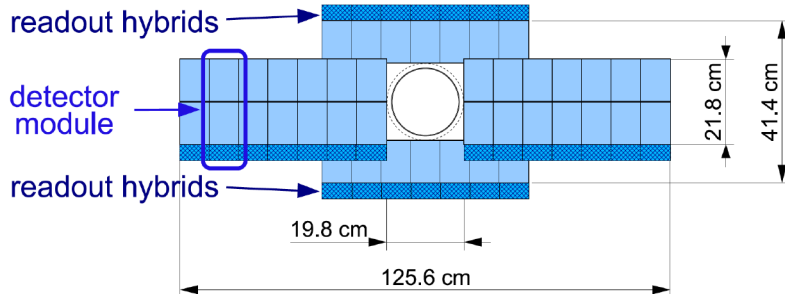


Figure 2.16 Layout of the  $x$  layer in IT of the T2 station. The circle indicates the LHCb beam pipe. Figure taken from Ref. [76].

up to  $300 \text{ GeV}/c$ <sup>[86]</sup>.

## 2.2.2 Particle identification

Two ring-imaging Cherenkov detectors, RICH1 and RICH2, are assembled to identify charged hadrons, *i.e.* pions, kaons and protons. The calorimeter system, consisting of the SPD, the PSD, the ECAL and the HCAL, is used to discriminate photons, electrons and hadrons. The muon chambers are equipped to trigger and identify muons.

### 2.2.2.1 RICH

When passing through a medium with refractive index  $n > 1$ , a charged particle radiates Cherenkov light if it has a velocity  $v$  larger than the speed of light in the medium.

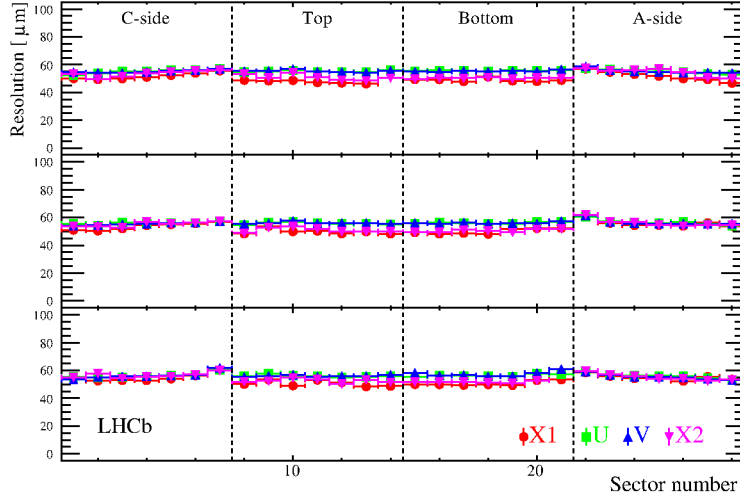


Figure 2.17 Single-hit resolutions for all modules in the IT. The sector numbers are positively correlated to the  $x$  coordinates. Figure taken from Ref. [86].

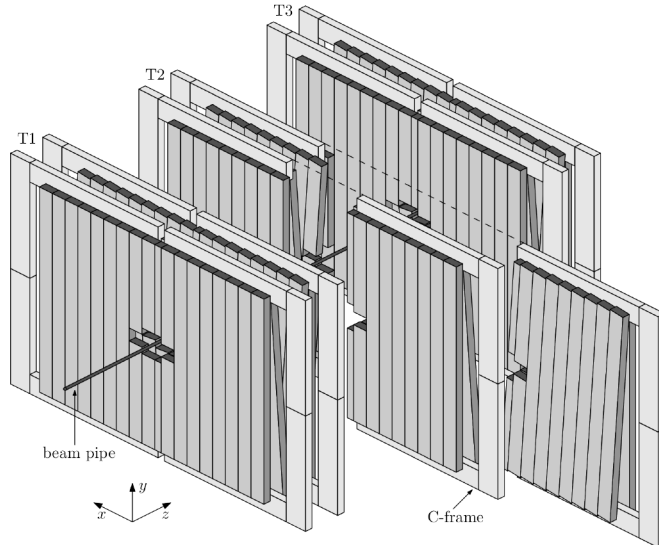


Figure 2.18 Arrangement of the straw-tube modules in the OT. Figure taken from Ref. [87].

The emission angle of the Cherenkov radiation,  $\theta_c$ , is related to  $v$  by

$$\cos \theta_c = c/nv, \quad (2-1)$$

where  $c$  stands for the speed of light in vacuum. The angle  $\theta_c$  can be derived by detecting the Cherenkov light. Together with the particle momentum obtained from the tracking system, it determines the invariant mass of the charged particle, thus identifies the particle. Different radiators apply to different momentum ranges when used to distinguish

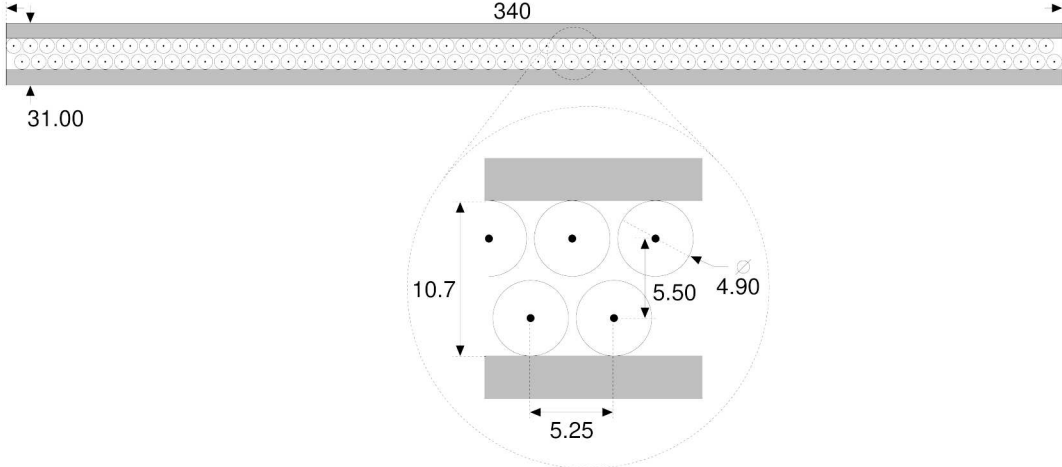


Figure 2.19 Cross section of a straw-tube module of the OT. Figure taken from Ref. [87].

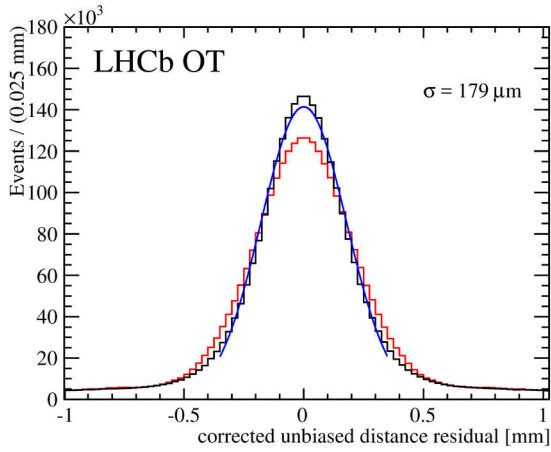


Figure 2.20 Hit distance residual distribution (red) before and (black) after the improvement of alignment. The blue solid line indicates the fit used to determine the single-hit resolution. Figure taken from Ref. [87].

particles. To cover the full momentum range of interest, two ring-imaging Cherenkov detectors are instrumented. The RICH1 detector uses a mixture of aerogel and  $\text{C}_4\text{F}_{10}$  as radiator, corresponding to the low momentum range of  $1 - 60 \text{ GeV}/c$ . The RICH2 detector uses the  $\text{CF}_4$  radiator, covering the momentum region from  $15 \text{ GeV}/c$  up to larger than  $100 \text{ GeV}/c$ . The relation between the emission angle  $\theta_c$  and the particle momentum for different types of particles is shown in Fig. 2.24 for the radiators used in RICH1 and RICH2. In both RICH1 and RICH2, spherical and plane mirrors are equipped to focus the Cherenkov light. They are also responsible for passing the light on to the pixel hybrid photon detectors (HPD), which are assembled out of the LHCb acceptance to reduce the material budget. In the HPD, photoelectrons are produced from photon conversions in

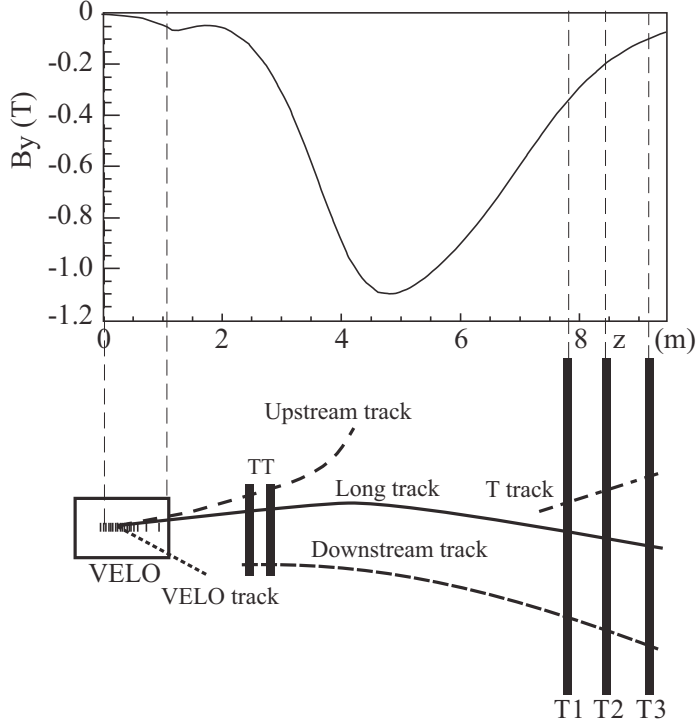


Figure 2.21 Illustration of different types of tracks in the LHCb experiment. The  $y$  component of the magnetic field is given as a reference. Figure taken from Ref. [86].

the photocathode, then accelerated onto the silicon detector. The pixel HPDs adopted in LHCb are segmented into 1024 pixels with the size of  $500 \mu\text{m} \times 500 \mu\text{m}$ .

The RICH1 detector is located between the VELO and the TT. The sectional view of RICH1 in the  $(y, z)$  plane is shown in Fig. 2.25. The Cherenkov light reaches the spherical mirrors first, which reflects it to the plane mirrors standing outside the LHCb acceptance. The plane mirrors direct the light to the HPDs, where the light is recorded. There are four spherical mirrors with a projected size of  $830 \text{ mm} \times 630 \text{ mm}$  on the  $(x, y)$  plane, and 16 rectangular plane mirrors of  $380 \text{ mm} \times 347.5 \text{ mm}$  in RICH1. The placement of the mirrors and the HPDs is determined to maximise the acceptance of the radiated photons and to minimise the error of the emission point measurement. The spherical mirrors are made of carbon fibre to reduce the material budget, as they are traversed by the particles. Glass is employed in the flat mirrors.

The RICH2 detector is located after the tracking stations. It covers only the polar angle range of  $\pm 120(100)$  mrad in the horizontal (vertical) plane, where the majority of high momentum particles pass. The sectional view in the  $(x, z)$  plane is illustrated in Fig. 2.26. The optical layout is similar to that of the RICH1 detector, except that it is horizontal in RICH2 but vertical in RICH1. There are two spherical mirror surfaces

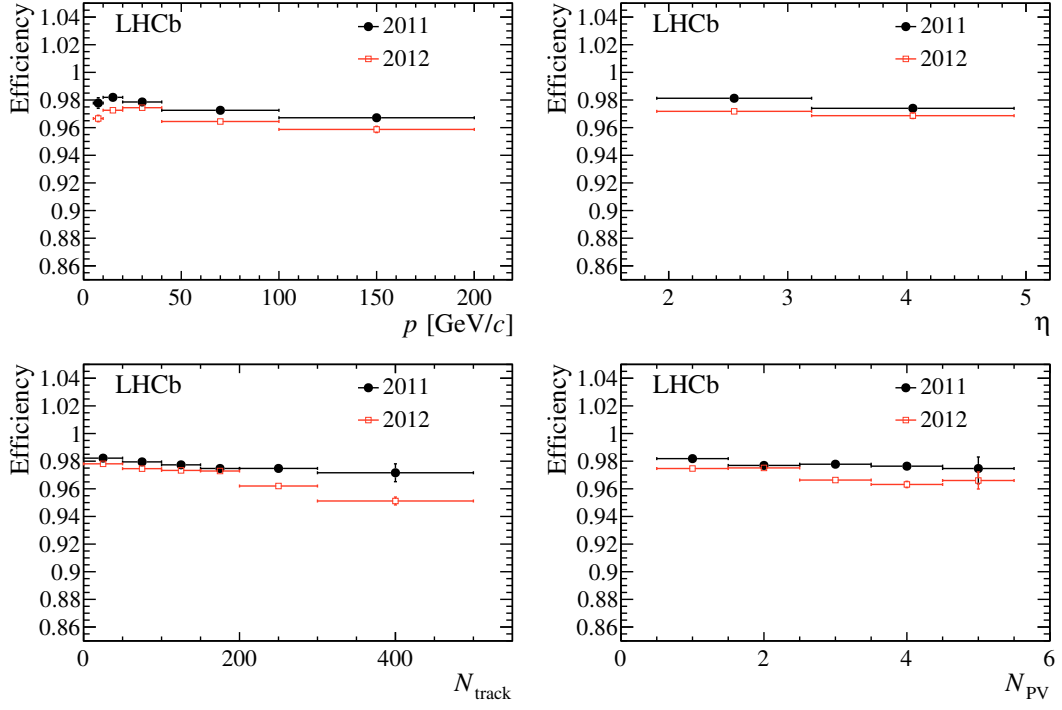


Figure 2.22 Track detection efficiency for long tracks as functions of (top left) the momentum, (top right) the pseudorapidity, (bottom left) the number of tracks and (bottom right) the number of PVs in the events. Figures taken from Ref. [86].

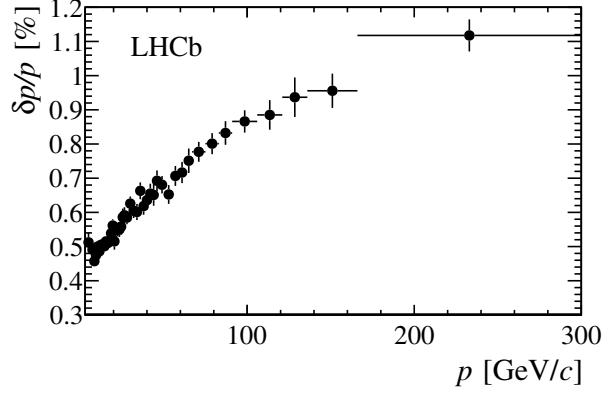


Figure 2.23 Relative momentum resolution as a function of the particle momentum. Figure taken from Ref. [86].

composed of 26 hexagonal mirrors, and two flat mirror planes consisting of 20 rectangular mirrors of  $410\text{ mm} \times 380\text{ mm}$ . The spherical mirrors adopt a thin glass substrate, the same as the plane mirrors.

Utilizing the Cherenkov emission angle information measured by the RICH1 and RICH2 detectors and the track momentum determined from the tracking system, the

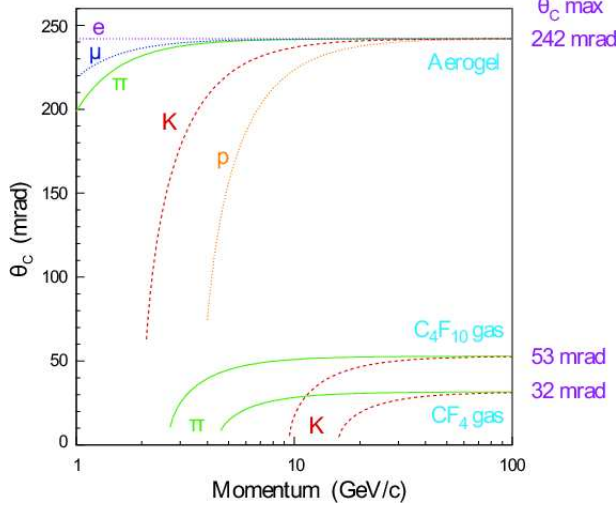


Figure 2.24 The emission angle  $\theta_c$  as a function of the particle momentum for various particles in the radiators used in RICH1 and RICH2. Figure taken from Ref. [76].

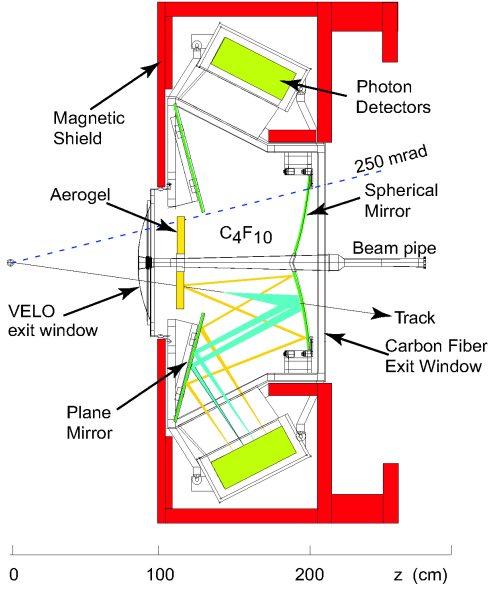


Figure 2.25 Cross section of the RICH1 detector in the  $(y, z)$  plane. Figure taken from Ref. [76].

log-likelihood difference  $\Delta \log \mathcal{L}$ , which identifies the particle type, can be calculated. The  $\Delta \log \mathcal{L}$  indicates the difference between the probability of the particle to be an electron, muon, proton or kaon and the probability that the particle is a pion. The pion is taken as the baseline since it has the largest yield among all final-state particles in the LHCb experiment. The performance of the PID is studied using the control samples, in which the particle type is known. As shown in Fig. 2.27, with the requirement of  $\Delta \log \mathcal{L}(K - \pi) > 0$ , the average kaon identification efficiency (identifying kaons as kaons) is around 95% for the momentum range of  $2 - 100 \text{ GeV}/c$ , and the average pion

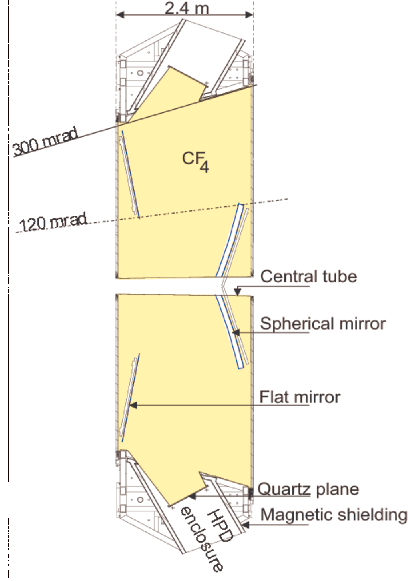


Figure 2.26 Cross section of the RICH2 detector in the  $(x, z)$  plane. Figure taken from Ref. [76].

misidentification rate (identifying pions as kaons) is around 10%<sup>[88]</sup>. They are reduced to 85% and 3% respectively if  $\Delta \log \mathcal{L}(K - \pi) > 5$  is required. The discrimination power of protons from pions and kaons from protons is also good as illustrated in Fig. 2.27.

### 2.2.2.2 Calorimeters

The calorimeter system is responsible for the discrimination of photons, electrons and hadrons, especially an efficient electron identification accomplished by selecting electrons with high transverse energy ( $E_T$ ). The widely used structure of the HCAL placed after the ECAL is adopted. To reject  $\pi^0$  candidates which can also deposit energy in the ECAL, the SPD is equipped before the ECAL. To achieve a more powerful suppression of the enormous charged pion contamination, the PSD is instrumented between the SPD and the ECAL. In all calorimeters, wavelength-shifting fibres are implemented to conduct scintillation light, and photomultipliers are used to detect the light.

The SPD and the PSD have a similar design, and are separated by around 56 mm along the  $z$  axis. In both detectors, there is a lead convertor of 15 mm thickness, equivalent to 2.5 times the radiation length  $X_0$ , sandwiched between two rectangular scintillator pads. Each scintillator plane is segmented into sections with areas of  $4 \text{ cm} \times 4 \text{ cm}$ ,  $6 \text{ cm} \times 6 \text{ cm}$  and  $12 \text{ cm} \times 12 \text{ cm}$  to make an exact projective correspondence to the cells in the ECAL.

The ECAL adopts a sampling scintillator/lead structure. The hit density decreases with increasing distance to the beam pipe by two orders of magnitude. To unify the

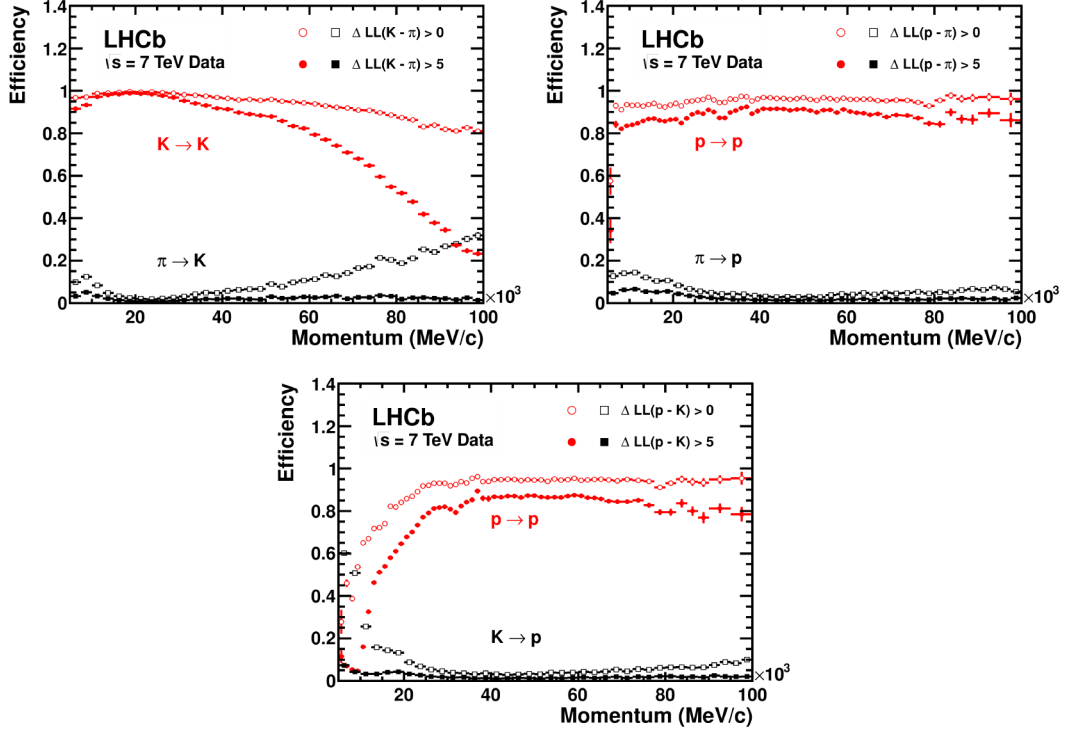


Figure 2.27 Top left: the kaon identification efficiencies and pion misidentification rates with different requirements on  $\Delta \log \mathcal{L}(K - \pi)$  as a function of the track momentum. Top right: the proton identification efficiencies and pion misidentification rates with different requirements on  $\Delta \log \mathcal{L}(p - \pi)$  as a function of the track momentum. Bottom: the proton identification efficiencies and kaon misidentification rates with different requirements on  $\Delta \log \mathcal{L}(p - K)$  as a function of the track momentum. The  $\Delta \log \mathcal{L}(p - K)$  equals  $\Delta \log \mathcal{L}(p - \pi) - \Delta \log \mathcal{L}(K - \pi)$ . Figures taken from Ref. [88].

occupancy, the ECAL is partitioned into the inner, middle and outer sections with inner and outer dimensions of  $(65 \times 65, 194 \times 145) \text{ cm}^2$ ,  $(194 \times 145, 388 \times 242) \text{ cm}^2$  and  $(388 \times 242, 776 \times 630) \text{ cm}^2$ , respectively. The modules for the inner, middle and outer sections comprise 9 cells of  $4.04 \text{ cm} \times 4.04 \text{ cm}$ , 4 cells of  $6.06 \text{ cm} \times 6.06 \text{ cm}$  and 1 cell of  $12.12 \text{ cm} \times 12.12 \text{ cm}$ , respectively, ending up with the same size. A module consists of 66 stacks formed from a 2 mm thick lead layer and a 4 mm thick scintillator layer separated by  $120 \mu\text{m}$  thick white paper. The module is in total 42 cm thick, amounting to  $25X_0$ .

The HCAL is a sampling calorimeter built from iron and scintillating tiles. Different from the ECAL, the layers are oriented along the  $z$  axis, as shown in Fig. 2.28. The HCAL is made of 52 modules placed one on top of another. In each module, alternating layers of 3 mm thick scintillator and 4 mm thick iron absorber, which are glued to 6 mm thick master plates, are repeated 216 times. Fibres are placed on the edges of the module. The

modules have a depth of 1.65 m, corresponding approximately to  $X_0$ . To accommodate the varying particle flux, the HCAL is subdivided into the inner and outer sections, with lateral dimensions of 4202 mm  $\times$  3676 mm and 8404 mm  $\times$  6828 mm, respectively. The partition is accomplished by banding different sets of fibres to the readout photomultipliers.

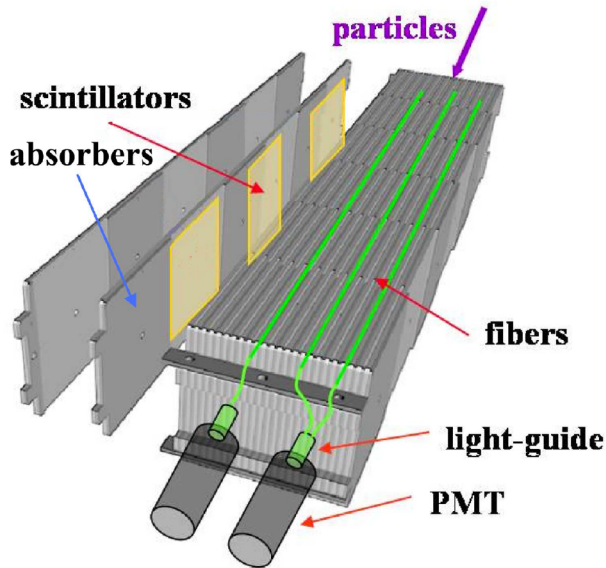


Figure 2.28 Layout of the internal module structure of HCAL. Figure taken from Ref. [76].

Using information from the calorimeters, the log-likelihood difference  $\Delta \log \mathcal{L}(e-h)$  can be determined for each track as the discriminating variable. A larger  $\Delta \log \mathcal{L}(e-h)$  value indicates a greater probability of the particle to be an electron rather than a hadron. The electron identification efficiencies and misidentification rates for various requirements on  $\Delta \log \mathcal{L}(e-h)$  are shown in Fig. 2.29.

### 2.2.2.3 Muon chambers

The muon system is dedicated to the reconstruction and identification of muons. It is composed of five stations M1-M5 in a projective geometry, leading to an increasing lateral dimension with a larger distance to the interaction point. The M1 station is followed by the calorimeters, which are upstream of the other four stations, as shown in Fig. 2.30. The stations M2-M5 are separated by 80 cm thick iron absorbers to select high-momentum muons. The muon trigger requires hits from all the five stations. To penetrate all the way through the calorimeters and the muon stations, which correspond to  $20X_0$ , the muons need to have a momentum larger than 6 GeV/c. The spatial resolution is better in M1-M3,

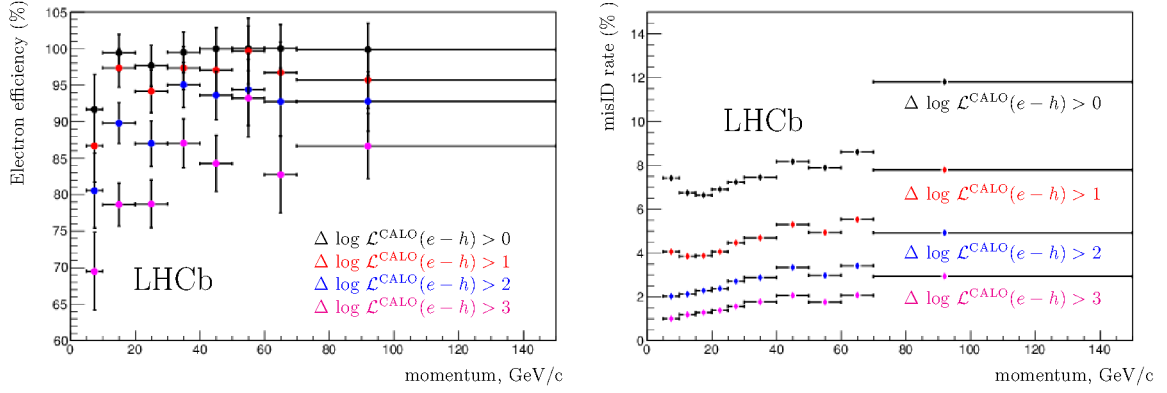


Figure 2.29 The efficiencies of (left) identifying electrons correctly and (right) misidentifying electrons as other particles with different  $\Delta \log \mathcal{L}(e - h)$  cut values as a function of the track momentum. Figures taken from Ref. [86].

allowing for the determination of the muon trajectories, and limited in M4-M5, which focus on identifying high-momentum particles. All stations are subdivided into four regions R1-R4 with an area ratio of  $1^2 : 2^2 : 4^2 : 8^2$  from the inner to the outer edge, as shown in Fig. 2.30 as well. The stations are composed of MWPCs, as shown on the left of Fig. 2.31. The only exception is the region R1 in the station M1, in which Gas electron multipliers (GEM) are used to deal with the large particle density. The MWPCs are subdivided into logical pads which provide independent readouts, as shown on the right of Fig. 2.31 for the M1 station. In M2-M3 (M4-M5), the pad number per row in each chamber is double (half) that in corresponding regions of M1, while the pad number per column is the same. To obtain a good time resolution, a mixture of Argon (40%), CO<sub>2</sub> (55%) and CF<sub>4</sub> (5%) is adopted in the chambers which ensures a fast drift time. In the stations M2-M5, there are four gas gaps interleaved with 9 mm thick panels, as shown in Fig. 2.32. The panels are made of an insulating plane sandwiched between two conducting pads, which hold the anode wires. The gas gaps are 5 mm thick, and a wire plane with a 2 mm wire spacing is placed in the centre of each gas gap. This design guarantees a time resolution of around 5 ns. In the station M1, only two gas gaps are instrumented.

To identify muons, the charged tracks reconstructed in the tracking system are extrapolated to the muon chambers. If there are hits that can be associated to a track in all five muon stations, the track is defined as a muon. The muon identification efficiencies and the rates of misidentifying protons, pions and kaons as muons are shown in Fig. 2.33 as a function of the track momentum for different  $p_T$  ranges. On average, the muon identifica-

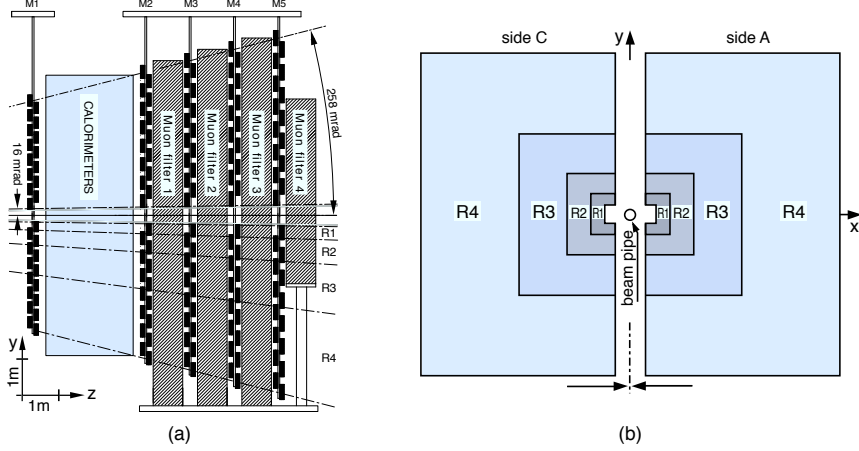


Figure 2.30 The (left) side and (right) front view of the muon system. Figures taken from Ref. [89].

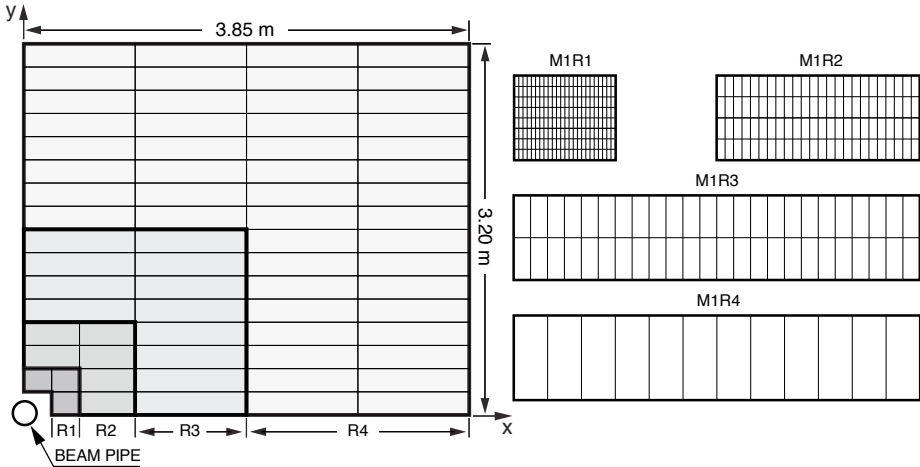


Figure 2.31 Left: sectional view of a quadrant of the M1 station. Right: arrangement of logical pads of chambers inside the R1-R4 regions in the M1 station. Figures taken from Ref. [89].

tion efficiency is as good as about 97% with a pion misidentification rate of approximately 2%<sup>[86]</sup>. Similar to the RICH detectors and the calorimeters, a log likelihood difference  $\Delta \log \mathcal{L}(\mu)$  can be calculated as the discriminating variable.

#### 2.2.2.4 Performance

To give a more powerful PID, measurements from the RICH, the calorimeter and the muon subsystems can be combined together. The combination is performed in two methods. The first approach is to linearly add the log likelihood difference determined by each subsystem together to form a global variable,  $\Delta \log \mathcal{L}(X - \pi)$ , where  $X$  stands for kaons, protons, electrons or muons. The second method applies the multivariate

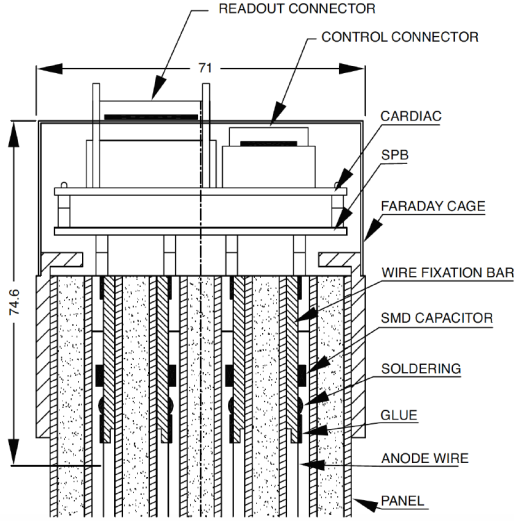


Figure 2.32 Cross section of the MWPC used in the stations M2-M5. Figure taken from Ref. [76].

technique, which includes not only the log likelihood differences but also some additional information. The response of the multivariate analysis is taken as the PID discriminant and denoted as ProbNNY, where  $Y$  represents pions, kaons, protons, electrons and muons. The performance of the two discriminants is compared in Fig. 2.34. They are both more powerful than the individual  $\Delta \log \mathcal{L}$  values, and the variable ProbNNY precedes the variable  $\Delta \log \mathcal{L}(X - \pi)$  in the identification<sup>[86]</sup>.

### 2.2.3 Trigger

At the designed peak instantaneous luminosity of  $10^{32} \text{ cm}^{-2} \text{ s}^{-1}$  with the 40 MHz bunch crossing rate, the frequency of bunch crossings containing at least one inelastic  $pp$  interaction thus visible by the LHCb detector is about 11 MHz. Within these visible interactions, the production rate of events containing  $b\bar{b}$  is roughly 100 kHz. Only about 15% of these events containing at least one  $b(\bar{b})$ -hadron whose decay products are all within the LHCb acceptance. In addition, the branching fractions of  $b(\bar{b})$ -hadron decay channels of interest are typically below  $10^{-3}$ . To preliminarily select the interesting candidates out of a huge amount of plain events, an efficient and robust two-level trigger system is implemented as shown in Fig. 2.35. It consists of the first level hardware trigger (L0) and the high level software trigger (HLT). The L0 decision is given by the decision units which collect information from the front-end electronics of the subdetectors. The HLT is performed on the event filter farm (EFF) with up to 1800 server nodes. The L0 trigger is designed to operate in synchronization with the LHC bunch crossing thus has an input rate of 40 MHz.

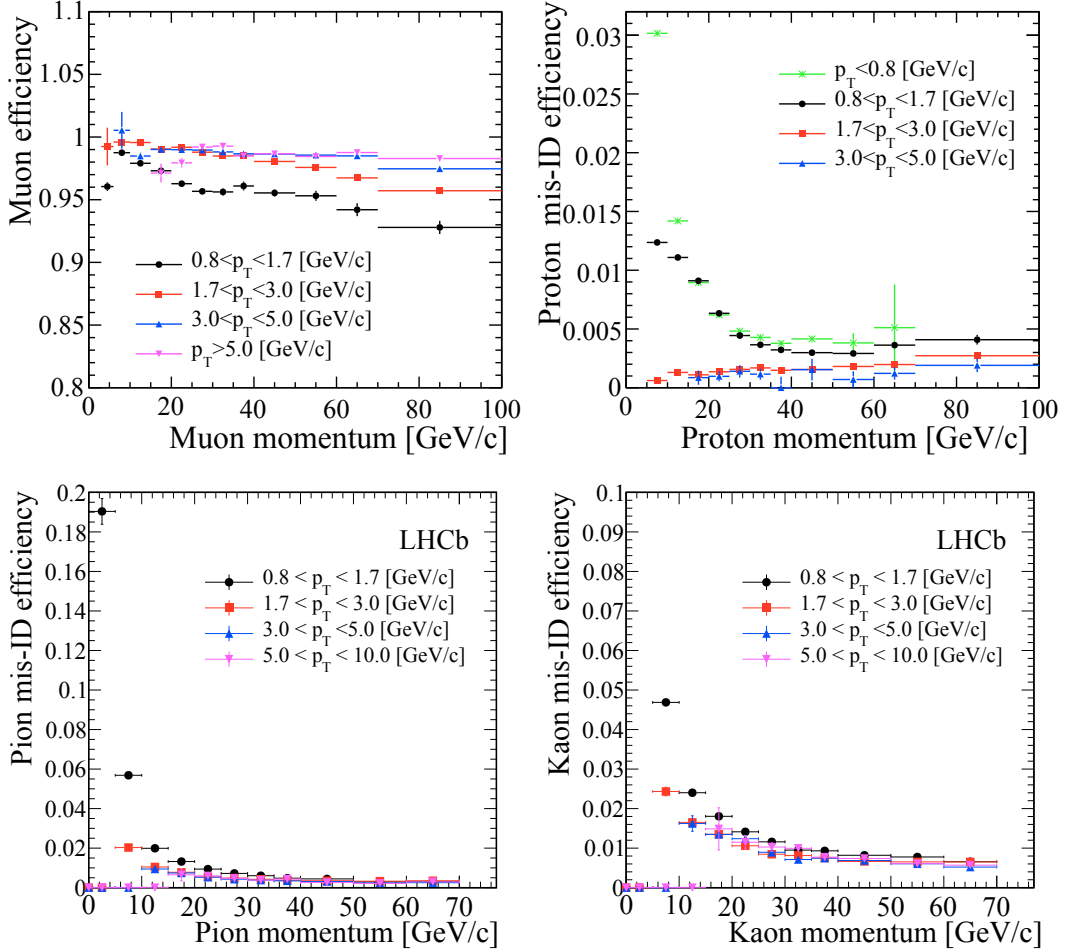


Figure 2.33 The (top left) muon identification efficiencies and the rates of misidentifying (top right) protons, (bottom left) pions and (bottom right) kaons as muons as a function of the track momentum for different  $p_T$  ranges. Figures taken from Ref. [86].

The rate is reduced to 1 MHz by the L0 trigger, then read out by the HLT. In Run1, events are filtered to a rate of 5 kHz by the HLT, and written to storage afterwards. While in Run2 the computing architecture is upgraded, allowing for a 12.5 kHz output rate of the HLT to storage.

### 2.2.3.1 L0 trigger

The L0 trigger comprises three components: the pile-up trigger, the calorimeter trigger and the muon trigger. The masses of  $b(\bar{b})$ -hadrons are large, resulting large  $p_T$  and  $E_T$  of the decay products. Taking advantage of this feature, the L0 trigger aims at looking for particles with large  $p_T$  or  $E_T$ .

The pile-up trigger is used to suppress events with multiple interactions or with too

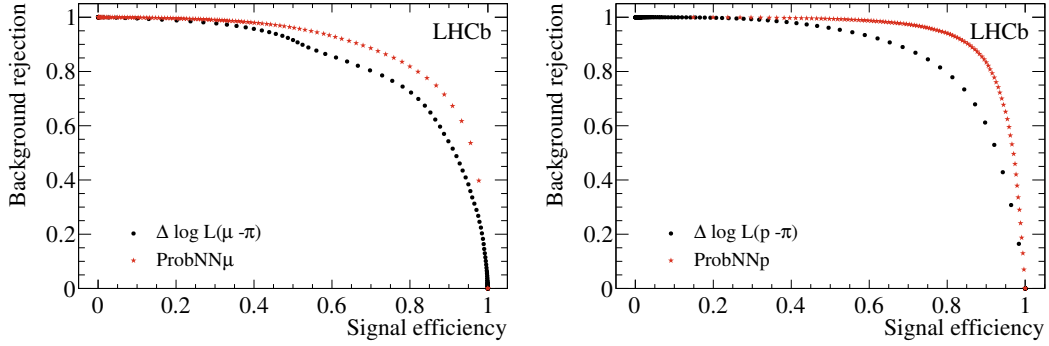


Figure 2.34 Background rejection rate versus signal identification efficiency for (left) muons and (right) protons. The values are averaged over the momentum range of  $5 - 10 \text{ GeV}/c$  and  $5 - 50 \text{ GeV}/c$  for muons and protons, respectively. Figures taken from Ref. [86].

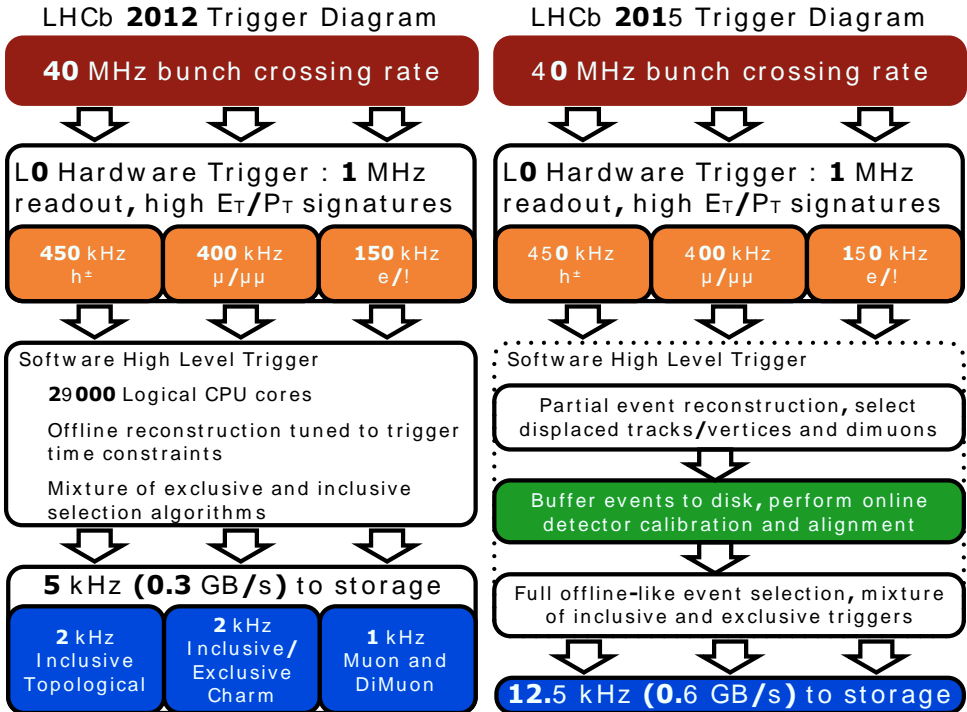


Figure 2.35 Layout of the trigger scheme applied in (left) Run1 and (right) Run2, respectively.

large track multiplicity, making use of information from the two veto stations upstream of the VELO and the SPD, respectively. Every two hits found in the veto stations are combined to form an origin point. A large overlap of the origin points indicates a  $pp$  interaction. Events with multiple interactions are then rejected. Events with too many hits found in the SPD, which demand too much computing power, are also removed.

The calorimeter trigger selects electrons, photons or hadrons with high  $E_T$  using measurements of the calorimeter system. The  $E_T$  of a particle is calculated by summing

the  $E_T$  in the zone of  $2 \times 2$  cells surrounding the particle trajectory, which is large enough to cover most of the energy deposits, and small enough to avoid crosstalk between different particles. The particle type is identified using information from all the calorimeters, and for each type only the candidate with the largest  $E_T$  is used for the trigger decision. Hadrons are the candidates with large energy deposits in the HCAL. Photons are the particles depositing energy in the ECAL and having one or two hits in the PSD in front of the ECAL shower, but with no SPD hits. Electrons are similar to photons except that they have at least one SPD hit ahead of the hit(s) in the PSD. Events containing any type of particle with the highest  $E_T$  larger than the set threshold are kept.

The muon trigger utilizes the muon system to look for muon tracks with large  $p_T$ . Each quadrant of the muon stations is connected to a L0 muon processor, which selects two muon tracks with the highest  $p_T$ . In the processors, hits found in the M3 station are taken as seeds. Then in the M2, M4 and M5 stations, hits are sought in the fields of interest (FOI) determined by the intersection points of these stations and the straight line traversing the seed position and the interaction point. The FOIs are roughly centred on the intersections and have a variable size depending on the station and the region being considered. At least one hit in the FOI for each of these stations is required, and the hit closest to the intersection is selected if there are more than one hit found. The FOI for M1 is determined by extrapolating the selected hits in M2 and M3, and the hit closest to the extrapolation point is used for the track reconstruction. The hit positions in the M1 and M2 stations determine the  $p_T$  of the muon track with a resolution of about 20%. There are in total eight muon candidates selected by the four L0 muon processors. Thresholds are set on the largest  $p_T$  or the product of the two largest  $p_T$  of the eight muons.

### 2.2.3.2 HLT

The HLT is divided into two stages, the first level (HLT1) and the second level (HLT2). In HLT1, the events are partially reconstructed using information from the VELO and the tracking stations. The event rate is significantly reduced by requiring the L0 objects, the VELO hits and the hits in the tracking stations to be matched with each other. In addition, primary vertices are reconstructed with tracks in the VELO. A further rate suppression is achieved by setting thresholds on the IP and the  $p_T$  of the tracks. The output rate of the HLT1 is restricted to around 150 kHz. In HLT2, a full event reconstruction is performed using information from all the subdetectors. Not only tracks are reconstructed, but also

composite particles are formed, which allows for an extended choice of cuts. In Run1, the HLT2 differs from the offline in track reconstruction by not considering the full covariance matrix of the tracks, due to the limitation of CPU power. In Run2, an algorithm identical to that of the offline reconstruction is accomplished in HLT2.

#### 2.2.3.3 Offline trigger decision

In the L0 trigger and HLT, the selection criteria are organised in trigger lines, which cover different physics channels. Triggered events are recorded no matter which trigger line(s) they can pass. In a physics measurement, typically only candidates passing one or several specific trigger lines are needed. To dig out these useful candidates, trigger decisions can be assigned to the events for each trigger line by comparing the offline hits to the hits stored online. To further identify which component of the event leads to the positive trigger decision, three types of trigger decisions are defined for a candidate:

- **TOS:** trigger on signal. The trigger is due to the signal candidate, regardless of the remaining tracks in the event.
- **TIS:** trigger independent of signal. The trigger is caused by tracks other than those of the signal candidate in the event.
- **TOB:** trigger on between. The event is triggered by tracks from both the signal candidate and the rest of the event.

The TIS and TOS decisions are often used in physics analyses.

#### 2.2.4 Data processing and simulation

The size of the data collected by the LHCb experiment is huge. The data need to be further processed and archived to allow for a feasible access to them for users interested in different physics topics. In Run1, the data that have passed the trigger requirements are referred to as the raw data. They are reconstructed to form both neutral and charged tracks with corresponding PID information, then stored as a new data format, the data summary tape (DST). The DST files are transformed to the reduced DST (rDST) files, in which information unnecessary to the following physics selections is eliminated. The data in rDST allow for the determination of the four-momentum vectors of the tracks, the location of the PVs and decay vertices, and the reconstruction of composite particles. Based on these quantities, various selection algorithms are defined to further filter the rDST files, each resulting in an individual output. The output files are divided into several streams,

which can be processed within a reasonable time. In Run2, in addition to the offline processing, the output of the HLT2 can be used directly to perform physics analyses, since the HLT2 can implement a reconstruction algorithm identical to that of the offline reconstruction.

During the event reconstruction, fits are performed to the detected hits to reconstruct tracks. The  $\chi^2$  per degree of freedom of the fit,  $\chi^2_{\text{track}}/\text{ndf}$ , defines the quality of the track. Similarly, tracks are fitted to form a vertex, and the vertex quality is defined by the  $\chi^2$  per degree of freedom,  $\chi^2_{\text{vertex}}/\text{ndf}$ , of the fit. It is possible that a track is misreconstructed from hits of other tracks. Such probability is denoted as `Track_GhostProb`. The impact parameter of a particle,  $\chi^2_{\text{IP}}$ , is used to indicate whether the particle comes from a given PV. It is calculated as the difference in the vertex fit  $\chi^2$  of the PV reconstructed with and without the particle under consideration. The decay tree fitter (DTF) is a tool to incorporate hypothesis into the decay chain. It can apply mass constraints on the daughter particles, and require the candidate to point to the PV. The  $\chi^2$  per degree of freedom of the fit performed with the DTF,  $\chi^2_{\text{DTF}}/\text{ndf}$ , can indicate the consistency of the candidate with the hypothesis. For example, if the DTF requires the candidate to point to the PV, a smaller  $\chi^2_{\text{DTF}}/\text{ndf}$  value means the candidate is more likely to come from the PV.

Simulation is necessary in most of the analyses. At the LHCb experiment, the  $pp$  collision processes are described using `PYTHIA`<sup>[90]</sup> which is specifically configured according to the LHCb condition. For the production of the  $B_c$  mesons, the dedicated generator `BCVEGPY`<sup>[91]</sup> is applied to simulate it. The decays of particles are simulated with `EvtGEN`<sup>[92]</sup>, in which `PHOTOS`<sup>[93]</sup> is used to describe the final-state radiation. The interaction of the produced particles with the detector materials and the response of the detector are simulated using the `GEANT4` toolkit<sup>[94]</sup> as described in Ref. [95]. The detector responses are digitalized and passed to the L0 trigger emulation system afterwards. The subsequent HLT and offline processing of the simulated data is identical to that of the real data.

## Chapter 3 $J/\psi$ production in $pp$ collisions at $\sqrt{s} = 13$ TeV

The measurement of the forward  $J/\psi$  production cross-section in  $pp$  collision at the centre-of-mass energy of  $\sqrt{s} = 13$  TeV is presented in this chapter, including the analysis strategy, the dataset, the candidate selection, the signal extraction, the efficiency estimation, the systematic uncertainties and the results with comparisons to the theoretical predictions. The analysis was done in collaboration with several colleagues at the LHCb collaboration. The author is responsible for the validation of the fit model and the determination of the muon identification efficiency.

### 3.1 Analysis strategy

There are three sources of  $J/\psi$  mesons in  $pp$  collisions: a) the scattering of partons inside the colliding protons; b) the feed-down from excited charmonium states; and c) the decays of  $b$ -hadrons. The  $J/\psi$  mesons produced from the former two processes are indistinguishable in experiments, thus are jointly referred to as “prompt  $J/\psi$ ”. Those from the last source are called “ $J/\psi$  from  $b$ ” hereafter. The NRQCD approach<sup>[22]</sup> models the production cross-section of prompt  $J/\psi$ , while the fixed order plus next-to-leading logarithms (FONLL) model<sup>[96]</sup> describes the production of  $J/\psi$  from  $b$ . They both show good agreement with the previous production measurements<sup>[28,29]</sup>.

The production cross-sections are determined separately for prompt  $J/\psi$  and  $J/\psi$  from  $b$  in the kinematic range of  $p_T < 14$  GeV/ $c$  and  $2 < y < 4.5$ , corresponding to the LHCb coverage. The  $J/\psi$  mesons are reconstructed using the  $J/\psi \rightarrow \mu^+ \mu^-$  decay, taking advantage of the efficient muon identification and trigger at LHCb. The double differential production cross-sections as functions of the  $J/\psi$  mesons’  $p_T$  and  $y$  are measured. The inclusive production cross-sections are determined by summing the double differential production cross-sections, taking into account the correlations of uncertainties between the kinematic bins.

In a given  $(p_T, y)$  bin, the double differential cross-section is defined as

$$\frac{d^2\sigma}{dydp_T} = \frac{N(J/\psi \rightarrow \mu^+ \mu^-)}{\mathcal{L} \times \varepsilon_{\text{tot}} \times \mathcal{B}(J/\psi \rightarrow \mu^+ \mu^-) \times \Delta y \times \Delta p_T}, \quad (3-1)$$

where  $N(J/\psi \rightarrow \mu^+ \mu^-)$  is the signal yield of either prompt  $J/\psi$  or  $J/\psi$  from  $b$  reconstructed

from the dimuon final state;  $\mathcal{L}$  is the integrated luminosity of the dataset;  $\varepsilon_{\text{tot}}$  is the total efficiency;  $\mathcal{B}(J/\psi \rightarrow \mu^+ \mu^-) = (5.961 \pm 0.033)\%$  is the known branching fraction of the  $J/\psi \rightarrow \mu^+ \mu^-$  decay<sup>[97]</sup>;  $\Delta y = 0.5$  and  $\Delta p_T = 1$  GeV/ $c$  are the fixed bin widths of  $y$  and  $p_T$ , respectively. The kinematic range and the bin widths of  $p_T$  and  $y$  correspond to a binning scheme with

- $p_T$  boundaries [ GeV/ $c$  ]: 0, 1, 2, 3, 4, 5, 6, 7, 8, 9, 10, 11, 12, 13, 14;
- $y$  boundaries: 2.0, 2.5, 3.0, 3.5, 4.0, 4.5.

In each  $(p_T, y)$  bin, the signal yield is determined from a simultaneous fit to the distributions of the dimuon invariant mass  $M(\mu^+ \mu^-)$  and the pseudo decay time  $t_z$ . The dimuon mass distribution is used to separate  $J/\psi$  signals from combinatorial backgrounds, while the pseudo decay time distribution is for the separation of prompt  $J/\psi$  and  $J/\psi$  from  $b$ . The pseudo decay time  $t_z$  is defined as

$$t_z = \frac{(z_{J/\psi} - z_{\text{PV}}) \times M(J/\psi)}{p_z}, \quad (3-2)$$

where  $z_{J/\psi}$  is the  $z$  coordinate of the  $J/\psi$  decay vertex,  $z_{\text{PV}}$  the  $z$  position of the PV,  $p_z$  the  $J/\psi$  momentum along the  $z$  axis, and  $M(J/\psi)$  the known mass of the  $J/\psi$  meson<sup>[97]</sup>. The efficiency  $\varepsilon_{\text{tot}}$  is estimated for each  $(p_T, y)$  bin, assuming that the efficiency is constant in a small  $p_T$  and  $y$  range. The efficiencies are estimated under the assumption that prompt  $J/\psi$  mesons have zero polarisation. The effect of the polarisation on the measured cross-sections is discussed in Sec. 3.6.8.

### 3.2 Dataset

The measurement is performed using the data collected by the LHCb experiment at  $\sqrt{s} = 13$  TeV, corresponding to an integrated luminosity of  $3.05 \pm 0.12$  pb $^{-1}$ . The integrated luminosity is determined using the beam-gas imaging method, which photographs the beams using beam-gas interactions taking advantage of the unique precision of the VELO.

The trigger requirements aim at selecting high quality muons that can form  $J/\psi$  mesons while rejecting background  $J/\psi$  candidates, which are mainly reconstructed with muons from semi-leptonic hadron decays or with kaons and pions misidentified as muons. The decisions are all TOS, *i.e.* based on the signal as introduced in Sec. 2.2.3.3. The L0 trigger requires the muon tracks to have  $p_T$  larger than 900 MeV/ $c$ . At the HLT1 trigger

stage, the tracks must be identified as muons by requiring a positive `isMuon`, which is determined with information from the muon stations. The muons are required to have  $p_T$  larger than  $500\text{ MeV}/c$ ,  $p$  larger than  $3000\text{ MeV}/c$  and  $\chi^2_{\text{track}}/\text{ndf}$  smaller than 3.0. The invariant mass of the muon pair should be greater than  $2700\text{ MeV}/c^2$ . The HLT2 trigger line reconstructs the  $J/\psi$  candidates. Candidates with good-quality vertices which satisfy  $\chi^2_{\text{vertex}}/\text{ndf} < 25$  are kept. The invariant mass of the muon pair is required to be within  $\pm 150\text{ MeV}/c^2$  of the known  $J/\psi$  mass<sup>[97]</sup>. The cuts applied in the HLT1 and HLT2 trigger lines are listed in Table. 3.1.

Table 3.1 HLT trigger lines applied and their corresponding cuts.

Trigger level	Trigger line	Cuts
HLT1	HLT1DiMuonHighMass	$p_T(\mu) > 500\text{ MeV}/c$ $p(\mu) > 3000\text{ MeV}/c$ $\chi^2_{\text{track}}/\text{ndf}(\mu) < 3.0$ <code>isMuon</code> ( $\mu$ ) == 1 $M(\mu^+\mu^-) > 2700\text{ MeV}/c^2$
HLT2	HLT2DiMuonJPsi	$\chi^2_{\text{track}}/\text{ndf}(\mu) < 4$ $M(\mu^+\mu^-) - M(J/\psi) \in \pm 150\text{ MeV}/c^2$ $\chi^2_{\text{vertex}}/\text{ndf}(\mu^+\mu^-) < 25$

Simulated samples with around 4 million  $J/\psi$  candidates are generated to study the signal efficiency. Prompt  $J/\psi$  and  $J/\psi$  from  $b$  are separated according to the truth information. The candidates are generated using PYTHIA8<sup>[98]</sup> with a specific LHCb configuration<sup>[99]</sup>. Decays of hadronic particles are simulated using EvtGEN<sup>[92]</sup>, in which the final state radiation is generated with PHOTOS<sup>[93]</sup>. The interaction of the particles with the detector and its response are described by the GEANT4 package<sup>[94,100]</sup>. The prompt charmonia are simulated with the contributions from both the LO colour-singlet and colour-octet mechanisms with zero polarisation. All the simulated events are digitized, reconstructed and selected with the same processes as the real data.

### 3.3 Candidate selection

Offline selections are applied to the  $J/\psi$  candidates that have passed the trigger selections to further reduce background. At least one PV is required to be reconstructed

in the event. The muons are required to be in the kinematic range of  $3 \text{ GeV}/c < p < 500 \text{ GeV}/c$  and  $p_T > 700 \text{ MeV}/c$ , since the track reconstruction efficiency outside of this region is poorly measured. It can also reduce a large amount of background candidates with low momenta. The muon tracks should have good quality with  $\chi^2_{\text{track}}/\text{ndf}$  smaller than 3. The fake tracks are removed by requiring the TRACK\_GhostProb smaller than 0.3. The muon pair is required to form a good-quality vertex with the fit probability of  $\chi^2_{\text{vertex}}/\text{ndf}$  larger than 0.5%. The Kullback-Leibler (KL) distance<sup>[101]</sup> between each two tracks should be larger than 5000 to remove duplicate tracks. The KL requirement reduces the rate of duplicate tracks to the level of  $0.5 \times 10^{-3}$ . The pseudo decay time is required to be in the range of  $|t_z| < 10 \text{ ps}$ , corresponding to around 6 times the typical  $b$ -hadron decay time, and to have an uncertainty smaller than 0.3 ps. The positive isMuon requirement on the muon tracks and the mass window cut on the  $J/\psi$  candidates are again applied offline to enable a simpler efficiency estimation. The offline selections as summarised in Table. 3.2.

Table 3.2 Summary of the offline selections.

Number of PV > 0	
$\mu^\pm$	$3 \text{ GeV}/c < p < 500 \text{ GeV}/c$
	$p_T > 700 \text{ MeV}/c$
	isMuon==1
	$\chi^2_{\text{track}}/\text{ndf} < 3$
	TRACK_GhostProb < 0.3
$J/\psi$	$\chi^2_{\text{vertex}}/\text{ndf}$ probability > 0.5%
	$M \in M(J/\psi) \pm 150 \text{ MeV}/c^2$
	$ t_z  < 10 \text{ ps}$
	Uncertainty of $t_z < 0.3 \text{ ps}$
	KL > 5000

### 3.4 Signal extraction

To extract the signal yields of prompt  $J/\psi$  and  $J/\psi$  from  $b$ , a simultaneous unbinned maximum likelihood fit is performed to the  $M(\mu^+\mu^-)$  and  $t_z$  distributions.

### 3.4.1 Determination of inclusive $J/\psi$ signal yield

The invariant mass distribution of the  $J/\psi$  signals is modelled with the sum of two Crystal Ball (CB) functions<sup>[102]</sup>, which is a Gaussian function with a power tail on the left side. The tail comes from the final state radiation of the  $J/\psi \rightarrow \mu^+ \mu^-$  decay. The CB function is defined as

$$g(x; M, \sigma, a_l, n_l) = \begin{cases} e^{-a_l^2/2} \left( \frac{n_l}{a_l} \right)^{n_l} \cdot \left( \frac{n_l}{a_l} - a_l - \frac{x - M}{\sigma} \right)^{-n_l} & \frac{x - M}{\sigma} < -a_l \\ \exp\left(-\frac{1}{2} \left( \frac{x - M}{\sigma} \right)^2\right) & \frac{x - M}{\sigma} \geq -a_l \end{cases}, \quad (3-3)$$

where  $M$  and  $\sigma$  are the mean value and the width for the central Gaussian function,  $a_l$  defines the starting point of the tail, and  $n_l$  determines the tail shape. The two CB functions have the common  $M$  value and different  $\sigma$  values, considering that the mass resolution is dependent on the kinematics of the  $J/\psi$  candidates. The ratio between the two CB functions are fixed from the studies of the simulated sample. The relation between  $\sigma_1$  and  $\sigma_2$ , which represent the widths of the narrower and wider CB functions respectively, is parameterised as a linear function, which is also determined from the simulation. The parameter  $a_l$  is parameterised as a function of the parameter  $\sigma$ , and  $n_l$  is fixed to one according to the probability of photon radiation. It leaves only two free parameters in the mass fit, *i.e.* the common mean value  $M$ , and the narrower width  $\sigma_1$ . The  $M(\mu^+ \mu^-)$  distribution of the combinatorial background candidates is described by an exponential function. The fit to the dimuon invariant mass distribution of the candidates in the entire kinematic range is shown in Fig. 3.1. To obtain the double differential cross-sections, the mass fit is performed to  $J/\psi$  candidates in each  $(p_T, y)$  bin independently.

### 3.4.2 Separation of prompt and detached $J/\psi$ candidates

At generation, the  $t_z$  distributions of prompt  $J/\psi$  and  $J/\psi$  from  $b$  follow a delta function and an exponential function, respectively. The measured  $t_z$  distributions are smeared by the detection resolution. It is taken into account by the convolution with a resolution function, which is the sum of two Gaussian functions with the same mean value. The resolution function is defined as

$$f_{\text{resolution}}(t_z; \mu, S_1, S_2, \beta) = \frac{\beta}{\sqrt{2\pi} S_1 \sigma} e^{-\frac{(t_z - \mu)^2}{2S_1^2 \sigma^2}} + \frac{1 - \beta}{\sqrt{2\pi} S_2 \sigma} e^{-\frac{(t_z - \mu)^2}{2S_2^2 \sigma^2}}, \quad (3-4)$$

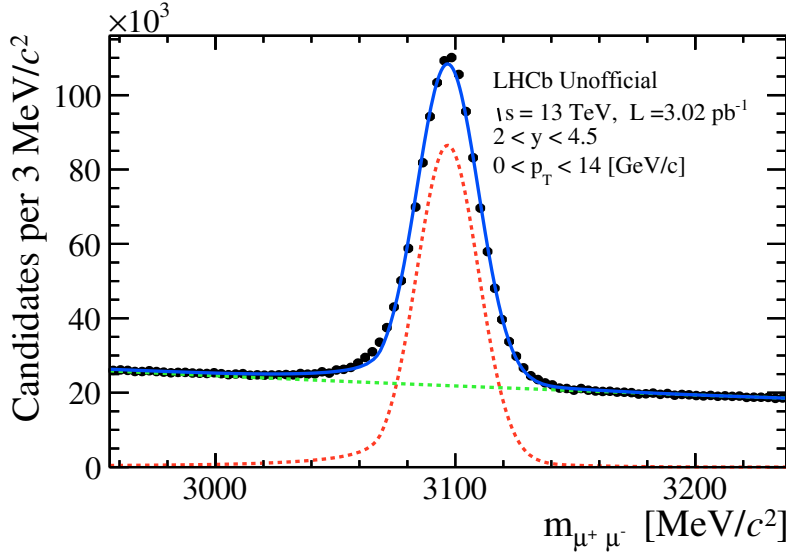


Figure 3.1 Fit to the dimuon invariant mass distribution for  $J/\psi$  candidates in the kinematic range of  $p_T < 14$  GeV/c and  $2.0 < y < 4.5$ .

where  $\mu$  is the common mean value which indicates the bias of the  $t_z$  measurement;  $\sigma$  is the event-by-event  $t_z$  uncertainty, which is propagated from the errors of  $z_{J/\psi}$ ,  $z_{PV}$  and  $p_z$  according to Eq. 3-2;  $S_1$  and  $S_2$  are the scale factors to correct the  $t_z$  uncertainty from imperfect estimation; and  $\beta$  is the fraction of either Gaussian function.

The  $t_z$  value relies on the position of the PV associated to the  $J/\psi$  candidate. It is possible that a wrong PV is associated to the  $J/\psi$  signal, which can be classified into two cases. The first case is that there are more than one PVs reconstructed, and the  $J/\psi$  candidate is attached to a wrong one which is close to the true PV. The positions of the wrong and the true PV are related. It results in a  $t_z$  component with a width much larger than the detection resolution, and can be described by adding a third Gaussian in the  $f_{\text{resolution}}$  function. However, the simulation shows that the fraction of this component is smaller than 1%, and the addition of the third Gaussian will not change the fit result significantly. Thus the third Gaussian function is not included in the nominal fit. The potential bias due to the exclusion of the third Gaussian is taken as a source of systematic uncertainty. The second case is that the true PV is not reconstructed, and the  $J/\psi$  candidate is attached to the nearest reconstructed PV. In this case, the wrong and the true PV have no correlation. It leads to a long tail in the  $t_z$  distribution. The tail can be modelled by the distribution of the next-event pseudo decay time, which is defined as

$$t_z^{\text{next}} = \frac{(z_{J/\psi} - z_{\text{PV}}^{\text{next}}) \times M(J/\psi)}{p_z}, \quad (3-5)$$

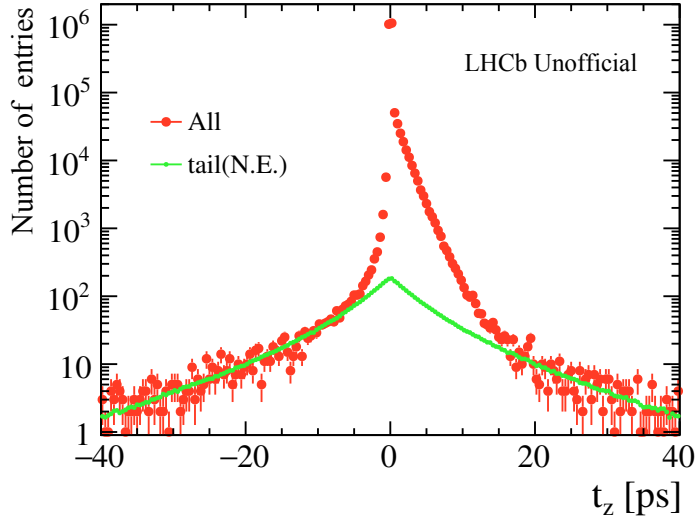


Figure 3.2 Comparison between the  $t_z$  distribution of the  $J/\psi$  signals and the  $t_z^{\text{next}}$  distribution. They are normalized to the same scale according to the left tail for the comparison.

where  $z_{\text{PV}}^{\text{next}}$  is the  $z$  coordinate of the PV closest to the  $J/\psi$  candidate in the next event. The comparison between the  $t_z$  and  $t_z^{\text{next}}$  distributions of the  $J/\psi$  signals is shown in Fig. 3.2. The tail dominates the  $t_z < -2$  ps region, and is in good consistency with the  $t_z^{\text{next}}$  distribution. There is no need to convolve the  $t_z^{\text{next}}$  distribution with the resolution function since it is much wider than the resolution function. The fraction of  $J/\psi$  from  $b$  in the tail is assumed to be the same as such fraction in the non-tail component, because prompt  $J/\psi$  and  $J/\psi$  from  $b$  have similar probabilities to reconstruct the true PV. Even if there is slight difference, it is negligible as the fraction of the tail component is small.

The  $t_z$  distribution of the combinatorial background is modelled by an empirical function, with parameters fixed according to the dimuon mass sidebands of  $60 < |M(\mu^+ \mu^-) - M(J/\psi)| < 150$  MeV/ $c^2$ . The muons in the background are either from the semi-leptonic  $b$ - and  $c$ -hadron decays or mis-identified kaons and pions. The former mainly contributes to positive  $t_z$  values, while the latter can have both positive and negative  $t_z$  values. They are described with the sum of a delta function and five exponential functions, among which three are for background candidates with positive  $t_z$  values, and two for negative. The function is convolved with a double-Gaussian function to account for the detection resolution. In total, the empirical function is defined as

$$f_{\text{background}} = \left[ (1 - f_1 - f_2 - f_3 - f_4) \delta(t_z) + \theta(t_z) \left( \frac{f_1}{\tau_1} e^{-t_z/\tau_1} + \frac{f_2}{\tau_2} e^{-t_z/\tau_2} \right) \right]$$

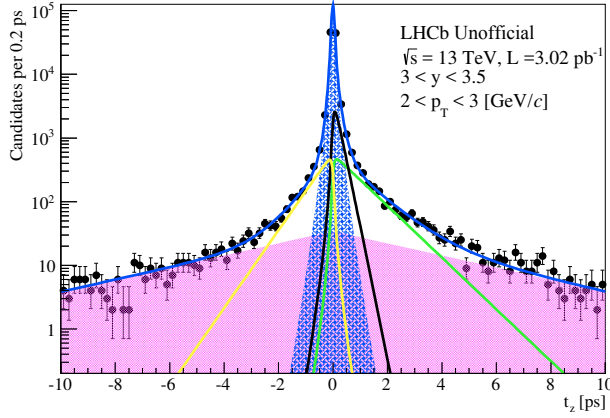


Figure 3.3 Fit to the background  $t_z$  distribution in the kinematic range of  $2 < p_T < 3$  GeV/c and  $3 < y < 3.5$ .

$$+ \theta(-t_z) \frac{f_3}{\tau_3} e^{t_z/\tau_3} + \frac{f_4}{2\tau_4} e^{-|t_z|/\tau_4} \right] * \left( \frac{\beta'}{\sqrt{2\pi} S'_1 \sigma} e^{-\frac{(t_z-\mu)^2}{2S'^2_1 \sigma^2}} + \frac{1-\beta'}{\sqrt{2\pi} S'_2 \sigma} e^{-\frac{(t_z-\mu)^2}{2S'^2_2 \sigma^2}} \right). \quad (3-6)$$

There are one negative and one positive exponential function sharing the same slope. The parameters of the two Gaussian functions are different from those for the signal, since the background candidates tend to have a worse resolution. The fit to the  $t_z$  distribution of the background is shown in Fig. 3.3 for candidates with  $2 < p_T < 3$  GeV/c and  $3 < y < 3.5$ , which demonstrates good fit quality.

In summary, the function to describe the  $t_z$  distribution is

$$F_{t_z}(t_z; N_p, N_t, N_b, N_{\text{BKG}}, \mu, S_1, S_2, \beta, \tau_b) = \left( N_p \delta(t_z) + \frac{N_b}{\tau_b} e^{-t_z/\tau_b} \right) * f_{\text{resolution}}(t_z; \mu, S_1, S_2, \beta) + N_t f_{\text{tail}}(t_z) + N_{\text{BKG}} f_{\text{background}}(t_z), \quad (3-7)$$

where  $N_{\text{BKG}}$ ,  $N_p$ ,  $N_b$  and  $N_t$  are the yields of the background, prompt  $J/\psi$ ,  $J/\psi$  from  $b$  and  $J/\psi$  candidates in the wrong-PV tail, respectively. The simultaneous fit to the dimuon mass and the  $t_z$  distribution is performed for  $J/\psi$  candidates in each  $(p_T, y)$  bin separately. The fit result for the kinematic bin of  $3 < p_T < 4$  GeV/c and  $2.5 < y < 3$  is shown in Fig. 3.4.

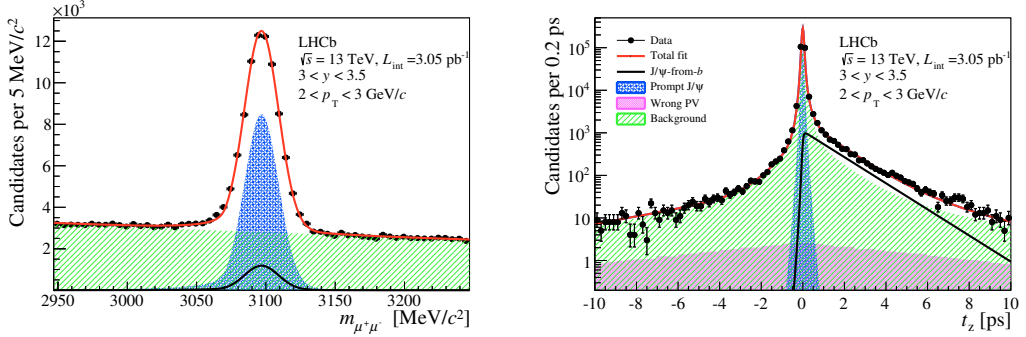


Figure 3.4 Simultaneous fit to (left) the dimuon mass distribution and (right) the  $t_z$  distribution for candidates in the kinematic range of  $2 < p_T < 3 \text{ GeV}/c$  and  $3 < y < 3.5$ .

### 3.5 Efficiency determination

The total efficiency  $\varepsilon_{\text{tot}}$  is composed of the geometrical acceptance efficiency  $\varepsilon_{\text{acc}}$ , the reconstruction and selection efficiency  $\varepsilon_{\text{rec\&sel}}$  (without the isMuon requirement), the muon identification (muonID) efficiency  $\varepsilon_{\text{muonID}}$  and the trigger efficiency  $\varepsilon_{\text{trig}}$ , as given by

$$\varepsilon_{\text{tot}} = \varepsilon_{\text{acc}} \times \varepsilon_{\text{rec\&sel}} \times \varepsilon_{\text{muonID}} \times \varepsilon_{\text{trig}}. \quad (3-8)$$

Each efficiency term is defined on the basis of the term it follows. The efficiencies are estimated in each  $(p_T, y)$  bin of the  $J/\psi$  mesons. The efficiencies for prompt  $J/\psi$  and  $J/\psi$  from  $b$  are independently determined using the corresponding simulated samples, unless the efficiency has no relation with the pseudo decay time thus should be the same for them.

#### 3.5.1 Geometrical acceptance

The geometrical acceptance efficiency  $\varepsilon_{\text{acc}}$  is defined as

$$\varepsilon_{\text{acc}} \equiv \frac{J/\psi \text{ with both muons in LHCb acceptance}}{\text{Generated } J/\psi}. \quad (3-9)$$

To be in the LHCb acceptance, the polar angle of the muon momentum with respect to the  $z$ -axis should be within  $(10, 400)$  mrad. The efficiency  $\varepsilon_{\text{acc}}$  is estimated using the simulated sample at the generation level, regardless of the interaction with the detector. The acceptance efficiencies in bins of  $J/\psi$   $p_T$  and  $y$  are shown in Fig. 3.5 for prompt  $J/\psi$  and  $J/\psi$  from  $b$ , respectively. The efficiencies of prompt  $J/\psi$  and  $J/\psi$  from  $b$  are consistent

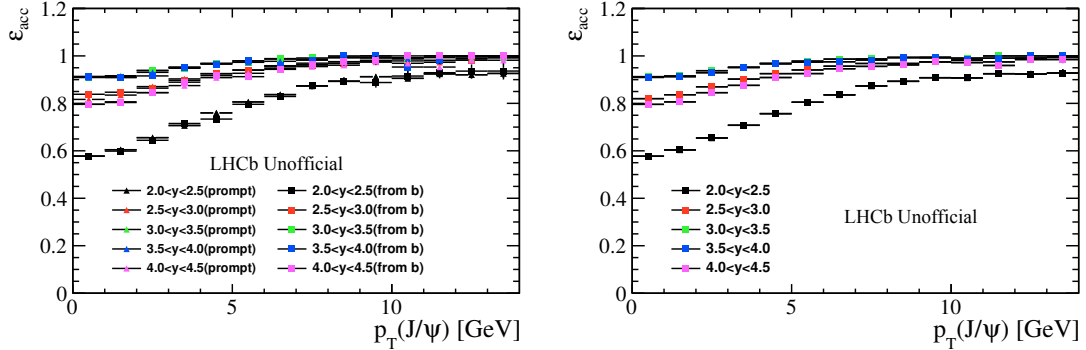


Figure 3.5 (Left) Geometrical acceptance efficiency  $\varepsilon_{\text{acc}}$  in bins of  $J/\psi$   $p_T$  and  $y$  for prompt  $J/\psi$  and  $J/\psi$  from  $b$ , respectively. (Right) Geometrical acceptance efficiency  $\varepsilon_{\text{acc}}$  averaged over prompt  $J/\psi$  and  $J/\psi$  from  $b$  in bins of  $J/\psi$   $p_T$  and  $y$ .

with each other. Therefore, the efficiency  $\varepsilon_{\text{acc}}$  is determined collectively for prompt  $J/\psi$  and  $J/\psi$  from  $b$  to benefit from a larger statistic, as shown on the right of Fig. 3.5.

### 3.5.2 Reconstruction and selection efficiency

The reconstruction and selection efficiency  $\varepsilon_{\text{rec\&sel}}$  is defined as

$$\varepsilon_{\text{rec\&sel}} \equiv \frac{J/\psi \text{ reconstructed and selected w/o isMuon}}{J/\psi \text{ with both muons in LHCb acceptance}}. \quad (3-10)$$

It takes into account the reconstruction of the two muon tracks and all the selection criteria applied to reduce background, excluding the isMuon requirement, whose efficiency will be estimated independently. The efficiency  $\varepsilon_{\text{rec\&sel}}$  is determined independently for prompt  $J/\psi$  and  $J/\psi$  from  $b$  using the simulated samples, as shown in Fig. 3.6. The reconstruction and selection efficiencies are slightly different between prompt  $J/\psi$  and  $J/\psi$  from  $b$ , because the  $|t_z| < 10$  ps cut can reject a small fraction of  $J/\psi$  from  $b$ , while keep all the prompt  $J/\psi$  candidates.

The track reconstruction efficiency is slightly different between the data and the simulation. The difference is considered by introducing a correction factor for each muon track. The correction factors are evaluated using the tag-and-probe method. For each  $J/\psi$  signal, one muon track is fully reconstructed and tightly selected as the tag track. The other muon track is the probe track reconstructed with information from the muon stations and the TT only, thus can probe the reconstruction efficiency of the VELO and the tracking stations. The single track reconstruction efficiency is calculated as the number of  $J/\psi$  signals with the probe track fully reconstructed divided by the total number of

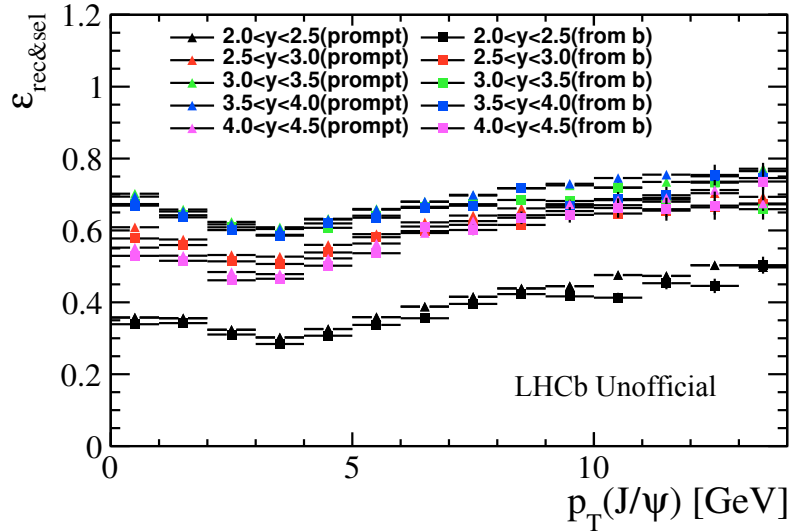


Figure 3.6 Reconstruction and selection efficiency  $\varepsilon_{\text{rec}\&\text{sel}}$  in bins of  $J/\psi$   $p_T$  and  $y$  for prompt  $J/\psi$  and  $J/\psi$  from  $b$ -hadron decays, respectively.

$J/\psi$  signals. In the data, the  $J/\psi$  signal yield is determined by performing a fit to the dimuon invariant mass distribution, while in the simulation, the signal number is directly counted as the truth information is known. The track reconstruction efficiency is estimated independently in the data and the simulation with the tag-and-probe method in kinematic bins of the muons. The ratios of the efficiencies in the data over those in the simulation are taken as the correction factors. The track reconstruction efficiency depends on the event multiplicity, whose distribution shows large discrepancy between the data and the simulation as displayed in Fig. 3.7. Therefore, before evaluating the correction factors, the multiplicity distribution in the simulation is weighted to that in the data. Here the number of hits in the SPD (nSPDHits) is taken as the event multiplicity variable. The correction factors in kinematic bins of the muons obtained after the multiplicity reweight are shown in Fig. 3.8. The event multiplicity distribution is similar for prompt  $J/\psi$  and  $J/\psi$  from  $b$ , thus the correction factors are assumed to be the same for them. The correction factors in kinematic bins of the  $J/\psi$  candidates are evaluated with the inclusive simulated  $J/\psi$  sample after the multiplicity reweight. For each  $J/\psi$  signal, the track reconstruction efficiency correction is calculated as the multiplication of the correction factors for its two muons. The corrections are at the level of a few percent depending on the  $(p_T, y)$  bins, as shown in Fig. 3.9.

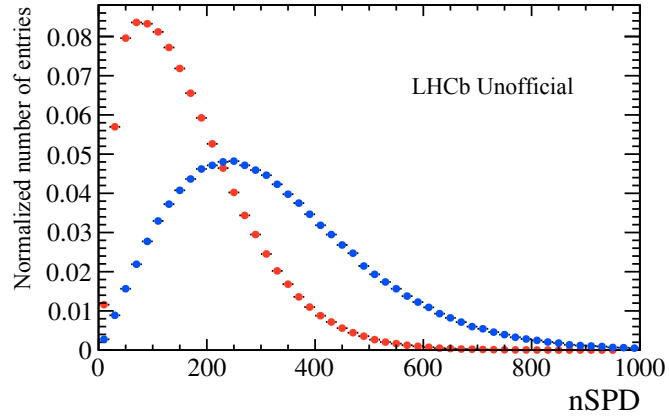


Figure 3.7 Comparison of the nSPDHits distribution between the (blue) data and (red) simulation.

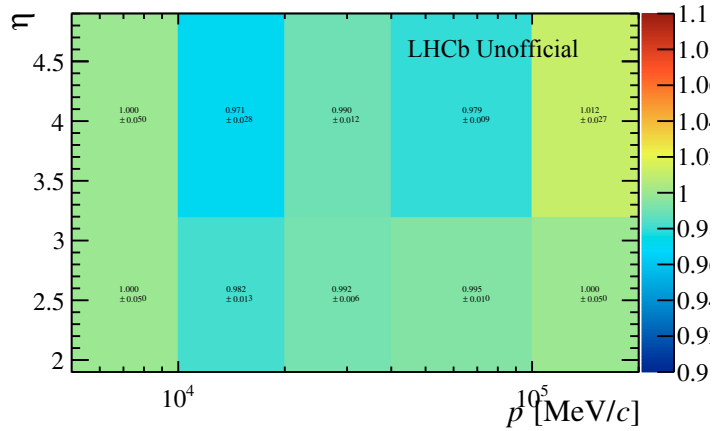


Figure 3.8 Correction factors for the track reconstruction efficiency in bins of  $p$  and  $\eta$  of the muons.

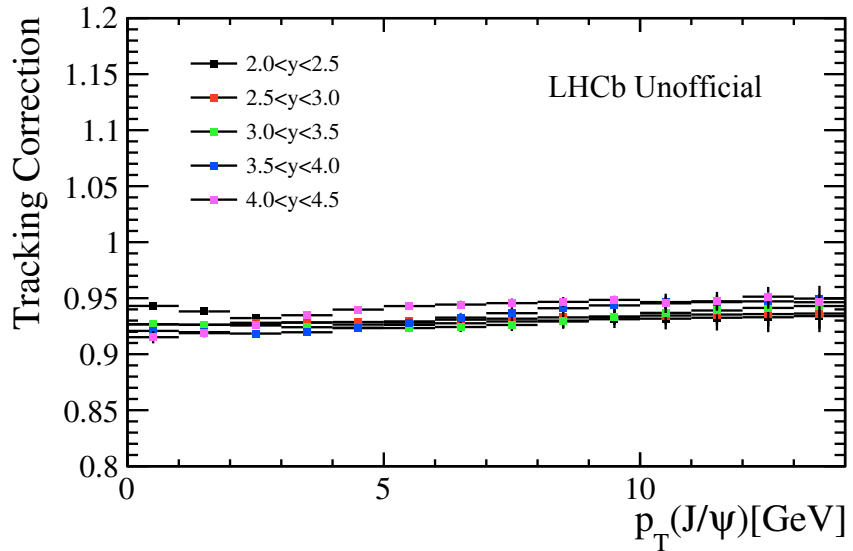


Figure 3.9 Track reconstruction efficiency correction factors in bins of  $J/\psi$   $p_T$  and  $y$ .

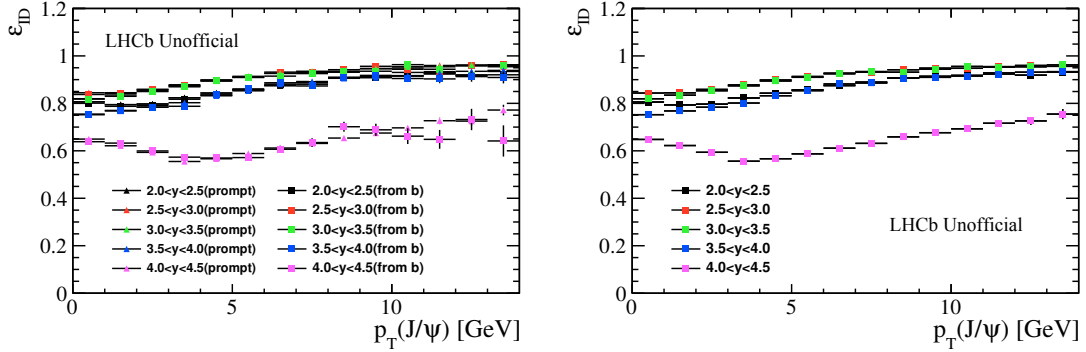


Figure 3.10 (Left) Muon identification efficiency  $\varepsilon_{\text{muonID}}$  in bins of  $J/\psi$   $p_T$  and  $y$  for prompt  $J/\psi$  and  $J/\psi$  from  $b$ , respectively. (Right) Muon identification efficiency  $\varepsilon_{\text{muonID}}$  averaged over prompt  $J/\psi$  and  $J/\psi$  from  $b$  in bins of  $J/\psi$   $p_T$  and  $y$ .

### 3.5.3 Muon identification efficiency

The muonID efficiency  $\varepsilon_{\text{muonID}}$  is defined as

$$\varepsilon_{\text{muonID}} \equiv \frac{J/\psi \text{ selected including isMuon}}{J/\psi \text{ reconstructed and selected w/o isMuon}}. \quad (3-11)$$

It is evaluated independently for prompt  $J/\psi$  and  $J/\psi$  from  $b$  using the simulated samples, as shown in Fig. 3.10. The muonID efficiency is consistent between prompt  $J/\psi$  and  $J/\psi$  from  $b$ , thus the efficiency is determined jointly for them to reduce the statistical uncertainty of the simulation, as shown on the right of Fig. 3.10.

To account for the imperfect simulation of muonID, the muonID efficiency derived from the simulation is calibrated using the data sample. Limited by the statistic, a global correction factor is applied to the whole kinematic range of  $p_T < 14$  GeV/ $c$  and  $2 < y < 4.5$ . The single muon identification efficiency in the data is evaluated using the tag-and-probe method, similar to the track reconstruction efficiency. The tag track is firmly identified as a muon, and there is no PID requirement on the other muon, the probe track. The single muon identification efficiency is calculated as the number of  $J/\psi$  signals with the probe track identified as a muon divided by the total number of  $J/\psi$  signals. The muonID efficiency depends slightly on the event multiplicity distribution, which is similar in the calibration sample and the analysis sample. Therefore no reweight of the multiplicity is applied. The potential bias introduced by this discrepancy is considered as a systematic uncertainty. The single muon identification efficiencies in the data are shown in Fig. 3.11 in bins of muon  $p$  and  $\eta$ . The calibrated muonID efficiency in the

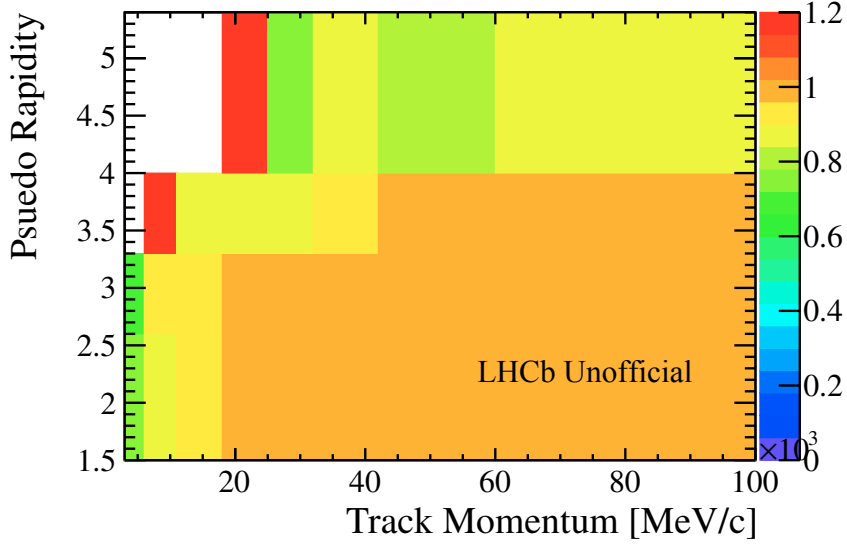


Figure 3.11 Single muon identification efficiency in the data in bins of  $p$  and  $\eta$  of the muons.

entire kinematic range is determined according to

$$\bar{\varepsilon} = \frac{\sum \varepsilon_{\mu^\pm}(p_{\mu^\pm}, \eta_{\mu^\pm}) \varepsilon_{\mu^\pm}(p_{\mu^\pm}, \eta_{\mu^\pm})}{N_{\text{rec\&sel}}}, \quad (3-12)$$

where  $N_{\text{rec\&sel}}$  is the number of  $J/\psi$  signals reconstructed and selected without the muonID requirement, and  $\varepsilon_{\mu^\pm}(p_{\mu^\pm}, \eta_{\mu^\pm})$  indicates the single muon identification efficiency taken from the efficiency table in Fig. 3.11. The ratio between the calibrated muonID efficiency and the efficiency determined from the simulation is 1.02. It is applied to each  $(p_T, y)$  bin of the  $J/\psi$  mesons.

### 3.5.4 Trigger efficiency

The trigger efficiency  $\varepsilon_{\text{trig}}$  is defined as

$$\varepsilon_{\text{trig}} \equiv \frac{J/\psi \text{ selected and triggered}}{J/\psi \text{ selected including isMuon}}. \quad (3-13)$$

It includes the trigger requirements in the L0, HLT1 and HLT2 trigger levels. As it is determined on the basis of the reconstruction and selection, the HLT2 trigger is 100% efficient since the offline selections are tighter than those in HLT2. The trigger efficiencies are determined from the simulation in bins of  $J/\psi$   $p_T$  and  $y$ , as shown in Fig. 3.12 for prompt  $J/\psi$  and  $J/\psi$  from  $b$ , respectively. The trigger efficiency also shows good consistency between prompt  $J/\psi$  and  $J/\psi$  from  $b$ , thus is determined together for them to increase the

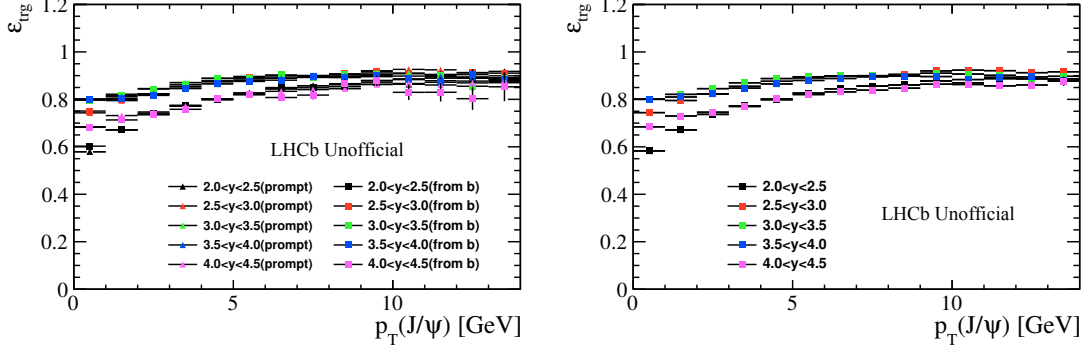


Figure 3.12 (Left) Trigger efficiency  $\varepsilon_{\text{trig}}$  in bins of  $J/\psi$   $p_T$  and  $y$  for prompt  $J/\psi$  and  $J/\psi$  from  $b$ , respectively. (Right) Trigger efficiency  $\varepsilon_{\text{trig}}$  averaged over prompt  $J/\psi$  and  $J/\psi$  from  $b$  in bins of  $J/\psi$   $p_T$  and  $y$ .

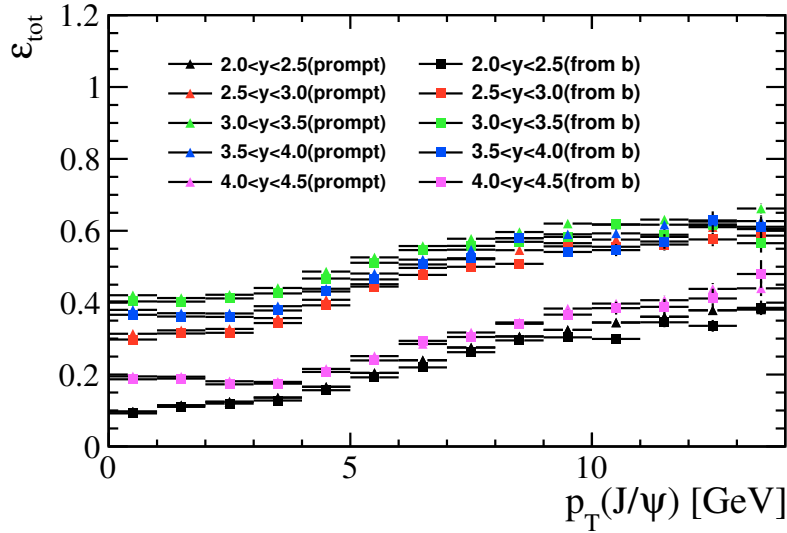


Figure 3.13 Total efficiency  $\varepsilon_{\text{tot}}$  in bins of  $J/\psi$   $p_T$  and  $y$  for prompt  $J/\psi$  and  $J/\psi$  from  $b$ , respectively.

statistic, as shown on the right of Fig. 3.12.

### 3.5.5 Total efficiency

The total efficiency  $\varepsilon_{\text{tot}}$  in kinematic bins of the  $J/\psi$  mesons is shown in Fig. 3.13 for prompt  $J/\psi$  and  $J/\psi$  from  $b$ , respectively. The correction of the track reconstruction efficiency and the calibration of the muonID efficiency are included.

## 3.6 Systematic uncertainties

The systematic uncertainties are studied comprehensively, as described in the following sections.

### 3.6.1 Signal mass shape

The sum of two CB functions, which is used in the nominal mass fit, is fitted to the dimuon mass spectrum of a simulated sample, whose signal yield is known. The signal yield obtained from the fit deviates from the true yield for about 1%, which indicates that the modelling of the signal mass shape can contribute to the systematic uncertainty. To estimate the uncertainty, the Hypatia function<sup>[103]</sup>, which is supposed to take into account the mass resolution event-by-event, is used to describe the signal mass distribution instead. The change in the signal yield compared to the nominal CB function is taken as the systematic uncertainty. The uncertainty is found to be almost consistent between different kinematic bins, thus it is studied in one  $(p_T, y)$  bin with large signal yield to increase the statistic. The uncertainty is estimated to be 1% and assigned to all bins. It is correlated between the  $J/\psi$  kinematic bins.

### 3.6.2 Fit to $t_z$

The imperfect modelling of the  $t_z$  distribution could bias the fraction of  $J/\psi$  from  $b$ , named  $F_b$  afterwards. The bias can arise from three aspects as discussed in the following:

- Imperfect description of the  $t_z$  resolution of the  $J/\psi$  signal. The  $t_z$  distribution of the prompt  $J/\psi$  mesons is dominated by the resolution. It is sensitive to the imperfect modelling of the resolution, and can significantly affect the  $F_b$  value. The possible bias introduced by the resolution is studied by adding a third wide Gaussian function to the resolution function. The deviation of  $F_b$  from the nominal result is negligible.
- Modelling of the  $t_z$  distribution of the background. Instead of using the mass sidebands, which have limited statistics, the background is extracted from the mass distribution using the sPlot technique, which is a statistical method to unfold the contributions from different sources taking a specific variable as the discriminant<sup>[104]</sup>. The parameters to describe the background  $t_z$  distribution are fixed according to the extracted background. The change of the  $F_b$  value from the nominal result is 0.05%, and is taken as the systematic uncertainty.
- Description of the wrong-PV  $t_z$  tail. An alternative function, an empirical bifurcated

exponential function with symmetrical positive and negative slopes, is used instead of the next-event model. The slope is left free in the fit. The difference of  $F_b$  between this and the nominal fit result, 0.073%, is taken as the systematic uncertainty.

Combining the three sources, the systematic uncertainty on  $F_b$  from the  $t_z$  fit is determined to be 0.1%.

### 3.6.3 MuonID efficiency

There are three sources of uncertainty for the estimation of the muonID efficiency:

- The uncertainty propagated from the statistical uncertainty of the calibration sample. It is studied using pseudoexperiments, in which the single muon identification efficiency in each  $(p, \eta)$  bin of the muons is varied within its statistical uncertainty. The efficiencies determined from the pseudoexperiments follow a Gaussian distribution, whose mean value is consistent with the nominal muonID efficiency. The ratio of the Gaussian width relative to the nominal muonID efficiency is taken as the corresponding systematic uncertainty, which is 1.7%.
- The uncertainty due to the binning scheme of the single muon identification efficiency table. The numbers of the  $p$  and  $\eta$  bins are varied respectively, which results in a deviation of 0.7% to the nominal efficiency. It is taken as the systematic uncertainty.
- The discrepancy of the event multiplicity distribution between the data and the calibration sample. The nSPDHits distribution in the calibration sample is weighted to match that in the data sample. The single muon identification efficiency table is determined after the reweight. The total muonID efficiency changes by 0.2%, which is negligible.

In total, the uncertainty of the muonID efficiency is 1.8%, which is correlated between the  $J/\psi$  kinematic bins.

### 3.6.4 Track reconstruction efficiency

The single track reconstruction efficiency correction table has statistical uncertainties due to the finite statistics of the data and simulated samples used for the calibration. These uncertainties are propagated to the track reconstruction efficiency using pseudoexperiments, in which the correction factors are varied within their uncertainties. It leads to a variation of around 1% for the track reconstruction efficiency, depending on the  $J/\psi$

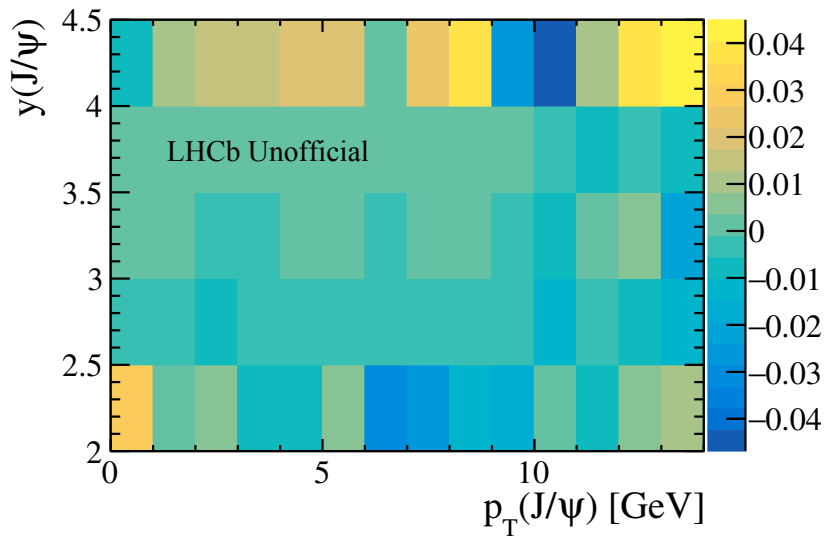


Figure 3.14 Systematic uncertainty due to the  $p_T$  and  $y$  spectrum for each  $J/\psi$  kinematic bin.

kinematic bins. The choice of the event multiplicity variable used in the reweight is another source of uncertainty. It is studied with alternative variables like the number of tracks. The uncertainty is determined to be 0.4% per muon track. The uncertainty of the track reconstruction efficiency is also correlated between the  $(p_T, y)$  bins of  $J/\psi$ .

### 3.6.5 Spectrum of $p_T$ and $y$

The efficiency is evaluated for each  $(p_T, y)$  bin of the  $J/\psi$  mesons. The difference in the  $p_T$  and  $y$  spectrum between the data and the simulation within the  $(p_T, y)$  bins can introduce a systematic uncertainty. The uncertainty is studied by weighting the  $p_T$  and  $y$  spectrum in the simulation to that in the data. The background in the data sample is subtracted according to the mass distribution using the sPlot technique<sup>[104]</sup>. The efficiencies are evaluated with the weighted simulated sample. The changes of the efficiencies are quoted as the systematic uncertainties, as shown in Fig. 3.14 for each kinematic bin. The uncertainty is taken to be the same for prompt  $J/\psi$  and  $J/\psi$  from  $b$ . It is uncorrelated across the  $J/\psi$  kinematic bins.

### 3.6.6 Offline selection efficiency

Among all the offline selections, the possible uncertainty arising from the kinematic cuts is taken into account in the  $p_T$  and  $y$  spectrum as studied in Sec. 3.6.5. The requirements on the muon track quality and the track ghost probability are loose, and the corresponding effect is included in the track reconstruction efficiency uncertainty, as

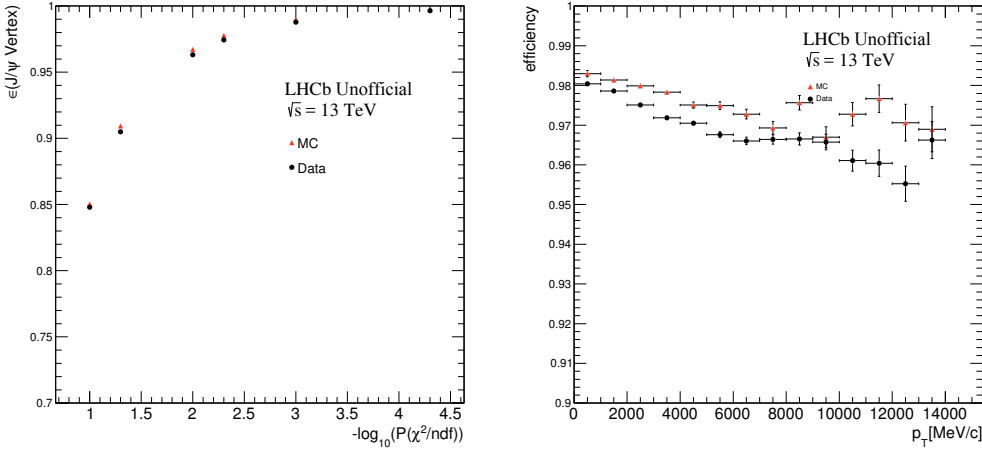


Figure 3.15 (Left) Comparison of the efficiencies with different cuts on the  $\chi^2_{\text{vertex}}/\text{ndf}$  probability between the data and the simulation. (Right) Comparison of the efficiencies of the nominal  $\chi^2_{\text{vertex}}/\text{ndf}$  probability cut in bins of  $J/\psi p_T$  between the data and the simulation.

described in Sec. 3.6.4. The muonID efficiency uncertainty is studied in Sec. 3.6.3. The requirement to find at least one PV is almost 100% efficient, thus any related uncertainty is negligible.

The  $\chi^2_{\text{vertex}}/\text{ndf}$  probability of the dimuon vertex is required to be larger than 0.5%. The difference in the vertex fit quality between the data and the simulation can be a source of uncertainty. The efficiencies with different cuts on the  $\chi^2_{\text{vertex}}/\text{ndf}$  probability are compared between the data and the simulation, as shown on the left of Fig. 3.15. The difference reaches 0.36% at the largest, which is taken as the systematic uncertainty. The efficiencies of the nominal cut in bins of the  $J/\psi p_T$  are also compared between the data and the simulation, as shown on the right of Fig. 3.15. The efficiency difference shows no large dependence on the  $J/\psi$  kinematics. This uncertainty is correlated between the  $J/\psi$  kinematic bins.

### 3.6.7 Trigger efficiency

The imperfect simulation of the trigger can introduce systematic uncertainty. The uncertainty is evaluated by comparing the trigger efficiency between the data and the simulation. The HLT2 trigger is 100% efficient thus will not result in any bias. For the L0 trigger, the single muon trigger efficiency is determined in both the data and the simulation using the tag-and-probe technique. The tag track is required to pass the L0 trigger requirement, while there is no trigger requirement on the probe muon. The HLT and offline selections are all applied to the  $J/\psi$  candidates. The single muon L0 trigger

efficiency is calculated as the number of  $J/\psi$  signals with the probe track firing the L0 trigger divided by the total number of  $J/\psi$  signals. It is evaluated independently for  $\mu^+$  and  $\mu^-$  in bins of the muon  $p$  and  $\eta$ , as shown in Fig. 3.16 for the data and the simulation, respectively. The trigger efficiency of the  $J/\psi$  meson is determined as

$$\frac{\sum(1 - \{(1 - \varepsilon(p_{\mu^+}, \eta_{\mu^+}))(1 - \varepsilon(p_{\mu^-}, \eta_{\mu^-}))\})}{N_{\text{tot}}}, \quad (3-14)$$

where  $N_{\text{tot}}$  is the total number of the tagged and selected  $J/\psi$  candidates, and  $\varepsilon_{\mu^\pm}(p_{\mu^\pm}, \eta_{\mu^\pm})$  indicates the single muon trigger efficiency taken from the efficiency table in Fig. 3.16. The relative difference of the efficiency between the data and the simulation is taken to be the systematic uncertainty for each  $J/\psi$  ( $p_{\text{T}}, y$ ) bin, as shown in Fig. 3.17. The uncertainty typically gets larger in the low  $p_{\text{T}}$  and high  $y$  region. The uncertainty is correlated between different  $J/\psi$  kinematic bins.

The HLT1 trigger efficiency is evaluated using the TISTOS method in both the simulation and the data. In the data sample, events not firing any trigger line are not collected, which makes it impossible to determine the trigger efficiency directly. Assuming that the TIS and TOS are uncorrelated, which is valid in most cases, the TOS efficiency can be evaluated on the basis of the TIS requirement. In the TISTOS method, the trigger efficiency is calculated as

$$\varepsilon_{\text{trig}} = \frac{N^{\text{TIS\&TOS}}}{N^{\text{TIS\&\overline{TOS}}} + N^{\text{TIS\&TOS}}}, \quad (3-15)$$

where  $N^{\text{TIS\&TOS}}$  is the number of events triggered simultaneously on TIS and TOS, and  $N^{\text{TIS\&\overline{TOS}}}$  is the number of events triggered on TIS only. The HLT1 trigger efficiencies determined with the TISTOS method for both the simulation and the data are shown in Fig. 3.18 in bins of  $J/\psi$   $p_{\text{T}}$  and  $y$ . Since the uncertainties of the efficiencies are large due to the limited size of the TIS sample, the efficiencies across the  $J/\psi$  kinematic bins are combined. The difference between the efficiencies of the data and the simulation, 1.5%, is taken as the systematic uncertainty. It is correlated between the  $J/\psi$   $p_{\text{T}}$  and  $y$  bins.

### 3.6.8 Polarisation scenarios

The detection efficiency of the  $J/\psi$  mesons can be affected by its polarisation. Considering that all the LHC analyses indicate a small polarisation for the prompt quarkonia<sup>[41–44]</sup>, the simulated sample is generated assuming that the prompt  $J/\psi$  mesons have

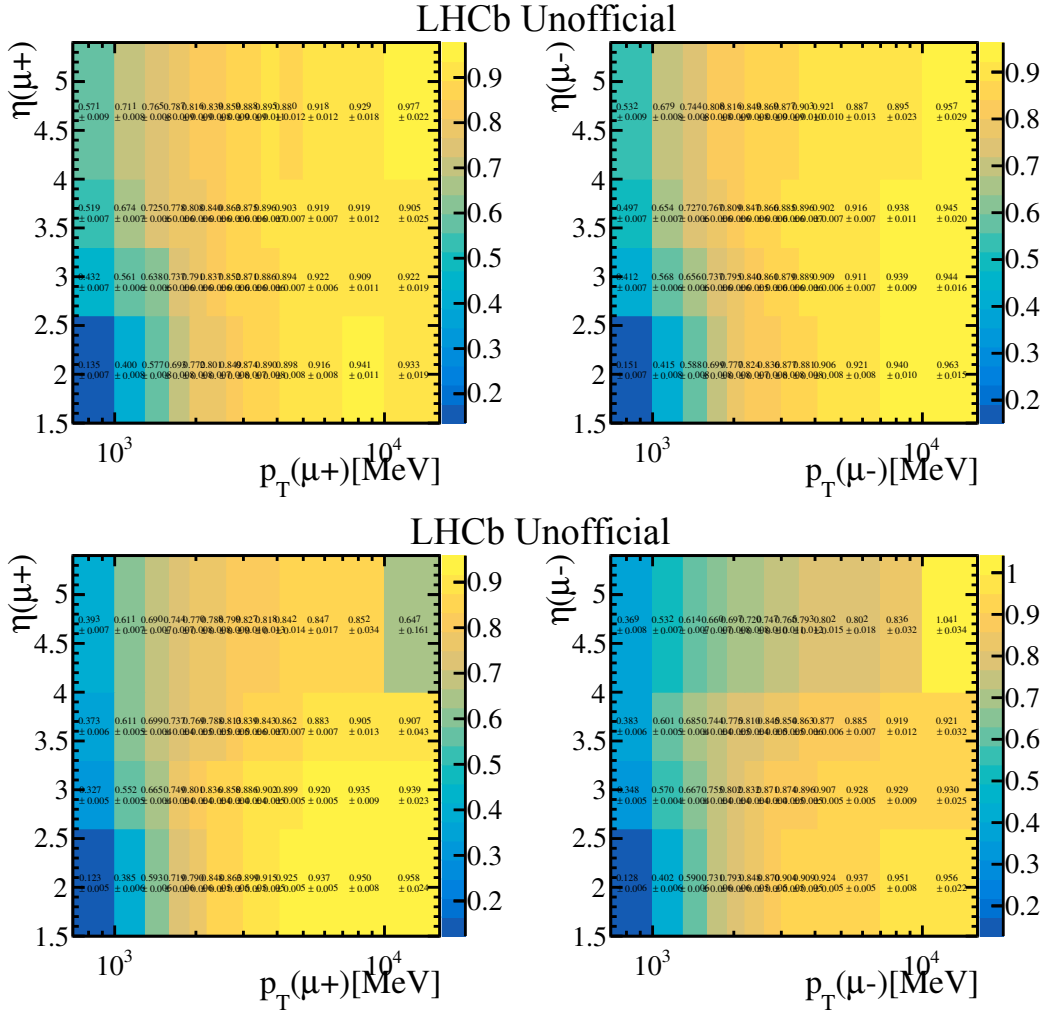


Figure 3.16 Single muon L0 trigger efficiency of (left)  $\mu^+$  and (right)  $(\mu^-)$  determined using the tag-and-probe technique for the (top) simulation and (bottom) data, respectively.

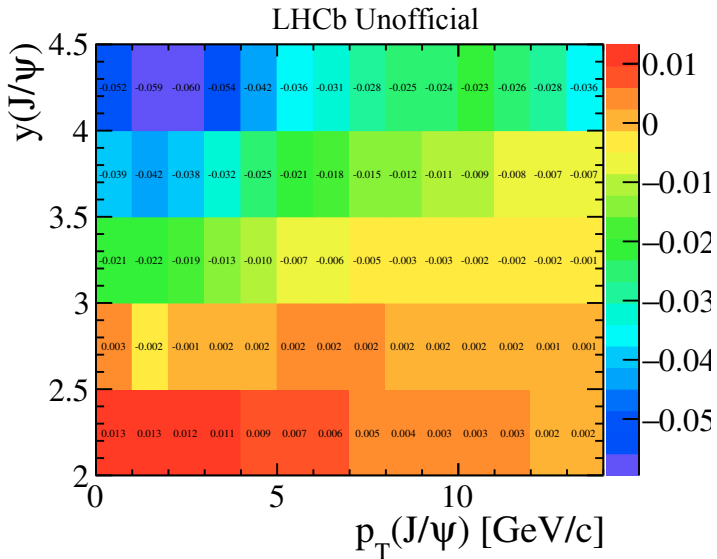


Figure 3.17 Systematic uncertainties of the L0 trigger efficiency in bins of  $J/\psi$   $p_T$  and  $y$ .

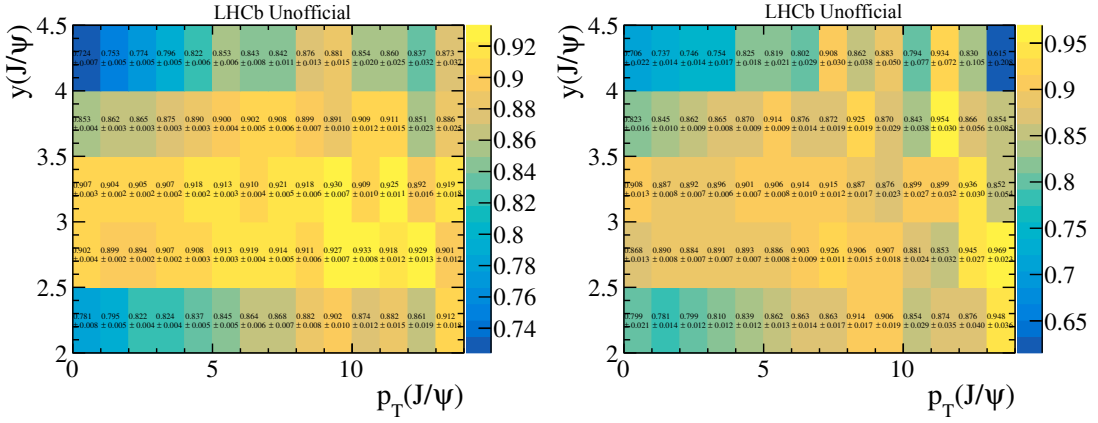


Figure 3.18 HLT1 trigger efficiency determined with the TISTOS method for the (left) simulation and (right) data.

zero polarisation. The variation of efficiency with respect to the  $J/\psi$  polarisation is studied. It shows that typically the efficiency changes linearly with the polarisation. The increase of the efficiency with a  $-20\%$  polarisation for the  $J/\psi$  mesons relative to the efficiency with zero polarisation is shown in Table 3.3. Since there is no experimental result for the  $J/\psi$  polarisation at  $\sqrt{s} = 13$  TeV yet, the production cross-sections are measured only under the assumption of zero prompt  $J/\psi$  polarisation. When the  $J/\psi$  polarisation is determined, the production cross-sections of prompt  $J/\psi$  can be updated accordingly. The effect of non-zero polarisation is not considered as a systematic uncertainty.

### 3.6.9 Other systematic uncertainties

There are several other sources of systematic uncertainties as following:

- The uncertainty propagated from  $\mathcal{B}(J/\psi \rightarrow \mu^+ \mu^-) = (5.961 \pm 0.033)\%$ <sup>[97]</sup>, which is common and correlated between the  $J/\psi$  kinematic bins. It doesn't affect the fraction of  $J/\psi$  from  $b$ .
- The statistical uncertainty of the simulated sample. It varies from  $0.3\%$  to  $5\%$  depending on the kinematic bins.
- The systematic uncertainty of the luminosity. It is determined to be  $3.9\%$ , and is equal and correlated for all  $(p_T, y)$  bins.
- A fraction of signal candidates in the radiative tail of the dimuon mass distribution are removed by the mass cut. The cut efficiency is included in the reconstruction and selection efficiency determined using the simulated sample. The imperfect simulation of the radiative effect can bias the efficiency. It is studied by changing the settings of PHOTOS, which is used to simulate the final state radiation. The result

Table 3.3 Increase of the total efficiency (in %) with a  $-20\%$  polarisation relative to the efficiency with zero polarisation in bins of  $J/\psi$   $p_T$  and  $y$ .

$p_T$ (GeV/c)	$2 < y < 2.5$	$2.5 < y < 3$	$3 < y < 3.5$	$3.5 < y < 4$	$4 < y < 4.5$
0 – 1	$6.24 \pm 0.35$	$4.89 \pm 0.10$	$3.45 \pm 0.11$	$3.31 \pm 0.09$	$4.66 \pm 0.17$
1 – 2	$5.58 \pm 0.18$	$4.30 \pm 0.07$	$2.94 \pm 0.06$	$2.55 \pm 0.03$	$2.82 \pm 0.12$
2 – 3	$4.88 \pm 0.14$	$3.47 \pm 0.06$	$1.97 \pm 0.04$	$1.52 \pm 0.06$	$1.65 \pm 0.13$
3 – 4	$4.77 \pm 0.14$	$3.39 \pm 0.06$	$1.94 \pm 0.04$	$1.17 \pm 0.07$	$1.13 \pm 0.15$
4 – 5	$4.68 \pm 0.14$	$3.34 \pm 0.08$	$1.97 \pm 0.04$	$1.20 \pm 0.07$	$0.73 \pm 0.14$
5 – 6	$4.43 \pm 0.12$	$3.28 \pm 0.10$	$2.03 \pm 0.06$	$1.42 \pm 0.06$	$0.75 \pm 0.14$
6 – 7	$4.21 \pm 0.09$	$3.03 \pm 0.12$	$2.05 \pm 0.08$	$1.57 \pm 0.04$	$0.77 \pm 0.14$
7 – 8	$3.88 \pm 0.04$	$2.81 \pm 0.15$	$1.98 \pm 0.10$	$1.69 \pm 0.05$	$0.74 \pm 0.14$
8 – 9	$3.59 \pm 0.15$	$2.65 \pm 0.20$	$1.81 \pm 0.11$	$1.65 \pm 0.11$	$1.01 \pm 0.13$
9 – 10	$3.53 \pm 0.18$	$2.44 \pm 0.24$	$1.81 \pm 0.15$	$1.68 \pm 0.16$	$1.17 \pm 0.14$
10 – 11	$3.39 \pm 0.27$	$2.30 \pm 0.26$	$1.88 \pm 0.22$	$1.73 \pm 0.26$	$1.26 \pm 0.14$
11 – 12	$3.09 \pm 0.32$	$2.18 \pm 0.38$	$1.47 \pm 0.18$	$1.65 \pm 0.27$	$1.35 \pm 0.43$
12 – 13	$3.25 \pm 0.45$	$1.65 \pm 0.32$	$1.93 \pm 0.36$	$1.49 \pm 0.26$	$1.48 \pm 0.21$
13 – 14	$2.72 \pm 0.58$	$1.68 \pm 0.32$	$1.71 \pm 0.38$	$1.17 \pm 0.27$	$1.36 \pm 0.51$

deviates for  $1\%$ , and it is taken as the corresponding uncertainty.

### 3.6.10 Summary of systematic uncertainties

The systematic uncertainties on the production cross-sections and the fraction of  $J/\psi$  from  $b$  are summarised in Table 3.4.

## 3.7 Results

### 3.7.1 $J/\psi$ production cross-sections

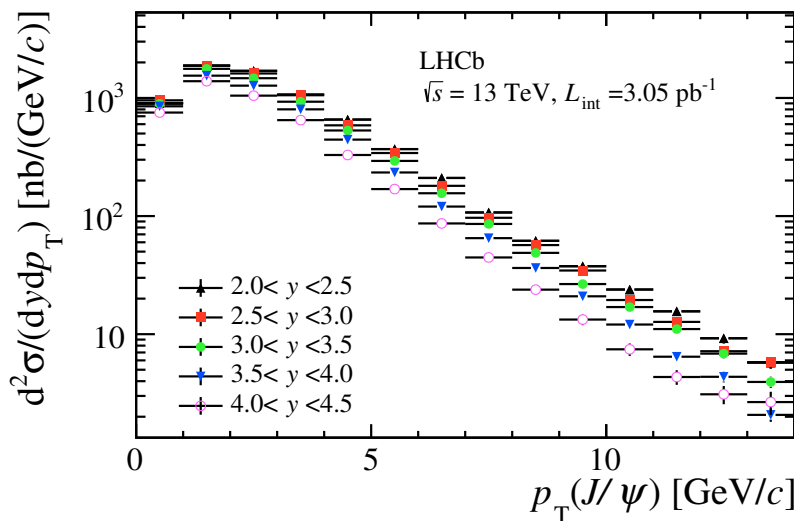
The measured double differential cross-sections as functions of  $J/\psi$   $p_T$  and  $y$  are shown in Figs. 3.19 and 3.20 for prompt  $J/\psi$  and  $J/\psi$  from  $b$ , respectively.

The total cross-sections for prompt  $J/\psi$  and  $J/\psi$  from  $b$  in the kinematic range of  $p_T < 14$  GeV/c and  $2 < y < 4.5$  are

$$\sigma(\text{prompt } J/\psi, p_T < 14 \text{ GeV/c}, 2 < y < 4.5) = 15.03 \pm 0.03 \text{ (stat)} \pm 0.91 \text{ (syst)} \mu\text{b} \quad (3-16)$$

Table 3.4 Summary of the systematic uncertainties.

Quantity	Systematic uncertainty	Comment
Luminosity	3.9%	Correlated between bins
LO Trigger	0.1-5.9%	Correlated between bins
HLT1 Trigger	1.5%	Correlated between bins
MuonID efficiency	1.8%	Correlated between bins
Track reconstruction efficiency	1.1-3.4%	Correlated between bins
Radiative tail	1%	Correlated between bins
Offline selections	0.36%	Correlated between bins
Signal mass shape	1%	Correlated between bins
$\mathcal{B}(J/\psi \rightarrow \mu^+ \mu^-)$	0.6%	Correlated between bins
$p_T$ -y spectrum	0.1 -5.0%	Bin dependent
Simulation statistic	0.3 -5.0%	Bin dependent
$t_z$ fit	0.1%	Affects $J/\psi$ from b

Figure 3.19 Double differential cross-sections for prompt  $J/\psi$  in bins of  $J/\psi$   $p_T$  and  $y$ . The error bars show the quadratic sum of the statistical and systematic uncertainties.

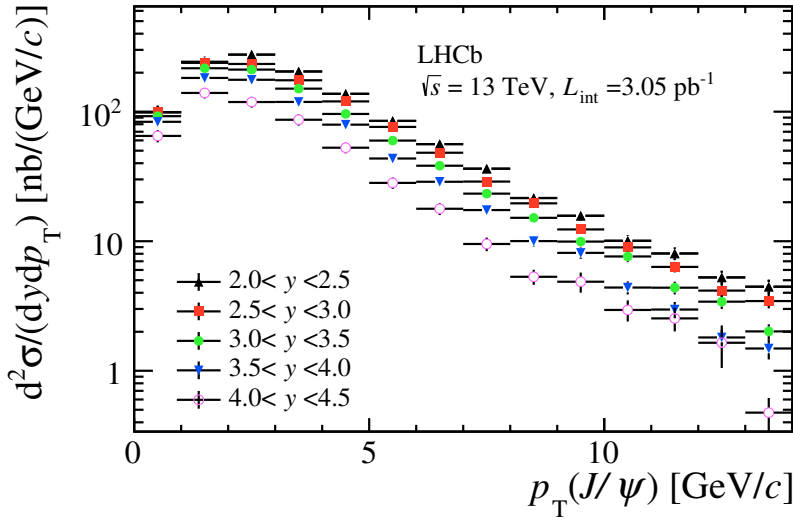


Figure 3.20 Double differential cross-sections for  $J/\psi$  from  $b$  in bins of  $J/\psi$   $p_T$  and  $y$ . The error bars show the quadratic sum of the statistical and systematic uncertainties.

and

$$\sigma(J/\psi \text{ from } b, p_T < 14 \text{ GeV}/c, 2 < y < 4.5) = 2.25 \pm 0.01 \text{ (stat)} \pm 0.13 \text{ (syst)} \mu\text{b} \quad (3-17)$$

respectively, where the first uncertainty is statistical, and the second systematic.

### 3.7.2 Fraction of $J/\psi$ from $b$

The fraction of  $J/\psi$  from  $b$  is calculated independently for each  $J/\psi$  kinematic bin as

$$F_b = \frac{N_b/\varepsilon_b}{N_b/\varepsilon_b + N_p/\varepsilon_p}, \quad (3-18)$$

where  $N_p$  and  $N_b$  are the yields of prompt  $J/\psi$  and  $J/\psi$  from  $b$  obtained from the simultaneous fit, and  $\varepsilon_p$  and  $\varepsilon_b$  are the total efficiencies for prompt  $J/\psi$  and  $J/\psi$  from  $b$ . The measured fractions of  $J/\psi$  from  $b$  in bins of  $J/\psi$   $p_T$  and  $y$  are shown in Fig. 3.21. Generally, the fraction of  $J/\psi$  from  $b$  gets larger with increasing  $p_T$  and decreasing  $y$  of the  $J/\psi$  mesons.

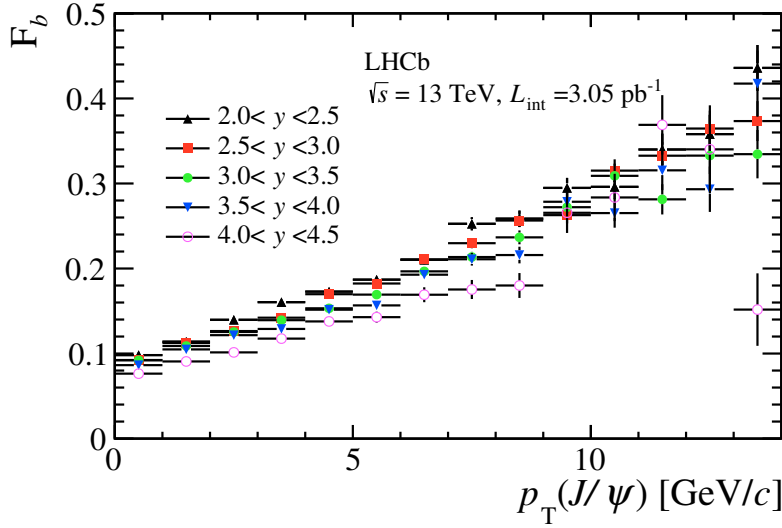


Figure 3.21 Fractions of  $J/\psi$  from  $b$  in bins of  $J/\psi$   $p_T$  and  $y$ . The error bars show the quadratic sum of the statistical and systematic uncertainties.

### 3.7.3 $b\bar{b}$ production cross-section

With the production cross-section of  $J/\psi$  from  $b$ , the production cross-section of  $b\bar{b}$  can be calculated as

$$\begin{aligned}\sigma(pp \rightarrow b\bar{b}X) &= \alpha_{4\pi} \frac{\sigma(J/\psi \text{ from } b, p_T < 14 \text{ GeV}/c, 2.0 < y < 4.5)}{2\mathcal{B}(b \rightarrow J/\psi X)} \\ &= 495 \pm 2 \text{ (stat)} \pm 52 \text{ (syst)} \mu\text{b},\end{aligned}$$

where  $\alpha_{4\pi} = 5.2$  is the factor to extrapolate the cross-section from the measured kinematic range to the full  $4\pi$  region, and  $\mathcal{B}(b \rightarrow J/\psi X) = (1.16 \pm 0.10)\%$  is the branching fraction of the inclusive  $b \rightarrow J/\psi X$  decay. The extrapolation factor  $\alpha_{4\pi}$  is determined from the generator PYTHIA 6<sup>[90]</sup> with the LHCb configuration. No uncertainty is assigned for  $\alpha_{4\pi}$ .

### 3.7.4 Comparison with low energy cross-sections

The  $J/\psi$  production cross-section has been measured at the centre-of-mass energies of 2.76 TeV<sup>[26]</sup>, 7 TeV<sup>[29]</sup> and 8 TeV<sup>[28]</sup> at LHCb. To compare with this measurement, the branching fraction  $\mathcal{B}(J/\psi \rightarrow \mu^+ \mu^-) = (5.94 \pm 0.06)\%$ <sup>[105]</sup> used in the previous measurements is updated to the latest value  $\mathcal{B}(J/\psi \rightarrow \mu^+ \mu^-) = (5.961 \pm 0.033)\%$ <sup>[97]</sup>. The  $J/\psi$  production cross-sections in the LHCb acceptance as functions of the centre-of-mass energy are shown in Fig. 3.22 for prompt  $J/\psi$  and  $J/\psi$  from  $b$ , respectively. The differential cross-sections as functions of  $p_T$  integrated over  $y$  at  $\sqrt{s} = 13$  TeV are compared to those

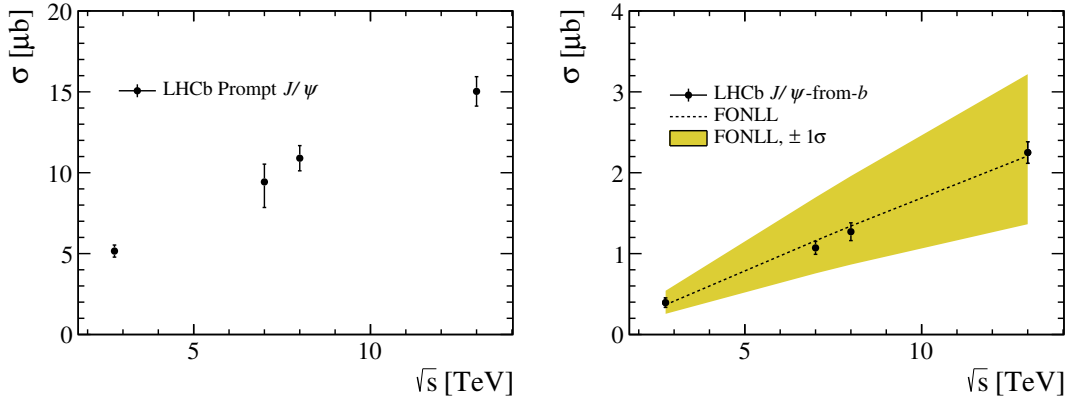


Figure 3.22 The  $J/\psi$  production cross-sections in the LHCb acceptance as functions of the centre-of-mass energy for (left) prompt  $J/\psi$  and (right)  $J/\psi$  from  $b$ , respectively. The cross-sections of  $J/\psi$  from  $b$  are compared to the FONLL prediction<sup>[106]</sup>.

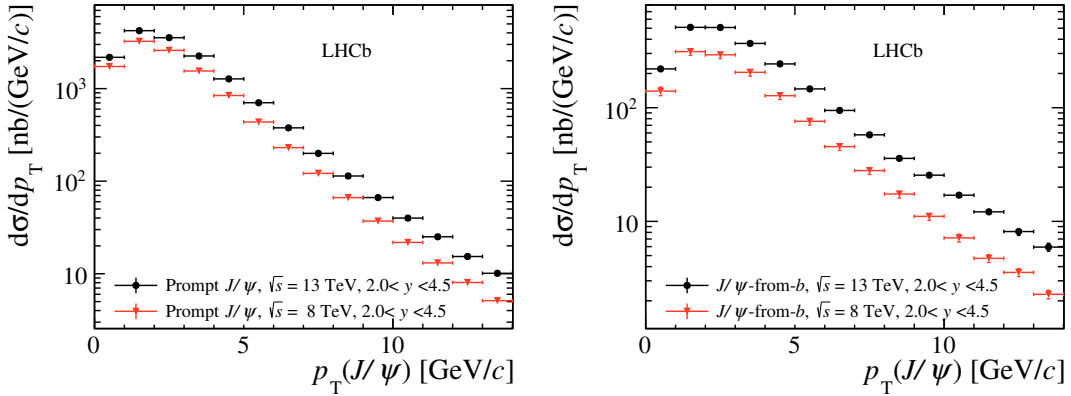


Figure 3.23 Comparison of the differential cross-sections as functions of  $p_T$  integrated over  $y$  between 8 TeV and 13 TeV for (left) prompt  $J/\psi$  and (right)  $J/\psi$  from  $b$ , respectively.

at  $\sqrt{s} = 8$  TeV, as shown in Fig. 3.23. The comparison of the differential cross-sections as functions of  $y$  integrated over  $p_T$  is shown in Fig. 3.24.

The ratio between the cross-sections at different collision energies can provide a more powerful test of the theoretical models, since the systematic uncertainty can largely cancel in the ratio for both the measurements and the theoretical calculations. The correlation between the systematic uncertainties of the 8 TeV and the 13 TeV measurement is evaluated as following:

- Signal mass shape. Both analyses use the CB function, but with different parameterisation. The correlation is set to be 50%.
- Radiative tail. The generator PHOTOS is used to simulate the final state radiation in both measurements. The corresponding uncertainty is 100% correlated.

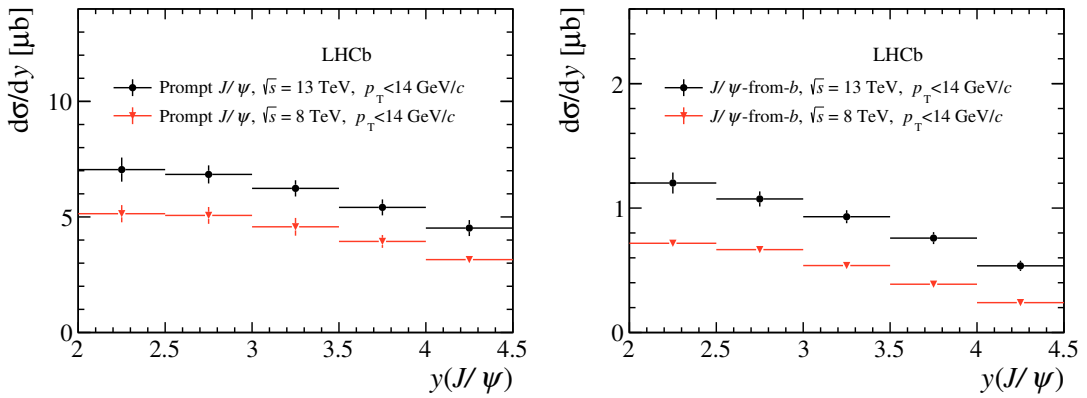


Figure 3.24 Comparison of the differential cross-sections as functions of  $J/\psi$   $y$  integrated over  $p_T$  between 8 TeV and 13 TeV for (left) prompt  $J/\psi$  and (right)  $J/\psi$  from  $b$ , respectively.

- MuonID efficiency. The dominant uncertainty for the muonID efficiency comes from the limited statistic of the calibration sample, which is totally uncorrelated between the two measurements.
- Track reconstruction efficiency. The uncertainty due to the choice of event multiplicity variable is correlated between the two analyses, while the one from the finite size of the calibration sample is uncorrelated. The correlation is taken as 50%.
- Offline selection. The vertex fit quality distribution is similar in the simulated samples for the two measurements. It is expected to be similar in the two data samples as well. The uncertainty can fully cancel.
- Trigger efficiency. With the same simulation configuration and similar selections applied in the trigger, the trigger uncertainty is largely correlated between the 8 TeV and 13 TeV measurements. The correlation is set to be 50% to be conservative.
- $\mathcal{B}(J/\psi \rightarrow \mu^+ \mu^-)$ . Totally correlated.
- $p_T$ - $y$  spectrum. There can be some correlation since the two analyses use the same generators for the simulation. But the agreement between the data and the simulation can be different for different centre-of-mass energies. To be conservative, it is assumed to be uncorrelated.
- Simulation statistic. Totally uncorrelated.
- Luminosity. The same method is used for the determination of luminosity at different collision energies, but the datasets are different. The correlation is taken to be 50%.
- $t_z$  fit. Although the same function is used to model the  $t_z$  distribution, statistical fluctuations can contribute to its systematic uncertainty. As a conservative estimation,

the correlation is set to be zero.

After the cancellation, the remaining systematic uncertainties in the cross-section ratios are summarised in Table 3.5. After performing the uncertainty cancellation, the ratios between the 13 TeV and 8 TeV cross-sections are shown in Figs. 3.25, 3.27, and 3.26, 3.28 for prompt  $J/\psi$  and  $J/\psi$  from  $b$ , respectively.

Table 3.5 Summary of the systematic uncertainties on the ratios between the 13 TeV and 8 TeV cross-sections.

Quantity	Systematic uncertainty
Luminosity	4.6%
Trigger	1.5%
Muon PID efficiency	2.2%
Track reconstruction efficiency	1%
Signal mass shape	2%
$p_T$ -y-spectrum, Simulation statistic, $t_z$ fit	1 - 8 %

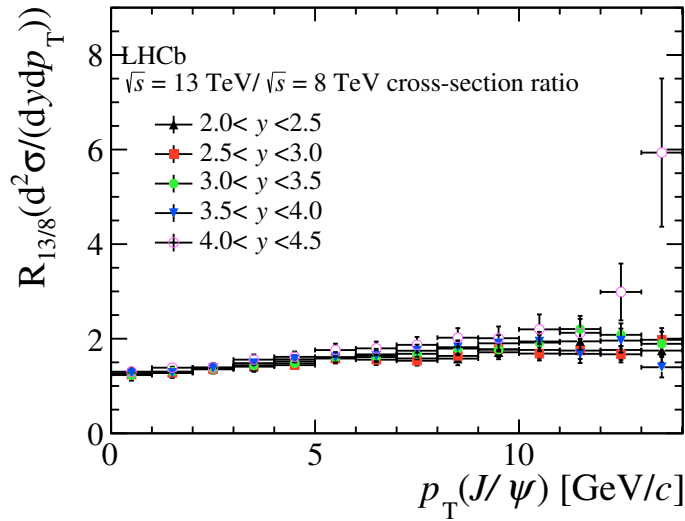


Figure 3.25 Ratios between the 13 TeV and 8 TeV double differential cross-sections in bins of  $J/\psi$   $p_T$  and  $y$  for prompt  $J/\psi$ .

### 3.7.5 Comparison with theoretical models

The differential production cross-sections at  $\sqrt{s} = 13$  TeV as functions of  $J/\psi$   $p_T$  integrated over  $2 < y < 4.5$  for prompt  $J/\psi$  and  $J/\psi$  from  $b$  are compared to the NLO

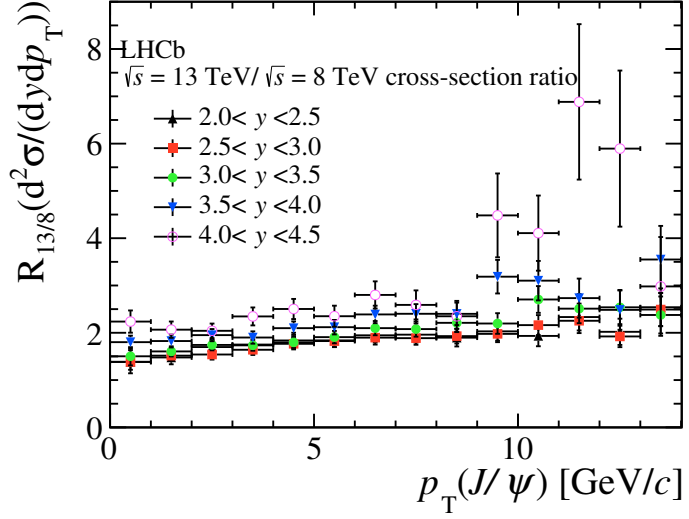


Figure 3.26 Ratios between the 13 TeV and 8 TeV double differential cross-sections in bins of  $J/\psi$   $p_T$  and  $y$  for  $J/\psi$  from  $b$ .

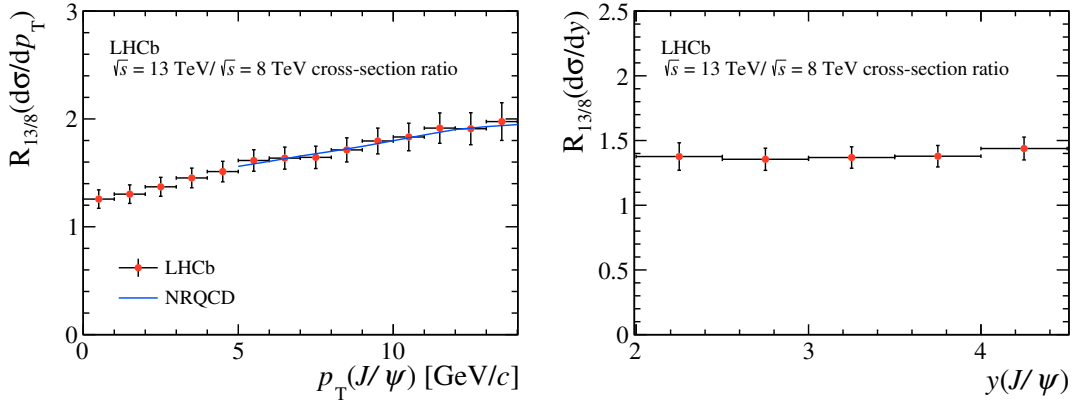


Figure 3.27 Ratios between the 13 TeV and 8 TeV differential cross-sections as functions of (left)  $J/\psi$   $p_T$  integrated over  $y$  and (right)  $J/\psi$   $y$  integrated over  $p_T$  for prompt  $J/\psi$ . The ratios in bins of  $J/\psi$   $p_T$  are compared to the NRQCD calculations at NLO<sup>[22]</sup>.

NRQCD<sup>[22]</sup> and FONLL<sup>[96]</sup> calculations, respectively, as shown in Fig. 3.29. The uncertainties of the NRQCD approach are propagated from the uncertainties of the LDMEs, which are dominant over all the other sources. The FONLL model considers the uncertainties from the mass of the  $b$  quark and the renormalisation and factorization scales. Both the NRQCD and the FONLL model can well describe the measurements. The cross-section ratios between the 13 TeV and 8 TeV measurements are also compared to the theoretical predictions. The ratios between the 13 TeV and 8 TeV differential cross-sections as functions of  $p_T$  integrated over  $y$  for prompt  $J/\psi$  are compared to the NLO NRQCD calculations<sup>[22]</sup>, as shown in Fig. 3.27. For  $J/\psi$  from  $b$ , the FONLL predictions<sup>[106]</sup> are

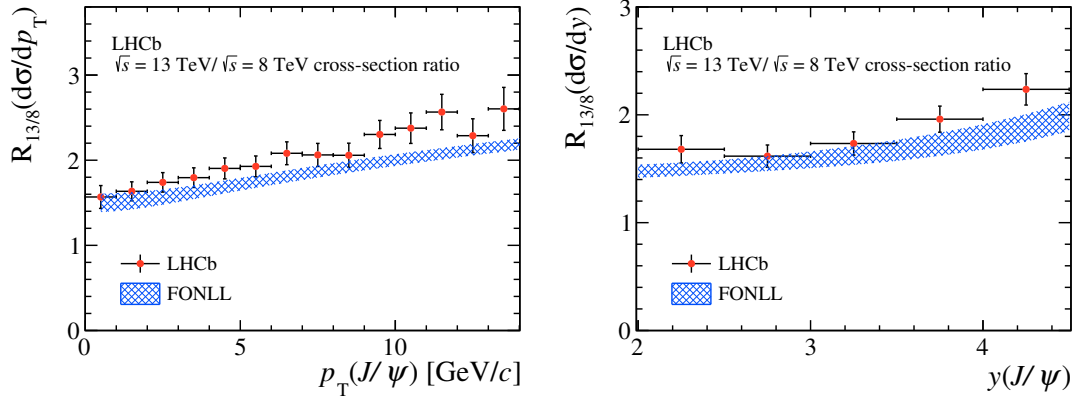


Figure 3.28 Ratios between the 13 TeV and 8 TeV differential cross-sections as functions of (left)  $J/\psi$   $p_T$  integrated over  $y$  and (right)  $J/\psi$   $y$  integrated over  $p_T$  for  $J/\psi$  from  $b$ . The ratios are compared to the FONLL calculations [106].

compared to the ratios as functions of  $p_T$  integrated over  $y$  and of  $y$  integrated over  $p_T$ , respectively, as shown in Fig. 3.28. For the NRQCD calculations, uncertainties of the LDMEs fully cancel between the cross-sections at the centre-of-mass energy of 13 TeV and 8 TeV. Therefore no uncertainty is assigned for the prediction of the cross-section ratio. The NRQCD predictions are consistent with the cross-section ratios of prompt  $J/\psi$ . For  $J/\psi$  from  $b$ , the cross-section ratios are slightly underestimated by the FONLL model.

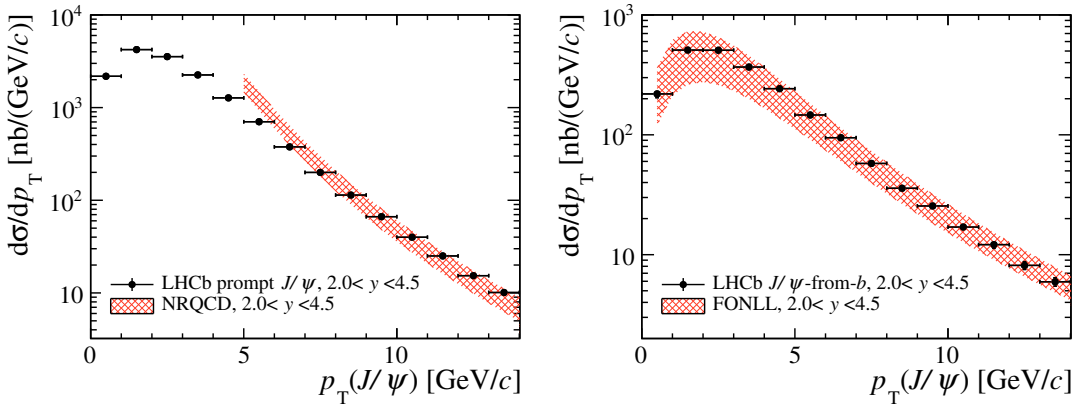


Figure 3.29 Differential production cross-sections as functions of  $J/\psi$   $p_T$  integrated over  $2 < y < 4.5$  for (left) prompt  $J/\psi$  and (right)  $J/\psi$  from  $b$ , which are compared to the NRQCD<sup>[22]</sup> and FONLL<sup>[96]</sup> predictions, respectively.

## Chapter 4 $J/\psi$ pair production in $pp$ collisions at $\sqrt{s} = 13$ TeV

This chapter presents the measurement of  $J/\psi$  pair production cross-section at the centre-of-mass energy of  $\sqrt{s} = 13$  TeV using  $pp$  collision data collected by the LHCb detector. In the following sections, the analysis strategy, the dataset, the candidate selection, the signal extraction, the efficiency estimation, the systematic uncertainties, the result and its comparison to theories are described in detail. The author is fully responsible for the analysis work.

### 4.1 Analysis strategy

The measurement is performed for  $J/\psi$  pair candidates produced promptly from  $pp$  collisions, either through the SPS or the DPS process. The disentanglement of the SPS and DPS contributions is essential to the test of the theoretical models for quarkonium production, and to the extraction of the effective cross-section  $\sigma_{\text{eff}}$ . In the DPS process, the two  $J/\psi$  mesons are produced from the scatterings of two sets of partons, which are expected to be uncorrelated. Both  $J/\psi$  mesons are supposed to have the same kinematics as the single prompt  $J/\psi$  mesons. While in the SPS process, the productions of the two  $J/\psi$  mesons are highly correlated. The two  $J/\psi$  mesons tend to be closer to each other compared to those in DPS. This difference makes it possible to distinguish the SPS and DPS components via the differential production cross-sections as functions of the kinematics of the  $J/\psi$  pairs.

The production cross-section is measured with both  $J/\psi$  mesons in the fiducial region of  $2 < y < 4.5$  and  $p_T < 10$  GeV/ $c$ . The  $J/\psi$  mesons are reconstructed with the dimuon final state. The production cross-section is measured as

$$\sigma(J/\psi J/\psi) = \frac{N^{\text{cor}}}{\mathcal{L} \times \mathcal{B}^2(J/\psi \rightarrow \mu^+ \mu^-)}, \quad (4-1)$$

where  $N^{\text{cor}}$  is the signal yield after the efficiency correction,  $\mathcal{L}$  is the integrated luminosity, and  $\mathcal{B}(J/\psi \rightarrow \mu^+ \mu^-)$  is the branching fraction of the  $J/\psi \rightarrow \mu^+ \mu^-$  decay. The efficiencies are determined assuming zero polarisation of the  $J/\psi$  mesons. The effect of the polarisation on the result is discussed in Sec. 4.9. The differential production cross-sections in bins of several kinematic variables of the  $J/\psi$  pairs are also determined.

## 4.2 Dataset

This measurement is performed with the  $pp$  collision data collected by LHCb during 2015 at the centre-of-mass energy of  $\sqrt{s} = 13$  TeV, corresponding to an integrated luminosity of  $279 \pm 11 \text{ pb}^{-1}$ . The luminosity is determined using two methods: the beam-gas imaging method, which photographs the beams using beam-gas interactions taking advantage of the unique precision of the VELO; and the van der Meer scan method for which the beam profiles are measured by separating them in the transverse plane<sup>[107,108]</sup>.

The trigger selections aim at selecting high quality muons. The trigger decisions are all TOS. At the L0 trigger level, two muons with the product of  $p_T$  larger than  $(1.3 \text{ GeV}/c)^2$  are required. A global event cut (GEC) requiring the nSPDHits smaller than 900 is applied to save the computing cost. Two trigger lines are used in the HLT1 trigger. Candidates firing either line are kept. The HLT1 trigger requires one or two muons to have large  $p_T$  and  $p$ . The muon(s) should also have good track quality with  $\chi^2_{\text{track}}/\text{ndf}$  smaller than 3, and be identified as muons by requiring positive isMuon. The HLT2 trigger requires four muons to be reconstructed. Each muon pair must have an invariant mass within  $\pm 120 \text{ MeV}/c^2$  of the known  $J/\psi$  mass<sup>[97]</sup>, and form a good quality vertex with  $\chi^2_{\text{vertex}}/\text{ndf}$  smaller than 25. The trigger lines employed and their corresponding cuts are summarised in Table 4.1. Since the L0 and HLT1 trigger requirements can be fulfilled by one  $J/\psi$  meson,  $J/\psi$  pair candidates with either  $J/\psi$  meson passing the L0 and HLT1 trigger are retained to increase the statistic. The total trigger decision is taken to be  $\left[ \left( J/\psi_1\text{-L0\_TOS} \& J/\psi_1\text{-HLT1\_TOS} \right) \text{ or } \left( J/\psi_2\text{-L0\_TOS} \& J/\psi_2\text{-HLT1\_TOS} \right) \right] \& J/\psi\text{ pair\_HLT2\_TOS}$ , where the two  $J/\psi$  candidates of the  $J/\psi$  pair are randomly denoted as either  $J/\psi_1$  or  $J/\psi_2$  respectively.

Simulated samples are generated to study the behaviour of the signal candidates. Around 6 million single  $J/\psi$  candidates are generated using the same settings as the  $J/\psi$  production cross-section measurement. The  $J/\psi$  mesons are produced under the zero polarisation assumption.

## 4.3 Candidate selection

Additional cuts are applied offline to further reduce the background, as listed in Table 4.2. The muons are required to be in the kinematic range of  $6 \text{ GeV}/c < p < 200 \text{ GeV}/c$ ,  $p_T > 650 \text{ GeV}/c$  and  $2 < \eta < 5$ . It enables a precise determination of the track reconstruction efficiency and can suppress background candidates with low

Table 4.1 Trigger lines used and their corresponding cuts.

Trigger level	Trigger line	#muons	Cuts
L0	L0DiMuon	2	$p_T(\mu_1) \times p_T(\mu_2) > (1.3 \text{ GeV}/c)^2$ $\text{nSPDHits} < 900$
HLT1	HLT1DiMuonHighMass	2	$p_T(\mu) > 300 \text{ MeV}/c$ $p(\mu) > 6000 \text{ MeV}/c$ $\chi_{\text{track}}^2/\text{ndf}(\mu) < 3.0$ $\text{isMuon}(\mu) == 1$ $M(\mu^+ \mu^-) > 2700 \text{ MeV}/c^2$
	HLT1SingleMuonHighPT	1	$p_T(\mu) > 4340 \text{ MeV}/c$ $p(\mu) > 6000 \text{ MeV}/c$ $\chi_{\text{track}}^2/\text{ndf}(\mu) < 3.0$ $\text{isMuon}(\mu) == 1$
HLT2	HLT2DPS:2x2mu	4	$\chi_{\text{track}}^2/\text{ndf}(\mu) < 5$ $M(\mu^+ \mu^-) - M(J/\psi) \in \pm 120 \text{ MeV}/c^2$ $\chi_{\text{vertex}}^2/\text{ndf}(\mu^+ \mu^-) < 25$

momenta. The muon  $\chi_{\text{track}}^2/\text{ndf}$  is required to be smaller than 3 to guarantee a good track quality. To suppress misidentified backgrounds, the muon PIDmu, corresponding to  $\Delta \log \mathcal{L}(\mu - \pi)$ , is required to be larger than 2 in addition to the isMuon requirement. The TRACK\_GhostProb of the muons is required to be smaller than 0.4 to remove fake tracks reconstructed from random combination of hits. The  $J/\psi$  mass window is tightened to be within  $[3000, 3200] \text{ MeV}/c^2$ . The  $\chi_{\text{DTF}}^2/\text{ndf}$  of the  $J/\psi$  meson, for which the DTF constrains the two muons to originate from the PV, is required to be smaller than 5 to reject muons mistakenly combined. It can significantly suppress the backgrounds with  $J/\psi$  from  $b$ . The  $\chi_{\text{DTF}}^2/\text{ndf}$  of the  $J/\psi$  pair, for which the DTF constrains the four muons to the PV, is also required to be smaller than 5 to reject  $J/\psi$  pairs that do not come from the same PV.

To remove duplicate tracks, a two dimensional (2D) cut is applied to  $M(\mu_1^\pm \mu_2^\pm)$  and  $\theta(\mu_1^\pm \mu_2^\pm)$ , where  $M(\mu_1^\pm \mu_2^\pm)$  is the invariant mass of  $\mu_1^\pm$  and  $\mu_2^\pm$ , and  $\theta(\mu_1^\pm \mu_2^\pm)$  is the angle between  $\mu_1^\pm$  and  $\mu_2^\pm$ . If the muon of one  $J/\psi$  is the duplicate of the muon from the other  $J/\psi$ ,  $M(\mu_1^\pm \mu_2^\pm)$  should be close to  $2 \times M(\mu)$ , and  $\theta(\mu_1^\pm \mu_2^\pm)$  should be close to zero. The 2D distribution of  $M(\mu_1^\pm \mu_2^\pm)$  and  $\theta(\mu_1^\pm \mu_2^\pm)$  is shown in Fig. 4.1. The distribution

of  $M(\mu_1^\pm \mu_2^\mp)$  versus  $\theta(\mu_1^\pm \mu_2^\mp)$  is also given for comparison, which is expected to have no contribution from duplicate tracks since the two muons have opposite signs. Those candidates with  $M(\mu_1^\pm \mu_2^\pm) < 220$  or  $\theta(\mu_1^\pm \mu_2^\pm) < 0.002$  are removed, as indicated by the red solid lines in Fig. 4.1. The fraction of rejected signal is negligible (0.1%), thus it can be safely assumed that the duplicate track cut is fully efficient. After the selection, candidates with both muons of one  $J/\psi$  meson to be the duplicates of the muons from the other  $J/\psi$  meson should be very few. The remaining candidates with one muon shared by the two  $J/\psi$  mesons shall be taken as background during the mass fit as described in Sec. 4.4. Theoretically, the probability to produce two  $J/\psi$  pairs in the same  $pp$  collision is negligibly small. If multiple  $J/\psi$  pair candidates are found in the same event, it should be due to false combination. Therefore, for two candidates in the same event, a) if they have the same  $J/\psi$  pair  $\chi^2_{\text{DTF}}$  value, which means they share the same four muons, one of them is rejected randomly; b) if they have different  $J/\psi$  pair  $\chi^2_{\text{DTF}}$  values, the one with a smaller  $J/\psi$  pair  $\chi^2_{\text{DTF}}$  is chosen. The removed multiple candidates account for around 1.4% of the total candidates. The two dimensional  $(M(\mu_1^+ \mu_1^-), M(\mu_2^+ \mu_2^-))$  mass distribution for the  $J/\psi$  pair candidates that have passed all the selections is presented in Fig. 4.2, which shows a clear signal peak of the  $J/\psi$  pair.

Table 4.2 Summary of the cuts applied offline.

All $\mu^\pm$	$6 \text{ GeV}/c < p < 200 \text{ GeV}/c$
	$p_T > 650 \text{ GeV}/c$
	$2 < \eta < 5$
	$\chi^2_{\text{track}}/\text{ndf} < 3$
	isMuon == 1
	PIDmu > 2
	TRACK_GhostProb < 0.4
Both $J/\psi$	$\chi^2_{\text{DTF}}/\text{ndf} < 5.0$ (constrain two muons to the PV)
	$M \in [3000, 3200] \text{ MeV}/c^2$
	$\chi^2_{\text{vertex}}/\text{ndf} < 20$
$J/\psi$ pair	$\chi^2_{\text{DTF}}/\text{ndf} < 5.0$ (constrain four muons to the PV)

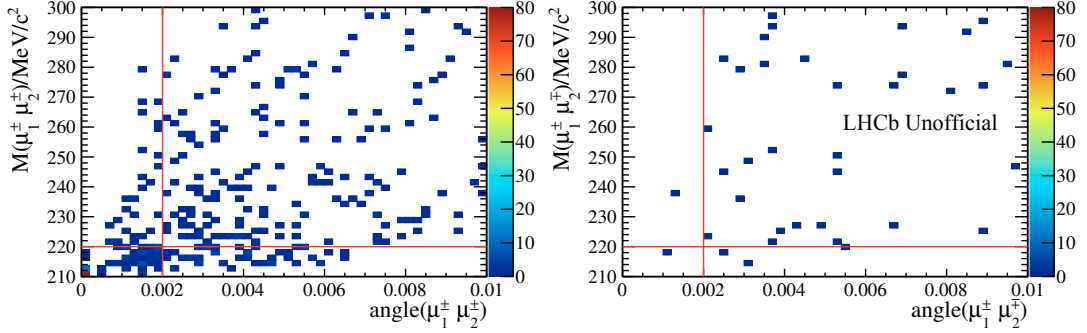


Figure 4.1 Two dimensional distribution of (left)  $M(\mu_1^\pm \mu_2^\pm)$  to  $\theta(\mu_1^\pm \mu_2^\pm)$  and (right)  $M(\mu_1^\pm \mu_2^\pm)$  to  $\theta(\mu_1^\pm \mu_2^\mp)$  in the data sample. The figures are zoomed in to this range for a better visualization. The red solid lines indicate the cuts applied.

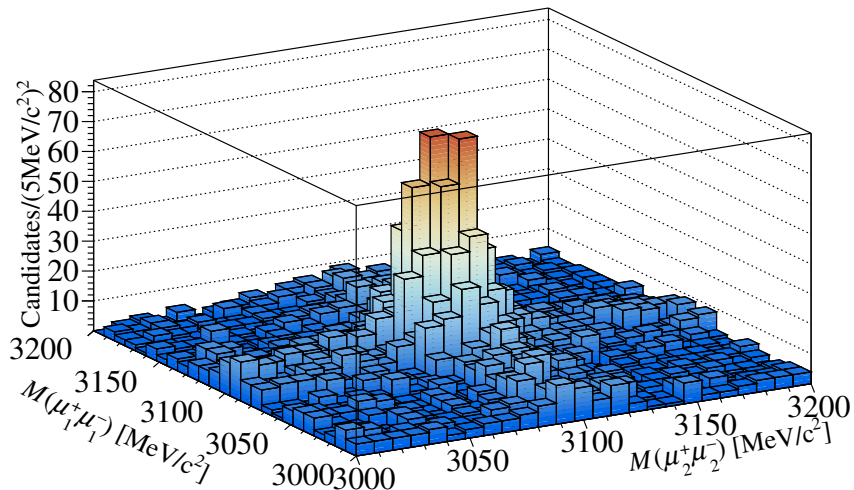


Figure 4.2 Two-dimensional  $(M(\mu_1^+ \mu_1^-), M(\mu_2^+ \mu_2^-))$  mass distribution for the selected  $J/\psi$  pair candidates.

#### 4.4 Signal extraction

The signal candidates are extracted by performing an unbinned extended maximum likelihood fit to the two dimensional  $(M(\mu_1^+ \mu_2^-), M(\mu_2^+ \mu_2^-))$  distribution. The mass distribution of  $J/\psi$  signal is modelled by the sum of a double-sided Crystal Ball (DSCB) function and a Gaussian function, taking the dependence of the resolution on the  $J/\psi$

kinematics into consideration. The DSCB function is defined as

$$g(x; \mu, \sigma, a_l, n_l, a_r, n_r) = \begin{cases} e^{-a_l^2/2} \left(\frac{n_l}{a_l}\right)^{n_l} \cdot \left(\frac{n_l}{a_l} - a_l - \frac{x - \mu}{\sigma}\right)^{-n_l} & \frac{x - \mu}{\sigma} < -a_l \\ \exp\left(-\frac{1}{2}\left(\frac{x - \mu}{\sigma}\right)^2\right) & -a_l \leq \frac{x - \mu}{\sigma} \leq a_r, \\ e^{-a_r^2/2} \left(\frac{n_r}{a_r}\right)^{n_r} \cdot \left(\frac{n_r}{a_r} - a_r + \frac{x - \mu}{\sigma}\right)^{-n_r} & \frac{x - \mu}{\sigma} > -a_r \end{cases} \quad (4-2)$$

where  $\mu$  and  $\sigma$  are the mean value and the width of the central Gaussian;  $a_l$  and  $a_r$  are the starting point of the left and right tail;  $n_l$  and  $n_r$  define the left and right tail shape, respectively. The DSCB and the Gaussian function share the same mean value but have different widths. The total signal model is

$$s(M(\mu^+ \mu^-)) = f \times g(M(\mu^+ \mu^-); \mu, \sigma_1, a_l, n_l, a_r, n_r) + (1-f) \times G(M(\mu^+ \mu^-); \mu, \sigma_2), \quad (4-3)$$

where  $f$  is the fraction of the DSCB function;  $g$  and  $G$  stand for the DSCB and the Gaussian function, respectively;  $\mu$  is the common mean value of the DSCB and the Gaussian function;  $\sigma_1$  and  $\sigma_2$  are the widths of the DSCB and the Gaussian function, respectively. When performing the fit to the data sample, the tail parameters ( $a_l$ ,  $n_l$ ,  $a_r$  and  $n_r$ ), the fraction of the DSCB function ( $f$ ) and the ratio  $\sigma_1/\sigma_2$  are all fixed according to the fit to the simulated sample. There are only two parameters,  $\mu$  and  $\sigma_1$ , left free in the fit. Therefore, the signal model  $s(M(\mu^+ \mu^-))$  can be simplified to  $s(M(\mu^+ \mu^-); \mu, \sigma)$ . The combinatorial background is described by an exponential function

$$b(x; \tau) = e^{\tau \cdot x}. \quad (4-4)$$

Since  $J/\psi_1$  and  $J/\psi_2$  are classified randomly, the 2D fit model should be symmetric with respect to  $M(\mu_1^+ \mu_1^-)$  and  $M(\mu_2^+ \mu_2^-)$ . The variables  $M(\mu_1^+ \mu_1^-)$  and  $M(\mu_2^+ \mu_2^-)$  are denoted as  $m_1$  and  $m_2$  respectively afterwards. The model for the total 2D mass distribution has three components:

- (a) the signal component:  $s(m_1; \mu, \sigma) \times s(m_2; \mu, \sigma)$ ;
- (b) the background which is the combination of the signal of one  $J/\psi$  and the combinatorial background of the other  $J/\psi$ :  $s(m_1; \mu, \sigma) \times b(m_2; \tau_a) + s(m_2; \mu, \sigma) \times b(m_1; \tau_a)$ ;
- (c) the purely combinatorial background:  $b(m_1; \tau_b) \times b(m_2; \tau_b)$ .

The 2D fit model can be formulated as

$$\begin{aligned}
 f(m_1, m_2) = & N_{sig} \times s(m_1; \mu, \sigma) \times s(m_2; \mu, \sigma) \\
 & + N_{bs} \times [s(m_1; \mu, \sigma) \times b(m_2; \tau_a) + s(m_2; \mu, \sigma) \times b(m_1; \tau_a)] \\
 & + N_{bb} \times b(m_1; \tau_b) \times b(m_2; \tau_b)
 \end{aligned} \quad (4-5)$$

assuming no correlation between  $m_1$  and  $m_2$ , where  $N_{sig}$ ,  $N_{bs}$  and  $N_{bb}$  represent the number of candidates for component (a), (b) and (c), respectively. The projections of the fit result to  $M(\mu_1^+ \mu_1^-)$  and  $M(\mu_2^+ \mu_2^-)$  are shown in Fig. 4.3. The signal yield obtained is  $1048 \pm 51$ , where the uncertainty is statistical only. By physics, there should be no correlation between the signal mass distributions of the two  $J/\psi$  mesons. The correlation between the background mass distributions of the two  $J/\psi$  mesons is checked by introducing a  $e^{\tau_c \cdot |m_1 - m_2|}$  term to account for the possible correlation, which leads to a 2D fit model as

$$\begin{aligned}
 f(m_1, m_2) = & N_{sig} \times s(m_1; \mu, \sigma) \times s(m_2; \mu, \sigma) \\
 & + N_{bs} \times [s(m_1; \mu, \sigma) \times b(m_2; \tau_a) + s(m_2; \mu, \sigma) \times b(m_1; \tau_a)] \\
 & + N_{bb} \times b(m_1; \tau_b) \times b(m_2; \tau_b) \times e^{\tau_c \cdot |m_1 - m_2|}.
 \end{aligned} \quad (4-6)$$

The parameter  $\tau_c$  is determined to be  $-0.000466 \pm 0.00058$  and is consistent with 0. The deviation of the signal yield to that of the nominal fit is negligible.

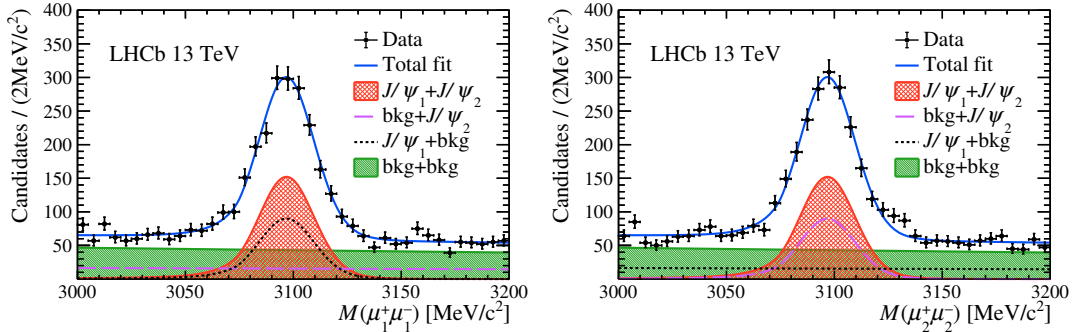


Figure 4.3 Projections of the 2D mass fit to (left)  $M(\mu_1^+, \mu_1^-)$  and (right)  $M(\mu_2^+, \mu_2^-)$ . The black points with error bars represent the data. The blue solid line is the total fit model. The red cross-hatched area represents the signal distribution. The black and magenta dashed lines show the background components due to the combination of a  $J/\psi$  signal with a combinatorial background. The green shaded area indicates the purely combinatorial background.

## 4.5 Efficiency estimation

The total efficiency  $\varepsilon_{\text{tot}}$  is estimated as

$$\varepsilon_{\text{tot}} = \varepsilon_{\text{acc}} \times \varepsilon_{\text{GEC}} \times \varepsilon_{\text{rec\&sel}} \times \varepsilon_{\text{muonID}} \times \varepsilon_{\text{trig}}, \quad (4-7)$$

in which  $\varepsilon_{\text{acc}}$  is the geometrical acceptance efficiency,  $\varepsilon_{\text{GEC}}$  is the global event cut efficiency,  $\varepsilon_{\text{rec\&sel}}$  is the reconstruction and selection (without the muonID selections, i.e. the positive `isMuon` and `PIDmu > 2` requirements) efficiency,  $\varepsilon_{\text{muonID}}$  is the muonID efficiency, and  $\varepsilon_{\text{trig}}$  is the trigger efficiency. Each efficiency term is defined based on the term before it. The determination of each efficiency term is given in detail below.

### 4.5.1 Acceptance efficiency

The geometrical acceptance efficiency  $\varepsilon_{\text{acc}}$  of the  $J/\psi$  pair can be factorized as

$$\varepsilon_{\text{acc}}(\text{J}/\psi \text{ pair}) = \varepsilon_{\text{acc}}(\text{J}/\psi_1) \times \varepsilon_{\text{acc}}(\text{J}/\psi_2), \quad (4-8)$$

where  $\varepsilon_{\text{acc}}(\text{J}/\psi_{1,2})$  is the single  $J/\psi$  acceptance efficiency. The efficiency  $\varepsilon_{\text{acc}}(\text{J}/\psi)$  is defined as

$$\varepsilon_{\text{acc}}(\text{J}/\psi) \equiv \frac{\text{J}/\psi \text{ with both muons in LHCb acceptance}}{\text{Generated J}/\psi}. \quad (4-9)$$

The LHCb acceptance means the polar angle region of  $(10, 400)$  mrad with respect to the  $z$ -axis. The efficiency  $\varepsilon_{\text{acc}}(\text{J}/\psi)$  is estimated using the single prompt  $J/\psi$  sample simulated at the generation level. It is determined in bins of  $J/\psi$   $p_{\text{T}}$  and  $y$ , as shown in Fig. 4.4. The efficiencies for candidates in the  $4.0 < y < 4.5$  bin are smaller than those within  $3.5 < y < 4.0$  because the candidates within  $4.0 < y < 4.5$  tend to have polar angle values smaller than 10 mrad.

### 4.5.2 Global event cuts efficiency

During the L0 trigger, a global event cut which requires `nSPDHits` to be smaller than 900 is applied. The efficiency  $\varepsilon_{\text{GEC}}$  is estimated by extrapolating the `nSPDHits` distribution of the selected  $J/\psi$  pair signals. The background candidates are subtracted using the sPlot technique<sup>[104]</sup>, with  $(M(\mu_1^+ \mu_1^-), M(\mu_2^+ \mu_2^-))$  as the discriminating variables.

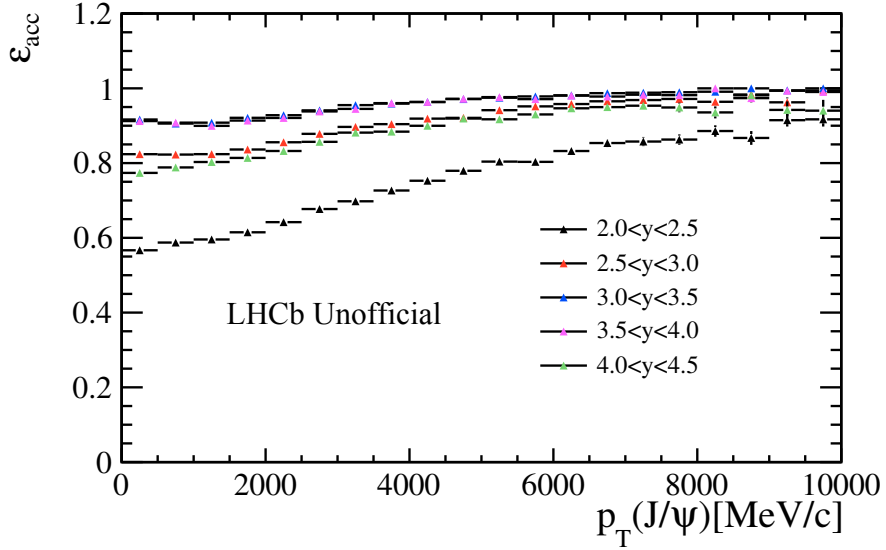


Figure 4.4 Acceptance efficiencies  $\varepsilon_{\text{acc}}(J/\psi)$  in bins of  $J/\psi$   $p_T$  and  $y$  for single prompt  $J/\psi$ .

The nSPDHits distribution is described by a  $\Gamma$  function, as displayed in Fig. 4.5. The efficiency  $\varepsilon_{\text{GEC}}$  is calculated to be the ratio between the integral of the fitted  $\Gamma$  function in the range of (0, 900) and the integral from 0 to infinity. It is determined to be 99.8%.

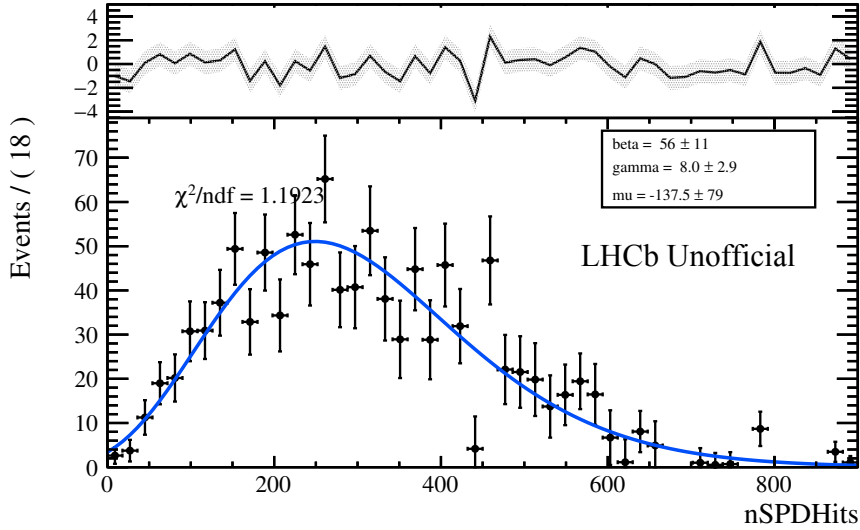


Figure 4.5 Fit to the nSPDHits distribution of  $J/\psi$  pair signal with the  $\Gamma$  function.

#### 4.5.3 Reconstruction and selection efficiency

The only selection criterion on the  $J/\psi$  pair is the  $\chi^2_{\text{DTF}}/\text{ndf} < 5.0$  requirement, while all the other cuts are separately applied to the two  $J/\psi$  mesons. For  $J/\psi$  pair signals in

which the two  $J/\psi$  mesons originate from the same PV, by definition there is

$$\chi^2_{\text{DTF}}/\text{ndf}(J/\psi \text{ pair}) = \frac{\chi^2_{\text{DTF}}/\text{ndf}(J/\psi_1) + \chi^2_{\text{DTF}}/\text{ndf}(J/\psi_2)}{2}. \quad (4-10)$$

With the same threshold for  $\chi^2_{\text{DTF}}/\text{ndf}(J/\psi \text{ pair})$  and  $\chi^2_{\text{DTF}}/\text{ndf}(J/\psi_{1,2})$ , the cut on  $\chi^2_{\text{DTF}}/\text{ndf}(J/\psi \text{ pair})$  should be 100% efficient. It allows for the factorization of the reconstruction and selection efficiency  $\varepsilon_{\text{rec\&sel}}$  of  $J/\psi$  pair as

$$\varepsilon_{\text{rec\&sel}}(J/\psi \text{ pair}) = \varepsilon_{\text{rec\&sel}}(J/\psi_1) \times \varepsilon_{\text{rec\&sel}}(J/\psi_2). \quad (4-11)$$

The efficiency  $\varepsilon_{\text{rec\&sel}}(J/\psi)$  is defined as

$$\varepsilon_{\text{rec\&sel}}(J/\psi) \equiv \frac{J/\psi \text{ reconstructed and selected w/o muonID}}{J/\psi \text{ with both muons in LHCb acceptance}}. \quad (4-12)$$

It is determined in bins of  $J/\psi$   $p_T$  and  $y$  using the simulated  $J/\psi$  sample, as shown in Fig. 4.6. The efficiency for  $J/\psi$  mesons within  $4.0 < y < 4.5$  drops rapidly at high  $p_T$  because the muon momentum is required to be smaller than  $200$  GeV/ $c$ .

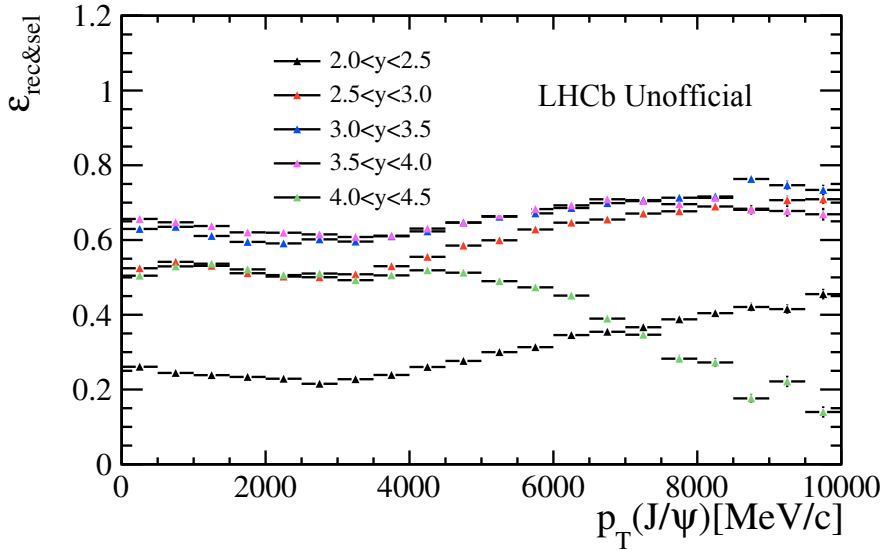


Figure 4.6 Reconstruction and selection efficiencies  $\varepsilon_{\text{rec\&sel}}(J/\psi)$  in bins of  $J/\psi$   $p_T$  and  $y$  for single prompt  $J/\psi$ .

In analogy with the  $J/\psi$  production measurement, the track reconstruction efficiency is calibrated with the data sample using the tag-and-probe technique. The correction

factors in bins of muon  $p$  and  $\eta$  are shown in Fig. 4.7. Before applying the corrections, the event multiplicity distribution in the simulated sample is weighted to match its distribution in the data sample. The event multiplicity variable is taken to be the total number of reconstructed tracks (nTracks). To extract the nTracks distribution of the  $J/\psi$  pair signals in the data sample, the backgrounds are subtracted according to the  $(M(\mu_1^+, \mu_1^-), M(\mu_2^+, \mu_2^-))$  distribution using the sPlot method<sup>[104]</sup>. Due to the large statistical fluctuation of the data sample, the nTracks distribution is fitted with an empirical function defined as

$$h(x; p0, p1, p2) = p0 \cdot x^{p1} \cdot e^{-p2 \cdot x}, \quad (4-13)$$

where  $p0$ ,  $p1$  and  $p2$  are the free parameters. The fit result is shown in Fig. 4.8. The nTracks distribution in the simulated sample is weighted to the fitted empirical function. Then the track reconstruction efficiency corrections are calculated in bins of  $J/\psi$   $p_T$  and  $y$ , as shown in Fig. 4.9.

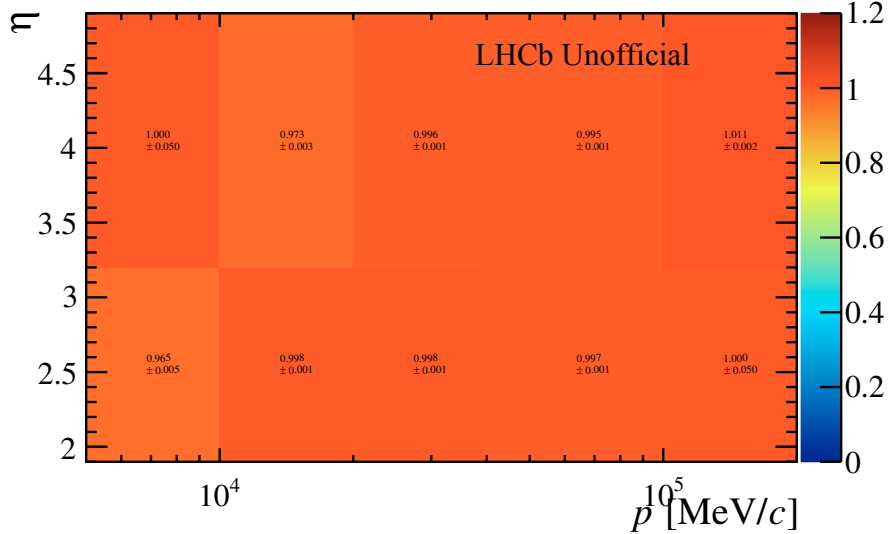


Figure 4.7 Track reconstruction efficiency correction factors in bins of  $p$  and  $\eta$  of the muons.

#### 4.5.4 Muon identification efficiency

The muon identification efficiency  $\varepsilon_{\text{muonID}}$  of the  $J/\psi$  pair can be factorized as

$$\varepsilon_{\text{muonID}}(J/\psi \text{ pair}) = \varepsilon_{\text{muonID}}(J/\psi_1) \times \varepsilon_{\text{muonID}}(J/\psi_2). \quad (4-14)$$

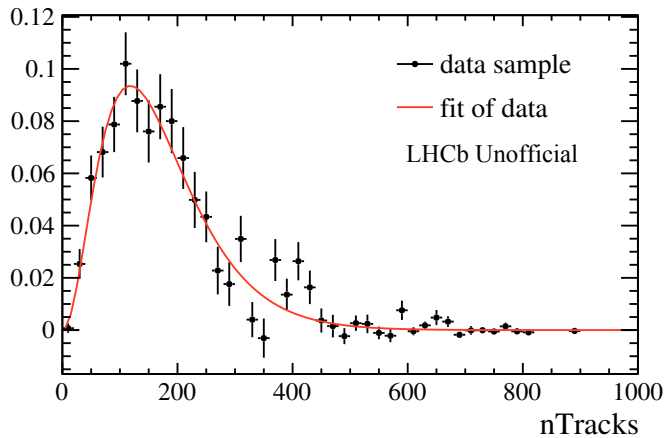


Figure 4.8 Fit to the  $n_{\text{Tracks}}$  distribution in the data sample, in which the backgrounds are subtracted using the sPlot method.

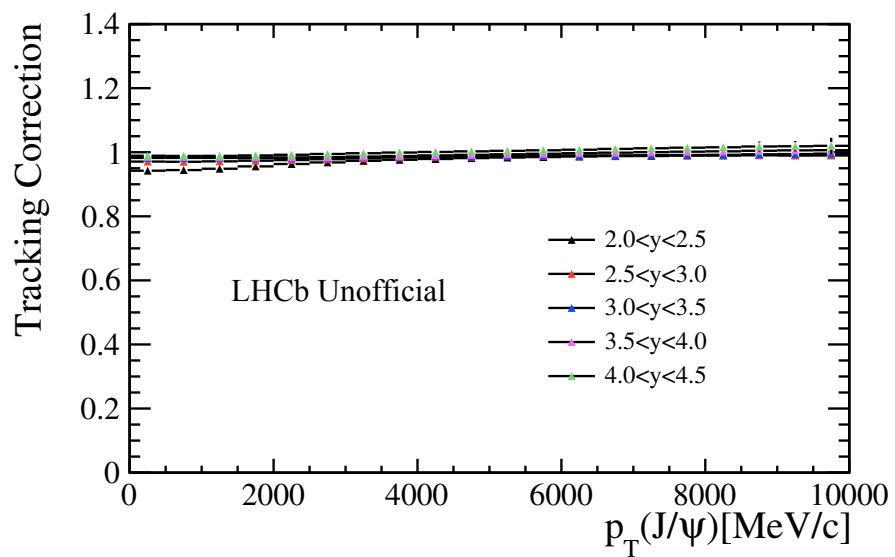


Figure 4.9 Track reconstruction efficiency correction factors in bins of  $J/\psi$   $p_T$  and  $y$ .

The efficiency  $\varepsilon_{\text{muonID}}(J/\psi)$  is defined as

$$\varepsilon_{\text{muonID}}(J/\psi) \equiv \frac{J/\psi \text{ selected including muonID}}{J/\psi \text{ reconstructed and selected w/o muonID}}. \quad (4-15)$$

It is estimated using the simulated  $J/\psi$  sample, with the single muonID efficiency evaluated in the data using the tag-and-probe technique as in the  $J/\psi$  production measurement. The single muonID efficiencies are determined in kinematic bins of the muons independently for data collected with the LHCb magnet pointing downwards (MagDown) and upwards (MagUp), as shown in Fig. 4.10. For each  $J/\psi$  signal, the efficiency  $\varepsilon_{\text{muonID}}(J/\psi)$  is calculated as the multiplication of the single muonID efficiencies of its two muons. It is determined in bins of  $J/\psi p_T$  and  $y$ , as shown in Fig. 4.11.

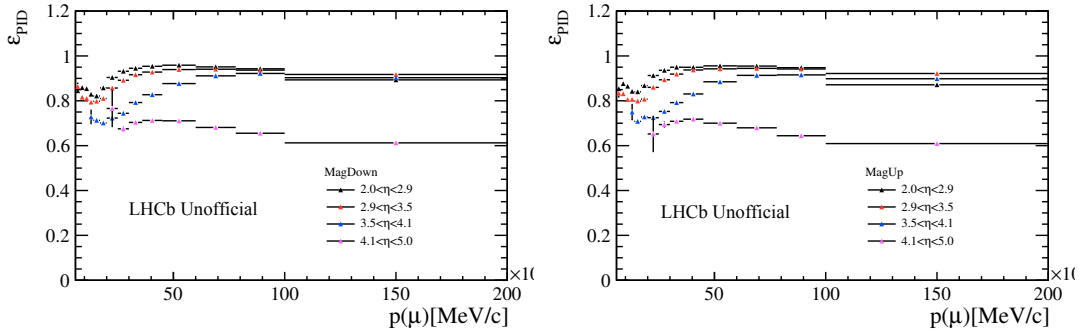


Figure 4.10 Single muonID efficiency in bins of muon  $p$  and  $\eta$  for (left) MagDown and (right) MagUp, respectively.

#### 4.5.5 Trigger efficiency

The offline selections are much tighter than the HLT2 requirements, so the efficiency of the HLT2 cuts should be 100%. The trigger efficiency  $\varepsilon_{\text{trig}}$  is equivalent to the L0 and HLT1 efficiency  $\varepsilon_{\text{L0\&HLT1}}$ . The efficiency  $\varepsilon_{\text{L0\&HLT1}}$  of the  $J/\psi$  pair signal can be factorized as

$$\varepsilon_{\text{L0\&HLT1}}(J/\psi \text{ pair}) = 1 - (1 - \varepsilon_{\text{L0\&HLT1}}(J/\psi_1)) \times (1 - \varepsilon_{\text{L0\&HLT1}}(J/\psi_2)), \quad (4-16)$$

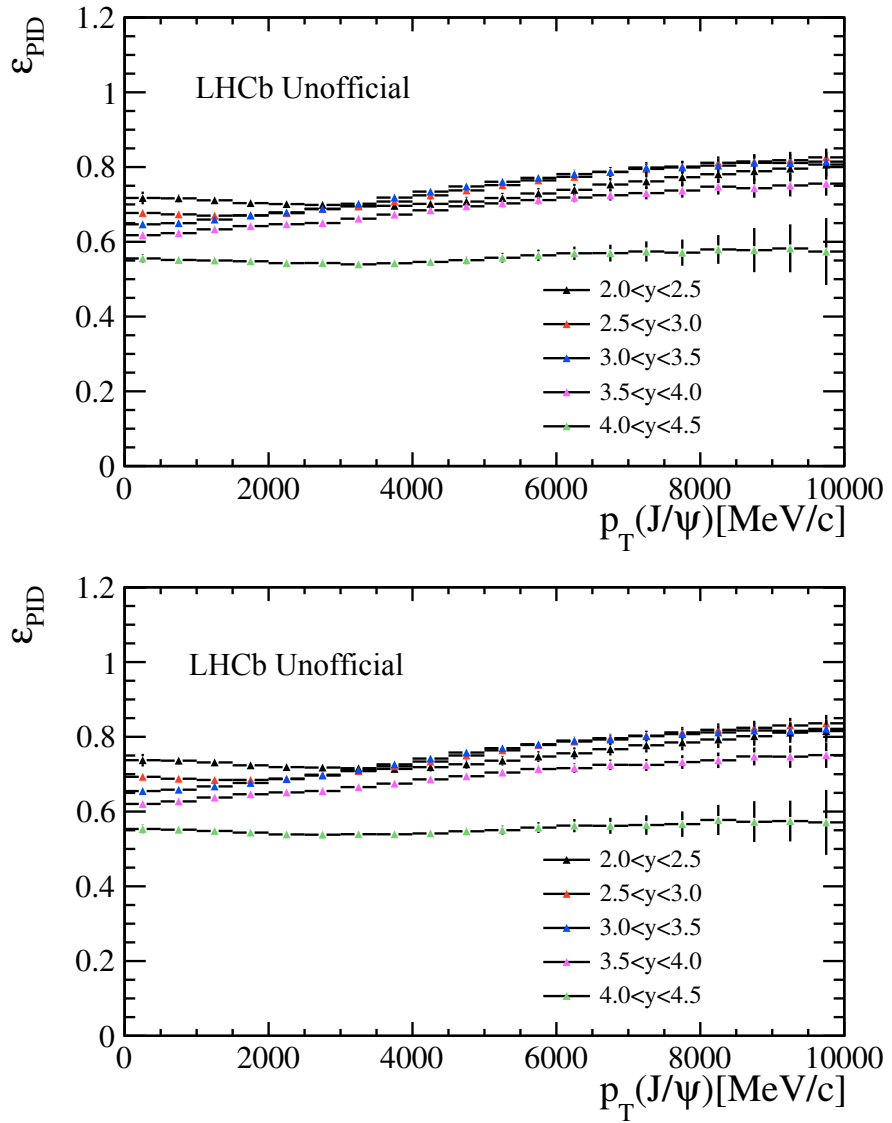


Figure 4.11 MuonID efficiencies  $\varepsilon_{\text{muonID}}(J/\psi)$  in bins of  $J/\psi$   $p_T$  and  $y$  for the (top) MagDown and (bottom) MagUp data, respectively.

since the L0 and HLT1 trigger requires either of the  $J/\psi$  meson to be triggered on. The efficiency  $\varepsilon_{\text{L0\&HLT1}}(J/\psi)$  is given by

$$\varepsilon_{\text{L0\&HLT1}}(J/\psi) \equiv \frac{J/\psi \text{ selected and triggered by L0\&HLT1\&HLT2}}{J/\psi \text{ selected and triggered by HLT2 w/o L0\&HLT1}}. \quad (4-17)$$

It is estimated using the simulated  $J/\psi$  sample in bins of  $J/\psi$   $p_T$  and  $y$  as shown in Fig. 4.12.

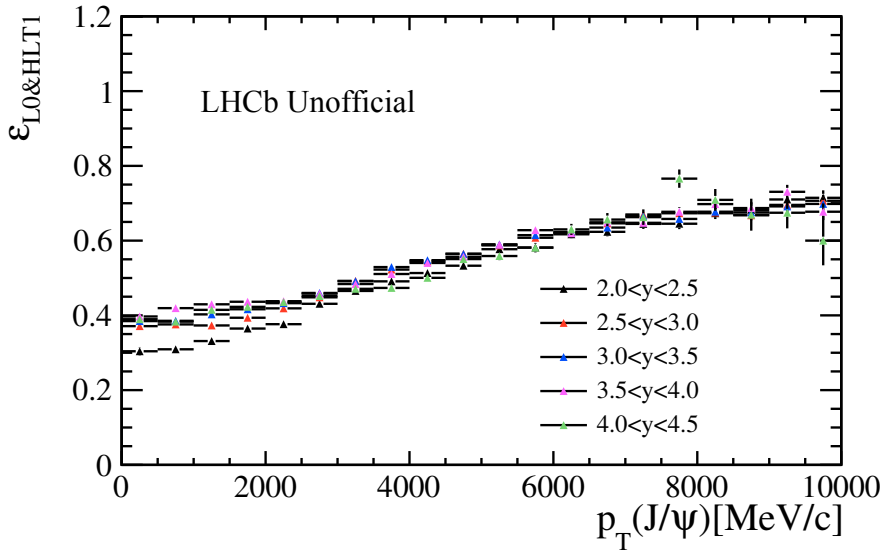


Figure 4.12 Efficiencies  $\varepsilon_{\text{L0\&HLT1}}(J/\psi)$  in bins of  $J/\psi$   $p_T$  and  $y$  for single prompt  $J/\psi$ .

## 4.6 From- $b$ component determination

After all the selections, there are still contaminations in which one or both  $J/\psi$  meson(s) come(s) from  $b$ -hadron decays. The prompt  $J/\psi$  and  $b\bar{b}$  production cross-section within the LHCb acceptance at  $\sqrt{s} = 13$  TeV are measured to be  $\sigma(\text{prompt } J/\psi) = 15.03 \pm 0.91 \mu\text{b}$  and  $\sigma(pp \rightarrow b\bar{b}) = 95 \pm 10 \mu\text{b}$ , as given in Chapter 3. The production cross-section of  $J/\psi$  pair with both  $J/\psi$  from  $b$  is estimated as

$$\sigma(\text{two } J/\psi \text{ from } b) = \sigma(pp \rightarrow b\bar{b}) \times \mathcal{B}(b \rightarrow J/\psi X) = 12.8 \pm 1.3 \text{ nb}, \quad (4-18)$$

where  $\mathcal{B}(b \rightarrow J/\psi X) = (1.16 \pm 0.10)\%$  is the branching fraction of the inclusive  $b \rightarrow J/\psi X$  decay<sup>[97]</sup>. The  $J/\psi$  pair candidates with one  $J/\psi$  from  $b$  are mainly produced from the DPS process according to the measurement of the associated production

of  $\gamma$  with open  $c$ -meson, where the DPS contribution exceeds the SPS contribution with a factor larger than  $10^{[109]}$ . Its production cross-section is calculated using the DPS formula as

$$\begin{aligned}\sigma(\text{one } J/\psi \text{ from } b) &= \frac{2 \times \sigma(pp \rightarrow b\bar{b}) \times \mathcal{B}(b \rightarrow J/\psi X) \times \sigma(\text{prompt } J/\psi)}{\sigma_{\text{eff}}} \\ &= 2.28 \pm 0.19 \text{ nb},\end{aligned}\quad (4-19)$$

where  $\sigma_{\text{eff}} = 14.5$  mb is taken from Refs. [110,111].

To evaluate the contribution of  $J/\psi$  pair with both  $J/\psi$  from  $b$ , a simulated sample at the generation level is produced for it. The number of remaining candidates after all the selections is calculated with an event-by-event efficiency multiplication, as given by

$$N = \sum_{i=1}^{N_{\text{gen}}} \varepsilon_{\text{GEC}}^i \times \varepsilon_{\text{rec\&sel}}^i(\text{two } J/\psi \text{ from } b) \times \varepsilon_{\text{muonID}}^i \times \varepsilon_{\text{trig}}^i, \quad (4-20)$$

in which  $N_{\text{gen}}$  is the number of generated candidates. As studied in the  $J/\psi$  production measurement, the efficiencies are consistent between prompt  $J/\psi$  and  $J/\psi$  from  $b$ , except for the reconstruction and selection efficiency  $\varepsilon_{\text{rec\&sel}}(\text{two } J/\psi \text{ from } b)$ . It is calculated as

$$\varepsilon_{\text{rec\&sel}}(\text{two } J/\psi \text{ from } b) = \varepsilon_{\text{rec\&sel}}^{\text{from } b}(J/\psi_1) \times \varepsilon_{\text{rec\&sel}}^{\text{from } b}(J/\psi_2). \quad (4-21)$$

The efficiency  $\varepsilon_{\text{rec\&sel}}^{\text{from } b}$  is estimated using the simulated sample of  $J/\psi$  from  $b$ . The efficiency  $\varepsilon_{\text{rec\&sel}}^{\text{from } b}$  in bins of  $J/\psi p_T$  and  $y$  is shown in Fig. 4.13. They are much smaller than the efficiencies of prompt  $J/\psi$  mainly due to the cut on  $\chi^2_{\text{DTF}}/\text{ndf}(J/\psi)$ . The yield  $N$  is normalized to the data sample with a scale factor of

$$N_{\text{norm}} = N \times \mathcal{L} \times \frac{\sigma(\text{two } J/\psi \text{ from } b) \times \mathcal{B}^2(J/\psi \rightarrow \mu^+ \mu^-)}{N_{\text{gen}}}, \quad (4-22)$$

where  $\mathcal{L}$  is the integrated luminosity of the data sample. The yield  $N_{\text{norm}}$  is determined to be 20, which accounts for  $20/1048 = 1.9\%$  of the total  $J/\psi$  pair signal. The contribution of  $J/\psi$  pair with one  $J/\psi$  from  $b$  is evaluated in the same way. The only difference is that the reconstruction and selection efficiency  $\varepsilon_{\text{rec\&sel}}(\text{one } J/\psi \text{ from } b)$  is given by

$$\varepsilon_{\text{rec\&sel}}(\text{one } J/\psi \text{ from } b) = \varepsilon_{\text{rec\&sel}}^{\text{prompt}}(J/\psi_1) \times \varepsilon_{\text{rec\&sel}}^{\text{from } b}(J/\psi_2). \quad (4-23)$$

It takes a fraction of 2.6% of the signal candidates. In summary, the from- $b$  contribution is determined to be 4.5%.

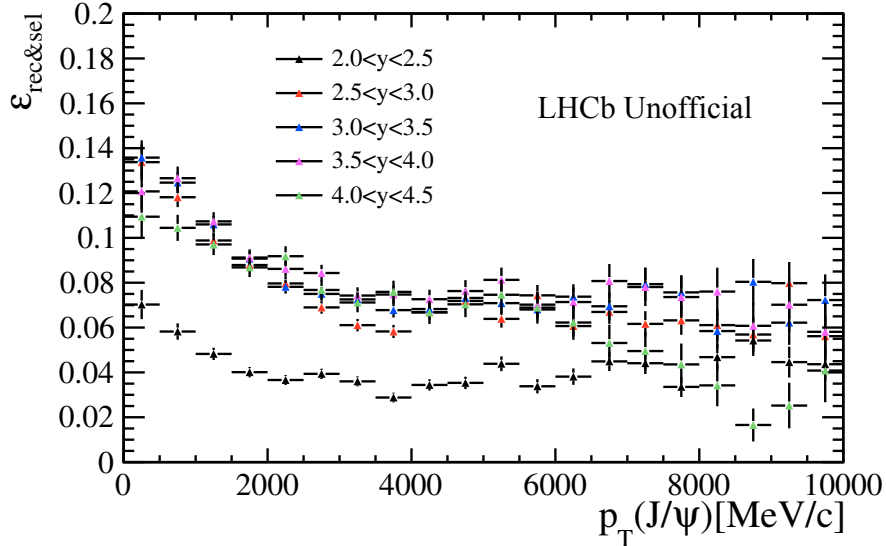


Figure 4.13 Reconstruction and selection efficiencies for  $J/\psi$  from  $b$  in bins of  $J/\psi$   $p_T$  and  $y$ .

## 4.7 Cross-section determination

The production cross-section of the  $J/\psi$  pair is determined according to Eq. 4-1, in which the integrated luminosity  $\mathcal{L}$  and the branching fraction  $\mathcal{B}(J/\psi \rightarrow \mu^+ \mu^-)$  is known. The yield  $N^{cor}$  is obtained by performing an unbinned extended maximum likelihood to the  $(M(\mu_1^+ \mu_2^-), M(\mu_2^+ \mu_1^-))$  distribution after the per-event efficiency correction. A bilinear interpolation is applied for all the efficiencies in bins of  $J/\psi$   $p_T$  and  $y$  to dilute dependence on the binning scheme. The fit model is the same with the one used for the mass fit without the efficiency correction, as given in Eq. 4-5. The projections of the 2D mass fit to  $M(\mu_1^+ \mu_1^-)$  and  $M(\mu_2^+ \mu_2^-)$  are shown in Fig. 4.14. The yield  $N^{cor}$  is determined to be  $(15.8 \pm 1.1) \times 10^3$ . After subtracting the from- $b$  component, the  $J/\psi$  pair production cross-section is determined to be  $15.2 \pm 1.0$  (stat) nb.

## 4.8 Systematic uncertainties

Several sources of systematic uncertainties are considered, as discussed in the following subsections.

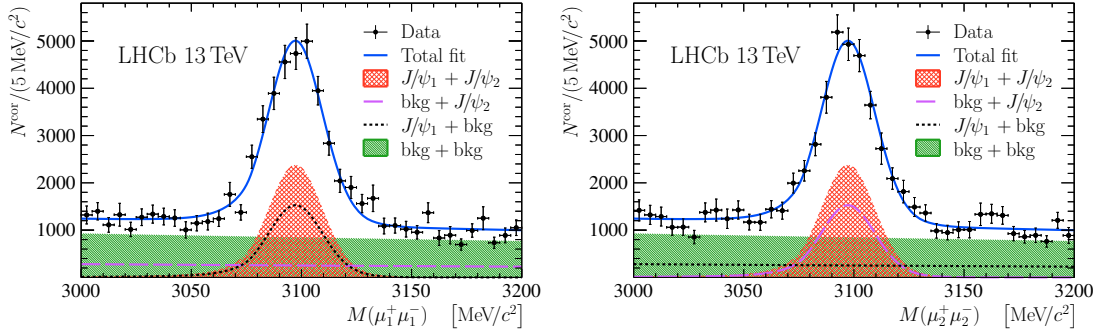


Figure 4.14 Projections of the 2D mass fit to (top)  $M(\mu_1^+, \mu_1^-)$  and (bottom)  $M(\mu_2^+, \mu_2^-)$ . The black points with error bars represent the data. The blue solid line is the total fit model. The red cross-hatched area represents the signal distribution. The black and magenta dashed lines show the background components due to the combination of a  $J/\psi$  signal with a combinatorial background. The green shaded area indicates the purely combinatorial background.

#### 4.8.1 Signal mass shape

To study the systematic uncertainty caused by the imperfect modelling of the signal mass shape, two alternative models are applied instead of the sum of the DSCB and Gaussian functions:

- The Hypatia function<sup>[103]</sup> with the tail parameters determined from the simulation. The difference of the signal yield to the nominal result is 1.6%.
- The dimuon invariant mass distribution extracted from the simulation using kernel estimation<sup>[112]</sup>. It is convolved with a Gaussian function considering the difference between the data and the simulation. The signal yield obtained from this fit varies by 1.3% from the nominal result.

The larger deviation, 1.6%, is taken to be the systematic uncertainty due to the signal shape modelling.

#### 4.8.2 Global event cut efficiency

When the parameters of the  $\Gamma$  function used to fit the nSPDHits distribution are varied within their uncertainties, the efficiency  $\varepsilon_{\text{GEC}}$  changes by  $+0.2(-0.1)$ , which is negligibly small. As a cross check, the nSPDHits distribution is modelled with the sum of two  $\Gamma$  functions as an alternative, as shown in Fig. 4.15. The extrapolation of this fit model gives a  $\varepsilon_{\text{GEC}}$  value of 99.9%. It is well consistent with the nominal result. Therefore, the systematic uncertainty introduced by the global event cut efficiency is safely neglected.

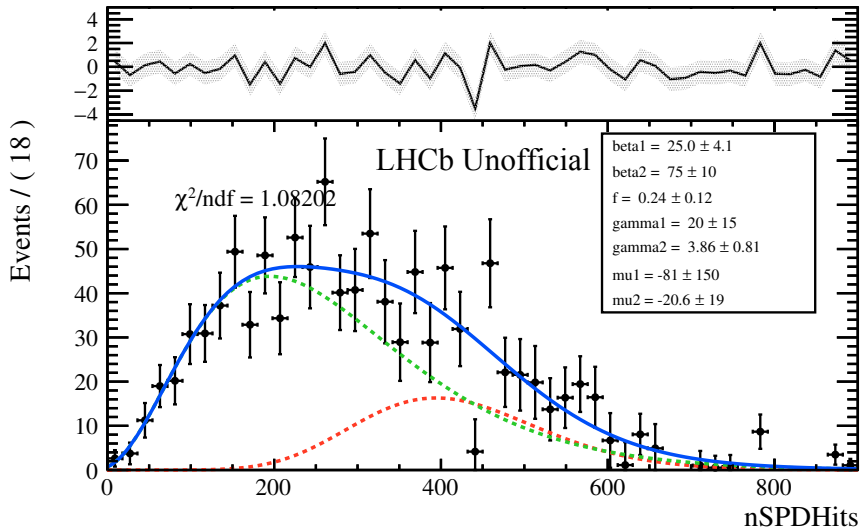


Figure 4.15 Fit to the nSPDHits distribution of the  $J/\psi$  pair signal with the sum of two  $\Gamma$  functions.

#### 4.8.3 Statistical uncertainty of the simulation

The limited statistic of the simulated sample can lead to a systematic uncertainty of the efficiencies. It is evaluated using pseudoexperiments, in which the efficiency terms  $\varepsilon_{\text{acc}}(p_{\text{T}}, y)$ ,  $\varepsilon_{\text{rec\&sel}}(p_{\text{T}}, y)$  and  $\varepsilon_{\text{trig}}(p_{\text{T}}, y)$  are varied within their uncertainties. The resulting signal yields obtained from the pseudoexperiments follow a Gaussian distribution, with a mean value consistent with the nominal result. The systematic uncertainty is calculated as the ratio of the Gaussian width to the nominal signal yield, which is 0.2%.

#### 4.8.4 Track detection efficiency

The systematic uncertainty from the track detection efficiency is determined similar to that in the  $J/\psi$  production measurement. The statistical uncertainty propagated from the limited size of the calibration sample is evaluated using pseudoexperiments, and is determined to be 0.1%. The uncertainty due to the choice of the event multiplicity variable is 0.8% per muon track. The quadratic sum of the two sources, 3.2%, is taken as the uncertainty.

#### 4.8.5 MuonID efficiency

The determination of the systematic uncertainty of the muonID efficiency is also similar to the that in the  $J/\psi$  production measurement. The uncertainty due to the

statistical uncertainty of the calibration sample is studied with pseudoexperiments, which turns out negligible. The uncertainty originating from the binning of the single muonID efficiency table is estimated with varied binning schemes. The largest deviation to the nominal result is 1.7%. The difference in the event multiplicity distribution between the data and the calibration sample can also introduce uncertainty. The single muonID efficiency is recalculated after weighting the nTracks distribution in the calibration sample to that in the data sample. With the updated single muonID efficiency, the result changes by 1.5%. The total uncertainty of the muonID efficiency is determined as the quadratic sum of the three sources, which is 2.3%.

#### 4.8.6 Trigger efficiency

The trigger efficiency uncertainty due to the imperfect simulation of the trigger is estimated by comparing the efficiencies determined from the data and the simulation using the TISTOS method. In the TISTOS approach, The efficiency  $\varepsilon_{L0\&HLT1}(J/\psi)$  is calculated as

$$\varepsilon_{L0\&HLT1}(J/\psi) = \frac{J/\psi \text{ selected and triggered by HLT2 and L0\_TIS\&L0\_TOS\&HLT1\_TIS\&HLT1\_TOS}}{J/\psi \text{ selected and triggered by HLT2 and L0\_TIS\&HLT1\_TIS}}. \quad (4-24)$$

The efficiency  $\varepsilon_{L0\&HLT1}(J/\psi)$  in the  $J/\psi$  kinematic bins is shown in Fig. 4.16 for both the data and the simulation. They are in good agreement with each other. The TISTOS efficiencies from the data and the simulation are used for the efficiency correction independently. The difference between the resulting signal yields is 1.0%. It is taken to be the uncertainty of the trigger efficiency.

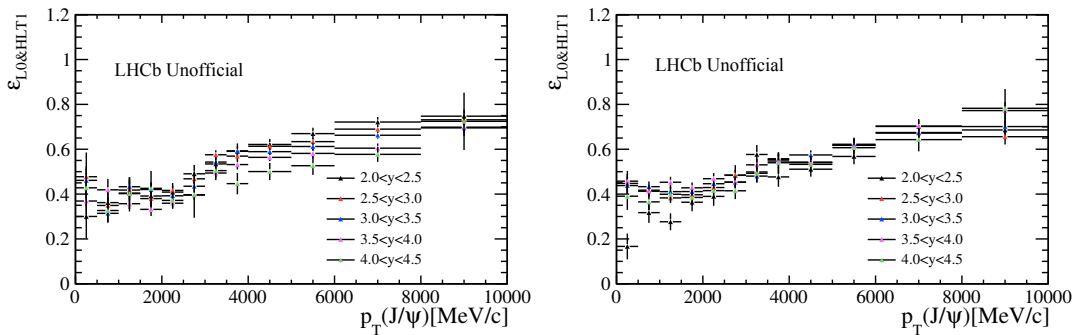


Figure 4.16 Efficiency  $\varepsilon_{L0\&HLT1}(J/\psi)$  in bins of  $J/\psi$   $p_T$  and  $y$  estimated using the TISTOS method with the (left) data and (right) simulated samples, respectively.

#### 4.8.7 From- $b$ component

In the determination of the from- $b$  contribution, both  $\sigma(\text{two } J/\psi \text{ from } b)$  and  $\sigma(\text{one } J/\psi \text{ from } b)$  have an uncertainty at the level of around 10%. The finite statistic of the generation level simulated sample is also a source of uncertainty. As the total fraction of the from- $b$  component is 4.5%, a systematic uncertainty of 1.0% is assigned for the from- $b$  contribution.

#### 4.8.8 $\chi^2_{\text{DTF}}/\text{ndf}(J/\psi)$ cut efficiency

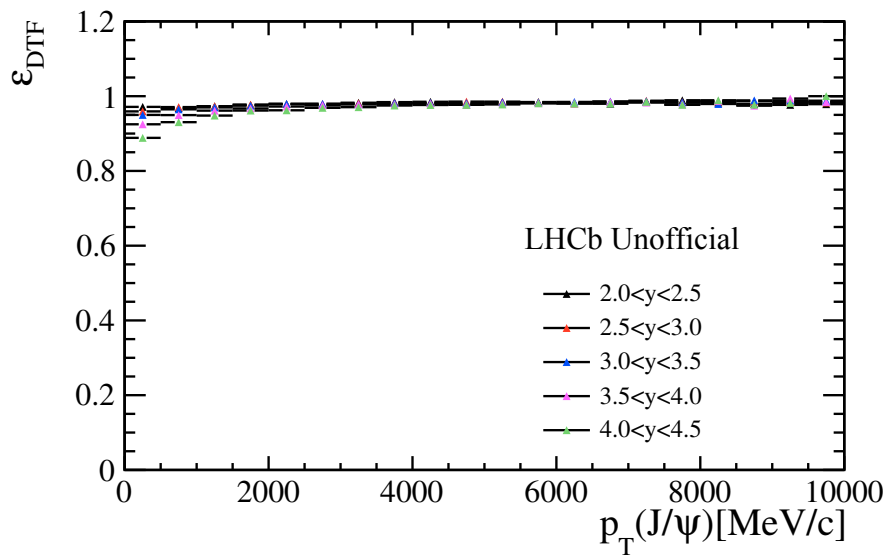
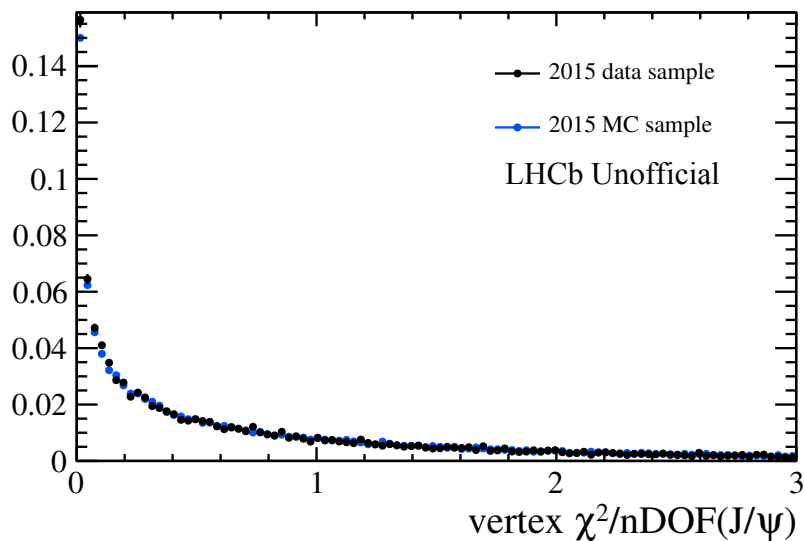
Among all the offline selections, the systematic uncertainties of the track reconstruction efficiency and the muonID efficiency are already considered separately. With the bilinear interpolation of the efficiencies in bins of  $J/\psi$   $p_{\text{T}}$  and  $y$ , the potential uncertainty from the  $J/\psi$   $p_{\text{T}}$  and  $y$  spectrum is reduced to a negligible level. The remaining uncertainty source is the difference between the  $\chi^2_{\text{DTF}}/\text{ndf}(J/\psi)$  distribution in the data and the simulation. The efficiency of the  $\chi^2_{\text{DTF}}/\text{ndf} < 5.0$  cut, defined as

$$\varepsilon_{\text{DTF}} \equiv \frac{J/\psi \text{ reconstructed and selected w/o muonID}}{J/\psi \text{ reconstructed and selected w/o DTF cut and muonID}} \quad (4-25)$$

is shown in Fig. 4.17. The efficiency  $\varepsilon_{\text{DTF}}$  is close to 100% across the whole kinematic region, so the systematic uncertainty introduced by it should be small. As a further check, the distribution of  $\chi^2_{\text{vertex}}/\text{ndf}$ , which is determined with the same track information as  $\chi^2_{\text{DTF}}/\text{ndf}$ , is compared between the data and the simulation as shown in Fig. 4.18. The comparison shows a good consistency between them. In the end, a conservative uncertainty of 1.0% is taken for the  $\chi^2_{\text{DTF}}/\text{ndf}(J/\psi)$  cut efficiency.

### 4.9 Polarisation scenario

The detection efficiency of the  $J/\psi$  pair candidates can be affected by the polarisation, but there is no experimental result for the polarisation of  $J/\psi$  pair yet. For the DPS process, the polarisation of  $J/\psi$  mesons in  $J/\psi$  pairs should be the same as that of the single prompt  $J/\psi$ . So far, all the LHC analyses indicate a small polarisation for the quarkonia<sup>[41–44]</sup>. For the SPS process, it is possible that the two  $J/\psi$  mesons have opposite correlated polarisations, in which case the polarisation effect can be partially cancelled. Therefore, the same as the  $J/\psi$  production measurement, the  $J/\psi$  pair production measurement is performed under the assumption that the  $J/\psi$  mesons are unpolarised, and no systematic


 Figure 4.17 The efficiency  $\varepsilon_{\text{DTF}}$  in bins of  $J/\psi$   $p_T$  and  $y$  for prompt  $J/\psi$ .

 Figure 4.18 Normalised distributions of  $\chi^2_{\text{vertex}}/\text{ndf}$  in the data and simulated samples.

uncertainty is assigned for the polarisation assumption. To give a quantified idea of the effect of the  $J/\psi$  polarisation on the result, a polarisation of  $\pm 20\%$  is introduced for both  $J/\psi$  mesons. With the polarisation of  $-20\% (+20\%)$ , the measured  $J/\psi$  pair production cross-section changes by  $-6.8\% (+6.5\%)$ .

#### 4.9.1 Other systematic uncertainties

There are several other sources of systematic uncertainties:

- The uncertainty introduced by  $\mathcal{B}(J/\psi \rightarrow \mu^+ \mu^-) = (5.961 \pm 0.033)\%$ <sup>[97]</sup>, which is 1.1%.
- The systematic uncertainty of the luminosity, which is 3.9%.

#### 4.9.2 Summary

All the systematic uncertainties on the  $J/\psi$  pair production cross-section are summarised in Table 6.4. The total systematic uncertainty, 6.1%, is the quadratic sum of all the sources.

Table 4.3 Summary of the systematics uncertainties on the  $J/\psi$  pair production cross-section.

Component	Uncertainty(%)
Signal mass shape	1.6
Global event cut efficiency	negligible
Simulation statistic	0.2
Track reconstruction efficiency	3.2
MuonID efficiency	2.3
Trigger efficiency	1.0
$\chi^2_{\text{DTF}}/\text{ndf}(J/\psi)$ cut	1.0
From- $b$ component	1.0
$\mathcal{B}(J/\psi \rightarrow \mu^+ \mu^-)$	1.1
Luminosity	3.9
Total	6.1

## 4.10 Results

### 4.10.1 Total production cross-section

The  $J/\psi$  pair production cross-section with both  $J/\psi$  mesons in the kinematic range of  $2.0 < y < 4.5$  and  $p_T < 10$  GeV/ $c$  is measured to be

$$\sigma(J/\psi J/\psi) = 15.2 \pm 1.0 \text{ (stat)} \pm 0.9 \text{ (syst)} \text{ nb},$$

assuming zero polarisation of the  $J/\psi$  mesons. The production cross-section ratio between  $J/\psi$  pair and single prompt  $J/\psi$  is calculated as

$$\frac{\sigma(J/\psi J/\psi)}{\sigma(J/\psi)} = (10.2 \pm 0.7 \text{ (stat)} \pm 0.9 \text{ (syst)}) \times 10^{-4}, \quad (4-26)$$

in which the prompt  $J/\psi$  production cross-section is extracted from the same kinematic range of  $2.0 < y < 4.5$  and  $p_T < 10$  GeV/ $c$  as  $\sigma(J/\psi) = 14.94 \pm 0.02 \text{ (stat)} \pm 0.91 \text{ (syst)} \mu\text{b}$ <sup>[113]</sup>. The systematic uncertainties on  $\sigma(J/\psi J/\psi)$  and  $\sigma(J/\psi)$  are taken as uncorrelated. According to Eq. 1-36, the minimum possible value of the effective cross-section  $\sigma_{\text{eff}}$  can be calculated as

$$\frac{1}{2} \frac{\sigma(J/\psi)^2}{\sigma(J/\psi J/\psi)} = 7.3 \pm 0.5 \text{ (stat)} \pm 1.0 \text{ (syst)} \text{ mb}, \quad (4-27)$$

in which all the  $J/\psi$  pairs are assumed to come from the DPS process.

The  $J/\psi$  pair production cross-section is compared to the DPS prediction and several theoretical calculations for the SPS mechanism, as summarised in Table 4.4. The DPS contribution is calculated with the prompt  $J/\psi$  production cross-section<sup>[113]</sup> according to Eq. 1-36, where  $\sigma_{\text{eff}} = 14.5 \pm 1.7^{+1.7}_{-2.3} \text{ mb}$  is taken from Refs. [110,114].

Theoretical predictions for  $J/\psi$  pair production via the SPS mechanism are implemented in the following approaches within the NRQCD framework:

- **LO CS:** leading-order colour-singlet model<sup>[115]</sup>. CT 14 PDFs<sup>[116]</sup> are used to model the gluon densities.
- **NLO\* CS':** incomplete next-to-leading-order colour-singlet model, in which the loop diagrams are not included<sup>[115]</sup>. The same as LO CS, the gluon densities are taken as CT 14 PDFs<sup>[116]</sup>. Since the incomplete NLO CS calculations can't converge at low  $p_T$  of the  $J/\psi$  pair, a cut off is applied on  $p_T(J/\psi J/\psi)$ <sup>[115]</sup>, which leads to the

three sets of production cross-sections for different  $p_T(J/\psi J/\psi)$  ranges as shown in Table. 4.4. This prediction includes the tiny contribution from  $J/\psi + \chi_c$  via the  $\chi_c \rightarrow J/\psi \gamma$  decay.

- **NLO\* CS''**: incomplete next-to-leading-order colour-singlet model, in which the loop diagrams are not included<sup>[47,117–120]</sup>. The gluon densities are taken to be NNPDF 3.0 NLO PDFs with  $\alpha_s(M_Z) = 0.118$ <sup>[121]</sup>. To cope with the divergence at small  $p_T(J/\psi J/\psi)$ , a cut is applied on the mass of any light parton pair<sup>[47,117–120]</sup>. Two Gaussian smearings are applied to the initial transverse momentum carried by the gluon ( $k_T$ ), with the widths of  $\langle k_T \rangle = 0.5$  and  $2$  GeV/ $c$ , respectively. The total production cross-section is independent of the  $k_T$  smearing, while some differential cross-sections depend significantly on it. This calculation includes the  $\psi(2S)$  feed-down contribution.
- **LO CO**: leading-order colour-octet calculations<sup>[119,120]</sup>. Like in NLO\* CS'', NNPDF 3.0 NLO PDFs with  $\alpha_s(M_Z) = 0.118$ <sup>[121]</sup> is used to describe the gluon densities. The LDMEs are taken from Refs. [22,122–128]. The same Gaussian smearing as in NLO\* CS'' is applied. The feed-downs from both the  $J/\psi + \psi(2S)$  and  $J/\psi + \chi_c$  productions are considered.
- **NLO CS**: complete next-to-leading-order colour-singlet model<sup>[46]</sup>. The gluon densities are modelled with CTEQ6L1 and CTEQ6M PDFs<sup>[129,130]</sup>.
- **LO  $k_T$** : a model based on the  $k_T$ -factorization approach<sup>[131–135]</sup> with LDMEs of the LO CS model<sup>[136,137]</sup>. It takes the gluon densities from Refs. [138–142]. The feed-down from  $\psi(2S)$  is taken into account.

The predicted production cross-sections are sensitive to the choice of PDFs for the gluon densities and the factorization and renormalisation scales. The uncertainties on the predictions due to the gluon densities are determined by using the CTEQ6 PDF set<sup>[143]</sup> instead of the nominal PDFs. For NLO CS, which uses CTEQ6L1 and CTEQ6M PDFs<sup>[129,130]</sup>, this uncertainty is omitted. The uncertainties from the factorization and renormalisation scales are evaluated by varying the scales by a factor of two. For LO CO, the calculation is also dependent on the choice of the LDMEs. The production cross-section varies from the maximal 0.7 nb, calculated with the LDMEs from Ref. [126] to the minimal 0.11 nb, using the LDMEs from Ref. [122], while the majority are around 0.5 nb.

According to the comparison, the LO CO contribution is predicted to be small. De-

Table 4.4 Comparison between the measured and predicted  $J/\psi$  pair production cross-section for different  $p_T(J/\psi J/\psi)$  ranges. For the SPS predictions, the first uncertainty is due to the choice of PDFs for the gluon densities, and the second corresponds to the variation of the factorization and renormalisation scales. For LO CS, the third uncertainty accounts for the choice of the LDMEs. For the NLO CS prediction, the uncertainty is due to the variation of the factorization and renormalisation scales. For the DPS prediction, the first uncertainty comes from the prompt  $J/\psi$  production cross-section measurement<sup>[113]</sup>, and the second corresponds to the uncertainty of  $\sigma_{\text{eff}}$ <sup>[110,114]</sup>.

	$\sigma(J/\psi J/\psi)$ [nb]		
	no $p_T$ cut	$p_T > 1$ GeV/c	$p_T > 3$ GeV/c
LO CS <sup>[115]</sup>	$1.3 \pm 0.1^{+3.2}_{-0.1}$	—	—
LO CO <sup>[119,120]</sup>	$0.45 \pm 0.09^{+1.42+0.25}_{-0.36-0.34}$	—	—
LO $k_T$ <sup>[136]</sup>	$6.3^{+3.8+3.8}_{-1.6-2.6}$	$5.7^{+3.4+3.2}_{-1.5-2.1}$	$2.7^{+1.6+1.6}_{-0.7-1.0}$
NLO* CS' <sup>[115]</sup>	—	$4.3 \pm 0.1^{+9.9}_{-0.9}$	$1.6 \pm 0.1^{+3.3}_{-0.3}$
NLO* CS'' <sup>[47,117-120]</sup>	$15.4 \pm 2.2^{+51}_{-12}$	$14.8 \pm 1.7^{+53}_{-12}$	$6.8 \pm 0.6^{+22}_{-5}$
NLO CS <sup>[46]</sup>	$11.9^{+4.6}_{-3.2}$	—	—
DPS <sup>[110,113,114]</sup>	$8.1 \pm 0.9^{+1.6}_{-1.3}$	$7.5 \pm 0.8^{+1.5}_{-1.2}$	$4.9 \pm 0.5^{+1.0}_{-0.8}$
Data	$15.2 \pm 1.0 \pm 0.9$	$13.5 \pm 0.9 \pm 0.9$	$8.3 \pm 0.6 \pm 0.5$

spite the large uncertainty, the LO  $k_T$ , LO CS and NLO\* CS' models require an additional DPS contribution to describe the data. The NLO\* CS'' and NLO CS predictions are consistent with the measurement by itself.

#### 4.10.2 Differential production cross-sections

The  $J/\psi$  pair candidates produced from the SPS and DPS processes are expected to have distinct kinematics due to the different production mechanisms. To distinguish the SPS and DPS contributions, the differential production cross-sections of  $J/\psi$  pair as functions of the following kinematic variables are measured and compared to the theoretical predictions:

- $p_T(J/\psi J/\psi)$ : transverse momentum of the  $J/\psi$  pair;
- $y(J/\psi J/\psi)$ : rapidity of the  $J/\psi$  pair;
- $p_T(J/\psi)$ : transverse momentum of either  $J/\psi$  meson;
- $y(J/\psi)$ : rapidity of either  $J/\psi$  meson;

- $|\Delta y|$ : absolute value of the rapidity difference between the two  $J/\psi$  mesons;
- $|\Delta\phi|$ : absolute value of the difference in azimuthal angle between the two  $J/\psi$  mesons;
- $m(J/\psi J/\psi)$ : invariant mass of the  $J/\psi$  pair;
- $\mathcal{A}_T$ : the transverse momentum asymmetry of the two  $J/\psi$  mesons, which is defined as

$$\mathcal{A}_T \equiv \left| \frac{p_T(J/\psi_1) - p_T(J/\psi_2)}{p_T(J/\psi_1) + p_T(J/\psi_2)} \right|.$$

The differential production cross-section of  $J/\psi$  pair as a function of a specific variable  $v$  is calculated as

$$\frac{d\sigma(J/\psi J/\psi)}{dv} = \frac{1}{\mathcal{L} \times \mathcal{B}(J/\psi \rightarrow \mu^+ \mu^-)^2} \times \frac{\Delta N_i^{\text{cor}}}{\Delta v_i},$$

where  $\Delta N_i^{\text{cor}}$  is the signal yield in the  $i$ -th bin after the efficiency correction, and  $\Delta v_i$  is the bin width of the variable  $v$ . The systematic uncertainties of the luminosity and  $\mathcal{B}(J/\psi \rightarrow \mu^+ \mu^-)$  are equal and 100% correlated in all bins. The uncertainties due to the muonID efficiency and the track reconstruction efficiency are significantly correlated across the kinematic bins. In the comparison to the theories, the systematic uncertainties are neglected as they are negligibly small compared to the statistical ones and almost fully correlated.

The DPS predictions are made with pseudoexperiments, in which  $J/\psi$  mesons evenly distributed across the azimuthal angle  $\phi$  are generated according to the measured double differential production cross-sections of single prompt  $J/\psi$  as functions of  $J/\psi$   $p_T$  and  $y$ <sup>[113]</sup>, and randomly associated as pairs. For the SPS calculations, the differential cross-sections are stable against the gluon densities, the factorization and renormalisation scales, and the LDMEs, which significantly affect the total production cross-section. On the contrary, the Gaussian smearing applied to LO CO and NLO\* CS'' significantly affects some differential cross-sections. As a result, the uncertainties of the predicted differential cross-sections are not shown. The LO CO and NLO\* CS'' predictions with the  $\langle k_T \rangle = 0.5$  and 2 GeV Gaussian smearings are both given. The comparison of the differential  $J/\psi$  pair production cross-sections between the measurements and the theories are shown in Figs. 4.19, 4.20 and 4.21 for the whole  $p_T(J/\psi J/\psi)$  range, in Figs. 4.22 and 4.23 for the  $p_T(J/\psi J/\psi) > 1$  GeV/c range, and in Figs. 4.24 and 4.25 for the  $p_T(J/\psi J/\psi) > 3$  GeV/c

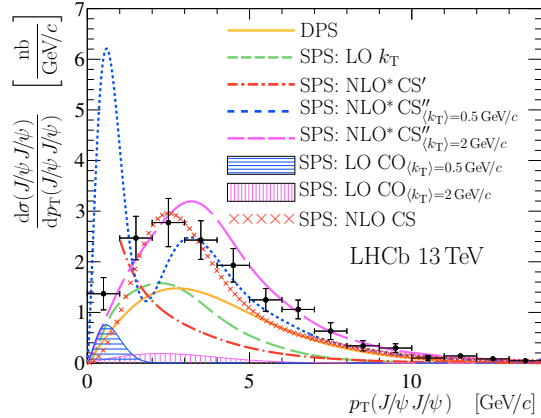


Figure 4.19 Comparisons of the measured  $J/\psi$  pair differential cross-sections in bins of  $p_T(J/\psi J/\psi)$  to the theoretical predictions. The black points with error bars are the measurements.

range.

In the LO CS model, the variables  $p_T(J/\psi J/\psi)$ ,  $|\Delta\phi|$  and  $\mathcal{A}_T$  are predicted to cluster around zero,  $\pi$  and zero, respectively. These distributions are trivial, thus omitted. In the NLO\* CS'' approach, the Gaussian smearing of  $\langle k_T \rangle = 2$  GeV is favoured against 0.5 GeV to get rid of the peaking structures in the  $p_T(J/\psi J/\psi)$  distribution, as presented in Fig. 4.19. According to the  $|\Delta y|$  and  $m(J/\psi J/\psi)$  distributions in Fig. 4.21, the DPS component is essential to describe the measurements, as there is typically no SPS contribution in the  $|\Delta y| > 1.5$  and  $m(J/\psi J/\psi) > 11$   $\text{GeV}/c^2$  regions. On the other hand, the DPS model is not able to describe the differential distributions satisfactorily by itself. The comparisons indicate that there are both SPS and DPS contributions in the  $J/\psi$  pair production.

#### 4.10.3 Separation of the SPS and DPS components

To distinguish the SPS and DPS components, the differential cross-sections are fitted with the templated SPS plus DPS model

$$\frac{d\sigma}{dv} = \sigma_{\text{DPS}} F_{\text{DPS}}(v) + \sigma_{\text{SPS}} F_{\text{SPS}}(v), \quad (4-28)$$

where  $v$  is the kinematic variable;  $F_{\text{DPS}}$  and  $F_{\text{SPS}}$  are the DPS and SPS templates fixed from the theoretical calculations;  $\sigma_{\text{DPS}}$  and  $\sigma_{\text{SPS}}$  are the total cross-sections of the DPS and SPS components, and are left free in the fit. The fraction of the DPS component is

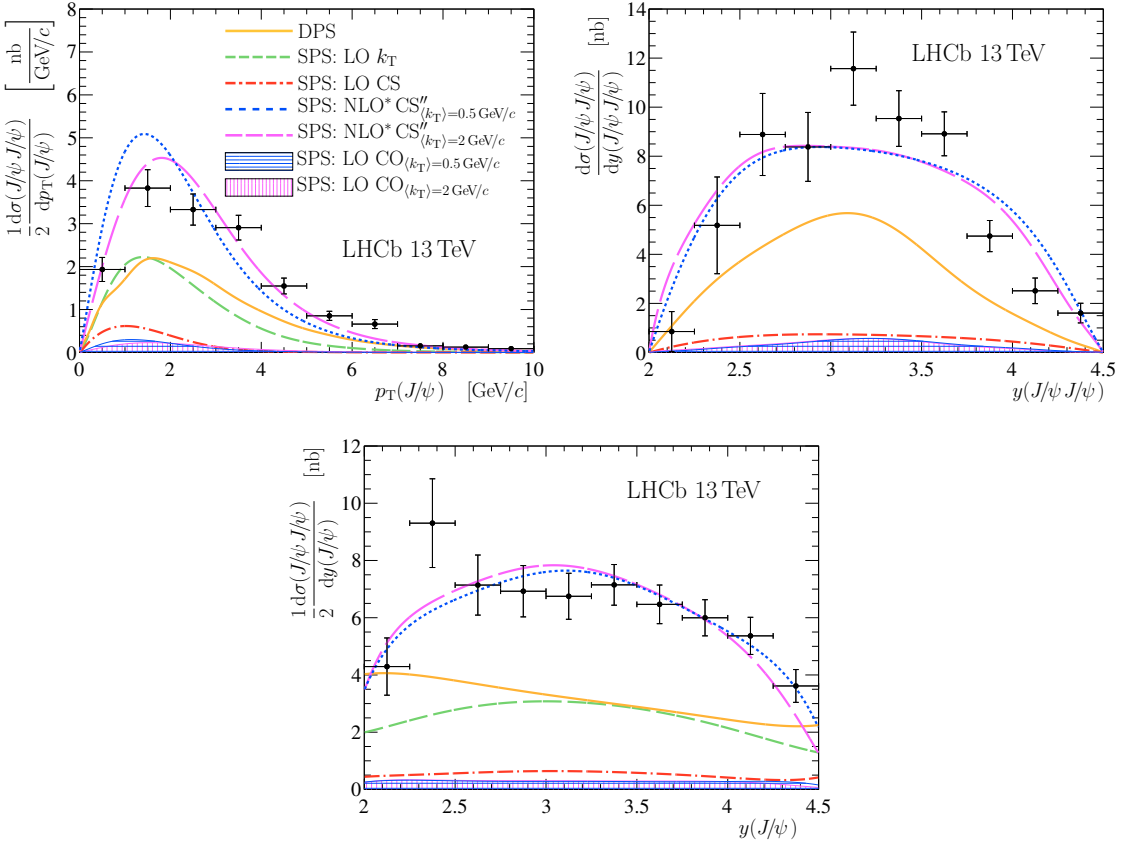


Figure 4.20 Comparisons of the measured  $J/\psi$  pair differential cross-sections in bins of (top left)  $p_T(J/\psi)$ , (top right)  $y(J/\psi J/\psi)$  and (bottom)  $y(J/\psi)$  to the theoretical predictions. The black points with error bars are the measurements.

defined as

$$f_{\text{DPS}} \equiv \frac{\sigma_{\text{DPS}}}{\sigma_{\text{SPS}} + \sigma_{\text{DPS}}}. \quad (4-29)$$

The distributions with little discriminating power are omitted from the templated fits. The LO CO contribution is calculated to be small, thus not included in the fit. The DPS fractions determined from the templated fits are summarised in Table 4.5. The fit results are given in Appendix A. The fits with all the given SPS models indicate a large contribution from the DPS process. The SPS production cross-section  $\sigma_{\text{SPS}}$ , calculated as  $(1 - f_{\text{DPS}}) \times \sigma(J/\psi J/\psi)$ , undershoots the predictions of the NLO\*  $CS''$ <sup>[47,117-120]</sup> and NLO CS<sup>[46]</sup> models, and is roughly consistent with the NLO\*  $CS'$ <sup>[115]</sup> and LO  $k_T$ <sup>[136]</sup> expectations.

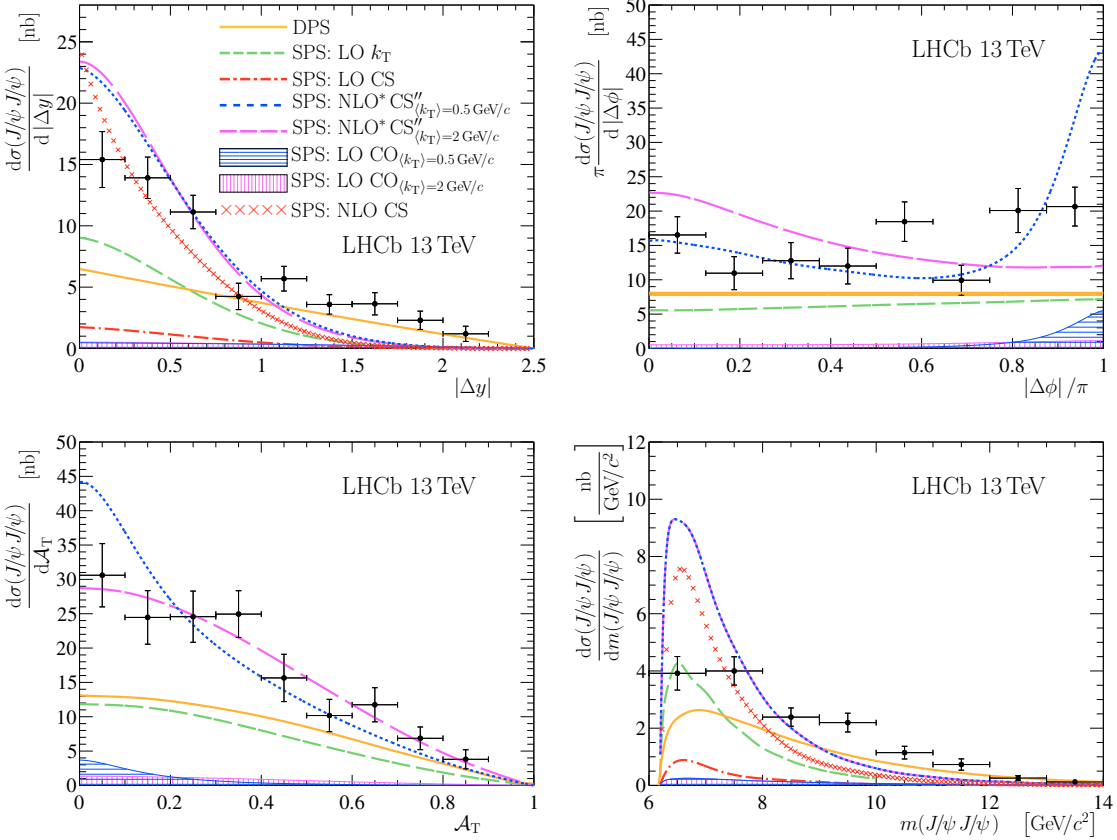


Figure 4.21 Comparisons of the measured  $J/\psi$  pair differential cross-sections in bins of (top left)  $|\Delta y|$ , (top right)  $|\Delta\phi|$ , (bottom left)  $\mathcal{A}_T$  and (bottom right)  $m(J/\psi J/\psi)$  to the theoretical predictions. The black points with error bars are the measurements.

According to Eq. 4-28, the effective cross-section  $\sigma_{\text{eff}}$  is determined from  $\sigma_{\text{DPS}}$  as

$$\sigma_{\text{eff}} = \frac{1}{2} \frac{\sigma(J/\psi)^2}{\sigma_{\text{DPS}}}. \quad (4-30)$$

The obtained  $\sigma_{\text{eff}}$  values are listed in Table 4.6. With the given SPS models, the values of  $\sigma_{\text{eff}}$  are found to be between 8.8 and 12.5 mb. Compared to the effective cross-sections measured by the previous experiments as shown in Fig. 1.13, the values measured in this analysis are smaller than the majority, including the  $J/\psi + cc$  and  $\Upsilon(1S) + D^{0+}$  measurements performed at LHCb, which give  $\sigma_{\text{eff}} \sim 15$  mb and  $\sigma_{\text{eff}} = 18.0 \pm 1.8$  mb, respectively. On the other hand, they slightly exceed the measurements of  $J/\psi$  pair production in the central rapidity region at LHC,  $\sigma_{\text{eff}} = 8.2 \pm 2.2$  mb<sup>[47]</sup> and  $\sigma_{\text{eff}} = 6.3 \pm 1.9$  mb<sup>[144]</sup>, and they are significantly larger than the D0 measurements of the  $J/\psi$  pair production,  $\sigma_{\text{eff}} = 4.8 \pm 2.5$  mb<sup>[145]</sup>, and the  $\Upsilon + J/\psi$  production,  $\sigma_{\text{eff}} = 2.2 \pm 1.1$  mb<sup>[146]</sup>.

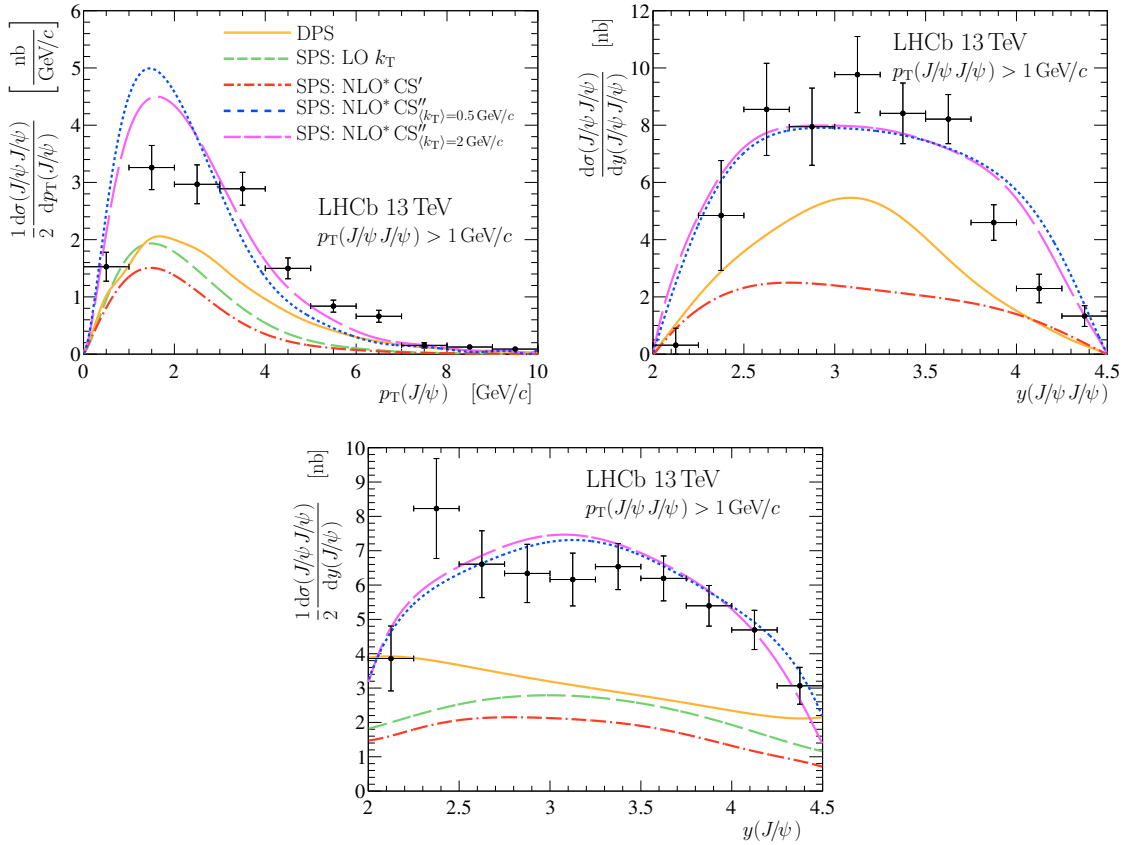


Figure 4.22 Comparisons of the measured differential cross-sections in bins of (top left)  $p_T(J/\psi)$ , (top right)  $y(J/\psi J/\psi)$  and (bottom)  $y(J/\psi)$  for  $J/\psi$  pairs within  $p_T(J/\psi J/\psi) > 1$  GeV/c to the theoretical predictions. The black points with error bars are the measurements.

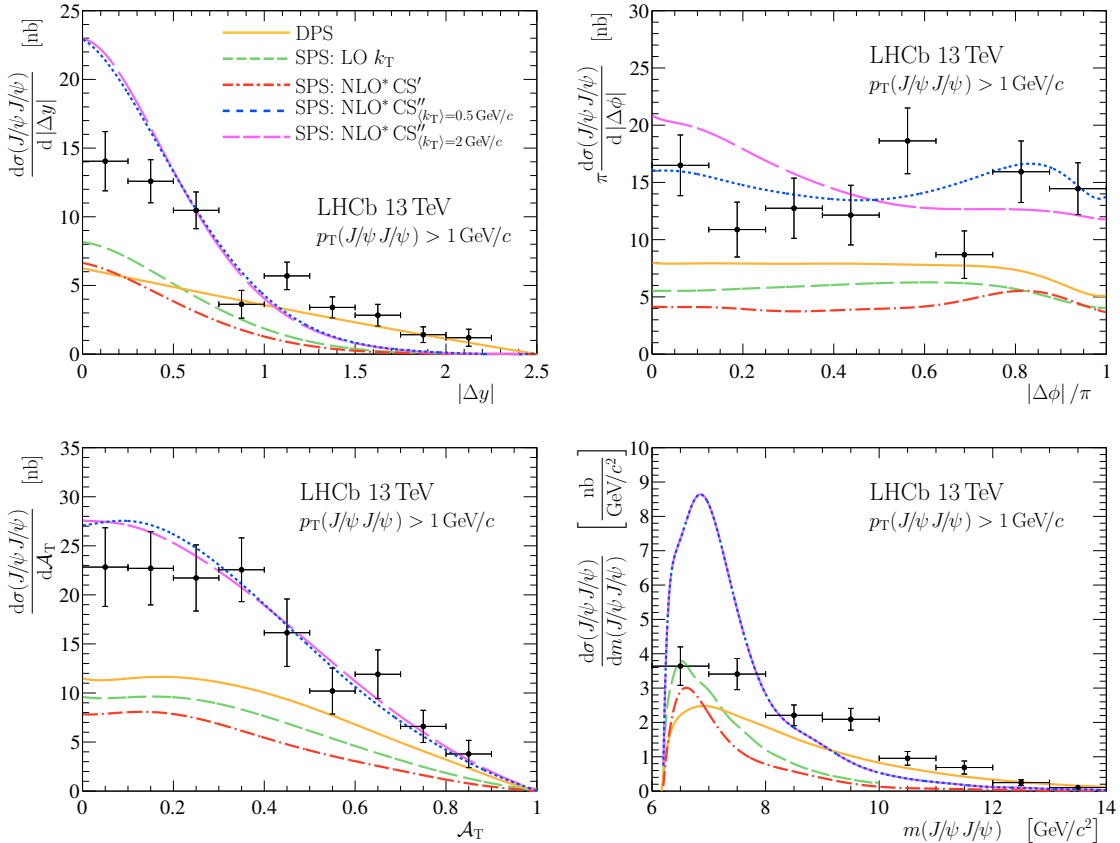


Figure 4.23 Comparisons of the measured differential cross-sections in bins of (top left)  $|\Delta y|$ , (top right)  $|\Delta\phi|$ , (bottom left)  $A_T$  and (bottom right)  $m(J/\psi J/\psi)$  for  $J/\psi$  pairs within  $p_T(J/\psi J/\psi) > 1$  GeV/c to the theoretical predictions. The black points with error bars are the measurements.

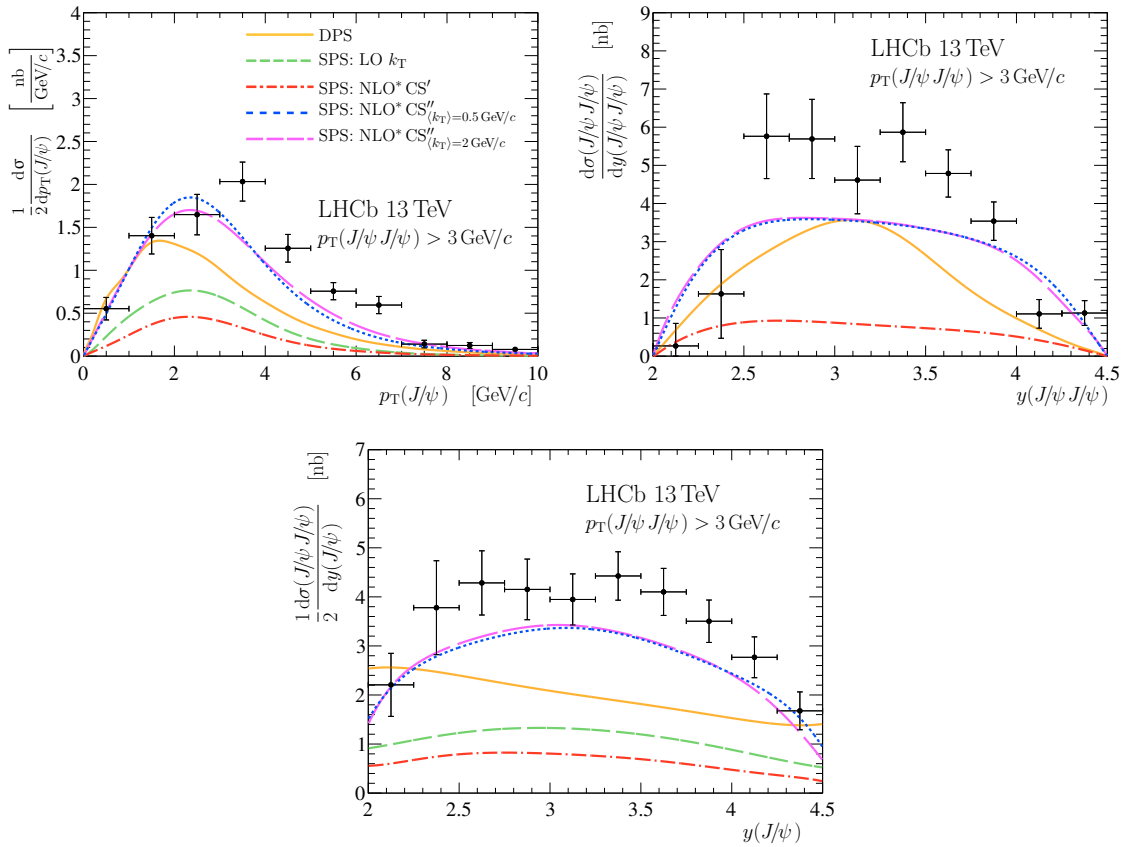


Figure 4.24 Comparisons of the measured differential cross-sections in bins of (top left)  $p_T(J/\psi)$ , (top right)  $y(J/\psi J/\psi)$  and (bottom)  $y(J/\psi)$  for  $J/\psi$  pairs within  $p_T(J/\psi J/\psi) > 3 \text{ GeV}/c$  to the theoretical predictions. The black points with error bars are the measurements.

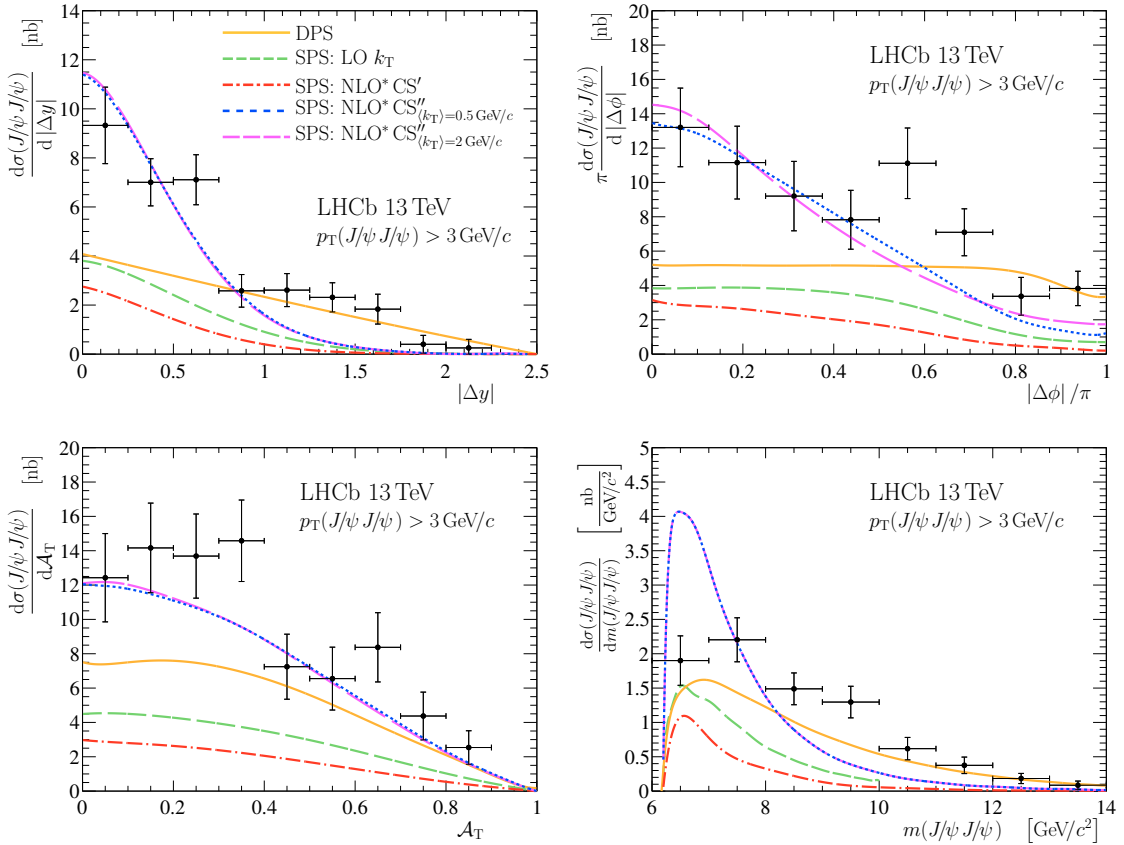


Figure 4.25 Comparisons of the measured differential cross-sections in bins of (top left)  $|\Delta y|$ , (top right)  $|\Delta\phi|$ , (bottom left)  $A_T$  and (bottom right)  $m(J/\psi J/\psi)$  for  $J/\psi$  pairs within  $p_T(J/\psi J/\psi) > 3 \text{ GeV}/c$  to the theoretical predictions. The black points with error bars are the measurements.

Table 4.5 DPS fractions,  $f_{\text{DPS}}$ , in percentage, which are determined from the templated fits to the differential cross-sections with different SPS models.

Variable	LO CS	LO $k_T$	NLO* CS'	NLO* CS''		NLO CS
				$\langle k_T \rangle = 2 \text{ GeV}/c$	$\langle k_T \rangle = 0.5 \text{ GeV}/c$	
no $p_T(J/\psi J/\psi)$ cut						
$p_T(J/\psi J/\psi)$	—	$78 \pm 2$	—	$86 \pm 55$	$81 \pm 7$	—
$y(J/\psi J/\psi)$	$83 \pm 39$	—	—	$75 \pm 37$	$68 \pm 34$	—
$m(J/\psi J/\psi)$	$76 \pm 7$	$74 \pm 7$	—	$78 \pm 7$	—	$77 \pm 7$
$ \Delta y $	$59 \pm 21$	$61 \pm 18$	—	$63 \pm 18$	$61 \pm 18$	$69 \pm 16$
$p_T(J/\psi J/\psi) > 1 \text{ GeV}/c$						
$y(J/\psi J/\psi)$	—	—	$75 \pm 24$	$71 \pm 38$	$68 \pm 34$	—
$m(J/\psi J/\psi)$	—	$73 \pm 8$	$76 \pm 7$	—	$88 \pm 1$	—
$ \Delta y $	—	$57 \pm 20$	$59 \pm 19$	$60 \pm 18$	$60 \pm 19$	—
$p_T(J/\psi J/\psi) > 3 \text{ GeV}/c$						
$y(J/\psi J/\psi)$	—	—	$77 \pm 18$	$64 \pm 38$	$64 \pm 35$	—
$m(J/\psi J/\psi)$	—	$76 \pm 10$	$84 \pm 7$	—	$87 \pm 2$	—
$ \Delta y $	—	$42 \pm 25$	$53 \pm 21$	$53 \pm 21$	$53 \pm 21$	—

 Table 4.6 Summary of  $\sigma_{\text{eff}}$  (in mb) obtained from the templated SPS plus DPS fits with different SPS models. The uncertainties are the statistical uncertainties originating from  $\sigma_{\text{DPS}}$ . The systematic uncertainty of  $\sigma(J/\psi J/\psi)$  and the total uncertainty of  $\sigma(J/\psi)$  lead to another common systematic uncertainty of 12%, which is not included.

Variable	LO $k_T$	NLO* CS''		NLO CS
		$\langle k_T \rangle = 2 \text{ GeV}/c$	$\langle k_T \rangle = 0.5 \text{ GeV}/c$	
$p_T(J/\psi J/\psi)$	$9.7 \pm 0.5$	$8.8 \pm 5.6$	$9.3 \pm 1.0$	—
$y(J/\psi J/\psi)$	—	$11.9 \pm 7.5$	$10.0 \pm 5.0$	—
$m(J/\psi J/\psi)$	$10.6 \pm 1.1$	—	$10.2 \pm 1.0$	$10.4 \pm 1.0$
$ \Delta y $	$12.5 \pm 4.1$	$12.2 \pm 3.7$	$12.4 \pm 3.9$	$11.2 \pm 2.9$

## Chapter 5 Measurement of the branching fraction ratio $\mathcal{B}(B_c^+ \rightarrow \psi(2S)\pi^+)/\mathcal{B}(B_c^+ \rightarrow J/\psi\pi^+)$

The measurement of the branching fraction ratio  $\mathcal{B}(B_c^+ \rightarrow \psi(2S)\pi^+)/\mathcal{B}(B_c^+ \rightarrow J/\psi\pi^+)$  is presented in this chapter, including the analysis strategy, the dataset, the candidate selection, the determination of the signal yield, the efficiency estimation, the systematic uncertainties and the final result. The whole analysis was performed by the author.

### 5.1 Analysis strategy

The branching fraction of the  $B_c^+ \rightarrow \psi(2S)\pi^+$  decay is measured with respect to that of the  $B_c^+ \rightarrow J/\psi\pi^+$  decay, defines as

$$R \equiv \frac{\mathcal{B}(B_c^+ \rightarrow \psi(2S)\pi^+)}{\mathcal{B}(B_c^+ \rightarrow J/\psi\pi^+)}, \quad (5-1)$$

with the  $pp$  collision data collected by LHCb during the year 2011 and 2012. The  $J/\psi$  and  $\psi(2S)$  mesons are both reconstructed with muon pairs. The  $B_c^+ \rightarrow J/\psi\pi^+$  decay is taken as the control channel since it has the same final state and similar topology with the  $B_c^+ \rightarrow \psi(2S)\pi^+$  decay. The same selection criteria are applied to the two decay modes. In consequence, the detection efficiency and the corresponding systematic uncertainties can largely cancel between the two channels. The relative branching fraction  $R$  is determined by

$$R = \frac{\mathcal{B}(B_c^+ \rightarrow \psi(2S)\pi^+, \psi(2S) \rightarrow \mu^+\mu^-)}{\mathcal{B}(B_c^+ \rightarrow J/\psi\pi^+, J/\psi \rightarrow \mu^+\mu^-)} \times \frac{\mathcal{B}(J/\psi \rightarrow \mu^+\mu^-)}{\mathcal{B}(\psi(2S) \rightarrow \mu^+\mu^-)}, \quad (5-2)$$

in which the branching fractions  $\mathcal{B}(J/\psi \rightarrow \mu^+\mu^-)$  and  $\mathcal{B}(\psi(2S) \rightarrow \mu^+\mu^-)$  are known<sup>[105]</sup>. The ratio of the branching fractions with  $J/\psi$  and  $\psi(2S)$  decaying to dimuon can be calculated as

$$R_{\mathcal{B}} \equiv \frac{\mathcal{B}(B_c^+ \rightarrow \psi(2S)\pi^+, \psi(2S) \rightarrow \mu^+\mu^-)}{\mathcal{B}(B_c^+ \rightarrow J/\psi\pi^+, J/\psi \rightarrow \mu^+\mu^-)} = \frac{N(\psi(2S))/\varepsilon(\psi(2S))}{N(J/\psi)/\varepsilon(J/\psi)}, \quad (5-3)$$

where  $N(\psi(2S))$  and  $N(J/\psi)$  are the signal yields for the  $B_c^+ \rightarrow \psi(2S)(\rightarrow \mu^+\mu^-)\pi^+$  and the  $B_c^+ \rightarrow J/\psi(\rightarrow \mu^+\mu^-)\pi^+$  decay chain respectively, and  $\varepsilon(\psi(2S))$  and  $\varepsilon(J/\psi)$  the corresponding efficiencies. The signal yields and efficiencies are determined separately for data from the year 2011 and 2012. To calculate the ratio  $R_{\mathcal{B}}$ , they are combined according to

$$R_{\mathcal{B}} = \frac{\frac{N_{2011}(\psi(2S))}{\varepsilon_{2011}(\psi(2S))} + \frac{N_{2012}(\psi(2S))}{\varepsilon_{2012}(\psi(2S))}}{\frac{N_{2011}(J/\psi)}{\varepsilon_{2011}(J/\psi)} + \frac{N_{2012}(J/\psi)}{\varepsilon_{2012}(J/\psi)}}, \quad (5-4)$$

where the subscripts 2011 and 2012 denote the yield or the efficiency of the corresponding year.

## 5.2 Dataset

The measurement is performed using data collected in the year 2011 and 2012 by the LHCb detector, corresponding to an integrated luminosity of  $1\text{ fb}^{-1}$  at  $\sqrt{s} = 7\text{ TeV}$  and  $2\text{ fb}^{-1}$  at  $\sqrt{s} = 8\text{ TeV}$ , respectively. The  $B_c^+ \rightarrow \psi(2S)\pi^+$  and  $B_c^+ \rightarrow J/\psi\pi^+$  candidates are reconstructed from the same dataset, so the integrated luminosity cancel between the two channels.

The trigger requirements are common to the  $B_c^+ \rightarrow \psi(2S)\pi^+$  and  $B_c^+ \rightarrow J/\psi\pi^+$  decays, aiming at selecting high quality muons decayed from the  $\psi$  meson. The  $\psi$  meson represents both the  $J/\psi$  and  $\psi(2S)$  mesons hereafter. The trigger decisions are all TOS. The L0 trigger requires at least one muon with large  $p_{\text{T}}$ . At the HLT1 trigger stage, either a single muon with large  $p$ ,  $p_{\text{T}}$  and small  $\chi^2_{\text{track}}/\text{ndf}$  or a muon pair with an invariant mass larger than  $2700\text{ MeV}/c^2$  is required. The requirements on the  $p$ ,  $p_{\text{T}}$  and track quality of the muon pair are slightly looser than those for the single muon. The muons need to be identified as muons with the positive `isMuon` requirement. At HLT2, two muons are required to form a  $\psi$  meson detached from the PV, since the  $B_c^+$  meson has a large decay time. The  $\psi$  meson should have a good quality vertex with  $\chi^2_{\text{vertex}}/\text{ndf}(\mu^+\mu^-)$  smaller than 25, an invariant mass larger than  $2950\text{ MeV}/c^2$ , and a decay length significance (DLS) larger than 5. All the trigger lines applied and their cuts are listed in Table 5.1.

Simulated samples are generated for the  $B_c^+ \rightarrow \psi(2S)\pi^+$  and  $B_c^+ \rightarrow J/\psi\pi^+$  decays to study their behaviour. The  $B_c^+$  signals are generated with the dedicated generator

Table 5.1 Trigger lines applied and their cuts.

Trigger level	Trigger line	Cuts	
		2011	2012
L0	Muon	$p_T(\mu) > 1400 \text{ MeV}/c$	
	DiMuon	$p_T(\mu_1) > 560 \text{ MeV}/c$ $p_T(\mu_2) > 480 \text{ MeV}/c$	
Hlt1	DiMuonHighMass	$p_T(\mu) > 500 \text{ MeV}/c$ $\text{isMuon}(\mu == 1)$ $p(\mu) > 6000 \text{ MeV}/c$ $\chi_{\text{track}}^2/\text{ndf}(\mu) < 4$ $M(\mu^+\mu^-) > 2700 \text{ MeV}/c^2$	$p(\mu) > 3000 \text{ MeV}/c$ $\chi_{\text{track}}^2/\text{ndf}(\mu) < 3$
		$\text{isMuon}(\mu == 1)$ $p_T(\mu) > 1000 \text{ MeV}/c$ $p(\mu) > 8000 \text{ MeV}/c$ $\chi_{\text{track}}^2/\text{ndf}(\mu) < 2$	$p(\mu) > 3000 \text{ MeV}/c$ $\chi_{\text{track}}^2/\text{ndf}(\mu) < 2.5$
TrackAllL0		$p_T(\mu) > 1700 \text{ MeV}/c$ $p(\mu) > 10000 \text{ MeV}/c$ $\chi_{\text{track}}^2/\text{ndf}(\mu) < 2$	$p_T(\mu) > 1600 \text{ MeV}/c$ $p(\mu) > 3000 \text{ MeV}/c$
		$\chi_{\text{track}}^2/\text{ndf}(\mu) < 5$ $p_T(\mu) > 500 \text{ MeV}/c$ $\chi_{\text{vertex}}^2/\text{ndf}(\mu^+\mu^-) < 25$ $M(\mu^+\mu^-) > 2950 \text{ MeV}/c^2$ $\text{DLS}(\mu^+\mu^-) > 5$	
Hlt2	DiMuonDetachedHeavy		

BCVEGPY<sup>[91,147]</sup> through the dominant hard sub-process  $gg \rightarrow B_c^+ + b + \bar{c}$ . The fragmentation and hadronisation processes are simulated with PYTHIA<sup>[90]</sup>. The detector simulation is based on the GEANT4 package<sup>[94,100]</sup>. All the simulated events are digitized, reconstructed and selected in the same process as the real data. Approximately 6 million candidates for the  $B_c^+ \rightarrow J/\psi\pi^+$  decay and 1 million for the  $B_c^+ \rightarrow \psi(2S)\pi^+$  decay are generated with the LHCb configuration in 2011, and 8 million candidates for the  $B_c^+ \rightarrow J/\psi\pi^+$  decay and 2 million for the  $B_c^+ \rightarrow \psi(2S)\pi^+$  decay with the LHCb configuration in 2012. They were generated with a  $B_c^+$  lifetime of 452 fs according to Ref. [148]. However, the  $B_c^+$  lifetime was measured to be  $\tau(B_c^+) = 509 \pm 8 \pm 12$  fs more recently by the LHCb experiment with a better precision<sup>[149]</sup>. The simulated samples are weighted to match the new lifetime

measurement. Each candidate is assigned a weight according to

$$\text{weight} = \tau_1/\tau_2 \cdot e^{\tau/\tau_2 - \tau/\tau_1}, \quad (5-5)$$

in which  $\tau_1$  and  $\tau_2$  denote the previous and the updated  $B_c^+$  lifetime respectively, and  $\tau$  indicates the  $B_c^+$  lifetime of this candidate.

### 5.3 Candidate selection

The  $B_c^+ \rightarrow \psi\pi^+$  candidates that have fired the trigger suffer from a much larger background contamination compared to the  $J/\psi$  mesons in the production measurement. As a result, a multivariate analysis is performed after the pre-selection which only includes some simple cuts. The multivariate analysis is based on the machine learning techniques<sup>[150]</sup>. It can provide a more powerful discrimination between the signals and backgrounds by applying a non-linear multi-dimensional cut.

#### 5.3.1 Pre-selection

In the pre-selection, the two muons are required to have  $p_T$  larger than 550 MeV/ $c$ , good track quality with  $\chi^2_{\text{track}}/\text{ndf}$  smaller than 3, and `TRACK_GhostProb` smaller than 0.5 to suppress fake tracks. The two muons should form a good quality  $\psi$  vertex with  $\chi^2_{\text{vertex}}/\text{ndf}$  smaller than 20. The  $\psi$  meson is required to have a DLS larger than 3 and an invariant mass within  $\pm 100$  MeV/ $c^2$  of the known  $\psi$  mass<sup>[105]</sup>. The bachelor pion must have  $p_T$  larger than 500 MeV/ $c^2$  and  $\chi^2_{\text{track}}/\text{ndf}$  smaller than 3. It is required to be away from the PV with the  $\chi^2_{\text{IP}}$  larger than 4 to reduce combinatorial backgrounds. The `TRACK_GhostProb` of the pion should be smaller than 0.5 to remove fake tracks. The pion should be identified as a pion by requiring `ProbNN $\pi$` , which is introduced in Sec. 2.2.2.4, larger than 0.2, to suppress the contaminants from kaons and protons misidentified as pions. The  $B_c^+$  vertex is required to be of good quality with  $\chi^2_{\text{vertex}}/\text{ndf}$  smaller than 16. The invariant mass of the  $B_c^+$  meson should be within  $\pm 500$  MeV/ $c^2$  of the known  $B_c^+$  mass<sup>[105]</sup>.

#### 5.3.2 Multivariate analysis

After the pre-selection, a multivariate analysis using the boosted decision tree (BDT) method is performed<sup>[150]</sup>. In multivariate analysis, a response value, which indicates

Table 5.2 Summary of the pre-selection requirements.

$\mu^\pm$	$p_T > 550 \text{ MeV}/c$ $\chi_{\text{track}}^2/\text{ndf} < 3$ $\text{TRACK\_GhostProb} < 0.5$
$\psi$	$M \in M(\psi) \pm 100 \text{ MeV}/c^2$ $\chi_{\text{vertex}}^2/\text{ndf} < 20$ $\text{DLS} > 3$
$\pi^+$	$p_T > 500 \text{ MeV}/c$ $\chi_{\text{track}}^2/\text{ndf} < 3$ $\chi_{\text{IP}}^2 > 4$ $\text{ProbNN}\pi > 0.2$ $\text{TRACK\_GhostProb} < 0.5$
$B_c^+$	$M \in M(B_c^+) \pm 500 \text{ MeV}/c^2$ $\chi_{\text{vertex}}^2/\text{ndf} < 16$

the probability that the candidate is a signal, is evaluated for each candidate based on the values of several input variables. The evaluation of the response value is defined by training the multivariate analysis tool with signal and background samples, in which the candidates are prior classified as signals and backgrounds, respectively. BDT is a method widely used for multivariate analysis. In a decision tree, sequential left or right decisions are made for each candidate on one input variable at a time, until the candidate can be classified as a signal or a background, as presented in Fig. 5.1. In the BDT method, a forest of decision trees is constructed. The response value is determined by combining the classifications made by all the trees<sup>[150]</sup>. Boosting is a way to improve the discrimination power by repeating the training with weighted samples, for which the weights are determined according to the performance of the former decision trees. There are several algorithms used to perform the boosting. With regard to BDT, the AdaBoost algorithm<sup>[151,152]</sup> is applied. Another frequently-used algorithm is the Gradient Boost, with which the classifier is named BDTG.

Two BDT classifiers, denoted as BDT1 and BDT2 respectively, are trained in an unbiased way. The simulated and the data sample of the  $B_c^+ \rightarrow J/\psi\pi^+$  decay are both randomly split into two halves, denoted as *MC1*, *MC2*, *data1* and *data2*, respectively. The upper sideband of the  $J/\psi\pi^+$  invariant mass distribution in the range of  $M(J/\psi\pi^+) \in$

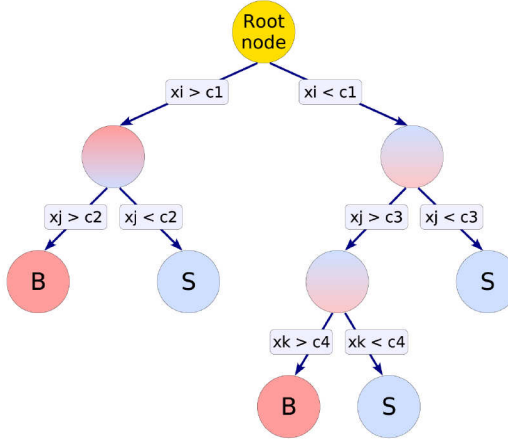


Figure 5.1 A diagram of the decision tree. Figure taken from Ref. [150].

(6346, 6444) MeV/ $c^2$  is extracted from the samples *data1* and *data2*, named *bkg1* and *bkg2* respectively. The  $J/\psi\pi^+$  invariant mass is calculated with the DTF, in which the dimuon mass is constrained to the known  $J/\psi$  mass and the  $B_c^+$  meson is required to come from the PV. The same goes to the  $\psi(2S)\pi^+$  mass. The sideband is approximately  $5 - 12\sigma_{M(J/\psi\pi^+)}$  away from the known  $B_c^+$  mass, where the mass resolution  $\sigma_{M(J/\psi\pi^+)} \sim 14$  MeV/ $c^2$  is determined from the simulation. The samples *MC1* and *bkg1* are used to train the BDT1 classifier as the signal and background sample, respectively. Similarly, the samples *MC2* and *bkg2* are used for BDT2. The BDT1 and BDT2 classifiers are applied to *data2* and *data1*, respectively. The classifiers trained with the  $B_c^+ \rightarrow J/\psi\pi^+$  decay are used for the  $B_c^+ \rightarrow \psi(2S)\pi^+$  decay as well. The BDT selection is performed independently for the datasets of 2011 and 2012.

The input variables should have distinct distributions in signal and background to give a powerful signal-background separation, and similar distributions for the  $B_c^+ \rightarrow J/\psi\pi^+$  and  $B_c^+ \rightarrow \psi(2S)\pi^+$  decays to ensure similar selection efficiencies. The following input variables are chosen:

- $\log(\chi^2_{\text{IP}})(\pi^+)$ ;
- $\chi^2_{\text{vertex}}/\text{ndf}(B_c^+)$ ;
- $\sqrt{\chi^2_{\text{IP}}}(B_c^+)$ ;
- $\sqrt{\chi^2_{\text{FD}}}(B_c^+)$  :  $\sqrt{\chi^2}$  of the flight distance (FD), which is the distance between the  $B_c^+$  decay vertex and the associated PV;
- $p_{\text{T}}(B_c^+)$ ;
- $\log(\chi^2_{\text{DTF}})$  : logarithm of the  $\chi^2_{\text{DTF}}$  obtained by the DTF with a constraint on the  $B_c^+$

candidate pointing to the PV and the mass constraint of the  $J/\psi$  or  $\psi(2S)$  meson;

- $\log(1 - \text{DIRA})(B_c^+)$  : the natural logarithm of one minus the cosine of the angle between directions of the momentum and the flight of  $B_c^+$  mesons;
- $p_T(\pi^+)$ .

The comparison of the input variable distributions between the signal and the background is shown in Fig. 5.2. The variable distributions of the signals are similar for the two decay modes, except for  $p_T(\pi^+)$ , whose distribution is slightly different between the two channels. The distributions of the signal and the background show significant differences.

The normalised distributions of the BDT response for both BDT1 and BDT2 are given in Fig. 5.3. As expected, the signal and background candidates are well distinguished for both channels, and the distributions for the signals of the two channels are similar. The threshold for the BDT response is chosen to maximise the signal significance,  $S/\sqrt{S + B}$ , of the  $B_c^+ \rightarrow \psi(2S)\pi^+$  decay in the data sample. The  $S$  is the number of the signal candidates with the  $\psi(2S)\pi^+$  invariant mass in the range of  $M(B_c^+) \pm 3\sigma_{M(\psi(2S)\pi^+)}$ , and  $B$  the number of the background candidates in the same mass range. The yield  $S$  is proportional to the BDT cut efficiency of the  $B_c^+ \rightarrow \psi(2S)\pi^+$  signals, denoted as  $\varepsilon_{\text{BDT}}$ , which is estimated with the simulated sample. The number  $S + B$  is the total number of candidates within the mass range of  $M(B_c^+) \pm 3\sigma_{M(\psi(2S)\pi^+)}$  in the data sample. The two BDT classifiers are combined to determine the BDT cut value. The ratio  $\varepsilon_{\text{BDT}}/\sqrt{S + B}$  for the  $B_c^+ \rightarrow \psi(2S)\pi^+$  decay as a function of the BDT threshold is shown in Fig. 5.4 for both 2011 and 2012. The BDT threshold is optimised to be greater than 0.28 for both the 2011 and 2012 samples.

After the BDT selection, slightly tighter mass cuts,  $3030 < M(\mu^+\mu^-) < 3170 \text{ MeV}/c^2$  and  $3620 < M(\mu^+\mu^-) < 3760 \text{ MeV}/c^2$ , are applied for the  $J/\psi$  and  $\psi(2S)$  candidates, respectively. The cuts correspond to  $\pm 5\sigma_{M(\mu^+\mu^-)}$  around the known  $\psi$  mass<sup>[97]</sup>. The mass resolution  $\sigma_{M(\mu^+\mu^-)} \sim 14 \text{ MeV}/c^2$  is determined from the simulated samples.

## 5.4 Determination of signal yields

The signal yields are obtained from an unbinned maximum likelihood fit to the  $\psi\pi^+$  invariant mass distribution. The  $\psi\pi^+$  mass is obtained with the  $\psi$  mass and from-PV constraints. The invariant mass distribution of the signals is described by the DSCB function as defined in Sec. 4.4. The mass resolution varies with the kinematics of the  $B_c^+$  meson. The sum of two DSCB functions sharing the mean value and the tail parameters

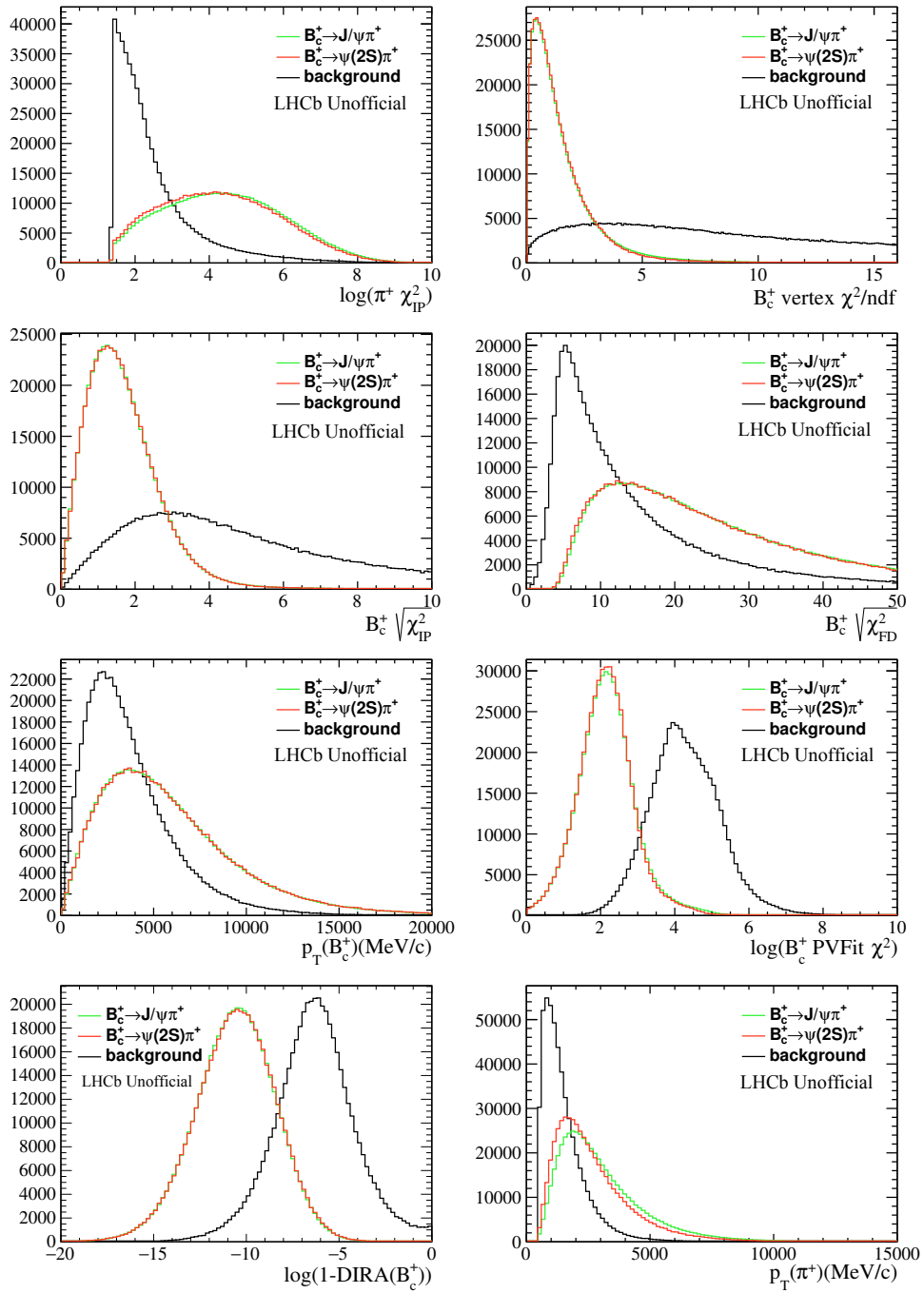


Figure 5.2 Comparison of input variable distributions between the signal and the background. The distributions are normalized to the same area.

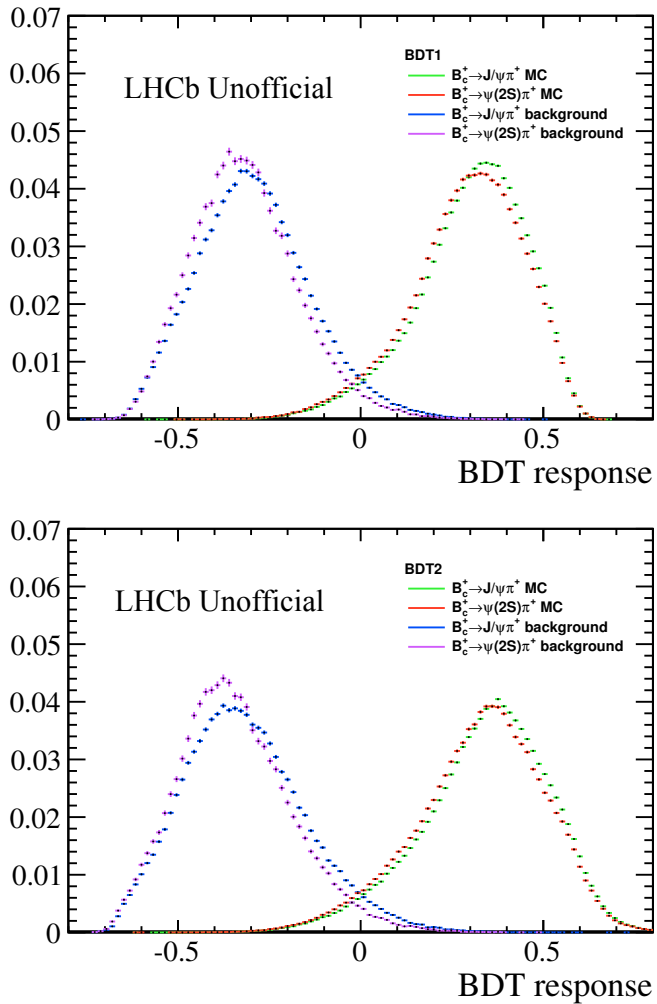


Figure 5.3 Normalised BDT response distributions of the signal and background samples for both channels for (top) BDT1 and (bottom) BDT2.

is used to fit the signals of the  $B_c^+ \rightarrow J/\psi\pi^+$  decay, while one DSCB function is enough for  $B_c^+ \rightarrow \psi(2S)\pi^+$ , since it has a smaller statistic. For the  $B_c^+ \rightarrow J/\psi\pi^+$  decay, the tail parameters, the fraction of either DSCB, and the ratio between the resolutions of two DSCB functions are fixed from the fit to the simulated sample. For the  $B_c^+ \rightarrow \psi(2S)\pi^+$  decay, the mean value of the DSCB is fixed to the mean value of the  $B_c^+ \rightarrow J/\psi\pi^+$  decay. The resolution is set to be

$$\sigma(B_c^+ \rightarrow J/\psi\pi^+)_{data}/\sigma(B_c^+ \rightarrow J/\psi\pi^+)_{MC} \times \sigma(B_c^+ \rightarrow \psi(2S)\pi^+)_{MC},$$

where the subscripts *data* and *MC* indicate the resolutions determined from the fit to the data and simulated samples, respectively.

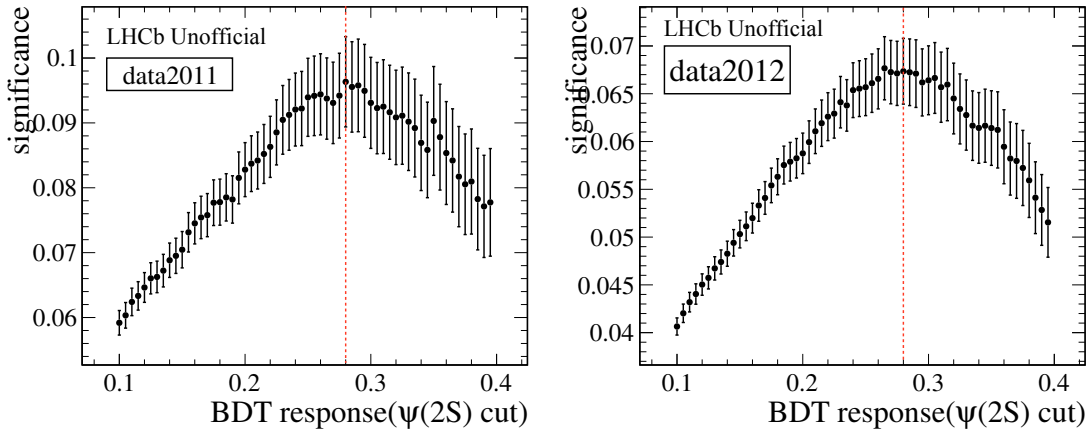


Figure 5.4 The ratio  $\varepsilon_{\text{BDT}}/\sqrt{S + B}$  for the  $B_c^+ \rightarrow \psi(2S)\pi^+$  decay as a function of the BDT threshold for the (left) 2011 and (right) 2012 data samples.

The backgrounds of the  $B_c^+ \rightarrow J/\psi\pi^+$  decay consist of three components:

- the combinatorial background, described with an exponential function  $e^{x\cdot\tau}$ ;
- the partially reconstructed background from the  $B_c^+ \rightarrow J/\psi\rho^+$  decay with  $\rho^+ \rightarrow \pi^+\pi^0$ , where  $\pi^0$  is not reconstructed. It is modelled with the  $J/\psi\pi^+$  invariant mass distribution extracted from the simulated  $B_c^+ \rightarrow J/\psi\rho^+$  sample convolved with a Gaussian function.
- The Cabibbo-suppressed channel  $B_c^+ \rightarrow J/\psi K^+$  with the kaon misidentified as a pion. It is described by a DSCB function with the parameters fixed from the simulation.

For the  $B_c^+ \rightarrow \psi(2S)\pi^+$  decay, the  $B_c^+ \rightarrow \psi(2S)K^+$  contamination can be safely ignored due to small statistic. The other two components are treated in the same way as  $B_c^+ \rightarrow J/\psi\pi^+$ .

The mass distributions of the two sub-samples of the same decay channel from the same year, which are applied with BDT1 and BDT2 respectively, are fitted separately, sharing the same fitting parameters. The fit results are shown in Figs. 5.5 and 5.6 for the year 2011 and 2012, respectively. The signal yields are corrected with the corresponding BDT cut efficiencies, which are evaluated with the simulated samples. The BDT cut efficiencies and the signal yields with the BDT efficiency correction are listed in Tables 5.3 and 5.4, respectively.

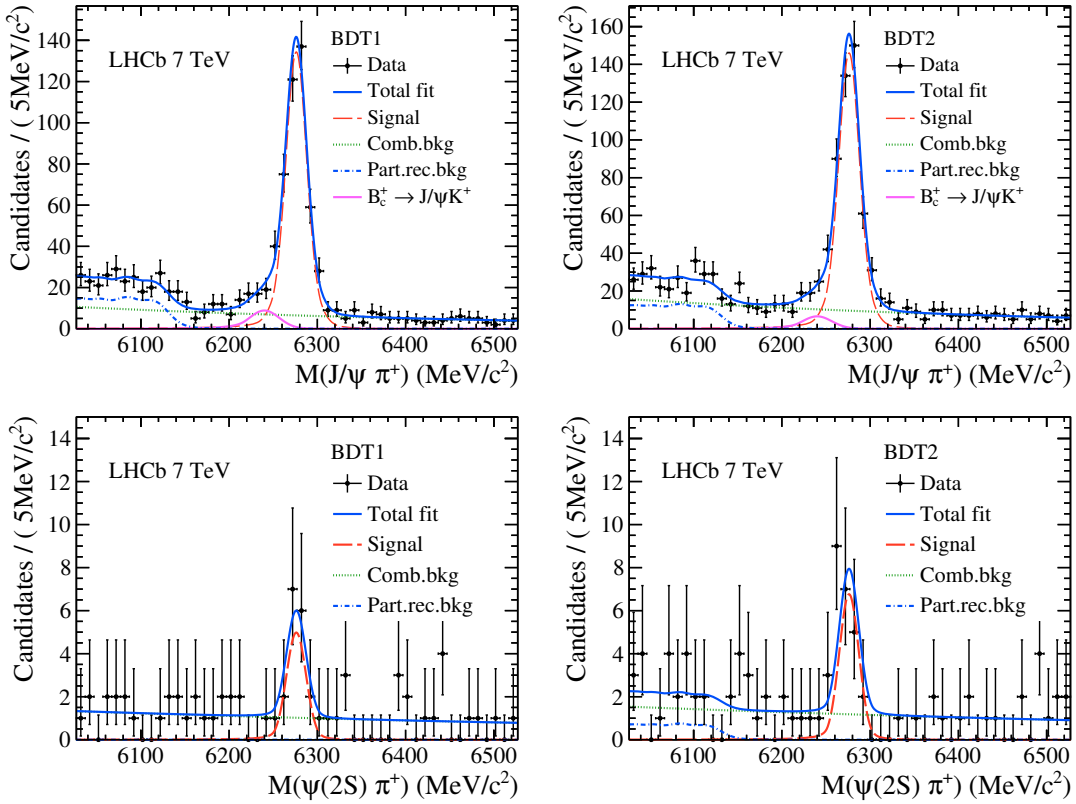


Figure 5.5 Fits to the  $\psi\pi^+$  mass distributions of the 2011 data samples applied with (left) BDT1 and (right) BDT2 for the (top)  $B_c^+ \rightarrow J/\psi\pi^+$  and (bottom)  $B_c^+ \rightarrow \psi(2S)\pi^+$  decays, respectively. The error bars are the data points. The blue solid line is the fitting of data. The red dashed line shows the signal distribution. The green dashed line shows the combinatorial background. The blue dashed line to the lower end shows the partially reconstructed background. The violet solid line next to the  $B_c^+ \rightarrow J/\psi\pi^+$  signal peak is the background from the  $B_c^+ \rightarrow J/\psi K^+$  channel.

## 5.5 Efficiency estimation

The total efficiency (excluding the BDT selection efficiency) consists of the geometrical acceptance efficiency, the reconstruction and selection efficiency without the pion identification (pionID), the pionID cut efficiency and the trigger efficiency. The efficiency terms are estimated one after another with the simulated samples. The efficiencies are estimated for the whole kinematic range. It makes sense since the BCVEGPY generator is found to well recreate the kinematics of the  $B_c^+$  mesons<sup>[153]</sup>. Even if there is slight difference in the  $B_c^+$  kinematics between the data and the simulation, it cancels between the  $B_c^+ \rightarrow \psi(2S)\pi^+$  and  $B_c^+ \rightarrow J/\psi\pi^+$  decays. To account for possible discrepancy in the pion identification between the data and the simulation, the pionID efficiency is calibrated using a data sample of pion from the  $D^* \rightarrow K^-\pi^+$  decay, in which the single

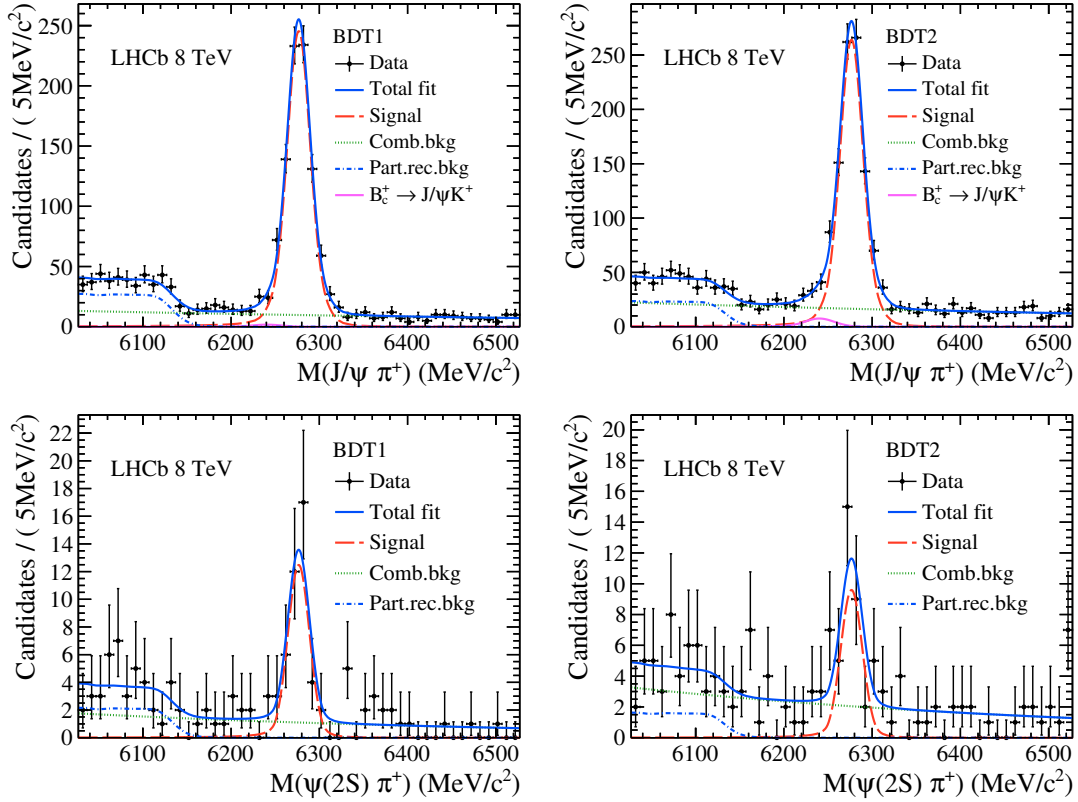


Figure 5.6 Fit to the  $B_c^+$  mass distribution of the data sample from 2012 applied with (left) *tmva1* and (right) *tmva2* for the (top)  $B_c^+ \rightarrow J/\psi\pi^+$  and (bottom)  $B_c^+ \rightarrow \psi(2S)\pi^+$  decay. The error bars are the data points. The blue solid line is the fitting of data. The red dashed line shows the signal distribution. The green dashed line shows the combinatorial background. The blue dashed line to the lower end shows the partially reconstructed background. The violet solid line next to the  $B_c^+ \rightarrow J/\psi\pi^+$  signal peak is the background from the  $B_c^+ \rightarrow J/\psi K^+$  channel.

pionID efficiency is determined using the tag-and-probe technique. For each decay mode, all the efficiencies are determined independently for the data from 2011 and 2012. The geometrical acceptance efficiencies are evaluated separately for the data with different magnet polarities, as listed in Table 5.5. The remaining efficiency terms are summarised in Table 5.6. The total efficiencies of the  $B_c^+ \rightarrow \psi(2S)\pi^+$  and  $B_c^+ \rightarrow J/\psi\pi^+$  decays for 2011 and 2012 are shown in Table 5.7. According to Eq. 5-4, the ratio  $R_{\mathcal{B}}$  is calculated to be

$$R_{\mathcal{B}} = 0.0354 \pm 0.0042 \text{ (stat)}.$$

Table 5.3 Summary of the BDT selection efficiencies.

	2011		2012	
	BDT1	BDT2	BDT1	BDT2
$B_c^+ \rightarrow J/\psi\pi^+$	$0.6299 \pm 0.0007$	$0.6929 \pm 0.0006$	$0.6233 \pm 0.0006$	$0.6850 \pm 0.0006$
$B_c^+ \rightarrow \psi(2S)\pi^+$	$0.5879 \pm 0.0011$	$0.6584 \pm 0.0011$	$0.5832 \pm 0.0008$	$0.6508 \pm 0.0008$

Table 5.4 Summary of the signal yields with the BDT efficiency correction.

	2011		2012	
	BDT1	BDT2	BDT1	BDT2
$B_c^+ \rightarrow J/\psi\pi^+$	$693.6 \pm 38.2$	$685.2 \pm 37.1$	$1415.7 \pm 54.4$	$1386.5 \pm 53.1$
	$1378.8 \pm 53.2$		$2802.3 \pm 76.0$	
$B_c^+ \rightarrow \psi(2S)\pi^+$	$24.6 \pm 7.7$	$29.8 \pm 8.1$	$68.7 \pm 12.2$	$47.3 \pm 10.7$
	$54.4 \pm 11.2$		$116.0 \pm 16.2$	

## 5.6 Systematic uncertainties

Several sources of systematic uncertainties are studied, as discussed below.

### 5.6.1 Signal shape

The possible imperfect modelling of the signal shape can lead to a systematic uncertainty. It is estimated using two strategies. Firstly, instead of the nominal DSCB functions, the signal shape is described by the kernel estimation<sup>[112]</sup> of the  $\psi\pi^+$  invariant mass distribution from the simulated samples convolved with a Gaussian function. The change in the final result compared to the nominal one is 0.6%. Secondly, the data samples

Table 5.5 Geometrical acceptance efficiencies. The uncertainties are due to the statistical uncertainties of the simulated samples.

Channel	2011		2012	
	MagDown	MagUp	MagDown	MagUp
$B_c^+ \rightarrow \psi(2S)\pi^+$	$0.1304 \pm 0.0003$	$0.1300 \pm 0.0002$	$0.1349 \pm 0.0003$	$0.1342 \pm 0.0003$
$B_c^+ \rightarrow J/\psi\pi^+$	$0.1322 \pm 0.0002$	$0.1325 \pm 0.0002$	$0.1369 \pm 0.0002$	$0.1366 \pm 0.0002$

Table 5.6 Summary of the efficiencies except the acceptance efficiency. The efficiencies of the  $\psi$  mass cut applied after the BDT classifier and the cut on  $M(\psi\pi^+)$  due to the fit range are evaluated separately. The uncertainties are due to the statistical uncertainties of the simulated samples.

	2011		2012	
	$B_c^+ \rightarrow \psi(2S)\pi^+$	$B_c^+ \rightarrow J/\psi\pi^+$	$B_c^+ \rightarrow \psi(2S)\pi^+$	$B_c^+ \rightarrow J/\psi\pi^+$
Pre-selection	$0.1771 \pm 0.0005$	$0.1626 \pm 0.0002$	$0.1622 \pm 0.0003$	$0.1547 \pm 0.0002$
(without pionID)				
pionID cut	$0.9423 \pm 0.0002$	$0.9218 \pm 0.0001$	$0.9251 \pm 0.0001$	$0.9016 \pm 0.0001$
$\psi$ mass cut	$0.9950 \pm 0.0002$	$0.9960 \pm 0.0001$	$0.9943 \pm 0.0002$	$0.9958 \pm 0.0001$
$M(\psi\pi^+)$ fit range	$0.9946 \pm 0.0002$	$0.9932 \pm 0.0001$	$0.9942 \pm 0.0002$	$0.9931 \pm 0.0001$
Trigger	$0.7586 \pm 0.0013$	$0.7094 \pm 0.0005$	$0.7659 \pm 0.0009$	$0.7101 \pm 0.0005$

Table 5.7 Total efficiencies of the  $B_c^+ \rightarrow \psi(2S)\pi^+$  and  $B_c^+ \rightarrow J/\psi\pi^+$  decays for 2011 and 2012. The uncertainties are due to the statistical uncertainties of the simulated samples.

Channel	2011	2012
$B_c^+ \rightarrow \psi(2S)\pi^+$	$(1.631 \pm 0.006)\%$	$(1.529 \pm 0.005)\%$
$B_c^+ \rightarrow J/\psi\pi^+$	$(1.392 \pm 0.003)\%$	$(1.339 \pm 0.003)\%$

for both channels from 2011 and 2012 are fitted with the same tail parameters, which are obtained from the fitting result of the simulation for the  $B_c^+ \rightarrow J/\psi\pi^+$  decay in 2012. The difference between this result and the nominal one is 0.5%. The systematic uncertainty of the signal shape modelling is taken as 0.6%.

### 5.6.2 Background shape

There could be inconsistency between the model of the background distribution and its true distribution. To estimate the corresponding systematic uncertainty, alternative methods are used to describe the misidentified  $B_c^+ \rightarrow J/\psi K^+$  background and the partially reconstructed background. The  $B_c^+ \rightarrow J/\psi K^+$  contamination is described by the kernel estimation<sup>[112]</sup> of the simulated mass distribution convolved with a Gaussian function instead of the DSCB function. The resulting relative branching fraction changes by 0.4% from the nominal one. For the partially reconstructed background, the systematic uncertainty is evaluated in two ways. Firstly, the fit range is adjusted to  $M(\psi\pi^+) \in$

(6164, 6527) MeV/ $c^2$  to remove its contribution. The result changes by 2.4%. Secondly, an Argus function is used to describe it. Compared to the nominal result, the difference is only 0.02%. The total uncertainty due to the background shape modelling is determined to be 2.4%.

### 5.6.3 Simulation statistics

The limited statistics of the simulation is another source of systematic uncertainty. According to Eq. 5-4, the uncertainty due to the statistical uncertainties of the efficiencies can be calculated as

$$\frac{\sigma_{\varepsilon}}{R_{\mathcal{B}}} = \sqrt{\sum_{i=1}^4 \left[ \left( \frac{\partial \log R_{\mathcal{B}}}{\partial \varepsilon_i} \right)^2 \cdot \sigma_{\varepsilon_i}^2 \right]}, \quad (5-6)$$

where  $\sigma_{\varepsilon}$  stands for the uncertainty on  $R_{\mathcal{B}}$  propagated from the efficiency uncertainties,  $\varepsilon_i$  ( $i = 1, 2, 3, 4$ ) indicate the efficiencies of the  $B_c^+ \rightarrow \psi(2S)\pi^+$  and  $B_c^+ \rightarrow J/\psi\pi^+$  decays in 2011 and 2012 respectively, and  $\sigma_{\varepsilon_i}$  ( $i = 1, 2, 3, 4$ ) are the corresponding uncertainties which are given in Table. 5.7. This leads to an uncertainty of 0.3% to the final result.

### 5.6.4 Lifetime of $B_c^+$

In the determination of the efficiencies, the simulated sample is weighted according to the newly measured  $B_c^+$  lifetime at LHCb<sup>[149]</sup>. To estimate the uncertainty due to the lifetime weight, the  $B_c^+$  lifetime is varied within the uncertainty of the new measurement. The result changes for a maximum of 0.1% from the nominal branching fraction ratio. It is taken as the systematic uncertainty.

### 5.6.5 Data and simulation discrepancy

The difference between the data and the simulation can introduce a systematic uncertainty through the efficiencies. To estimate this uncertainty, the distributions of all the input variables of the BDT classifiers are compared between the data and the simulation. The backgrounds are subtracted from the data sample using the sPlot technique<sup>[104]</sup> according to the  $\psi\pi^+$  invariant mass distribution. The comparisons for the  $B_c^+ \rightarrow J/\psi\pi^+$  decay in 2012 are shown in Fig. 5.8 as an example. The complete comparisons for the  $B_c^+ \rightarrow J/\psi\pi^+$  and  $B_c^+ \rightarrow \psi(2S)\pi^+$  decays in both 2011 and 2012 are given in Appendix B.

The agreement level is evaluated using the KolmogorovTest function. The  $\chi_{\text{IP}}^2(\pi^+)$  distribution shows the largest discrepancy between the data and simulated samples. A set of weights for the simulation are obtained by dividing the  $\chi_{\text{IP}}^2(\pi^+)$  distribution in the data by that in the simulation, as shown in Fig. 5.7. A wider bin width is taken in the region where the statistic is limited. Since the statistic of the  $B_c^+ \rightarrow \psi(2S)\pi^+$  decay is too small, the weights for the  $B_c^+ \rightarrow J/\psi\pi^+$  decay are assigned to the  $B_c^+ \rightarrow \psi(2S)\pi^+$  candidates as well. The comparisons between the data and the simulation after applying the weights are shown in Fig. 5.9 for the  $B_c^+ \rightarrow J/\psi\pi^+$  decay in 2012, where the agreement between the data and the simulation becomes reasonably well. The complete comparisons after the weighting are shown in Appendix B. The efficiencies are recalculated with the weighted simulated samples. The result changes by 0.2%, which is taken as the systematic uncertainty.

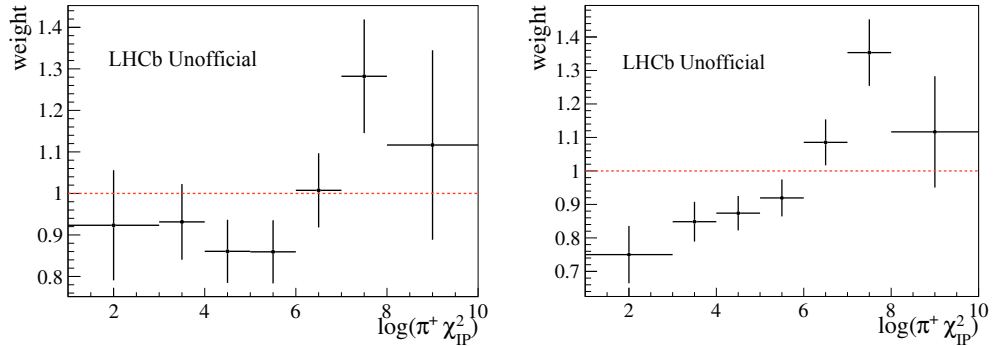


Figure 5.7 Weights determined according to the  $\chi_{\text{IP}}^2(\pi^+)$  distribution for the simulated samples from (left) 2011 and (right) 2012, respectively.

### 5.6.6 Trigger efficiency

The trigger efficiency is determined from the simulated sample. A systematic uncertainty of trigger efficiency could be introduced by the imperfect simulation of the trigger process. It is estimated by comparing the trigger efficiencies determined using the TISTOS method from the data and the simulation. The study has been performed in plenty of previous analyses<sup>[154,155]</sup>. There is a much larger statistic with the  $b$ -hadron decays in Ref. [155], in which the trigger lines used in this analysis are all applied. Therefore the result determined in Ref. [155], 1.1%, is quoted as the systematic uncertainty of the trigger efficiency.

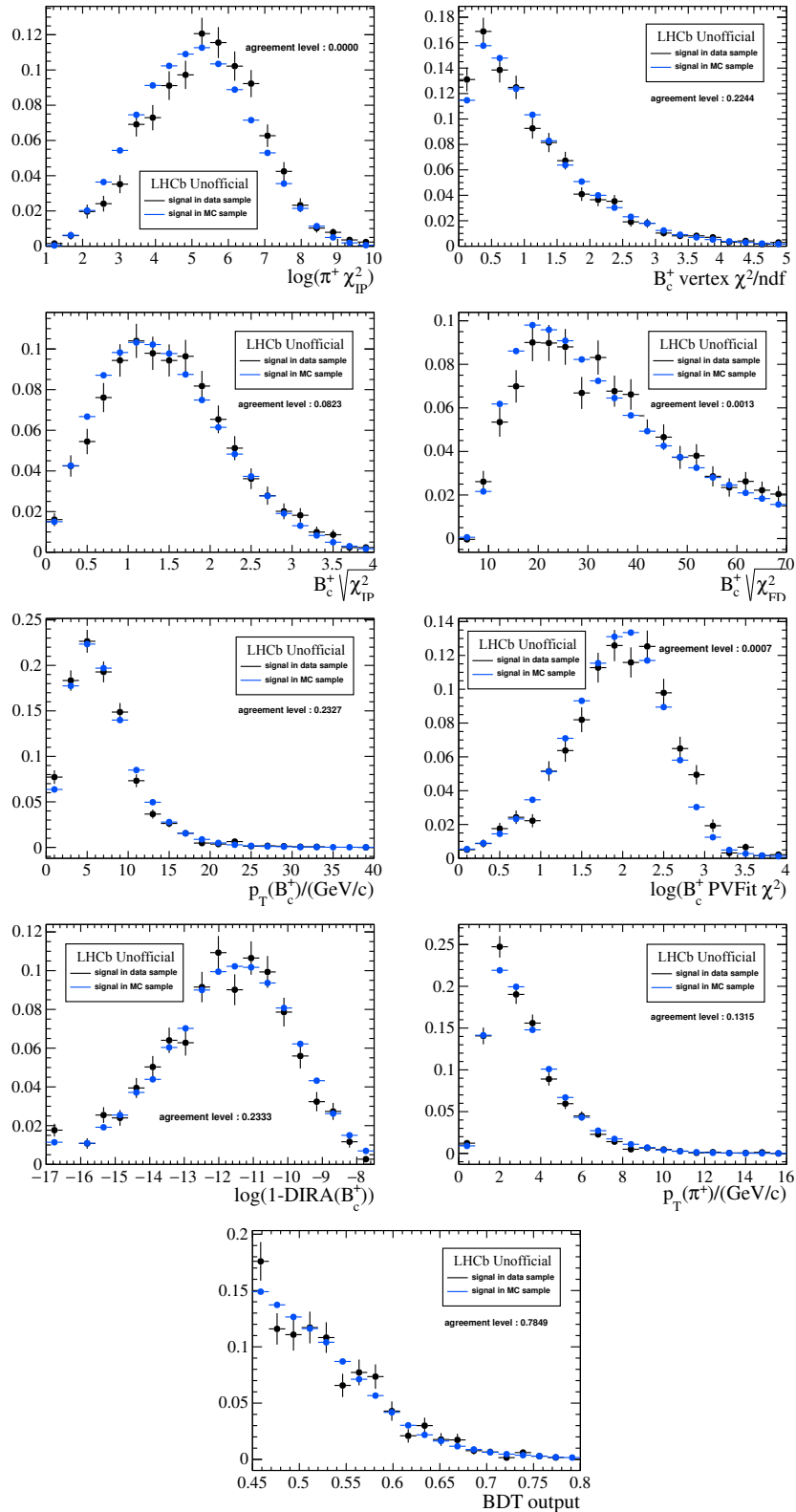


Figure 5.8 Comparison of the distributions of the input variables for the BDT classifiers between the data and the simulation for the  $B_c^+ \rightarrow J/\psi\pi^+$  decay in 2012.

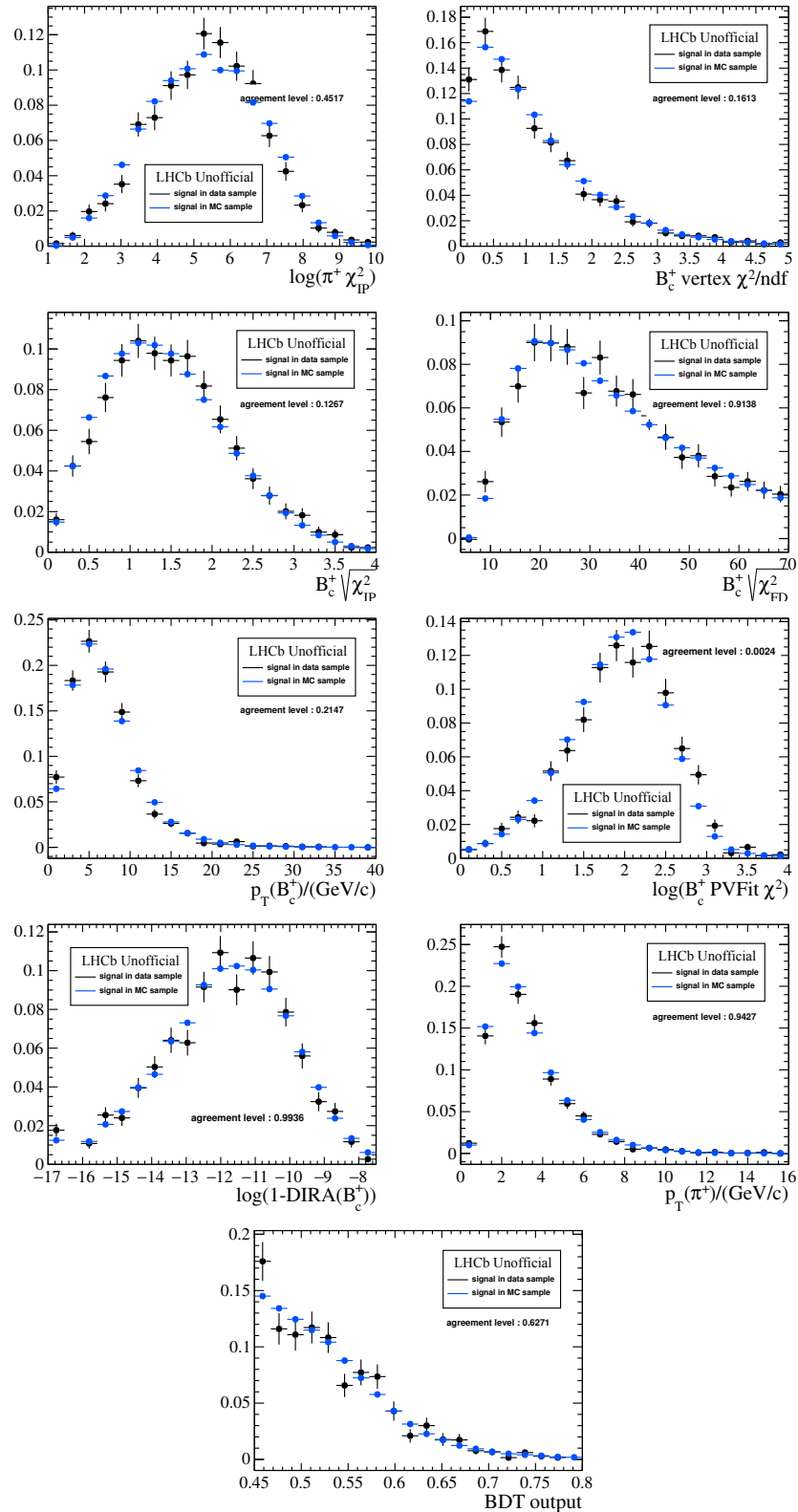


Figure 5.9 Comparison of the distributions of the input variables for the BDT classifiers between the data and the simulation for the  $B_c^+ \rightarrow J/\psi\pi^+$  decay in 2012 after weighting the simulation.

### 5.6.7 Summary

The systematic uncertainties on the ratio  $R_{\mathcal{B}}$  are summarised in Table 5.8. The total systematic uncertainty is summed up to be 2.7%.

Table 5.8 Summary of the systematic uncertainties on  $R_{\mathcal{B}}$ .

Component	Uncertainty Value
Signal shape	0.6%
Background shape	2.4%
Simulation statistics	0.3%
$B_c^+$ lifetime	0.1%
Data and simulation discrepancy	0.2%
Trigger efficiency	1.1%
Total	2.7%

## 5.7 Results and comparison to theories

Assuming electroweak universality, one has

$$\frac{\mathcal{B}(J/\psi \rightarrow \mu^+\mu^-)}{\mathcal{B}(\psi(2S) \rightarrow \mu^+\mu^-)} = \frac{\mathcal{B}(J/\psi \rightarrow e^+e^-)}{\mathcal{B}(\psi(2S) \rightarrow e^+e^-)} = \frac{(5.971 \pm 0.032)\%}{(7.89 \pm 0.17) \times 10^{-3}},$$

through which the uncertainty is reduced. According to Eq. (5-2), the result determined from the 2011 data is

$$R = 0.255 \pm 0.053 \text{ (stat)} \pm 0.007 \text{ (syst)} \pm 0.006(\mathcal{B}),$$

where the last term is the uncertainty due to the uncertainty of  $\mathcal{B}(J/\psi \rightarrow \mu^+\mu^-)/\mathcal{B}(\psi(2S) \rightarrow \mu^+\mu^-)$ . This is consistent with the previous measurement using the  $1 \text{ fb}^{-1}$  data at  $\sqrt{s} = 7 \text{ TeV}$ <sup>[53]</sup>, which gives

$$R = 0.250 \pm 0.068 \text{ (stat)} \pm 0.014 \text{ (syst)} \pm 0.006(\mathcal{B}).$$

The result determined from the 2012 data is

$$R = 0.275 \pm 0.039 \text{ (stat)} \pm 0.007 \text{ (syst)} \pm 0.006(\mathcal{B}).$$

The result measured with the total  $3 \text{ fb}^{-1}$  data is

$$R = 0.268 \pm 0.032 \text{ (stat)} \pm 0.007 \text{ (syst)} \pm 0.006(\mathcal{B}).$$

There are several theoretical predictions on the branching ratio, as summarised in Table 5.9. The measurement coincides with the calculations of NRQCD at NLO<sup>[58]</sup> and the  $k_T$  factorization method<sup>[60]</sup> within one standard deviation. The predictions from the various relativistic quark models<sup>[61-63]</sup> tend to underestimate the result.

Table 5.9 List of the theoretical predictions on  $R$ .

Theoretical model	Prediction
Relativistic quark model I <sup>[62]</sup>	0.18
Relativistic quark model II <sup>[61]</sup>	0.07
Relativistic quark model III <sup>[63]</sup>	0.15
Non-relativistic quark model <sup>[59]</sup>	0.13
NRQCD at NLO <sup>[58]</sup>	0.26
$k_T$ factorization <sup>[60]</sup>	0.29

## Chapter 6 Search for excited $B_c^+$ states

This chapter presents the search for the  $B_c(2^1S_0)^+$  and  $B_c(2^3S_1)^+$  states in the  $B_c^+\pi^+\pi^-$  invariant mass distribution using the  $pp$  collision data collected by LHCb at  $\sqrt{s} = 8$  TeV, corresponding to an integrated luminosity of  $2\text{ fb}^{-1}$ . Since no evidence of the signal is found, upper limits are set on the product of the production cross-sections of the  $B_c(2^1S_0)^+$  and  $B_c(2^3S_1)^+$  states and the branching fractions of  $B_c(2^1S_0)^+ \rightarrow B_c^+\pi^+\pi^-$  and  $B_c(2^3S_1)^+ \rightarrow B_c(1^3S_1)^+\pi^+\pi^-$  with respect to the  $B_c^+$  production cross-section. The analysis strategy, the dataset, the candidate reconstruction and selection, and the determination of the upper limits are described in detail in the following sections. The author is fully responsible for the analysis work.

### 6.1 Analysis strategy

Following the ATLAS measurement, the  $B_c^+\pi^+\pi^-$  mass spectrum is explored to search for the  $B_c(2^1S_0)^+$  and  $B_c(2^3S_1)^+$  states at LHCb. Hereafter, the  $B_c(2^1S_0)^+$ ,  $B_c(2^3S_1)^+$  and  $B_c(1^3S_1)^+$  states are abbreviated as  $B_c(2S)^+$ ,  $B_c^*(2S)^+$  and  $B_c^{*+}$ , respectively. The search is performed with the  $B_c^+$  and  $B_c^{*(*)}(2S)^+$  mesons in the kinematic region  $p_T \in (0, 20)$  GeV/c and  $y \in (2.0, 4.5)$ , corresponding to the LHCb coverage. The  $B_c^+$  meson is reconstructed using the  $B_c^+ \rightarrow J/\psi \pi^+$  decay followed by  $J/\psi \rightarrow \mu^+ \mu^-$ . With no signal observed, upper limits are set on

$$\begin{aligned} \mathcal{R} &= \frac{\sigma_{B_c^{*(*)}(2S)^+} \cdot \mathcal{B}(B_c^{*(*)}(2S)^+ \rightarrow B_c^{*(*)} \pi^+ \pi^-)}{\sigma_{B_c^+}} \\ &= \frac{N_{B_c^{*(*)}(2S)^+}}{N_{B_c^+}} \cdot \frac{\varepsilon_{B_c^+}}{\varepsilon_{B_c^{*(*)}(2S)^+}}, \end{aligned} \quad (6-1)$$

where  $\sigma$  represents the production cross-section,  $N$  the yield, and  $\varepsilon$  the efficiency.

Because the low-energy photon is not reconstructed in the decay of  $B_c^*(2S)^+$ , the centre of the  $B_c^*(2S)^+$  mass peak in the  $M(B_c^+\pi^+\pi^-)$  distribution shifts down to  $M(B_c(2S)^+) - \Delta M$ , where

$$\Delta M \equiv [M(B_c^{*+}) - M(B_c^+)] - [M(B_c^*(2S)^+) - M(B_c(2S)^+)]. \quad (6-2)$$

The mass  $M(B_c(2S)^+)$  is predicted to be in the range of [6830, 6890] MeV/ $c^2$ , and the mass difference  $\Delta M$  within [0, 35] MeV/ $c^2$ <sup>[19,64–73]</sup>. In consequence, the  $B_c^*(2S)^+$  state should peak within [6795, 6890] MeV/ $c^2$  in the  $B_c^+\pi^+\pi^-$  mass spectrum. The upper limits are determined considering two cases: a) when  $\Delta M = 0$ , which means the mass peaks of the  $B_c(2S)^+$  and  $B_c^*(2S)^+$  states fully overlap; b) when  $\Delta M$  is large enough that the mass peaks of the  $B_c(2S)^+$  and  $B_c^*(2S)^+$  states are fully separated.

## 6.2 Dataset

The analysis is performed using the  $pp$  collision data collected by LHCb at  $\sqrt{s} = 8$  TeV, corresponding to an integrated luminosity of  $2\text{ fb}^{-1}$ . The trigger decisions are TOS aiming at selecting the  $B_c^+$  meson, so that the trigger efficiency cancels between  $\varepsilon_{B_c^{(*)}(2S)^+}$  and  $\varepsilon_{B_c^+}$  in the ratio  $R$ . The L0 trigger requires either at least one muon with large  $p_T$  or a hadron with large  $E_T$ . At the HLT1 and HLT2 stages, two muons or three charged tracks with large  $p_T$  are required to form a vertex detached from the PV.

Simulated samples are generated for the  $B_c^{(*)}(2S)^+$  and  $B_c^+$  mesons to study their behaviour. The generator BCVEGPY<sup>[91,147]</sup> is used to simulate the generations of the  $B_c^{(*)}(2S)^+$  and  $B_c^+$  mesons from  $pp$  collisions. The  $B_c^*(2S)^+$  state is produced with zero polarisation. In the default setting, the masses of the excited  $B_c$  mesons are taken to be  $M(B_c(2S)^+) = 6858\text{ MeV}/c^2$ ,  $M(B_c^*(2S)^+) = 6890\text{ MeV}/c^2$  and  $M(B_c^{*+}) = 6342\text{ MeV}/c^2$ . To study the dependence of efficiency on the  $B_c^{(*)}(2S)^+$  mass, simulated samples with the values of  $M(B_c(2S)^+)$  and  $M(B_c^*(2S)^+)$  varied within the predicted mass range are also generated.

## 6.3 Candidate reconstruction and selection

The candidate reconstruction and selection is implemented in two steps. First is to reconstruct and select the  $B_c^+$  meson, second the  $B_c^{(*)}(2S)^+$  meson.

### 6.3.1 Reconstruction and selection of $B_c^+ \rightarrow J/\psi \pi^+$

The  $B_c^+$  candidates are reconstructed from the  $B_c^+ \rightarrow J/\psi \pi^+$  decay, and selected using a BDT classifier after a cut-based pre-selection. The cuts applied in the pre-selection are summarised in Table 6.1. A pair of opposite-sign muons, which are identified by the positive isMuon and PIDmu>0 requirements, are required to have  $p_T$  larger than 550 GeV/ $c$  and good track quality with  $\chi^2_{\text{track}}/\text{ndf}$  smaller than 3. The muon pair should

Table 6.1 Cut-based pre-selections for the  $B_c^+ \rightarrow J/\psi \pi^+$  decay. DOCA stands for the distance of closest approach.

$\mu^\pm$	isMuon&PIDmu>0
	$p_T > 550 \text{ MeV}/c$
	$\chi_{\text{track}}^2/\text{ndf} < 3$
$J/\psi$	$3.04 < M < 3.14 \text{ GeV}/c^2$
	$\chi_{\text{vertex}}^2/\text{ndf} < 9$
	DOCA < 30 mm
$\pi^+$	$p_T > 1 \text{ GeV}/c$
	$\chi_{\text{track}}^2/\text{ndf} < 3$
	TRACK_GhostProb < 0.4
	$\chi_{\text{IP}}^2 > 9$
$B_c^+$	$\chi_{\text{vertex}}^2/\text{ndf} < 9$
	$\chi_{\text{IP}}^2 < 25$
	$\tau > 0.2 \text{ ps}$

form a  $J/\psi$  candidate, which has a good-quality vertex with  $\chi_{\text{vertex}}^2/\text{ndf}$  smaller than 9 and a mass within  $[3.04, 3.14] \text{ GeV}/c^2$ . The closest distance between the two muons is required to be smaller than 30 mm. The bachelor pion must have a  $p_T$  larger than  $1 \text{ GeV}/c$ , good track quality with  $\chi_{\text{track}}^2/\text{ndf}$  smaller than 3, a TRACK\_GhostProb smaller than 0.4, and a  $\chi_{\text{IP}}^2$  larger than 9 to be away from the PV. Only  $B_c^+$  candidates with  $\chi_{\text{vertex}}^2/\text{ndf}$  smaller than 9,  $\chi_{\text{IP}}^2$  smaller than 25 and lifetime  $\tau$  larger than 0.2 ps are kept. The masses of the  $B_c^+$  candidates are calculated with the  $J/\psi$  mass and from-PV constraints.

The BDT classifier is trained with the simulated  $B_c^+ \rightarrow J/\psi \pi^+$  sample as signals, and the upper mass sideband with  $6376 \text{ MeV}/c^2 < M(J/\psi \pi^+) < 6600 \text{ MeV}/c^2$  of the data sample as backgrounds. The training samples are randomly divided into halves, half used for the training and the other half for the test. The input variables are taken as

- $\chi_{\text{IP}}^2$  of all particles, *i.e.* the  $\mu^\pm$ ,  $\pi^+$ ,  $J/\psi$  and  $B_c^+$  mesons, with respect to its own associated PV;
- $p_T$  of the  $\mu^\pm$ ,  $J/\psi$  and  $\pi^+$  mesons;
- decay length and decay time of the  $B_c^+$  meson;
- $\chi_{\text{DTF}}^2$  with both  $J/\psi$  mass and from-PV constraints implemented in the DTF.

The BDTG method is used as it gives a better performance than the other boosting algorithms. The cut value of the BDTG classifier is determined by maximizing the

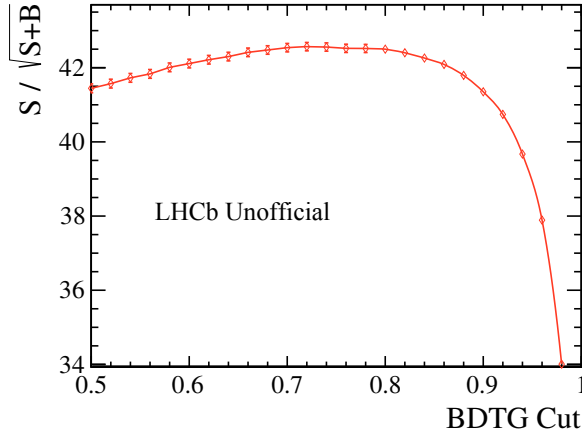


Figure 6.1 Signal significance,  $S/\sqrt{S+B}$ , as a function of the BDT cut for the  $B_c^+ \rightarrow J/\psi \pi^+$  decay.

signal significance  $S/\sqrt{S+B}$ , where  $S$  and  $B$  are the expected numbers of signal and background in the  $M(J/\psi \pi^+) \pm 2\sigma_{M(J/\psi \pi^+)}$  mass window. The number  $S$  is determined from the simulation, and the number  $B$  is evaluated by extrapolating the upper mass sideband to the signal region assuming the background shape is flat. The ratio  $S/\sqrt{S+B}$  as a function of the BDT threshold is shown in Fig. 6.1, according to which the BDTG threshold of 0.82 is chosen. The  $J/\psi \pi^+$  mass distribution after the selections is shown in Fig. 6.2, in which there is clear signal peak for the  $B_c^+$  meson. The  $M(J/\psi \pi^+)$  distribution is fitted using the same strategy as that in the  $B_c^+ \rightarrow \psi(2S)\pi^+$  measurement as described in Sec. 5.4. There are  $3325 \pm 73$   $B_c^+$  candidates obtained from the fit.

### 6.3.2 Reconstruction and selection of $B_c^{(*)}(2S)^+ \rightarrow B_c^{(*)+} \pi^+ \pi^-$

The selected  $B_c^+$  mesons with  $M(J/\psi \pi^+) \in [6200, 6340] \text{ MeV}/c^2$  are associated to two pions to reconstruct the  $B_c^{(*)}(2S)^+$  state. The two pions should be long tracks to improve the resolution of the  $B_c^+ \pi^+ \pi^-$  mass. The pions are required to have  $p_T$  larger than  $0.25 \text{ GeV}/c$ ,  $p$  larger than  $2 \text{ GeV}/c$ , TRACK\_GhostProb smaller than 0.5, and be identified as pions with ProbNN $\pi$  larger than 0.2. The vertex fit  $\chi^2_{\text{vertex}}/\text{ndf}$  of the  $B_c^{(*)}(2S)^+$  candidates is required to be smaller than 16. The cut-based selections are summarised in Table 6.2. The  $B_c^+ \pi^+ \pi^-$  mass is obtained after constraining the  $J/\psi \pi^+$  mass to the known  $B_c^+$  mass<sup>[156]</sup> and requiring the  $B_c^{(*)}(2S)^+$  meson to come from the PV, in order to improve its resolution.

To improve the sensitivity to the  $B_c^{(*)}(2S)^+ \rightarrow B_c^{(*)+} \pi^+ \pi^-$  decay, a second multivariate analysis with the multilayer perceptron (MLP) classifier is used. In the MLP method,

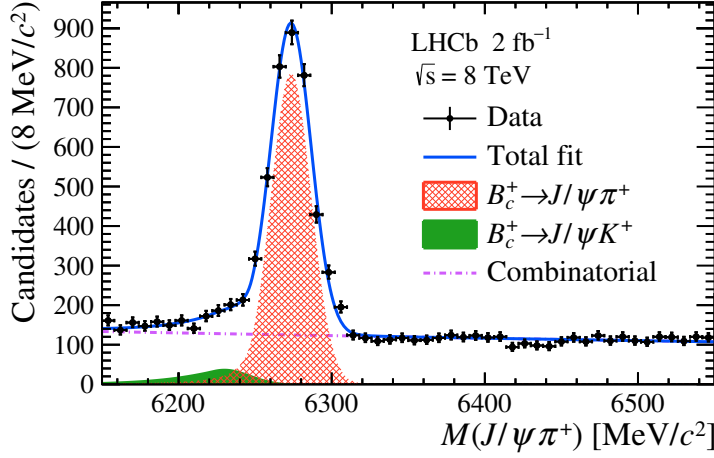


Figure 6.2 Fit to the  $J/\psi\pi^+$  mass distribution of the data sample. Black points with error bars represent the data. The blue solid line is the total fit. The red cross-hatched area shows the signal distribution. The green shaded area is the misidentified  $B_c^+ \rightarrow J/\psi K^+$  background. The violet dash-dotted line represents the combinatorial background.

Table 6.2 Cut-based selections for the  $B_c^{(*)}(2S)^+ \rightarrow B_c^{(*)+}\pi^+\pi^-$  decays.

$\pi^\pm$	Long track
	$p_T > 0.25 \text{ GeV}/c$
	$p > 2 \text{ GeV}/c$
	$\text{ProbNN}\pi > 0.2$
	$\text{TRACK\_GhostProb} < 0.5$
$B_c^{(*)}(2S)^+$	$\chi^2_{\text{vertex}}/\text{ndf} < 16$

the response value is calculated from a multilayer non-linear function of the input variables. The MLP classifier is trained with signals from the simulated samples of both the  $B_c(2S)^+ \rightarrow B_c^+\pi^+\pi^-$  and  $B_c^*(2S)^+ \rightarrow B_c^{*+}(\rightarrow B_c^+\gamma)\pi^+\pi^-$  decays, and backgrounds from the lower and upper mass sidebands in the ranges of  $M(B_c^+\pi^+\pi^-) < 6785 \text{ MeV}/c^2$  and  $6900 \text{ MeV}/c^2 < M(B_c^+\pi^+\pi^-) < 7500 \text{ MeV}/c^2$ , respectively. The input variables are taken to be

- $p_T(B_c^+)$ ;
- $\chi^2_{\text{vertex}}(B_c^{(*)}(2S)^+)$ ;
- angles between the  $B_c^+$  and  $\pi^+$  mesons, the  $B_c^+$  and  $\pi^-$  mesons, and the pion pair in the transverse plane;
- decay angles of the  $B_c^+$ ,  $\pi^+$  and  $\pi^-$  mesons, which are the angles between their directions after being boosted to the centre-of-mass system of  $B_c^{(*)}(2S)^+$  and the

$B_c^{(*)}(2S)^+$  direction;

- the minimum cosine value of the angles between a daughter particle of  $B_c^{(*)}(2S)^+$  and a final particle from  $B_c^+$ , after testing all pairwise combinations.

The comparisons of the input variable distributions between the signal and background are shown in Fig. 6.3. The signal and background are well distinguished in all these distributions. The same-sign sample, in which the  $B_c^+$  meson is combined with a pair of same-sign pions,  $\pi^+\pi^+$  or  $\pi^-\pi^-$ , is expected to have the same kinematics as the combinatorial backgrounds. The same as the  $B_c^+ \rightarrow \psi(2S)\pi^+$  measurement, two MLP classifiers are trained in an unbiased way as described in Sec. 5.3.2. The two classifiers show good consistency for the MLP response distribution, hence the data sub-samples applied with either of them are combined directly. The MLP response distribution of the signal candidates is transformed to an even distribution between zero and unity, while the distribution of background clusters near zero accordingly, as shown in Fig. 6.4. The candidates with the transformed MLP response smaller than 0.02 are rejected to remove a large fraction of background while keep around 98% of the signal candidates. The retained candidates are split into four categories with the MLP response value in the ranges of (0.02, 0.2), [0.2, 0.4), [0.4, 0.6) and [0.6, 1.0], respectively.

The  $M(B_c^+\pi^+\pi^-)$  distribution of candidates in the range of  $[6795, 6890] \text{ MeV}/c^2$  are shown in Fig. 6.5 for the four MLP categories, respectively. According to the simulation, the mass resolutions of  $M(B_c^+\pi^+\pi^-)$ ,  $\sigma_w$ , for the  $B_c(2S)^+$  and  $B_c^*(2S)^+$  states are determined to be  $\sigma_w(B_c(2S)^+) = 2.05 \pm 0.05 \text{ MeV}/c^2$  and  $\sigma_w(B_c^*(2S)^+) = 3.17 \pm 0.03 \text{ MeV}/c^2$ , respectively. The mass difference between the data and the simulation is taken into account by applying a scale factor obtained from the  $B_c^+ \rightarrow J/\psi\pi^+\pi^-\pi^+$  decay mode, which has the same final state as the  $B_c^{(*)}(2S)^+$  decay. No peak structure consistent with the  $B_c^{(*)}(2S)^+$  states is observed in any of the  $M(B_c^+\pi^+\pi^-)$  distributions.

## 6.4 Upper limit

With no sign of the  $B_c^{(*)}(2S)^+$  signal, upper limits are quoted on the ratio  $\mathcal{R}$  as a function of the expected  $B_c(2S)^+$  mass, taken to be in the range of  $6830 \text{ MeV}/c^2 < M(B_c^+\pi^+\pi^-) < 6890 \text{ MeV}/c^2$  according to the predictions, with different  $\Delta M$  assumptions. For the  $\Delta M = 0$  case, upper limits are set on the sum of the ratio  $\mathcal{R}$  of the  $B_c(2S)^+$  and  $B_c^*(2S)^+$  states. For the case when the  $B_c(2S)^+$  and  $B_c^*(2S)^+$  states are fully separated, the  $\Delta M$  value is fixed to  $\{15, 25, 35\} \text{ MeV}/c^2$ . For each mass point  $M$ , the upper limit is

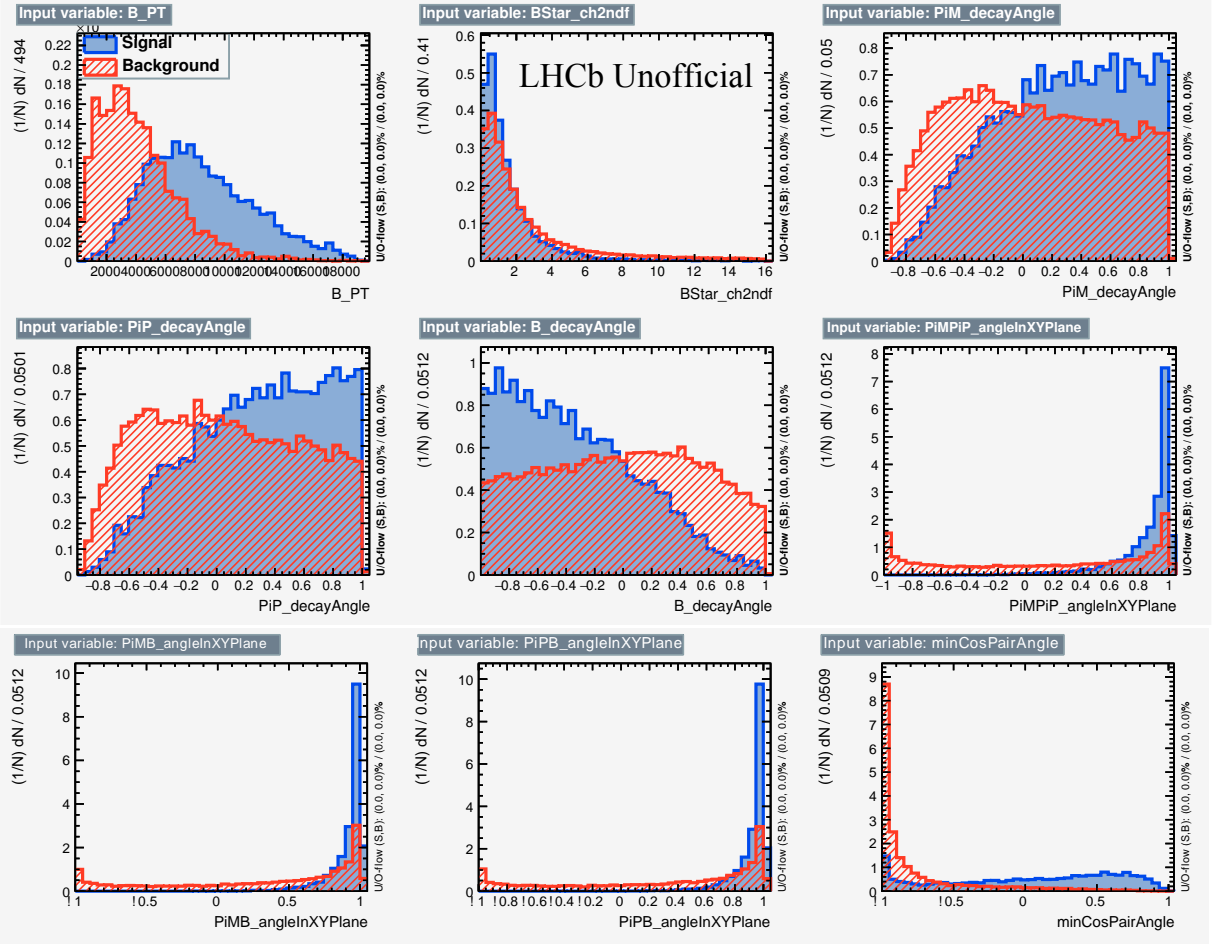


Figure 6.3 Comparisons of the distributions of the input variables for the MLP classifier between signal and background.

evaluated in the search window of  $[M - 1.4\sigma(B_c^{(*)}(2S)^+), M + 1.4\sigma(B_c^{(*)}(2S)^+)]$ , which is supposed to give the best sensitivity to signals according to Ref. [157].

The upper limits are calculated using the  $CL_s$  method<sup>[158]</sup>, in which the upper limit on the ratio  $\mathcal{R}$  is determined from the  $CL_s$  values as a function of  $\mathcal{R}$ . The statistical test is the likelihood ratio of the signal plus background hypothesis to the background-only hypothesis. It is defined as

$$Q(N_{\text{obs}}; N_S, N_B) = \frac{\mathcal{L}(N_{\text{obs}}; N_S + N_B)}{\mathcal{L}(N_{\text{obs}}; N_B)}, \quad (6-3)$$

where  $N_{\text{obs}}$  is the number of observed candidates in the search window,  $N_S$  is the expected

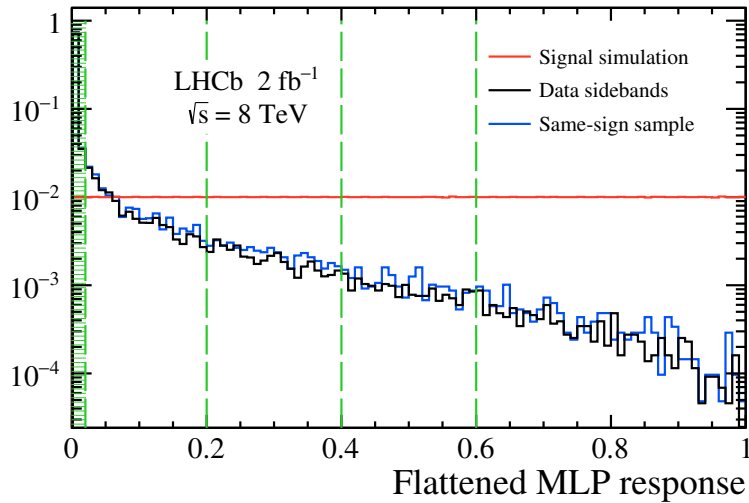


Figure 6.4 Flattened distribution of the MLP response for the signal sample from simulation, together with the distributions for the background from the sidebands and same-sign samples. The red line stands for the signal simulation, the black line the data sidebands, and the blue line the same-sign sample. The vertical green lines indicate the boundaries of the MLP categories.

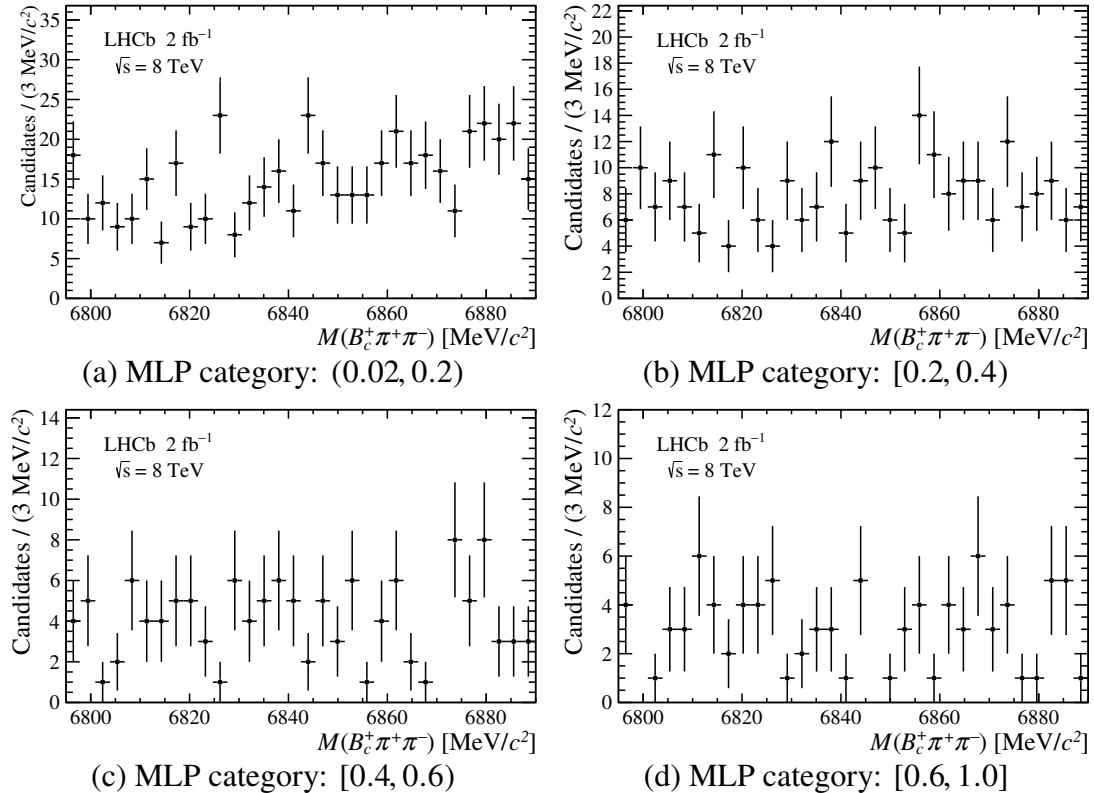


Figure 6.5 Distributions of  $M(B_c^+ \pi^+ \pi^-)$  in the range of  $[6795, 6890] \text{ MeV}/c^2$  for the four MLP categories respectively.

signal number,  $N_B$  is the expected background number, and  $\mathcal{L}$  is defined as

$$\mathcal{L}(n; x) = \frac{e^{-x}}{n!} \cdot x^n \quad (6-4)$$

according to the Poisson distribution. The statistical test values of the four MLP categories can be combined according to

$$Q_{\text{tot}} = \prod_{i=1}^4 Q_i. \quad (6-5)$$

The probability to get a  $Q_{\text{tot}}$  value smaller than the observed one under the background-only hypothesis is defined as

$$\text{CL}_b = P(\ln Q_b \leq \ln Q_{\text{obs}}), \quad (6-6)$$

where  $Q_b = Q(n_B; N_S, N_B)$  and  $Q_{\text{obs}} = Q(N_{\text{obs}}; N_S, N_B)$ . The number  $n_B$  follows a Poisson distribution with the expectation of  $N_B$ . The probability to get a  $Q_{\text{tot}}$  value smaller than the observed one under the signal plus background hypothesis is defined as

$$\text{CL}_{s+b} = P(\ln Q_{s+b} \leq \ln Q_{\text{obs}}), \quad (6-7)$$

where  $Q_{s+b} = Q(n_S + n_B; N_S, N_B)$ . The number  $n_S + n_B$  follows a Poisson distributions with the expectation of  $N_S + N_B$ . The  $\text{CL}_s$  value is calculated as

$$\text{CL}_s = \frac{\text{CL}_{s+b}}{\text{CL}_b}. \quad (6-8)$$

To calculate the  $\text{CL}_s$  value for a given ratio  $\mathcal{R}$ , the expected numbers of background and signal in the search window,  $N_B$  and  $N_S$ , are needed. According to Eq. 6-1,  $N_S$  can be determined as

$$N_S = \mathcal{R} \times N_{B_c^+} \times \frac{\varepsilon_{B_c^{(*)}(2S)^+}}{\varepsilon_{B_c^+}}, \quad (6-9)$$

in which  $\mathcal{R}$  is given and  $N_{B_c^+}$  has been determined to be  $3325 \pm 73$ . As a result, the efficiencies  $\varepsilon_{B_c^{(*)}(2S)^+}$  and  $\varepsilon_{B_c^+}$  are needed to determine  $N_S$ . When calculating the  $\text{CL}_s$  values,

Table 6.3 The efficiencies  $\varepsilon_{B_c^{(*)}(2S)^+}$  for the four MLP categories. The uncertainties come from the finite statistic of the simulated sample.

MLP category	(0.02, 0.2)	[0.2, 0.4)	[0.4, 0.6)	[0.6, 1.0]
Efficiencies in %				
$B_c(2S)^+$	$0.148 \pm 0.006$	$0.140 \pm 0.006$	$0.130 \pm 0.006$	$0.256 \pm 0.008$
$B_c^*(2S)^+$	$0.118 \pm 0.003$	$0.140 \pm 0.004$	$0.144 \pm 0.004$	$0.288 \pm 0.005$

the systematic uncertainties of all the input parameters are included. The determinations of the number  $N_B$ , the efficiencies and the systematic uncertainties are described below.

#### 6.4.1 Efficiency calculation

The efficiency  $\varepsilon_{B_c^+}$  is composed of the geometrical acceptance efficiency, the reconstruction and selection efficiency, and the trigger efficiency. The efficiency  $\varepsilon_{B_c^{(*)}(2S)^+}$  consists of the geometrical acceptance efficiency, the reconstruction and selection efficiency, the trigger efficiency, the pion identification efficiency, and the MLP categorization efficiency, which is determined for each MLP category independently. The efficiencies are all evaluated with the simulation. There is possible discrepancy between the data and the simulation in the trigger, the particle identification and the track detection efficiency. The trigger efficiencies in  $\varepsilon_{B_c^+}$  and  $\varepsilon_{B_c^{(*)}(2S)^+}$  cancel since the trigger requirements are based on the  $B_c^+$  meson. The efficiency to reconstruct and select the  $B_c^+$  meson also cancels between  $\varepsilon_{B_c^+}$  and  $\varepsilon_{B_c^{(*)}(2S)^+}$ . The remaining efficiencies need to be calibrated with the data are the track detection efficiency and the pionID efficiency of the two pions decayed from the  $B_c^{(*)}(2S)^+$  meson. The calibration procedure is the same as in the previous chapters. In conclusion, the efficiency  $\varepsilon_{B_c^+}$  is estimated to be  $0.0931 \pm 0.0005$ , in which the uncertainty comes from the finite statistic of the simulated sample. The efficiency  $\varepsilon_{B_c^{(*)}(2S)^+}$  determined with the default mass assumptions,  $M(B_c(2S)^+) = 6858 \text{ MeV}/c^2$ ,  $M(B_c^*(2S)^+) = 6890 \text{ MeV}/c^2$  and  $M(B_c^{*+}) = 6342 \text{ MeV}/c^2$ , is summarised in Table 6.3 for the four MLP categories, respectively.

The efficiency  $\varepsilon_{B_c^{(*)}(2S)^+}$  relies on the kinematics of the daughters, *i.e.*  $B_c^+$  and  $\pi^\pm$ , decayed from the  $B_c^{(*)}(2S)^+$  state, thus change with the mass assumption of the excited  $B_c$  states. The  $B_c^{(*)}(2S)^+$  mass is varied in the simulation, with which the efficiency  $\varepsilon_{B_c^{(*)}(2S)^+}$  is recalculated. The relative differences of the recalculated efficiencies to the one with  $M(B_c(2S)^+) = 6858 \text{ MeV}/c^2$  and  $M(B_c^*(2S)^+) = 6890 \text{ MeV}/c^2$  are shown in Figs. 6.6 and 6.7 for the  $B_c(2S)^+$  and  $B_c^*(2S)^+$  states, respectively. The efficiencies in the four MLP

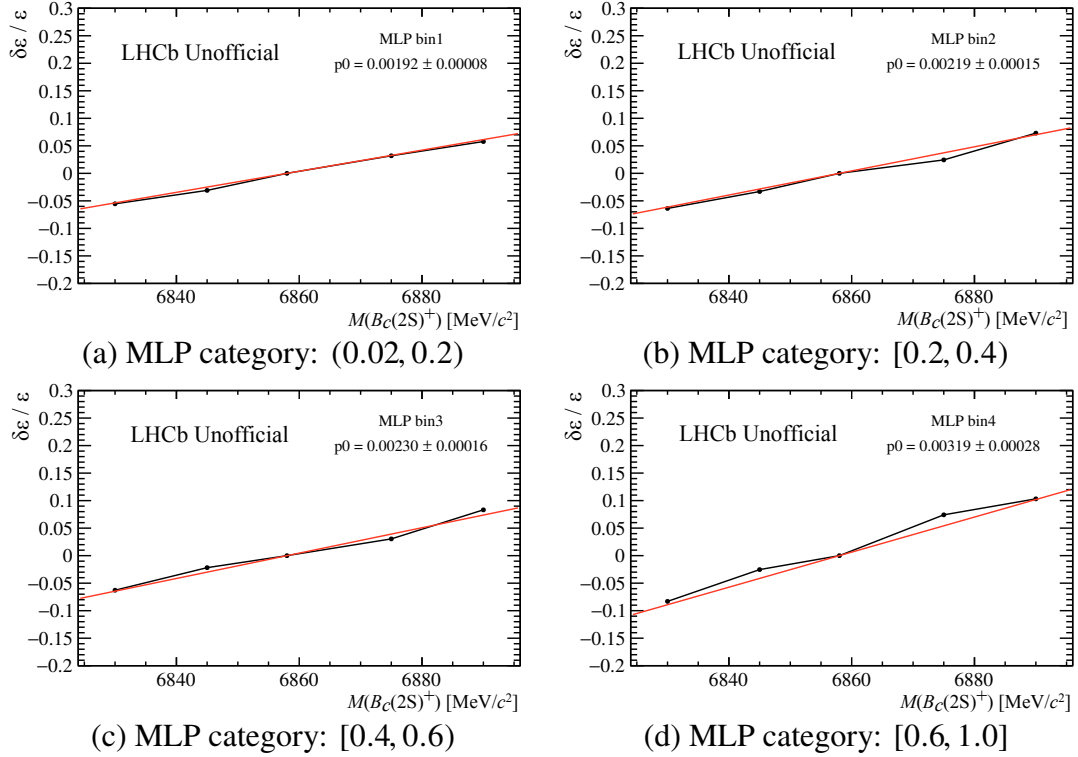


Figure 6.6 Relative differences between the efficiencies  $\epsilon_{B_c(2S)^+}$  under different mass assumptions to the efficiency with  $M(B_c(2S)^+) = 6858 \text{ MeV}/c^2$ , overlapped with a fitted linear function.

categories all change linearly with the assumed mass. Correction factors are applied to the efficiencies according to the fitted linear functions.

#### 6.4.2 Background estimation

The expected background number in the search window is estimated via extrapolation from the  $M(B_c^+\pi^+\pi^-)$  sidebands for each MLP category individually. The  $M(B_c^+\pi^+\pi^-)$  distribution of the backgrounds is modelled by an empirical function, defined as

$$F(x; t, f, c1, p1, c2, p2) = \begin{cases} 0 & x \leq t, \\ f \cdot (x-t)^{p1} \cdot \exp[-c1 \cdot (x-t)] + (1-f) \cdot (x-t)^{p2} \cdot \exp[-c2 \cdot (x-t)] & x > t \end{cases} \quad (6-10)$$

where  $t$  stands for the threshold and is taken to be  $M(B_c^+) + M(\pi^+) + M(\pi^-) = 6555 \text{ MeV}/c^2$ . The other parameters are fixed from the  $M(B_c^+\pi^+\pi^-)$  distribution of the same-sign sample, which is supposed to be consistent with the  $M(B_c^+\pi^+\pi^-)$  distribution of the combinatorial background. The fit results are shown in Fig. 6.8. The lineshapes can well describe

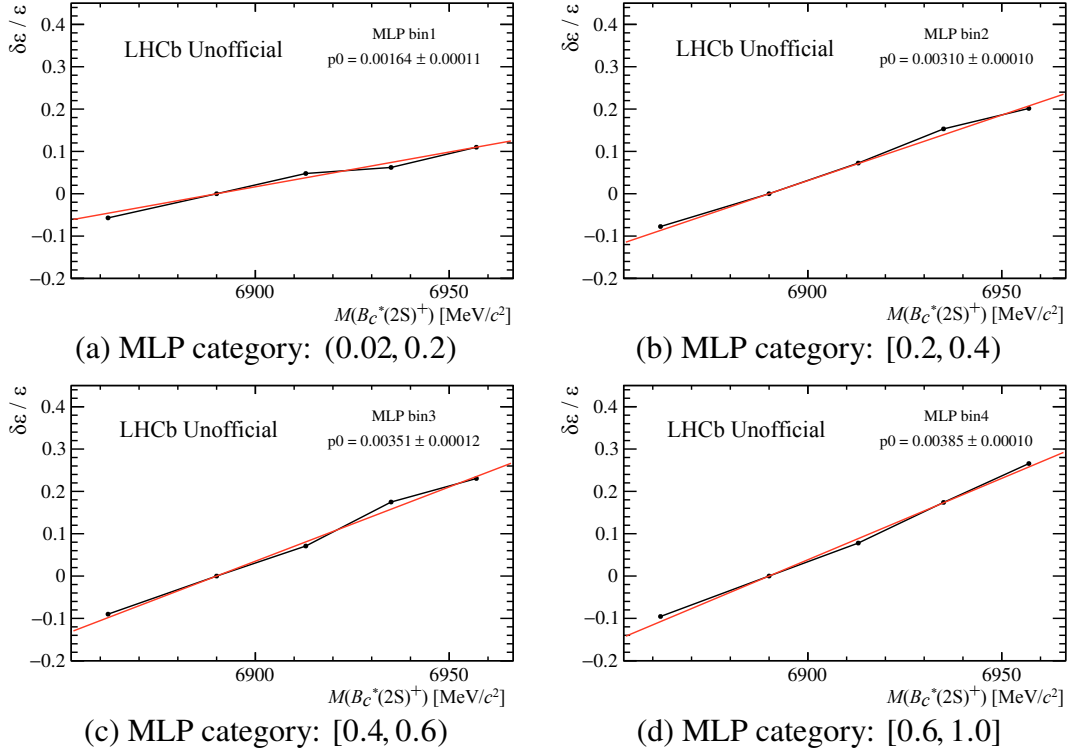


Figure 6.7 Relative differences between the efficiencies  $\varepsilon_{B_c^*(2S)^+}$  under different mass assumptions to the efficiency with  $M(B_c^*(2S)^+) = 6890 \text{ MeV}/c^2$ , overlapped with a fitted linear function.

the  $M(B_c^+\pi^+\pi^-)$  distributions of the data sample in the sidebands for all the four MLP categories.

#### 6.4.3 Systematic uncertainties

Systematic uncertainties can arise from the yield  $N(B_c^+)$ , the efficiencies  $\varepsilon_{B_c^+}$  and  $\varepsilon_{B_c^{(*)}(2S)^+}$ , and the expected background number  $N_B$ . The sources of systematic uncertainties are discussed in detail below.

##### 6.4.3.1 Uncertainty on $N(B_c^+)$

The signal shape modelling of the  $M(J/\psi\pi^+)$  distribution can introduce a systematic uncertainty to the yield  $N(B_c^+)$ . It is studied with pseudoexperiments, in which the signal shape is used to fit the simulated  $M(J/\psi\pi^+)$  distribution. The difference between the signal yield obtained from the fit and its true value is around 1.0%. A systematic uncertainty of 1.0% is assigned to the yield  $N(B_c^+)$ .

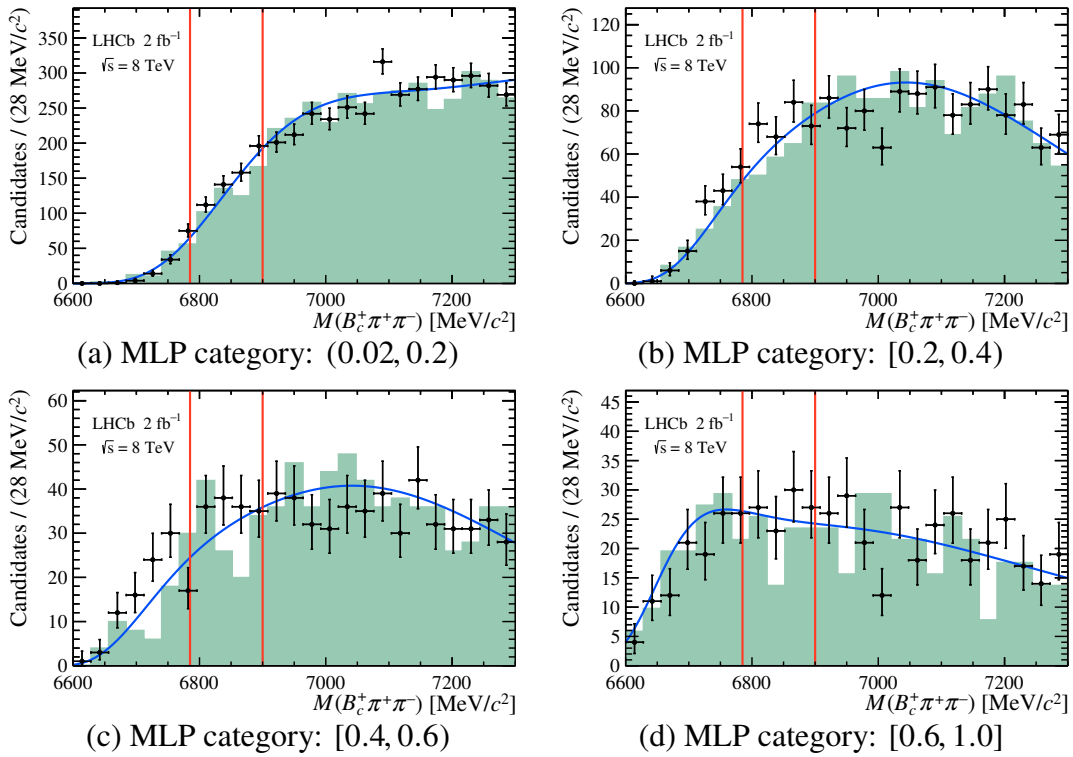


Figure 6.8 Fits to the  $B_c^+ \pi^+ \pi^-$  mass distributions of the data sample with parameters fixed from the same-sign sample for the four MLP categories, respectively.

#### 6.4.3.2 Uncertainty on efficiencies

For all the efficiencies, *i.e.*  $\varepsilon_{B_c^+}$ ,  $\varepsilon_{B_c(2S)^+}$  and  $\varepsilon_{B_c^*(2S)^+}$ , there is a systematic uncertainty due to the statistical uncertainty of the simulated sample. For the efficiencies  $\varepsilon_{B_c(2S)^+}$  and  $\varepsilon_{B_c^*(2S)^+}$ , there are three other sources of uncertainties. First is the pionID efficiency, for which uncertainties arise from the limited size of the calibration sample and the binning scheme of the single pionID efficiency table. The former is evaluated with pseudoexperiments, in which the single pionID efficiency in each pion kinematic bin is varied within its uncertainty. The latter is estimated by varying the binning scheme. The total pionID uncertainty is determined to be 0.4% for both  $\varepsilon_{B_c(2S)^+}$  and  $\varepsilon_{B_c^*(2S)^+}$ . Second is the track reconstruction efficiency of the two pions. The uncertainties are due to the finite size of the calibration sample and the choice of the event multiplicity variable. The former is estimated with pseudoexperiments, in which the single pion correction factor in each pion kinematic bin is varied within its uncertainty. The latter is evaluated by alternating the multiplicity variable. The total uncertainty on the track reconstruction efficiency is determined to be 2.2% for both the  $B_c(2S)^+$  and  $B_c^*(2S)^+$  states. Third is due to the efficiency variation for different mass assumptions. As shown in Figs. 6.6

and 6.7, the slope of the linear function to describe the dependence of the efficiency on the mass has an uncertainty. This uncertainty is propagated to the efficiencies. In addition, the  $p_T$  spectrum of the  $B_c^{(*)}(2S)^+$  state is varied by changing the setting in the BCVEGPY generator. With the variation, the efficiency  $\varepsilon_{B_c(2S)^+}$  changes by 0.6%, 1.3%, 1.8% and 2.7% for the four MLP categories, respectively. The changes are taken as the systematic uncertainties. Similarly, the corresponding uncertainties for the efficiency  $\varepsilon_{B_c^*(2S)^+}$  are 1.0%, 1.8%, 2.5% and 4.3% for the four MLP categories, respectively.

#### 6.4.3.3 Uncertainty on $N_B$

The uncertainty on the background estimation can come from the discrepancy between the data and same-sign samples, and the imperfect modelling of the empirical function. To estimate the former one, a large number of pseudosamples are generated, in which the  $M(B_c^+\pi^+\pi^-)$  distribution in the sideband ranges of [6600, 6785] MeV/ $c^2$  and [6900, 7300] MeV/ $c^2$  is simulated according to the data sample, and the distribution in the signal region of [6785, 6900] MeV/ $c^2$  is taken from the same-sign sample. The pseudosamples are used to fix the background shape instead of the same-sign sample. The number of expected background candidates within [6785, 6900] MeV/ $c^2$  obtained from these fits follows a Gaussian distribution. The difference between the Gaussian mean value and the number derived from the nominal fit is taken as the uncertainty, which is determined to be 4.2%, 7.0%, 11.8% and 6.1% for the four MLP categories respectively. For the latter uncertainty source, an alternative empirical function, the Bukin function, is used. The expected background number changes by 0.5%, 5.6%, 9.2% and 3.2% for the four MLP categories respectively. The total uncertainty is taken to be the quadratic sum of the two sources.

#### 6.4.3.4 Summary

All the systematic uncertainties that will enter the upper limit calculation are summarised in Table. 6.4.

#### 6.4.4 Upper limit calculation

To determine the upper limit for a certain mass assumption, the ratio  $\mathcal{R}$  is varied in steps. For a given value of  $\mathcal{R}$ , according to Eq. 6-9, the number  $N_S$  can be determined with the efficiencies. The number  $N_B$  has also been obtained. A large number of

Table 6.4 Summary of the systematic uncertainties for the upper limit calculation. The uncertainties on the efficiencies due to the efficiency variation with different mass assumptions are given individually.

MLP category	(0.02, 0.2)	[0.2, 0.4)	[0.4, 0.6)	[0.6, 1.0]
$N_{B_c^+}$		1.0%		
$\varepsilon_{B_c^+}$		0.5%		
$N_B$	4.2%	9.0%	15.0%	6.9%
$B_c(2S)^+ \rightarrow B_c^+ \pi^+ \pi^-$				
$\varepsilon_{B_c(2S)^+}$	4.6%	4.7%	4.9%	3.6%
Efficiency variation vs. $M(B_c(2S)^+)$	0.6%	1.3%	1.8%	2.7%
$B_c^*(2S)^+ \rightarrow B_c^{*+} \pi^+ \pi^-$				
$\varepsilon_{B_c^*(2S)^+}$	3.5%	3.3%	3.3%	2.7%
Efficiency variation vs. $M(B_c^*(2S)^+)$	1.0%	1.8%	2.5%	4.3%

 Table 6.5 The expected background number and the observed candidate number in the scan window for the  $B_c(2S)^+$  and  $B_c^*(2S)^+$  states in the four MLP categories, respectively, when assuming  $M = 6858 \text{ MeV}/c^2$  and  $\Delta M = 35 \text{ MeV}/c^2$ .

MLP category	(0.02, 0.2)	[0.2, 0.4)	[0.4, 0.6)	[0.6, 1.0]
$B_c(2S)^+$ at $6858 \text{ MeV}/c^2$				
$N_B$	$30.0 \pm 1.4$	$13.9 \pm 1.3$	$6.5 \pm 1.0$	$4.9 \pm 0.4$
$N_{\text{obs}}$	33	24	4	4
$B_c^*(2S)^+$ at $6823 \text{ MeV}/c^2$				
$N_B$	$33.5 \pm 1.5$	$18.6 \pm 1.8$	$8.9 \pm 1.4$	$7.7 \pm 0.7$
$N_{\text{obs}}$	41	20	9	12

pseudoexperiments are performed under the background-only hypothesis, in which the values of  $Q_b$  and  $Q_{\text{obs}}$  are compared. By counting the number of pseudoexperiments in which the  $Q_b$  value is smaller than the value of  $Q_{\text{obs}}$ , the probability  $\text{CL}_b$  is determined. Similarly, the probability  $\text{CL}_{s+b}$  is determined from pseudoexperiments under the signal plus background hypothesis. The  $\text{CL}_s$  value is calculated as the ratio of  $\text{CL}_{s+b}$  to  $\text{CL}_b$ .

Taking the case with  $M = 6858 \text{ MeV}/c^2$  and  $\Delta M = 35 \text{ MeV}/c^2$  as an example, the expected background number and the observed candidate number in the scan window for the  $B_c(2S)^+$  and  $B_c^*(2S)^+$  states are listed in Table 6.5 for the four MLP categories, respectively. The  $\mathcal{R}$  versus  $\text{CL}_s$  curve is shown in Fig. 6.9. The data is consistent with background-only assumption.

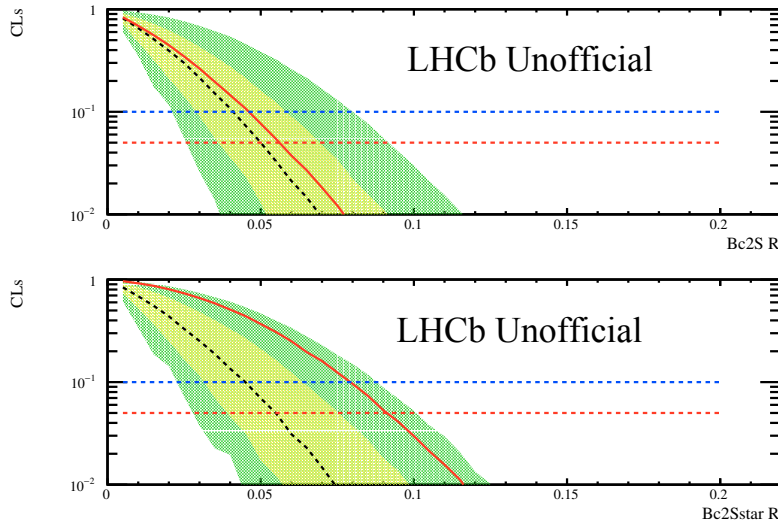


Figure 6.9 The  $\mathcal{R}$  versus  $CL_s$  curve with  $M = 6858 \text{ MeV}/c^2$  and  $\Delta M = 35 \text{ MeV}/c^2$ . The red solid line is the observed  $CL_s$  curve. The black dashed line is the expected  $CL_s$  curve under the background-only hypothesis. The yellow and green area are the  $1\sigma$  and  $2\sigma$  confidence regions of the expected  $CL_s$  curve respectively. The blue and red dashed horizontal line represent the 90% and 95% confidence levels, respectively.

#### 6.4.5 Result

The upper limits on  $\mathcal{R}(B_c^{(*)}(2S)^+)$  at 95% and 90% confidence levels under all mass hypotheses are shown in Fig. 6.10. The ratio  $\mathcal{R}$  is predicted to be not significantly dependent on the kinematics of the  $B_c^+$  mesons<sup>[91]</sup>. It enables the comparison of this analysis to the ATLAS measurement<sup>[20]</sup>. For the overlapping case, the sum of the  $\mathcal{R}$  values of the  $B_c(2S)^+$  and  $B_c^*(2S)^+$  states is compared to the ATLAS result. For the separated case, it is most probable that the ATLAS observation corresponds to the  $B_c^*(2S)^+$  state, as the production cross-section of the  $B_c^*(2S)^+$  state is expected to be more than twice the cross-section of the  $B_c(2S)^+$  state<sup>[19,91,159,160]</sup>. Therefore, the  $\mathcal{R}$  value of the  $B_c^*(2S)^+$  state is compared to the ATLAS result. Considering both cases, the comparison between the upper limits on  $\mathcal{R}$  determined by LHCb in the mass region around the ATLAS signal peak at  $M(B_c^{(*)}(2S)^+) = 6842 \text{ MeV}/c^2$  and the ratio  $\mathcal{R}$  measured by ATLAS is shown in Table 6.6. The ATLAS measurement didn't quote any efficiency, then the ratio  $\mathcal{R}$  from ATLAS contains an unknown relative efficiency  $\varepsilon_{7,8}$ , which are the efficiencies to reconstruct the  $B_c^{(*)}(2S)^+$  meson from the  $B_c^+$  meson for 7 and 8 TeV, respectively. The LHCb and ATLAS results are consistent if the relative efficiency  $\varepsilon_8$  at ATLAS is very large.

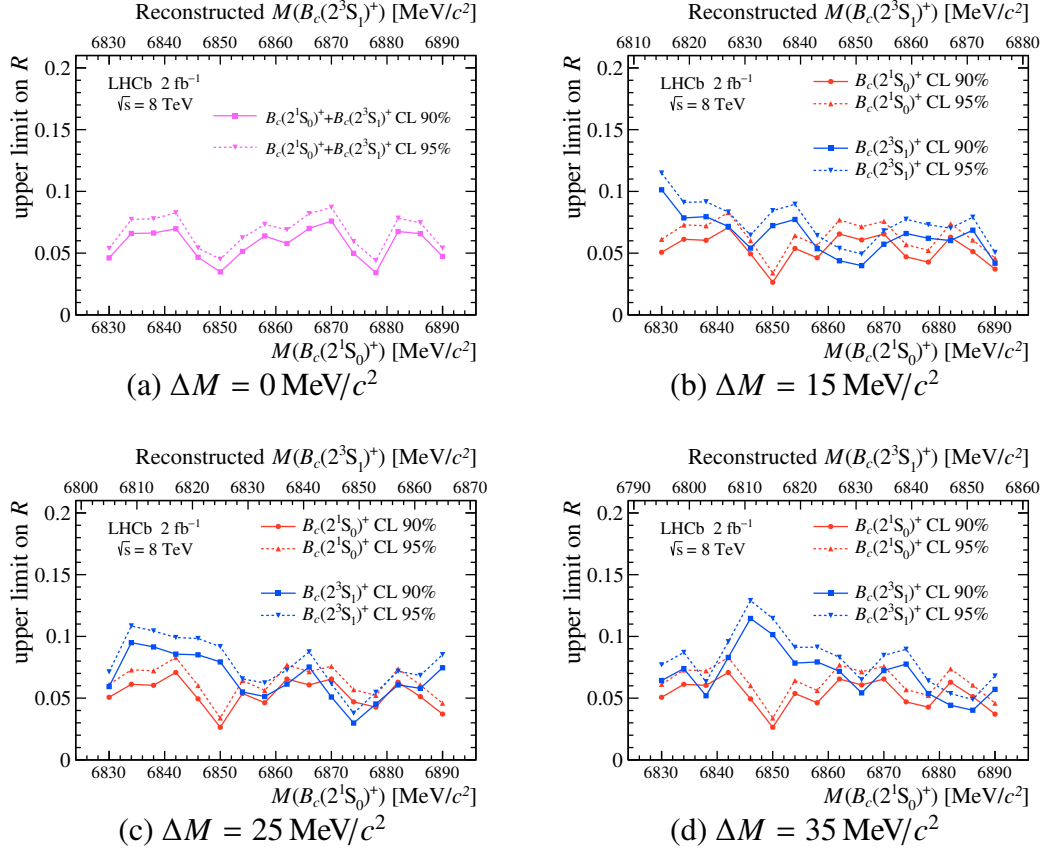


Figure 6.10 The upper limits on  $\mathcal{R}(B_c^{(*)}(2S)^+)$  at 95% and 90% confidence levels under different mass splitting  $\Delta M$  hypotheses. The various line styles are indicated in the legends.

Table 6.6 Comparison between the upper limits on  $\mathcal{R}$  determined by LHCb at 95% confidence level and the ratio  $\mathcal{R}$  measured by ATLAS<sup>[20]</sup>, in which  $0 < \varepsilon_{7,8} \leq 1$  represent the efficiencies to reconstruct the  $B_c^{(*)}(2S)^+$  meson on basis of the  $B_c^+$  meson for 7 and 8 TeV, respectively.

	$\sqrt{s} = 7 \text{ TeV}$	$\sqrt{s} = 8 \text{ TeV}$
ATLAS	$(0.22 \pm 0.08 \text{ (stat)})/\varepsilon_7$	$(0.15 \pm 0.06 \text{ (stat)})/\varepsilon_8$
LHCb	—	$< [0.04, 0.09]$

## Chapter 7 Summary and prospects

In summary, measurements of charmonium production and the  $B_c$  mesons are performed with the  $pp$  collision data collected by the LHCb experiment, providing tests of various QCD models, especially those implemented under the NRQCD framework.

In  $pp$  collisions, heavy quarkonium production can be factorized into two stages: the perturbative creation of the  $Q\bar{Q}$  pair, and the non-perturbative hadronisation of the  $Q\bar{Q}$  pair into quarkonium. The description of the non-perturbative process relies on experimental inputs. The experimental studies can also test the perturbative calculations. The  $J/\psi$  production cross-section in  $pp$  collisions at  $\sqrt{s} = 13$  TeV is measured for  $J/\psi$  mesons in the kinematic range of  $p_T < 14$  GeV/c and  $2.0 < y < 4.5$ , with data corresponding to an integrated luminosity of  $3.05 \text{ pb}^{-1}$ . The double differential cross-sections as functions of  $p_T$  and  $y$  of the  $J/\psi$  mesons are measured separately for prompt  $J/\psi$  mesons and  $J/\psi$  mesons from  $b$ -hadron decays, assuming that prompt  $J/\psi$  mesons are unpolarised. The total production cross-sections integrated in the kinematic coverage are measured to be

$$\sigma(\text{prompt } J/\psi, p_T < 14 \text{ GeV/c}, 2 < y < 4.5) = 15.03 \pm 0.03 \text{ (stat)} \pm 0.91 \text{ (syst)} \mu\text{b}$$

and

$$\sigma(J/\psi \text{ from } b, p_T < 14 \text{ GeV/c}, 2 < y < 4.5) = 2.25 \pm 0.01 \text{ (stat)} \pm 0.13 \text{ (syst)} \mu\text{b}$$

for prompt  $J/\psi$  mesons and  $J/\psi$  mesons from  $b$ -hadron decays, respectively. The prompt  $J/\psi$  production cross-sections are consistent with the NRQCD predictions at NLO<sup>[22]</sup>, and the production cross-sections of  $J/\psi$  mesons from  $b$ -hadron decays are in good agreement with the FONLL calculations<sup>[96]</sup>. The ratios of the differential production cross-sections as functions of  $J/\psi$   $p_T$  and  $y$  at  $\sqrt{s} = 13$  TeV to those at  $\sqrt{s} = 8$  TeV are determined to benefit from the cancellation of uncertainties both theoretically and experimentally. The cross-section ratios for prompt  $J/\psi$  mesons agree well with the NRQCD calculation at NLO<sup>[22]</sup>, while the FONLL calculations<sup>[96]</sup> slightly underestimate the cross-section ratios.

Quarkonium pairs can be produced either through the DPS process or the SPS process in  $pp$  collisions. In SPS, the mechanism to produce two  $Q\bar{Q}$  pairs is different from that

to produce a single  $Q\bar{Q}$  pair, while the quarkonium hadronisation process is common. Measurements of quarkonium pair production can act as a new way to test the QCD models. DPS is an intriguing process, since it can probe the parton transverse profile inside the proton, and help determine the contributions from various crucial backgrounds in the search for new physics. The key parameter in DPS, the effective cross-section  $\sigma_{\text{eff}}$ , which is assumed to be universal, shows a large variation in the previous measurements. Measurements of the  $J/\psi$  pair production in the DPS process at LHCb can provide important inputs to the DPS study. The  $J/\psi$  pair production cross-section in  $pp$  collisions at  $\sqrt{s} = 13$  TeV is measured to be  $\sigma(J/\psi J/\psi) = 15.2 \pm 1.0 \text{ (stat)} \pm 0.9 \text{ (syst)} \text{ nb}$  for  $J/\psi$  mesons in the kinematic range of  $p_T < 10 \text{ GeV}/c$  and  $2.0 < y < 4.5$ , with data corresponding to an integrated luminosity of  $279 \text{ pb}^{-1}$ . The differential production cross-sections as functions of several kinematic variables of the  $J/\psi$  pair are determined. Clear evidence of the DPS contribution is shown in the differential cross-sections as functions of  $\Delta y$  and  $m(J/\psi J/\psi)$ . The SPS and DPS components are separated by performing templated SPS plus DPS fits to the differential cross-sections based on various SPS models. The DPS contribution leads to the values of the effective cross-section  $\sigma_{\text{eff}}$  within 8.8 and 12.5 mb. The measured SPS cross-section is smaller than the predictions of the NLO\* CS''<sup>[47,117–120]</sup> and NLO CS<sup>[46]</sup> models, and is roughly in agreement with the NLO\* CS'<sup>[115]</sup> and LO  $k_T$ <sup>[136]</sup> calculations.

The decays of the  $B_c^+$  meson and the  $B_c$  spectroscopy are described by various QCD models, which can be tested by measurements. The branching fraction ratio  $\mathcal{B}(B_c^+ \rightarrow \psi(2S)\pi^+)/\mathcal{B}(B_c^+ \rightarrow J/\psi\pi^+)$  is measured to be  $R = 0.268 \pm 0.032 \text{ (stat)} \pm 0.007 \text{ (syst)} \pm 0.006(\mathcal{B})$  with the  $pp$  collision data at  $\sqrt{s} = 7$  TeV and 8 TeV, corresponding to integrated luminosities of  $1 \text{ fb}^{-1}$  and  $2 \text{ fb}^{-1}$ , respectively. The result favours the calculations of NRQCD at NLO<sup>[58]</sup> and the  $k_T$  factorization method<sup>[60]</sup>. The predictions of various relativistic quark models<sup>[61–63]</sup> tend to underestimate the result.

The  $B_c(2^1S_0)^+$  and  $B_c(2^3S_1)^+$  states are searched for in the  $B_c^+\pi^+\pi^-$  mass spectrum, using the data at  $\sqrt{s} = 8$  TeV corresponding to an integrated luminosity of  $2 \text{ fb}^{-1}$ . The  $B_c(2^1S_0)^+$  and  $B_c(2^3S_1)^+$  states are searched for in the mass ranges of  $[6830, 6890] \text{ MeV}/c^2$  and  $[6795, 6890] \text{ MeV}/c^2$  according to the theoretical predictions, respectively. No evidence of either state is found. Upper limits are set on the product of the  $B_c^{(*)}(2S)^+$  production cross-section and the branching fraction of the decay  $B_c^{(*)}(2S)^+ \rightarrow B_c^+\pi^+\pi^-$  relative to the  $B_c^+$  production cross-section for different assumptions of the  $B_c^{(*)}(2S)^+$

masses. The upper limits are determined to be within 0.02 and 0.14 at 95% confidence level. They are consistent with the ATLAS measurement if the efficiency to reconstruct the  $B_c^{(*)}(2S)^+$  meson from the  $B_c^+$  meson at ATLAS, which is not published, is very large.

By the end of 2018, the LHCb experiment is expected to collect a total amount of data corresponding to integrated luminosities of  $1\text{ fb}^{-1}$  at  $\sqrt{s} = 7\text{ TeV}$ ,  $2\text{ fb}^{-1}$  at  $\sqrt{s} = 8\text{ TeV}$ , and  $5\text{ fb}^{-1}$  at  $\sqrt{s} = 13\text{ TeV}$ . The huge amount of data opens opportunities for many kinds of further experimental studies of quarkonium production and the  $B_c$  mesons. The measurement of the  $J/\psi$  polarisation in  $pp$  collisions at  $\sqrt{s} = 13\text{ TeV}$  is another good test of the NRQCD approach. Measurements of the production cross-sections of heavy quarkonium other than  $J/\psi$ , *e.g.* the  $\psi(2S)$ ,  $\Upsilon$  and  $\eta_c$  mesons, in  $pp$  collisions at  $\sqrt{s} = 13\text{ TeV}$  are also on the way. Using the whole Run2 data, the statistic of the  $J/\psi$  pair candidates will increase by more than 15 times. The uncertainties of the differential production cross-sections of  $J/\psi$  pair can be significantly suppressed. It is also possible to measure the double differential production cross-sections of  $J/\psi$  pair which can reveal more about the production mechanism. Several new quarkonium pair channels, *e.g.*  $\Upsilon + J/\psi$  and  $\Upsilon$  pair, stand a good chance to be discovered. Measurements of their production cross-sections are helpful to both the test of the NRQCD approach and the exploration of the DPS mechanism. With the largely increased sample size, there is even possibility to observe triple quarkonium production. The production cross-section of the  $B_c^+$  meson at the centre-of-mass energy of  $\sqrt{s} = 13\text{ TeV}$  is expected to be roughly twice that at  $\sqrt{s} = 7$  and  $8\text{ TeV}$ . With the full dataset, the statistic of the  $B_c^+$  meson will be more than four times that of the Run1 dataset only. For the  $B_c^+$  decays, the statistical uncertainties of the existing branching fraction ratio measurements can be halved, and it will be possible to discover many new channels. The search for the  $B_c(2^1S_0)^+$  and  $B_c(2^3S_1)^+$  states can be performed with a data sample corresponding to a statistic around 6.5 times larger than that used in this dissertation. There is a good chance to observe the excited  $B_c^+$  states. These emerging experimental results can help further develop the QCD models and improve our understanding of QCD.

## References

- [1] Gell-Mann, Murray. *A Schematic Model of Baryons and Mesons*. Phys. Lett., 1964, 8:214–215.
- [2] Glashow, Sheldon L. *The renormalizability of vector meson interactions*. Nucl. Phys., 1959, 10:107–117.
- [3] Salam, Abdus and Ward, John Clive. *Weak and electromagnetic interactions*. Nuovo Cim., 1959, 11:568–577.
- [4] Weinberg, Steven. *A Model of Leptons*. Phys. Rev. Lett., 1967, 19:1264–1266.
- [5] Glashow, S. L. and Iliopoulos, J. and Maiani, L. *Weak Interactions with Lepton-Hadron Symmetry*. Phys. Rev., 1970, D2:1285–1292.
- [6] Kobayashi, Makoto and Maskawa, Toshihide. *CP Violation in the Renormalizable Theory of Weak Interaction*. Prog. Theor. Phys., 1973, 49:652–657.
- [7] Aubert, J. J. and others. *Experimental Observation of a Heavy Particle J*. Phys. Rev. Lett., 1974, 33:1404–1406.
- [8] Augustin, J. E. and others. *Discovery of a Narrow Resonance in  $e^+e^-$  Annihilation*. Phys. Rev. Lett., 1974, 33:1406–1408. [Adv. Exp. Phys. 5, 141(1976)].
- [9] Perl, Martin L. and others. *Evidence for Anomalous Lepton Production in  $e^+ - e^-$  Annihilation*. Phys. Rev. Lett., 1975, 35:1489–1492. [, 193(1975)].
- [10] Herb, S. W. and others. *Observation of a Dimuon Resonance at 9.5-GeV in 400-GeV Proton-Nucleus Collisions*. Phys. Rev. Lett., 1977, 39:252–255.
- [11] Arnison, G. and others. *Experimental Observation of Isolated Large Transverse Energy Electrons with Associated Missing Energy at  $s^{**}(1/2) = 540$ -GeV*. Phys. Lett., 1983, B122:103–116. [, 611(1983)].
- [12] Arnison, G. and others. *Experimental Observation of Lepton Pairs of Invariant Mass Around 95-GeV/c $^{**2}$  at the CERN SPS Collider*. Phys. Lett., 1983, B126:398–410. [, 7.55(1983)].
- [13] Banner, M. and others. *Observation of Single Isolated Electrons of High Transverse Momentum in Events with Missing Transverse Energy at the CERN anti-p p Collider*. Phys. Lett., 1983, B122:476–485. [, 7.45(1983)].
- [14] Bagnaia, P. and others. *Evidence for  $Z0 \rightarrow e^+ e^-$  at the CERN anti-p p Collider*. Phys. Lett., 1983, B129:130–140. [, 7.69(1983)].
- [15] Chatrchyan, Serguei and others. *Observation of a new boson at a mass of 125 GeV with the CMS experiment at the LHC*. Phys. Lett., 2012, B716:30–61.
- [16] Aad, Georges and others. *Observation of a new particle in the search for the Standard Model Higgs boson with the ATLAS detector at the LHC*. Phys. Lett., 2012, B716:1–29.
- [17] Patrignani, C. and others. *Review of particle physics*. Chin. Phys., 2016, C40:100001. and 2017 update.
- [18] Colangelo, Pietro and Khodjamirian, Alexander. *QCD sum rules, a modern perspective*. 2000. 1495–1576.

[19] Godfrey, Stephen. *Spectroscopy of  $B_c$  mesons in the relativized quark model*. Phys. Rev., 2004, D70:054017.

[20] Aad, Georges and others. *Observation of an excited  $B_c^\pm$  meson state with the ATLAS detector*. Phys. Rev. Lett., 2014, 113:212004.

[21] Bodwin, Geoffrey T. and Braaten, Eric and Lepage, G. Peter. *Rigorous QCD analysis of inclusive annihilation and production of heavy quarkonium*. Phys. Rev., 1995, D51:1125–1171. [Erratum: Phys. Rev.D55,5853(1997)].

[22] Shao, Hua-Sheng and Han, Hao and Ma, Yan-Qing and Meng, Ce and Zhang, Yu-Jie and Chao, Kuang-Ta. *Yields and polarizations of prompt  $J/\psi$  and  $\psi(2S)$  production in hadronic collisions*. JHEP, 2015, 05:103.

[23] Einhorn, M. B. and Ellis, S. D. *Hadronic Production of the New Resonances - Are Gluons Important?* Phys. Rev. Lett., 1975, 34:1190–1193.

[24] Yang, Chen-Ning. *Selection Rules for the Dematerialization of a Particle Into Two Photons*. Phys. Rev., 1950, 77:242–245.

[25] Abe, F. and others.  *$J/\psi$  and  $\psi(2S)$  Production in  $p\bar{p}$  Collisions at  $\sqrt{s} = 1.8$  TeV*. Phys. Rev. Lett., 1997, 79:572–577.

[26] Aaij, R. and others. *Measurement of  $J/\psi$  production in  $pp$  collisions at  $\sqrt{s} = 2.76$  TeV*. JHEP, 2013, 02:041.

[27] Aaij, R. and others. *Measurement of  $J/\psi$  production in  $pp$  collisions at  $\sqrt{s} = 7$  TeV*. Eur. Phys. J., 2011, C71:1645.

[28] Aaij, R. and others. *Production of  $J/\psi$  and  $\Upsilon$  mesons in  $pp$  collisions at  $\sqrt{s} = 8$  TeV*. JHEP, 2013, 06:064.

[29] Aaij, R. and others. *Measurement of  $J/\psi$  polarization in  $pp$  collisions at  $\sqrt{s} = 7$  TeV*. Eur. Phys. J., 2013, C73:2631.

[30] Aad, Georges and others. *Measurement of the differential cross-sections of prompt and non-prompt production of  $J/\psi$  and  $\psi(2S)$  in  $pp$  collisions at  $\sqrt{s} = 7$  and 8 TeV with the ATLAS detector*. Eur. Phys. J., 2016, C76(5):283.

[31] Khachatryan, Vardan and others. *Prompt and non-prompt  $J/\psi$  production in  $pp$  collisions at  $\sqrt{s} = 7$  TeV*. Eur. Phys. J., 2011, C71:1575.

[32] Chatrchyan, Serguei and others.  *$J/\psi$  and  $\psi_{2S}$  production in  $pp$  collisions at  $\sqrt{s} = 7$  TeV*. JHEP, 2012, 02:011.

[33] Abelev, B. and others. *Inclusive  $J/\psi$  production in  $pp$  collisions at  $\sqrt{s} = 2.76$  TeV*. Phys. Lett., 2012, B718:295–306. [Erratum: Phys. Lett.B748,472(2015)].

[34] Aamodt, K. and others. *Rapidity and transverse momentum dependence of inclusive  $J/\psi$  production in  $pp$  collisions at  $\sqrt{s} = 7$  TeV*. Phys. Lett., 2011, B704:442–455. [Erratum: Phys. Lett.B718,692(2012)].

[35] Aaij, R. and others. *Measurement of the relative rate of prompt  $\chi_{c0}$ ,  $\chi_{c1}$  and  $\chi_{c2}$  production at  $\sqrt{s} = 7$  TeV*. JHEP, 2013, 10:115.

[36] Aaij, R. and others. *Measurement of the  $\chi_b(3P)$  mass and of the relative rate of  $\chi_{b1}(1P)$  and  $\chi_{b2}(1P)$  production*. JHEP, 2014, 10:088.

[37] Aaij, R. and others. *Measurement of the  $\eta_c(1S)$  production cross-section in proton-proton collisions via the decay  $\eta_c(1S) \rightarrow p\bar{p}$* . Eur. Phys. J., 2015, C75:311.

[38] Sirunyan, A. M. and others. *Measurement of quarkonium production cross sections in pp collisions at  $\sqrt{s} = 13$  TeV*. Phys. Lett., 2018, B780:251–272.

[39] Aaij, R and others. *Measurement of  $\psi(2S)$  meson production in pp collisions at  $\sqrt{s} = 7$  TeV*. Eur. Phys. J., 2012, C72:2100.

[40] Ma, Yan-Qing and Wang, Kai and Chao, Kuang-Ta. *A complete NLO calculation of the  $J/\psi$  and  $\psi'$  production at hadron colliders*. Phys. Rev., 2011, D84:114001.

[41] Abulencia, A. and others. *Polarization of  $J/\psi$  and  $\psi(2S)$  mesons produced in  $p\bar{p}$  collisions at  $\sqrt{s} = 1.96$  TeV*. Phys. Rev. Lett., 2007, 99:132001.

[42] Abelev, Betty and others.  *$J/\psi$  polarization in pp collisions at  $\sqrt{s} = 7$  TeV*. Phys. Rev. Lett., 2012, 108:082001.

[43] Chatrchyan, Serguei and others. *Measurement of the prompt  $J/\psi$  and  $\psi(2S)$  polarizations in pp collisions at  $\sqrt{s} = 7$  TeV*. Phys. Lett., 2013, B727:381–402.

[44] Aaij, R and others. *Measurement of  $J/\psi$  polarization in pp collisions at  $\sqrt{s} = 7$  TeV*. Eur. Phys. J., 2013, C73(11):2631.

[45] Chao, Kuang-Ta and Ma, Yan-Qing and Shao, Hua-Sheng and Wang, Kai and Zhang, Yu-Jie.  *$J/\psi$  Polarization at Hadron Colliders in Nonrelativistic QCD*. Phys. Rev. Lett., 2012, 108:242004.

[46] Sun, Li-Ping and Han, Hao and Chao, Kuang-Ta. *Impact of  $J/\psi$  pair production at the LHC and predictions in nonrelativistic QCD*. Phys. Rev., 2016, D94:074033.

[47] Lansberg, Jean-Philippe and Shao, Hua-Sheng.  *$J/\psi$ -pair production at large momenta: indications for double parton scatterings and large  $\alpha_s^5$  contributions*. Phys. Lett., 2015, B751:479.

[48] Aaboud, Morad and others. *Measurement of the prompt  $J/\psi$  pair production cross-section in pp collisions at  $\sqrt{s} = 8$  TeV with the ATLAS detector*. Eur. Phys. J., 2017, C77(2):76.

[49] Abe, F. and others. *Observation of the  $B_c$  meson in  $p\bar{p}$  collisions at  $\sqrt{s} = 1.8$  TeV*. Phys. Rev. Lett., 1998, 81:2432–2437.

[50] Abe, F. and others. *Observation of  $B_c$  mesons in  $p\bar{p}$  collisions at  $\sqrt{s} = 1.8$  TeV*. Phys. Rev., 1998, D58:112004.

[51] Altonen, T. and others. *Observation of the decay  $B_c^\pm \rightarrow J/\psi \pi^\pm$  and measurement of the  $B_c^\pm$  mass*. Phys. Rev. Lett., 2008, 100:182002.

[52] Aaij, R. and others. *First observation of the decay  $B_c^+ \rightarrow J/\psi \pi^+ \pi^- \pi^+$* . Phys. Rev. Lett., 2012, 108:251802.

[53] Aaij, R. and others. *Observation of the decay  $B_c^+ \rightarrow \psi(2S) \pi^+$* . Phys. Rev., 2013, D87:071103(R).

[54] Aaij, R. and others. *Observation of  $B_c^+ \rightarrow J/\psi D_s^+$  and  $B_c^+ \rightarrow J/\psi D_s^{*+}$  decays*. Phys. Rev., 2013, D87:112012.

[55] Aaij, R. and others. *First observation of the decay  $B_c^+ \rightarrow J/\psi K^+$* . JHEP, 2013, 09:075.

[56] Aaij, R. and others. *Observation of the decay  $B_c^+ \rightarrow B_s^0 \pi^+$* . Phys. Rev. Lett., 2013, 111:181801.

[57] Aaij, R. and others. *Observation of the decay  $B_c^+ \rightarrow J/\psi K^+ K^- \pi^+$* . JHEP, 2013, 11:094.

[58] Qiao, Cong-Feng and Sun, Peng and Yang, Deshan and Zhu, Rui-Lin.  *$B_c$  Exclusive Decays to Charmonia and Light Mesons in QCD Factorization at Next-to-Leading Order Accuracy*. Phys. Rev., 2014, D89:034008.

[59] Chang, Chao-Hsi and Chen, Yu-Qi. *Decays of the  $B_c$  meson*. Phys. Rev., 1994, D49:3399–3411.

[60] Rui, Zhou and Wang, Wen-Fei and Wang, Guang-xin and Song, Li-hua and Lu, Cai-Dian. *The  $B_c \rightarrow \psi(2S)\pi, \eta_c(2S)\pi$  decays in the perturbative QCD approach*. 2015..

[61] Liu, Jia-Fu and Chao, Kuang-Ta.  *$B(c)$  meson weak decays and CP violation*. Phys. Rev., 1997, D56:4133–4145.

[62] Ebert, D. and Faustov, R. N. and Galkin, V. O. *Weak decays of the  $B/c$  meson to charmonium and D mesons in the relativistic quark model*. Phys. Rev., 2003, D68:094020.

[63] Colangelo, Pietro and De Fazio, Fulvia. *Using heavy quark spin symmetry in semileptonic  $B/c$  decays*. Phys. Rev., 2000, D61:034012.

[64] Gershtein, S. S. and Kiselev, V. V. and Likhoded, A. K. and Slabospitsky, S. R. and Tkabladze, A. V. *Production cross-section and spectroscopy of  $B_c$  mesons*. Sov. J. Nucl. Phys., 1988, 48:327.

[65] Chen, Yu-Qi and Kuang, Yu-Ping. *Improved QCD-motivated heavy quark potentials with explicit  $\Lambda_{\overline{\text{MS}}}$  dependence*. Phys. Rev., 1992, D46:1165–1171.

[66] Eichten, Estia J. and Quigg, Chris. *Mesons with beauty and charm: spectroscopy*. Phys. Rev., 1994, D49:5845–5856.

[67] Kiselev, V. V. and Likhoded, A. K. and Tkabladze, A. V.  *$B_c$  spectroscopy*. Phys. Rev., 1995, D51:3613–3627.

[68] Gupta, Suraj N. and Johnson, James M.  *$B_c$  spectroscopy in a quantum-chromodynamic potential model*. Phys. Rev., 1996, D53:312–314.

[69] Fulcher, Lewis P. *Phenomenological predictions of the properties of the  $B_c$  system*. Phys. Rev., 1999, D60:074006.

[70] Ebert, D. and Faustov, R. N. and Galkin, V. O. *Properties of heavy quarkonia and  $B_c$  mesons in the relativistic quark model*. Phys. Rev., 2003, D67:014027.

[71] Wei, Ke-Wei and Guo, Xin-Heng. *Mass spectra of doubly heavy mesons in Regge phenomenology*. Phys. Rev., 2010, D81:076005.

[72] Rai, Ajay Kumar and Vinodkumar, P. C. *Properties of  $B_c$  meson*. Pramana, 2006, 66:953–958.

[73] Abd El-Hady, A. and Spence, J. R. and Vary, J. P. *Radiative decays of  $B_c$  mesons in a Bethe-Salpeter model*. Phys. Rev., 2005, D71:034006.

[74] Davies, C. T. H. and others.  *$B_c$  spectroscopy from lattice QCD*. Phys. Lett., 1996, B382:131–137.

[75] Evans, Lyndon and Bryant, Philip. *LHC Machine*. JINST, 2008, 3:S08001.

[76] Alves Jr., A. A. and others. *The LHCb detector at the LHC*. JINST, 2008, 3:S08005.

[77] Jean-Luc Caron. CERN Accelerator Complex (operating and approved projets). Chaine des accelerateurs du CERN (en fonctionnement et avec les projets aprouves). AC Collection. Legacy of AC. Pictures from 1992 to 2002., Jun, 1991.

[78] Aad, G. and others. *The ATLAS Experiment at the CERN Large Hadron Collider*. JINST, 2008, 3:S08003.

[79] Chatrchyan, S. and others. *The CMS Experiment at the CERN LHC*. JINST, 2008, 3:S08004.

[80] Aamodt, K. and others. *The ALICE experiment at the CERN LHC*. JINST, 2008, 3:S08002.

[81] Anelli, G. and others. *The TOTEM experiment at the CERN Large Hadron Collider*. JINST, 2008, 3:S08007.

[82] Adriani, O. and others. *The LHCf detector at the CERN Large Hadron Collider*. JINST, 2008, 3:S08006.

[83] Pinfold, James. *The MoEDAL experiment at the LHC*. EPJ Web Conf., 2017, 145:12002.

[84] Jean-Luc Caron. LHC Layout. Schema general du LHC. AC Collection. Legacy of AC. Pictures from 1992 to 2002., Sep, 1997.

[85] Aaij, R. and others. *Performance of the LHCb Vertex Locator*. JINST, 2014, 9:P09007.

[86] Aaij, R. and others. *LHCb detector performance*. Int. J. Mod. Phys., 2015, A30:1530022.

[87] Arink, R. and others. *Performance of the LHCb Outer Tracker*. JINST, 2014, 9:P01002.

[88] Adinolfi, M. and others. *Performance of the LHCb RICH detector at the LHC*. Eur. Phys. J., 2013, C73:2431.

[89] Alves Jr., A A and others. *Performance of the LHCb muon system*. JINST, 2013, 8:P02022.

[90] Sjöstrand, Torbjörn and Mrenna, Stephen and Skands, Peter". *PYTHIA 6.4 physics and manual*. JHEP, 2006, 05:026.

[91] Chang, Chao-Hsi and Wang, Jian-Xiong and Wu, Xing-Gang. *BCVEGPY2.0: An upgrade version of the generator BCVEGPY with an addendum about hadroproduction of the P-wave  $B_c$  states*. Comput. Phys. Commun., 2006, 174:241–251.

[92] Lange, D. J. *The EvtGen particle decay simulation package*. Nucl. Instrum. Meth., 2001, A462:152–155.

[93] Golonka, Piotr and Was, Zbigniew. *PHOTOS Monte Carlo: A precision tool for QED corrections in Z and W decays*. Eur. Phys. J., 2006, C45:97–107.

[94] Allison, John and Amako, K. and Apostolakis, J. and Araujo, H. and Dubois, P.A. and others. *Geant4 developments and applications*. IEEE Trans.Nucl.Sci., 2006, 53:270.

[95] Clemencic, M and others. *The LHCb simulation application, Gauss: Design, evolution and experience*. J. Phys. Conf. Ser., 2011, 331:032023.

[96] Cacciari, Matteo and Greco, Mario and Nason, Paolo. *The  $P(T)$  spectrum in heavy flavor hadroproduction*. JHEP, 1998, 9805:007.

[97] Olive, K. A. and others. *Review of particle physics*. Chin. Phys., 2014, C38:090001.

[98] Sjöstrand, Torbjörn and Mrenna, Stephen and Skands, Peter". *A brief introduction to PYTHIA 8.1*. Comput. Phys. Commun., 2008, 178:852–867.

[99] Belyaev, I. and others. *Handling of the generation of primary events in Gauss, the LHCb simulation framework*. J. Phys. Conf. Ser., 2011, 331:032047.

[100] Agostinelli, S. and others. *Geant4: A simulation toolkit*. Nucl. Instrum. Meth., 2003, A506:250.

---

- [101] Kullback, S. and Leibler, R. A. *On information and sufficiency*. Ann. Math. Statist., 1951, 22:79.
- [102] Skwarnicki, Tomasz. *A study of the radiative cascade transitions between the Upsilon-prime and Upsilon resonances*[D]. Institute of Nuclear Physics, Krakow, 1986. DESY-F31-86-02.
- [103] Martínez Santos, Diego and Dupertuis, Frederic. *Mass distributions marginalized over per-event errors*. Nucl.Instrum.Meth., 2014, A764:150–155.
- [104] Pivk, Muriel and Le Diberder, Francois R. *sPlot: A statistical tool to unfold data distributions*. Nucl. Instrum. Meth., 2005, A555:356–369.
- [105] Beringer, J. and others. *Review of particle physics*. Phys. Rev., 2012, D86:010001. and 2013 partial update for the 2014 edition.
- [106] Cacciari, Matteo and Mangano, Michelangelo L. and Nason, Paolo. *Gluon PDF constraints from the ratio of forward heavy quark production at the LHC at  $\sqrt{S}=7$  and 13 TeV*. 2015..
- [107] Aaij, R. and others. *Absolute luminosity measurements with the LHCb detector at the LHC*. JINST, 2012, 7:P01010.
- [108] Aaij, R. and others. *Precision luminosity measurements at LHCb*. JINST, 2014, 9:P12005.
- [109] Aaij, R. and others. *Production of associated  $\Upsilon$  and open charm hadrons in  $pp$  collisions at  $\sqrt{s} = 7$  and 8 TeV via double parton scattering*. JHEP, 2016, 07:052.
- [110] Abe, F. and others. *Double parton scattering in  $\bar{p}p$  collisions at  $\sqrt{s} = 1.8$  TeV*. Phys. Rev., 1997, D56:3811.
- [111] Abe, F. and others. *Measurement of double parton scattering in  $\bar{p}p$  collisions at  $\sqrt{s} = 1.8$  TeV*. Phys. Rev. Lett., 1997, 79:584.
- [112] Cranmer, Kyle S. *Kernel estimation in high-energy physics*. Comput. Phys. Commun., 2001, 136:198–207.
- [113] Aaij, R. and others. *Measurement of forward  $J/\psi$  production cross-sections in  $pp$  collisions at  $\sqrt{s} = 13$  TeV*. JHEP, 2015, 10:172.
- [114] Abe, F. and others. *Measurement of double parton scattering in  $\bar{p}p$  collisions at  $\sqrt{s} = 1.8$  TeV*. Phys. Rev. Lett., 1997, 79:584–589.
- [115] Likhoded, A. K. and Luchinsky, A. V. and Poslavsky, S. V. *Production of  $J/\psi + \chi_c$  and  $J/\psi + J/\psi$  with real gluon emission at LHC*. Phys. Rev., 2016, D94:054017.
- [116] Dulat, Sayipjamal and Hou, Tie-Jiun and Gao, Jun and Guzzi, Marco and Huston, Joey and Nadolsky, Pavel and Pumplin, Jon and Schmidt, Carl and Stump, Daniel and Yuan, C. P. *New parton distribution functions from a global analysis of quantum chromodynamics*. Phys. Rev., 2016, D93:033006.
- [117] Lansberg, Jean-Philippe and Shao, Hua-Sheng. *Production of  $J/\psi + \eta_c$  versus  $J/\psi + J/\psi$  at the LHC: Importance of real  $\alpha_s^5$  corrections*. Phys. Rev. Lett., 2013, 111:122001.
- [118] Lansberg, Jean-Philippe and Shao, Hua-Sheng. *Double-quarkonium production at a fixed-target experiment at the LHC (AFTER@LHC)*. Nucl. Phys., 2015, B900:273–294.
- [119] Shao, Hua-Sheng. *HELAC-ONIA: An automatic matrix element generator for heavy quarkonium physics*. Comput. Phys. Commun., 2013, 184:2562.

---

- [120] Shao, Hua-Sheng. *HELAC-ONIA 2.0: An upgraded matrix-element and event generator for heavy quarkonium physics*. *Comput. Phys. Commun.*, 2016, 198:238.
- [121] Ball, Richard D. and others. *Parton distributions for the LHC Run II*. *JHEP*, 2015, 04:040.
- [122] Butenschoen, Mathias and Kniehl, Bernd A. *World data of  $J/\psi$  production consolidate NRQCD factorization at NLO*. *Phys. Rev.*, 2011, D84:051501.
- [123] Sharma, Rishi and Vitev, Ivan. *High transverse momentum quarkonium production and dissociation in heavy ion collisions*. *Phys. Rev.*, 2013, C87:044905.
- [124] Gong, Bin and Wan, Lu-Ping and Wang, Jian-Xiong and Zhang, Hong-Fei. *Polarization for prompt  $J/\psi$  and  $\psi(2S)$  production at the Tevatron and LHC*. *Phys. Rev. Lett.*, 2013, 110:042002.
- [125] Sun, Peng and Yuan, C.-P. and Yuan, Feng. *Heavy quarkonium production at low  $p_T$  in NRQCD with soft gluon resummation*. *Phys. Rev.*, 2013, D88:054008.
- [126] Bodwin, Geoffrey T. and Chung, Hee Sok and Kim, U-Rae and Lee, Jungil. *Fragmentation contributions to  $J/\psi$  production at the Tevatron and the LHC*. *Phys. Rev. Lett.*, 2014, 113:022001.
- [127] Krämer, Michael. *Quarkonium production at high-energy colliders*. *Prog. Part. Nucl. Phys.*, 2001, 47:141–201.
- [128] Braaten, Eric and Kniehl, Bernd A. and Lee, Jungil. *Polarization of prompt  $J/\psi$  at the Tevatron*. *Phys. Rev.*, 2000, D62:094005.
- [129] Lai, H. L. and Huston, J. and Kuhlmann, S. and Morfin, J. and Olness, Fredrick I. and Owens, J. F. and Pumplin, J. and Tung, W. K. *Global QCD analysis of parton structure of the nucleon: CTEQ5 parton distributions*. *Eur. Phys. J.*, 2000, C12:375–392.
- [130] Pumplin, J. and Stump, D. R. and Huston, J. and Lai, H. L. and Nadolsky, Pavel M. and Tung, W. K. *New generation of parton distributions with uncertainties from global QCD analysis*. *JHEP*, 2002, 07:012.
- [131] Gribov, L. V. and Levin, E. M. and Ryskin, M. G. *Semihard processes in QCD*. *Phys. Rept.*, 1983, 100:1.
- [132] Levin, E. M. and Ryskin, M. G. *High-energy hadron collisions in QCD*. *Phys. Rept.*, 1990, 189:267.
- [133] Andersson, Bo and others. *Small- $x$  phenomenology: summary and status*. *Eur. Phys. J.*, 2002, C25:77.
- [134] Andersen, Jeppe R. and others. *Small- $x$  phenomenology: summary and status 2002*. *Eur. Phys. J.*, 2004, C35:67.
- [135] Andersen, Jeppe R. and others. *Small- $x$  phenomenology: summary of the 3rd Lund Small- $x$  Workshop in 2004*. *Eur. Phys. J.*, 2006, C48:53.
- [136] Baranov, S. P. *Pair production of  $J/\psi$  mesons in the  $k_T$ -factorization approach*. *Phys. Rev.*, 2011, D84:054012.
- [137] Baranov, S. P. and Jung, H. *Double  $J/\psi$  production: A probe of gluon polarization?* *Z. Phys.*, 1995, C66:647.
- [138] Jung, Hannes. *Un-integrated PDFs in CCFM*. Deep Inelastic Scattering, 2004. 299.

[139] Jung, H. and others. *The CCFM Monte Carlo generator CASCADE version 2.2.03*. Eur. Phys. J., 2010, C70:1237.

[140] Jung, Hannes and Hautmann, Francesco. *Determination of transverse momentum dependent gluon density from HERA structure function measurements*. Deep Inelastic Scattering, 2012. 433.

[141] Hautmann, F. and Jung, H. *Transverse momentum dependent gluon density from DIS precision data*. Nucl. Phys., 2014, B883:1.

[142] Jung, Hannes and Hautmann, Francesco. *Transverse momentum dependent gluon density from DIS precision data*. PoS, 2014, DIS2014:042.

[143] Nadolsky, Pavel M. and Lai, Hung-Liang and Cao, Qing-Hong and Huston, Joey and Pumplin, Jon and Stump, Daniel and Tung, Wu-Ki and Yuan, C. -P. *Implications of CTEQ global analysis for collider observables*. Phys. Rev., 2008, D78:013004.

[144] Aaboud, Morad and others. *Measurement of the prompt  $J/\psi$  pair production cross-section in  $pp$  collisions at  $\sqrt{s} = 8$  TeV with the ATLAS detector*. 2016..

[145] Abazov, Victor Mukhamedovich and others. *Observation and studies of double  $J/\psi$  production at the Tevatron*. Phys. Rev., 2014, D90:111101.

[146] Abazov, Victor Mukhamedovich and others. *Evidence for simultaneous production of  $J/\psi$  and  $\gamma$  mesons*. Phys. Rev. Lett., 2016, 116:082002.

[147] Chang, Chao-Hsi and Driouichi, Chafik and Eerola, Paula and Wu, Xing Gang. *BCVEGPY: An event generator for hadronic production of the  $B/c$  meson*. Comput. Phys. Commun., 2004, 159:192–224.

[148] Aaltonen, T. and others. *Measurement of the  $B_c^-$  meson lifetime in the decay  $B_c^- \rightarrow J/\psi \pi^-$* . Phys. Rev., 2013, D87:011101.

[149] Aaij, R. and others. *Measurement of the  $B_c^+$  meson lifetime using  $B_c^+ \rightarrow J/\psi \mu^+ \nu_\mu X$  decays*. Eur. Phys. J., 2014, C74:2839.

[150] Hoecker, A. and others. *TMVA: Toolkit for multivariate data analysis*. PoS, 2007, ACAT:040.

[151] Breiman, L. and Friedman, J. H. and Olshen, R. A. and Stone, C. J. Classification and regression trees. Belmont, California, USA: Wadsworth international group, 1984.

[152] Freund, Yoav and Schapire, Robert E. *A decision-theoretic generalization of on-line learning and an application to boosting*. J. Comput. Syst. Sci., 1997, 55:119.

[153] Aaij, R. and others. *Measurement of  $B_c^+$  production at  $\sqrt{s} = 8$  TeV*. Phys. Rev. Lett., 2015, 114:132001.

[154] Gligorov, Vladimir and Thomas, Christopher and Williams, Michael. *The HLT inclusive  $B$  triggers*. 2011..

[155] Aaij, R. and others. *Measurement of relative branching fractions of  $B$  decays to  $\psi(2S)$  and  $J/\psi$  mesons*. Eur. Phys. J., 2012, C72:2118.

[156] Aaij, R. and others. *Measurements of  $B_c^+$  production and mass with the  $B_c^+ \rightarrow J/\psi \pi^+$  decay*. Phys. Rev. Lett., 2012, 109:232001.

[157] Tisserand, Vincent. *Optimisation du détecteur ATLAS pour la recherche du boson de Higgs se désintégrant en deux photons au LHC[D]*. LAL (Orsay), 1997. CERN-THESIS-99-032.

- [158] Read, Alexander L. *Presentation of search results: the  $CL_s$  technique*. *J. Phys.*, 2002, G28:2693–2704.
- [159] Gouz, I. P. and Kiselev, V. V. and Likhoded, A. K. and Romanovsky, V. I. and Yushchenko, O. P. *Prospects for the  $B_c$  studies at LHCb*. *Phys. Atom. Nucl.*, 2004, 67:1559–1570.
- [160] Gao, Yuan-Ning and He, Jibo and Robbe, Patrick and Schune, Marie-Helene and Yang, Zhen-Wei. *Experimental prospects of the  $B_c$  studies of the LHCb experiment*. *Chin. Phys. Lett.*, 2010, 27:061302.

## Acknowledgments

I would like to express my sincerest gratitude to my supervisor Prof. Yuanning Gao and Assoc. Prof. Zhenwei Yang. They took me into the field of particle physics, and gave me meticulous guidance in both scientific activities and life. Their edification will benefit me lifelong.

I deeply appreciate the enlightenments and constructive helps from Yiming Li, Yanxi Zhang, Vanya Belyaev, Tatsuya Nakada, Jibo He, Hua-Sheng Shao, and Yan-Qing Ma. Without their assistance, I would not be able to finish my thesis successfully.

I want to convey grateful appreciation to Prof. Shaomin Chen, Assoc. Prof. Liming Zhang, Assoc. Prof. Xianglei Zhu and Assoc. Prof. Zhe Wang for the helpful suggestions and vigorous support on my PhD work. Also a lot of thanks to my colleagues at the Center for High Energy Physics, Tsinghua University, and the LHCb experiment.

My earnest affection goes to my parents and my boyfriend Jianxiong Pan. Thank you for accompanying, understanding and supporting me all along.

### Declaration

本人郑重声明：所呈交的学位论文，是本人在导师指导下，独立进行研究工作所取得的成果。尽我所知，除文中已经注明引用的内容外，本学位论文的研究成果不包含任何他人享有著作权的内容。对本论文所涉及的研究工作做出贡献的其他个人和集体，均已在文中以明确方式标明。

签 名： \_\_\_\_\_ 日 期： \_\_\_\_\_

## Appendix A Fits to the differential $J/\psi$ pair production cross-sections with SPS and DPS predictions

The results of the templated SPS plus DPS fits used for the determination of  $\sigma_{\text{eff}}$  are shown in Figs. A.1, A.2 and A.3. The templated fits used only to determine  $f_{\text{DPS}}$  in the  $p_{\text{T}}(J/\psi J/\psi) > 1 \text{ GeV}/c$  and  $p_{\text{T}}(J/\psi J/\psi) > 3 \text{ GeV}/c$  kinematic regions are shown in Figs. A.4, A.5, A.6 and A.7.

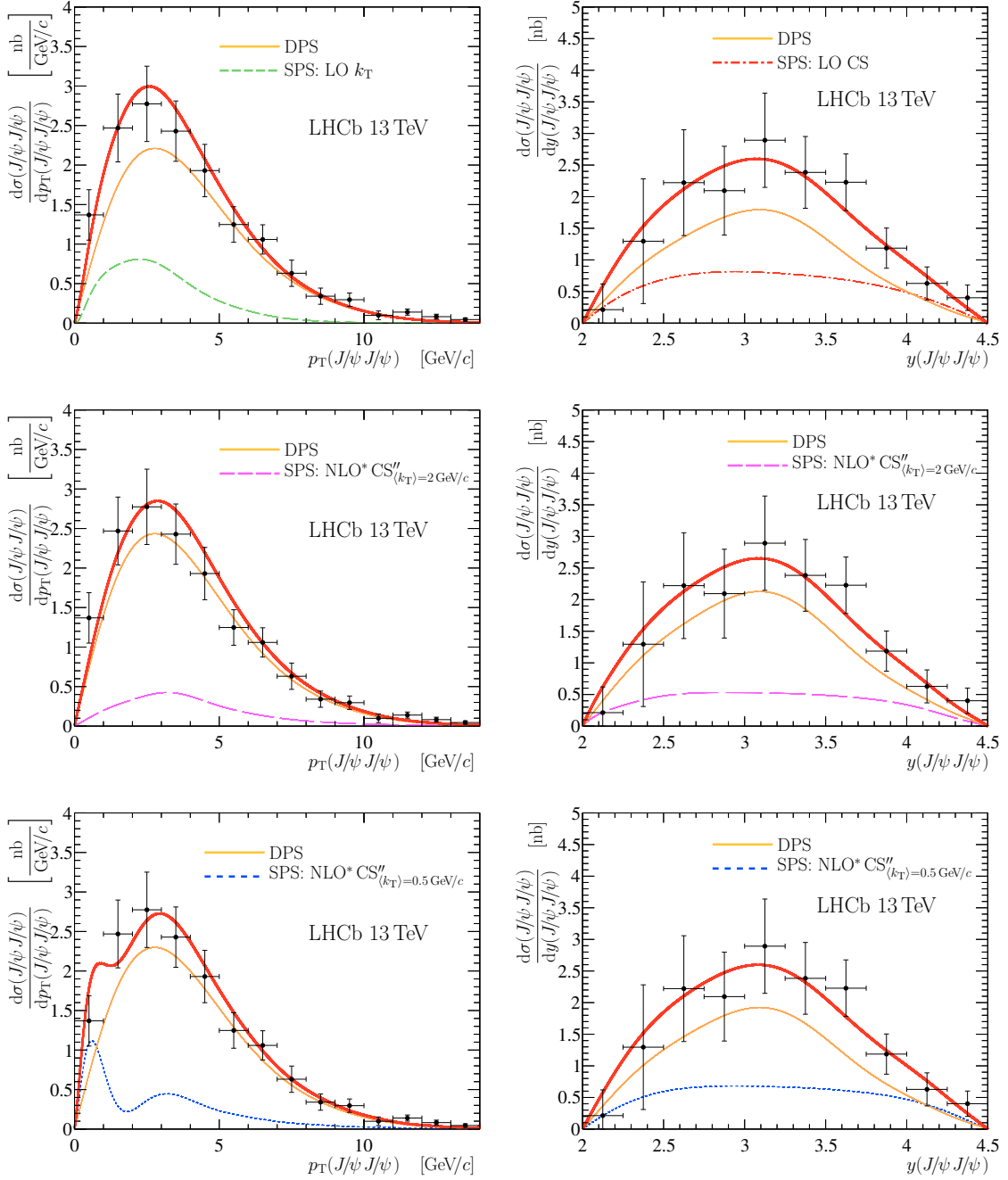


Figure A.1 Templated SPS plus DPS fits to  $\frac{d\sigma(J/\psi J/\psi)}{dp_T(J/\psi J/\psi)}$  and  $\frac{d\sigma(J/\psi J/\psi)}{dy(J/\psi J/\psi)}$ . The black points with error bars are the measurements. The thick red solid line represents the total fit result. The thin orange solid line represents the DPS contribution.

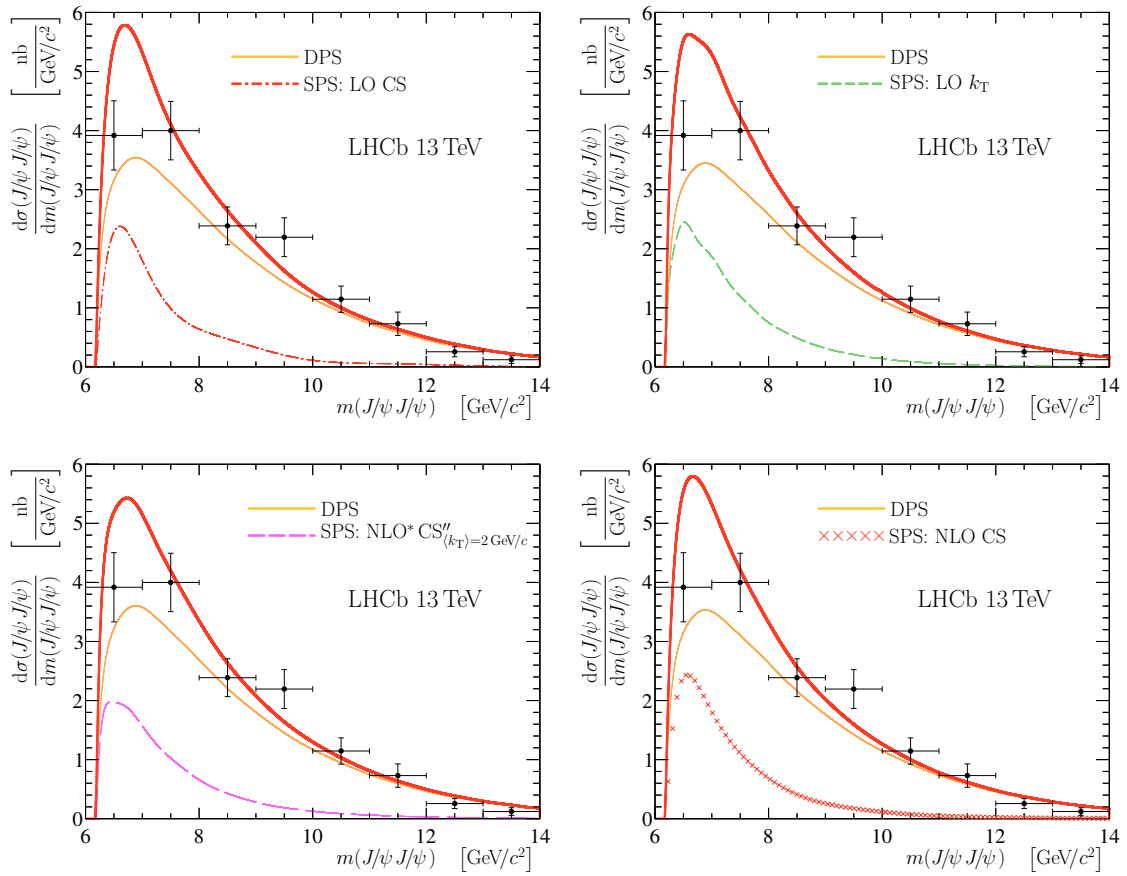


Figure A.2 Templated SPS plus DPS fits to  $\frac{d\sigma(J/\psi J/\psi)}{dm(J/\psi J/\psi)}$ . The black points with error bars are the measurements. The thick red solid line represents the total fit result. The thin orange solid line represents the DPS contribution.

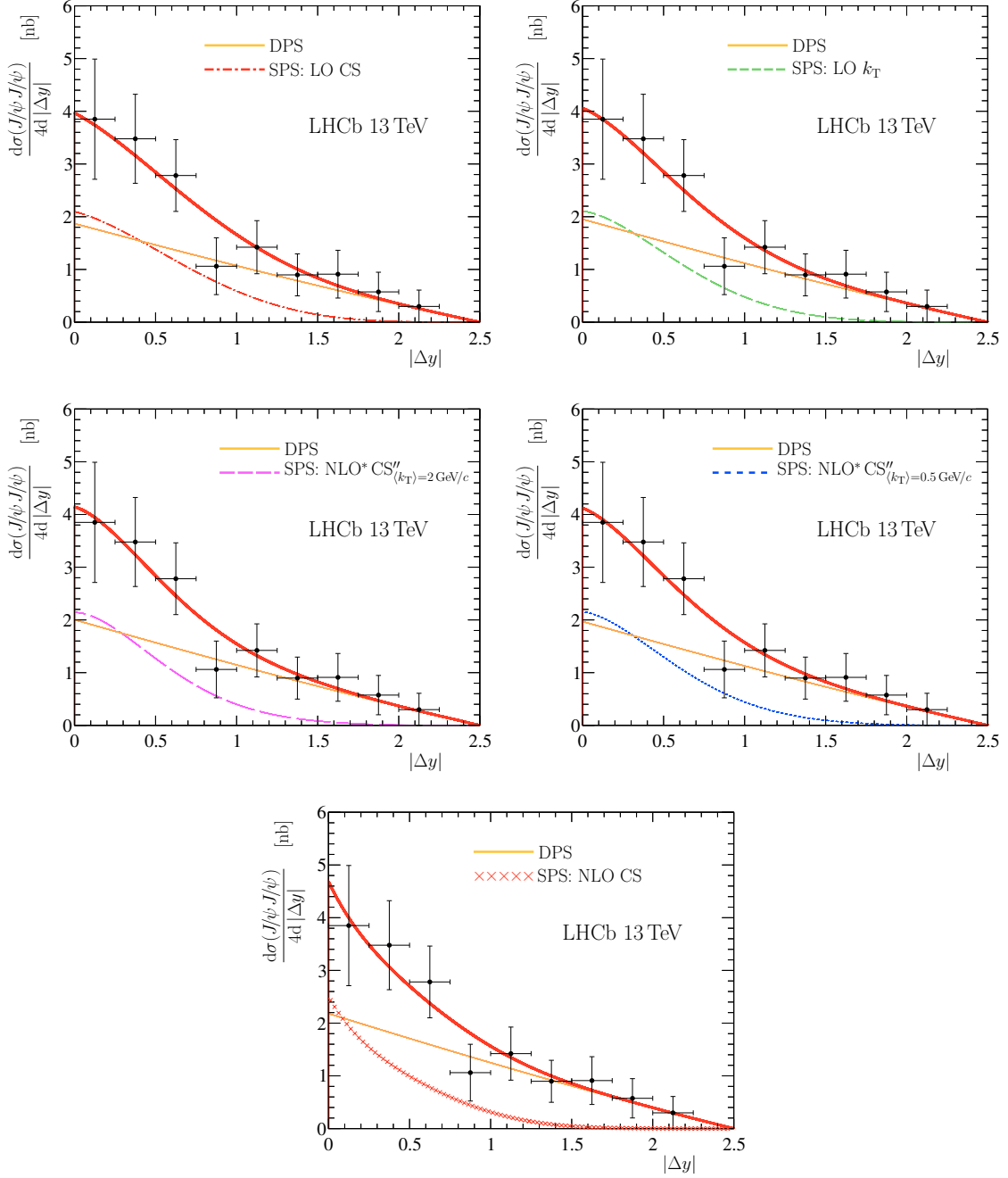


Figure A.3 Templated SPS plus DPS fits to  $\frac{d\sigma(J/\psi J/\psi)}{d|\Delta y|}$ . The black points with error bars are the measurements. The thick red solid line represents the total fit result. The thin orange solid line represents the DPS contribution.

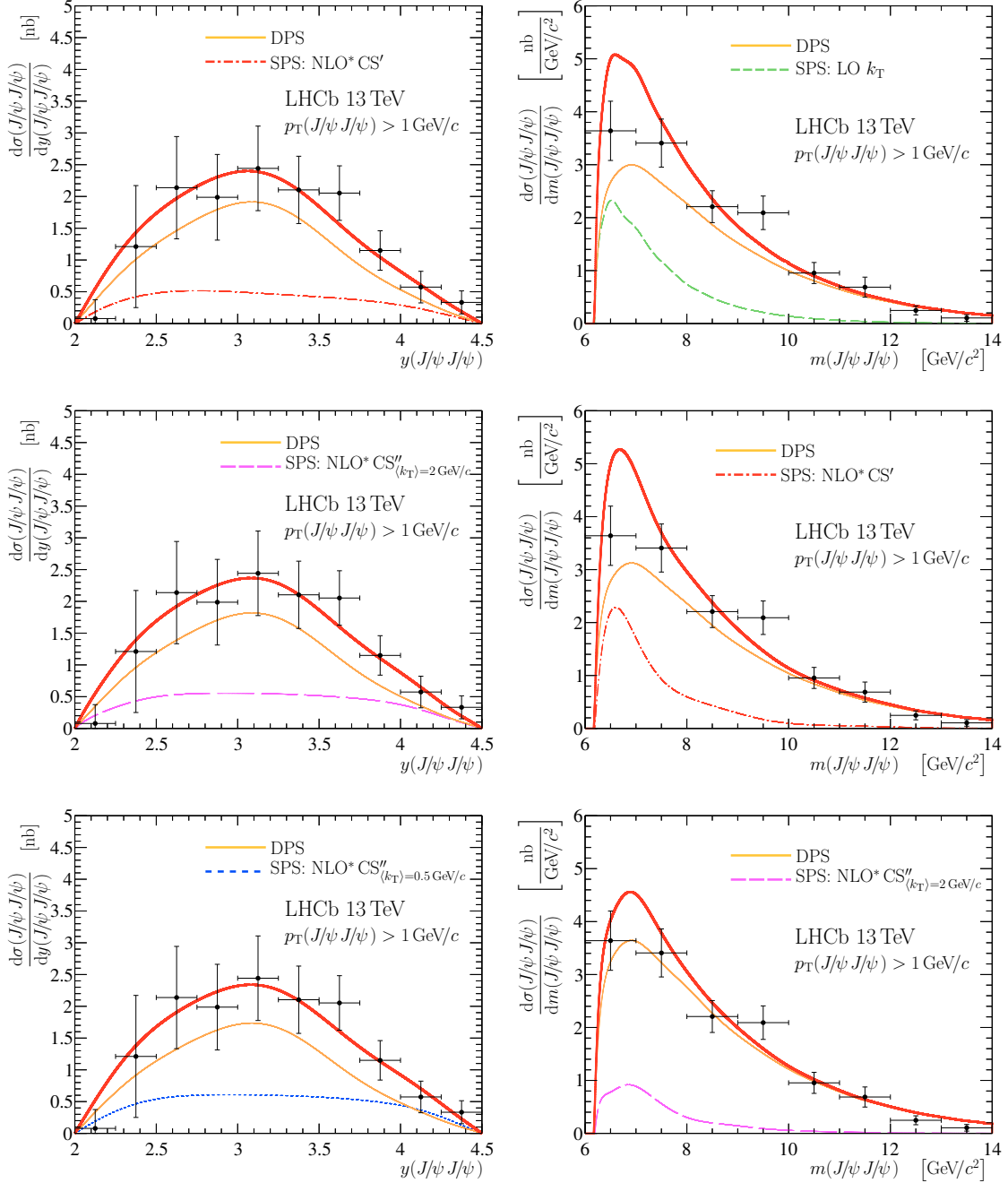


Figure A.4 Templated SPS plus DPS fits to  $\frac{d\sigma(J/\psi J/\psi)}{dy(J/\psi J/\psi)}$  and  $\frac{d\sigma(J/\psi J/\psi)}{dm(J/\psi J/\psi)}$  for the  $p_T(J/\psi J/\psi) > 1 \text{ GeV}/c$  region. The black points with error bars are the measurements. The thick red solid line represents the total fit result. The thin orange solid line represents the DPS contribution.

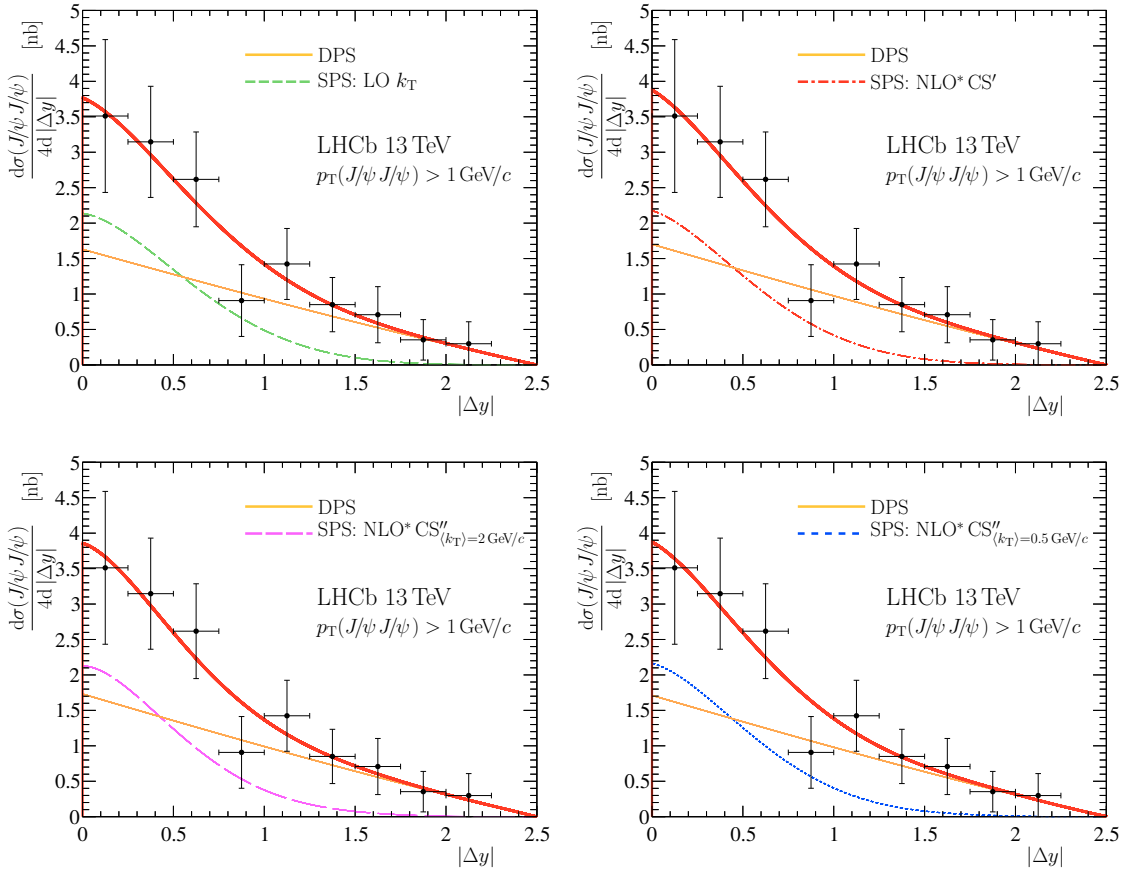


Figure A.5 Templated SPS plus DPS fits to  $\frac{d\sigma(J/\psi J/\psi)}{d|\Delta y|}$  for the  $p_T(J/\psi J/\psi) > 1 \text{ GeV}/c$  region. The black points with error bars are the measurements. The thick red solid line represents the total fit result. The thin orange solid line represents the DPS contribution.

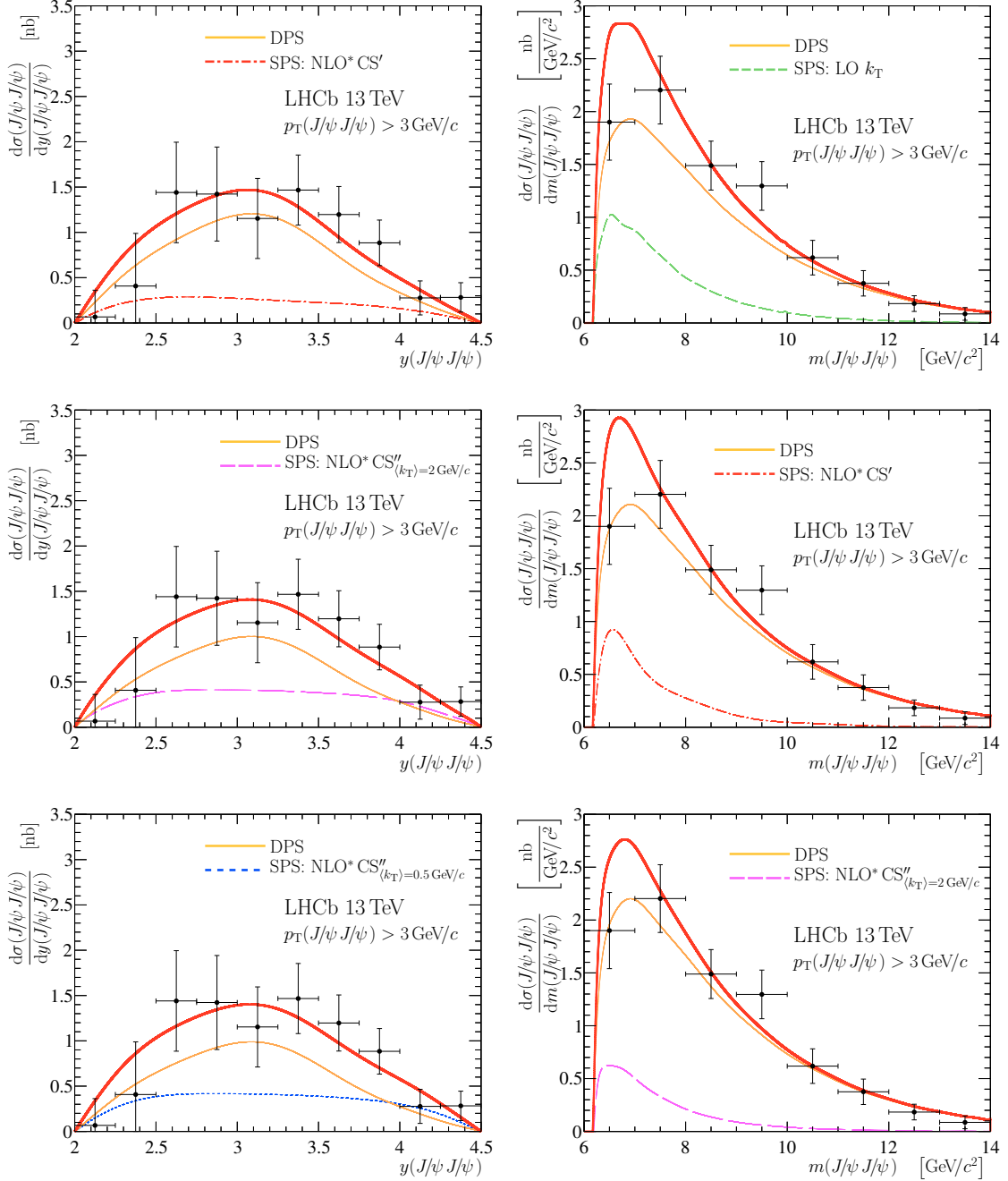


Figure A.6 Templated SPS plus DPS fits to  $\frac{d\sigma(J/\psi J/\psi)}{dy(J/\psi J/\psi)}$  and  $\frac{d\sigma(J/\psi J/\psi)}{dm(J/\psi J/\psi)}$  for the  $p_T(J/\psi J/\psi) > 3 \text{ GeV}/c$  region. The black points with error bars are the measurements. The thick red solid line represents the total fit result. The thin orange solid line represents the DPS contribution.

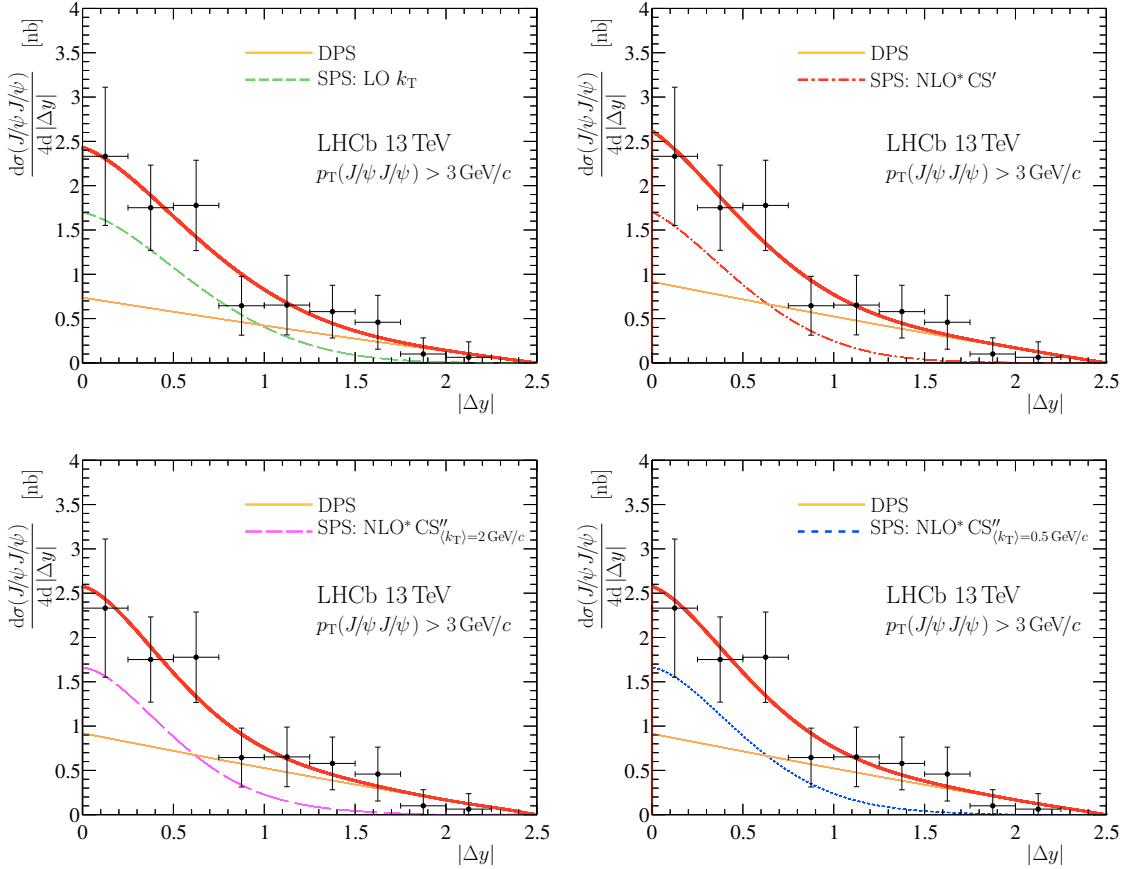


Figure A.7 Templated SPS plus DPS fits to  $\frac{d\sigma(J/\psi J/\psi)}{d|\Delta y|}$  for the  $p_T(J/\psi J/\psi) > 3 \text{ GeV}/c$  region. The black points with error bars are the measurements. The thick red solid line represents the total fit result. The thin orange solid line represents the DPS contribution.

## Appendix B Comparison of the BDT input variable distributions for the $B_c^+ \rightarrow J/\psi \pi^+$ and $B_c^+ \rightarrow \psi(2S)\pi^+$ decays

The comparisons of the BDT input variable distributions between the data and the simulation are shown in Figs. B.1, B.2, B.3 and B.4 for the  $B_c^+ \rightarrow J/\psi \pi^+$  and  $B_c^+ \rightarrow \psi(2S)\pi^+$  decays in 2011 and 2012, respectively. The comparisons between the data and the simulation after applying the weights to the simulation are shown in Figs. B.5, B.6, B.7 and B.8,

Appendix B Comparison of the BDT input variable distributions for the  $B_c^+ \rightarrow J/\psi \pi^+$  and  $B_c^+ \rightarrow \psi(2S)\pi^+$  decays

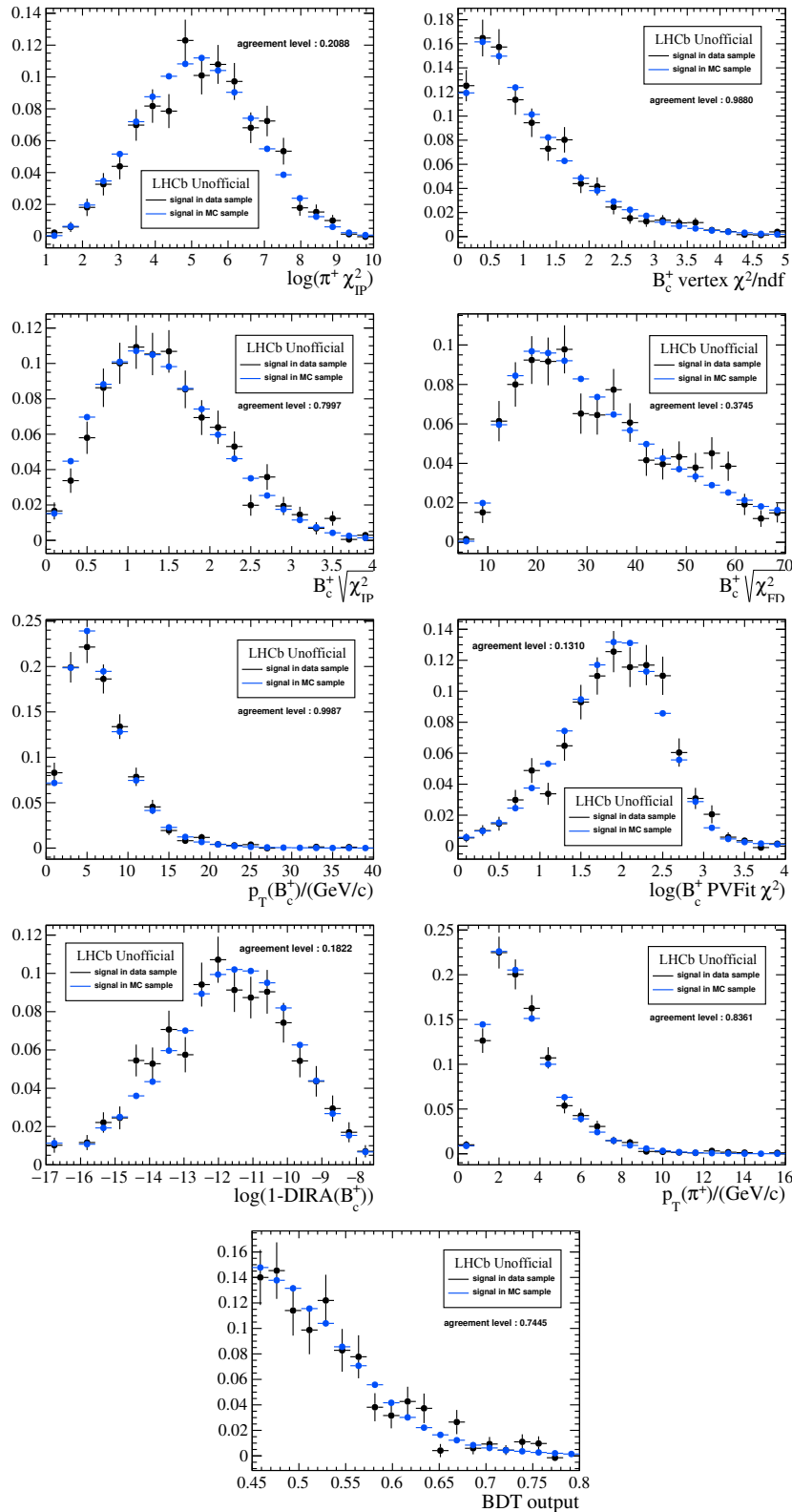


Figure B.1 Comparison of the distributions of the input variables for the BDT classifiers between the data and the simulation for the  $B_c^+ \rightarrow J/\psi \pi^+$  decay in 2011.

Appendix B Comparison of the BDT input variable distributions for the  $B_c^+ \rightarrow J/\psi \pi^+$  and  $B_c^+ \rightarrow \psi(2S)\pi^+$  decays

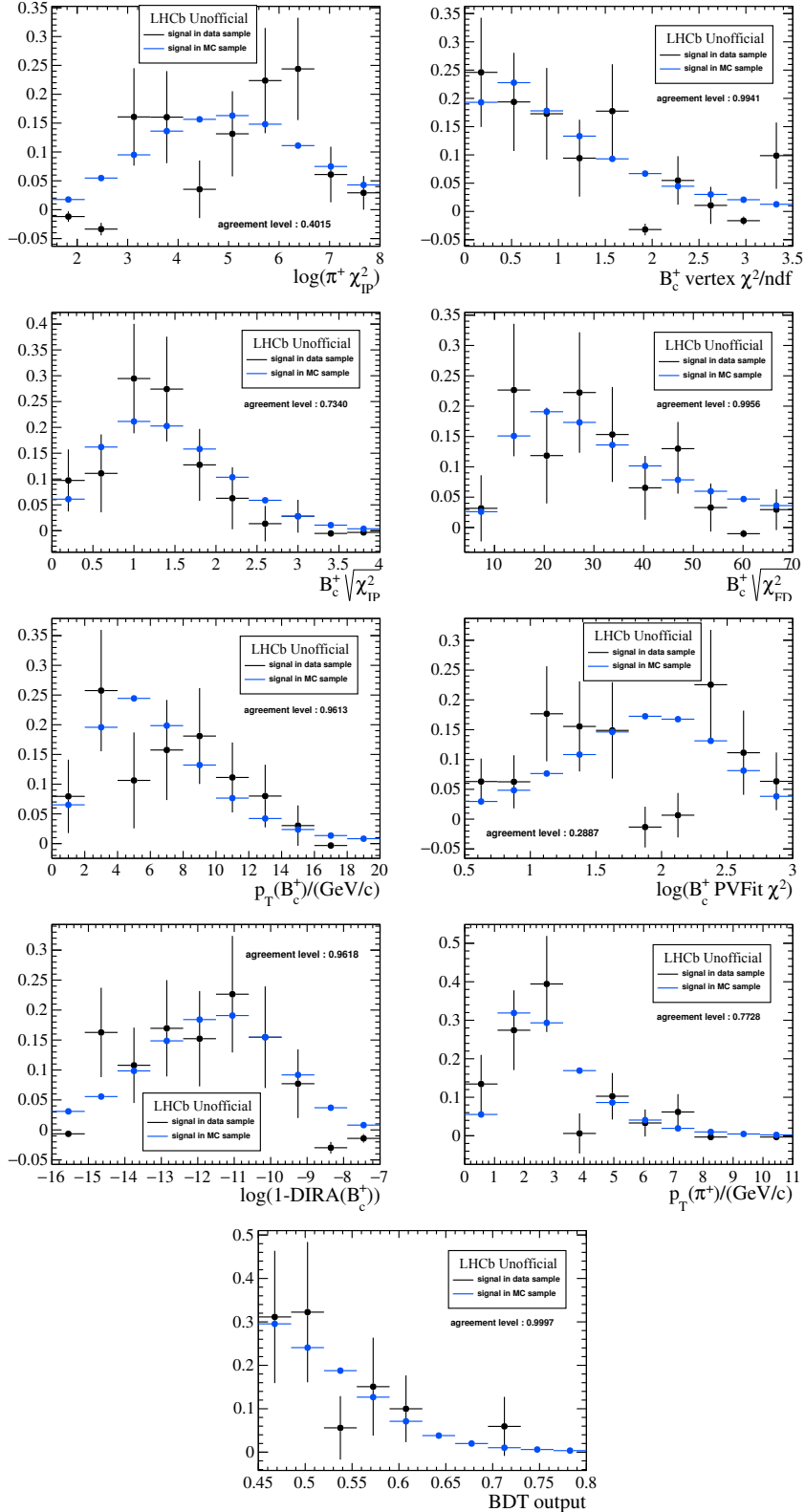


Figure B.2 Comparison of the distributions of the input variables for the BDT classifiers between the data and the simulation for the  $B_c^+ \rightarrow \psi(2S)\pi^+$  decay in 2011.

Appendix B Comparison of the BDT input variable distributions for the  $B_c^+ \rightarrow J/\psi \pi^+$  and  $B_c^+ \rightarrow \psi(2S)\pi^+$  decays

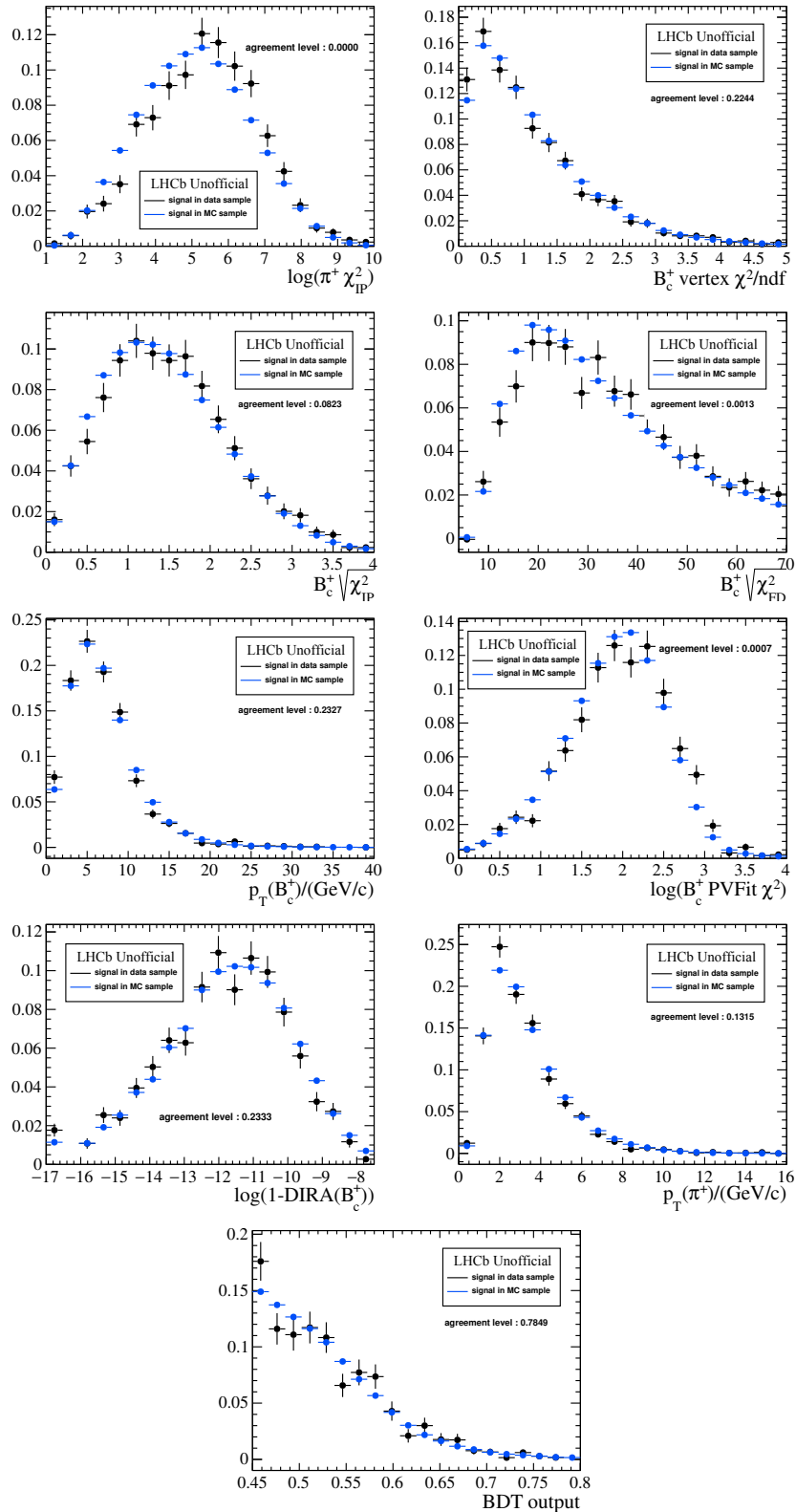


Figure B.3 Comparison of the distributions of the input variables for the BDT classifiers between the data and the simulation for the  $B_c^+ \rightarrow J/\psi \pi^+$  decay in 2012.

## Appendix B Comparison of the BDT input variable distributions for the $B_c^+ \rightarrow J/\psi \pi^+$ and $B_c^+ \rightarrow \psi(2S) \pi^+$ decays

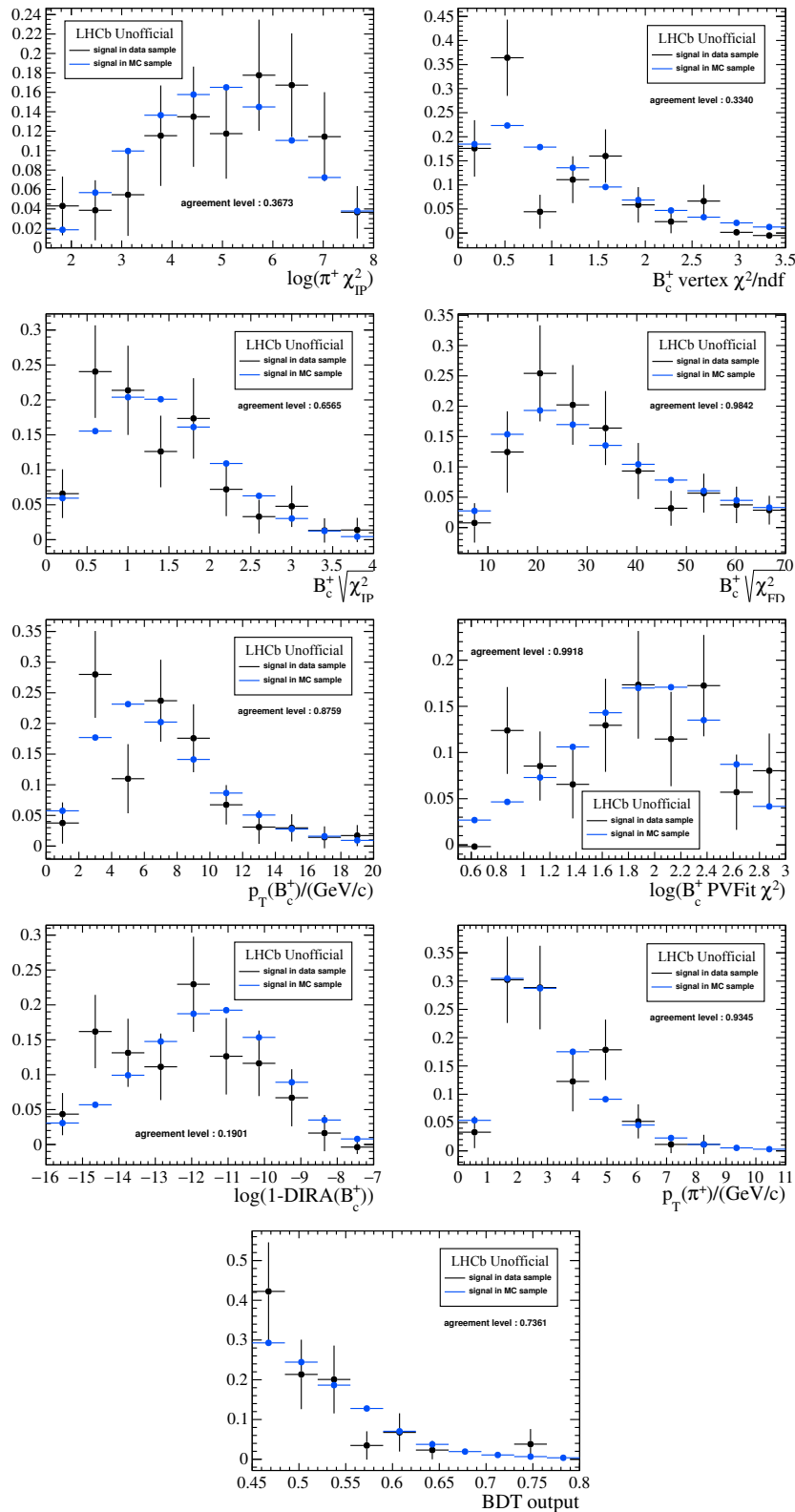


Figure B.4 Comparison of the distributions of the input variables for the BDT classifiers between the data and the simulation for the  $B_c^+ \rightarrow \psi(2S)\pi^+$  decay in 2012.

Appendix B Comparison of the BDT input variable distributions for the  $B_c^+ \rightarrow J/\psi \pi^+$  and  $B_c^+ \rightarrow \psi(2S)\pi^+$  decays

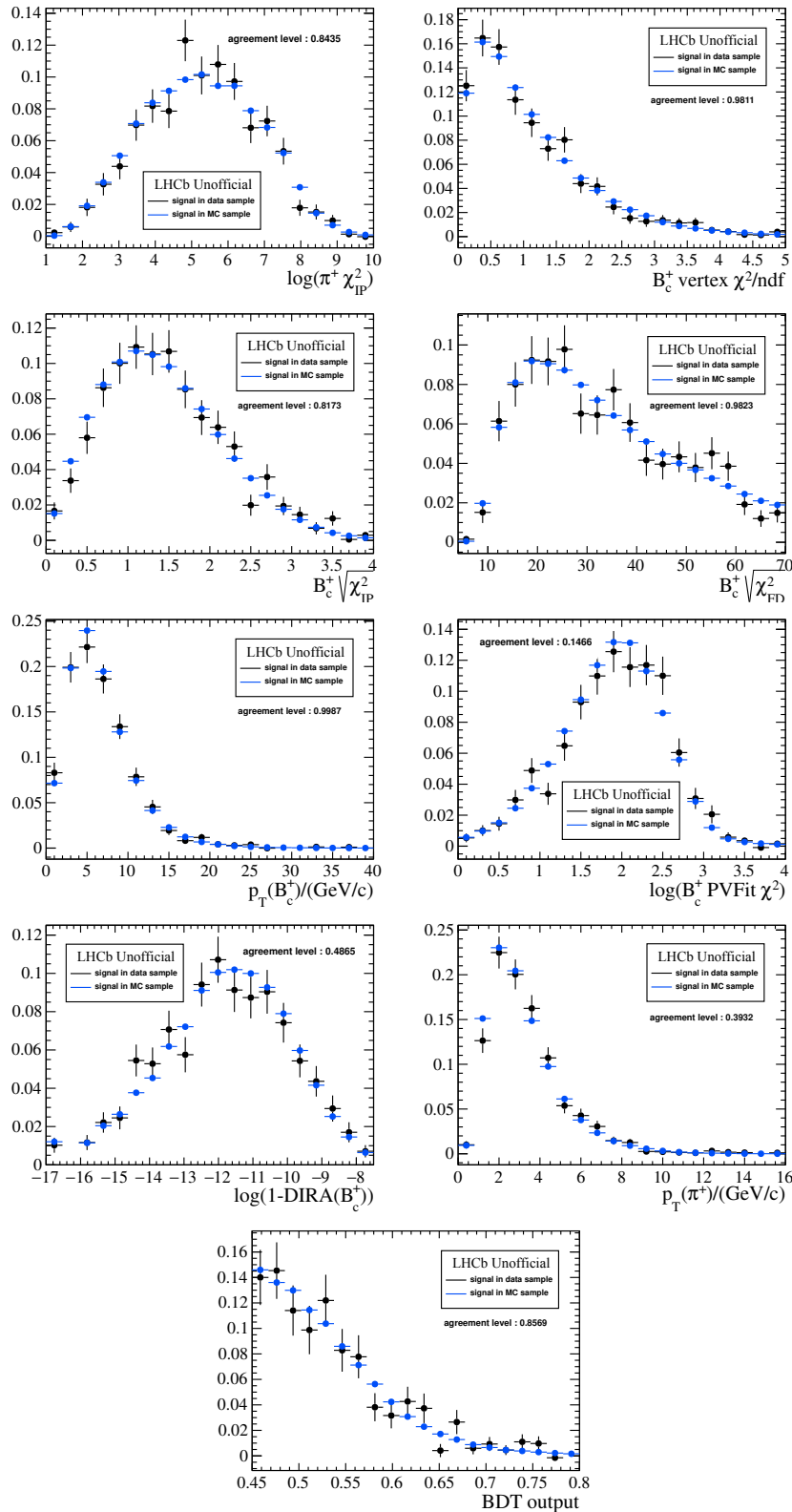


Figure B.5 Comparison of the distributions of the input variables for the BDT classifiers between the data and the simulation for the  $B_c^+ \rightarrow J/\psi \pi^+$  decay in 2011 after weighting the simulation.

Appendix B Comparison of the BDT input variable distributions for the  $B_c^+ \rightarrow J/\psi \pi^+$  and  $B_c^+ \rightarrow \psi(2S)\pi^+$  decays

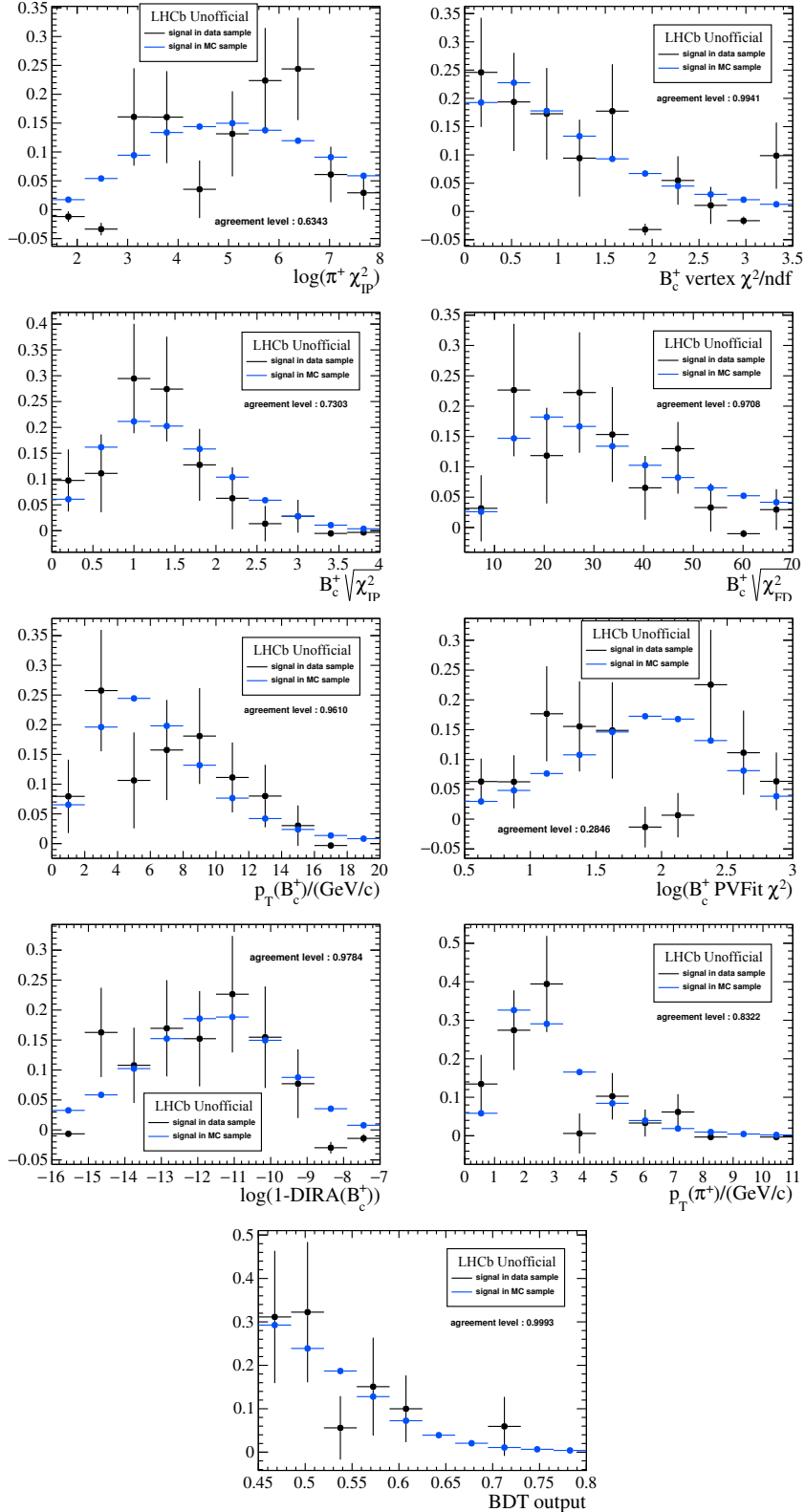


Figure B.6 Comparison of the distributions of the input variables for the BDT classifiers between the data and the simulation for the  $B_c^+ \rightarrow \psi(2S)\pi^+$  decay in 2011 after weighting the simulation.

Appendix B Comparison of the BDT input variable distributions for the  $B_c^+ \rightarrow J/\psi \pi^+$  and  $B_c^+ \rightarrow \psi(2S)\pi^+$  decays

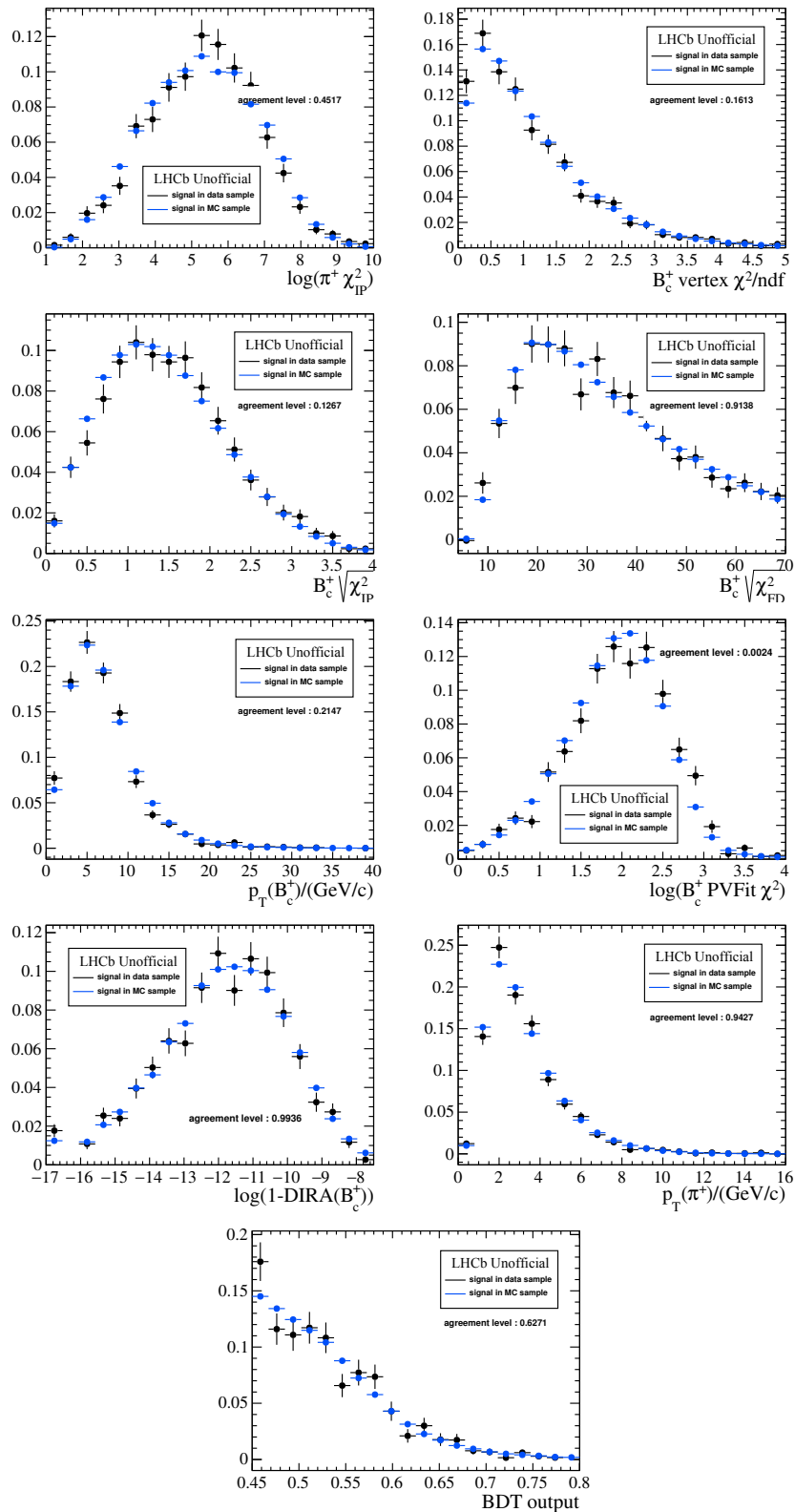


Figure B.7 Comparison of the distributions of the input variables for the BDT classifiers between the data and the simulation for the  $B_c^+ \rightarrow J/\psi \pi^+$  decay in 2012 after weighting the simulation.

Appendix B Comparison of the BDT input variable distributions for the  $B_c^+ \rightarrow J/\psi \pi^+$  and  $B_c^+ \rightarrow \psi(2S)\pi^+$  decays

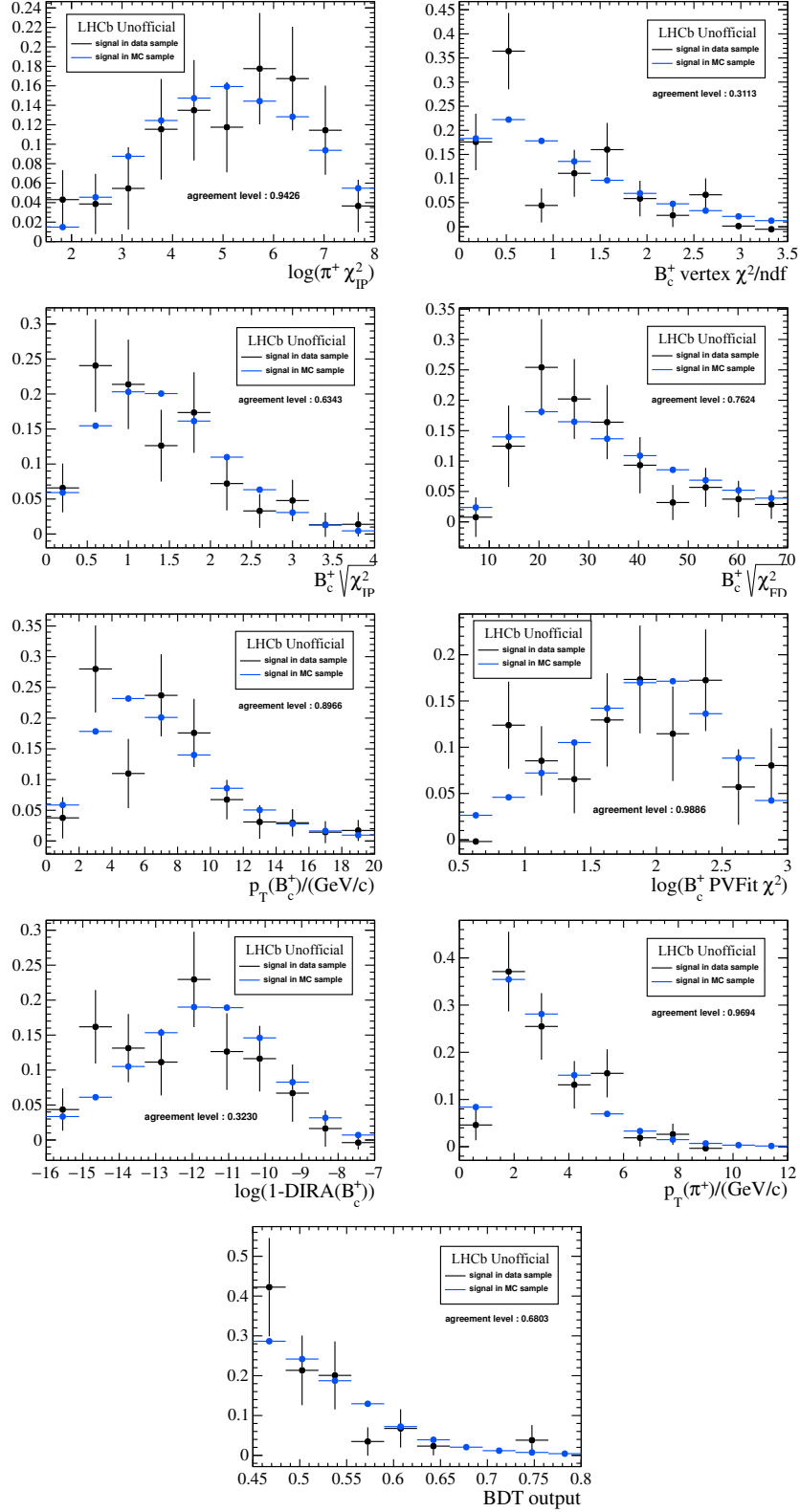


Figure B.8 Comparison of the distributions of the input variables for the BDT classifiers between the data and the simulation for the  $B_c^+ \rightarrow \psi(2S)\pi^+$  decay in 2012 after weighting the simulation.

## Resume and Publications

### 个人简历

1992 年 9 月 13 日出生于河北省无极县。  
2003 年 9 月进入河北省无极县实验中学学习。  
2006 年 9 月考入河北省衡水中学学习。  
2009 年 9 月考入清华大学工程物理系核工程与核技术专业，2013 年 7 月本科毕业并获得工学学士学位。  
2013 年 9 月免试进入清华大学工程物理系攻读物理学博士学位至今。

### 发表的学术论文

- [1] LHCb Collaboration, R. Aaij *et al.*, *Measurement of the branching fraction ratio  $\mathcal{B}(B_c^+ \rightarrow \psi(2S)\pi^+)/\mathcal{B}(B_c^+ \rightarrow J/\psi\pi^+)$* , Phys. Rev. D92 072007
- [2] LHCb Collaboration, R. Aaij *et al.*, *Measurement of forward  $J/\psi$  production cross-sections in  $pp$  collisions at  $\sqrt{s} = 13$  TeV*, JHEP 10 (2015) 172, Erratum *ibid.* 1705 (2017) 063
- [3] LHCb Collaboration, R. Aaij *et al.*, *Measurement of the  $J/\psi$  pair production cross-section in  $pp$  collisions at  $\sqrt{s} = 13$  TeV*, JHEP 06 (2017) 047, Erratum *ibid.* JHEP 10 (2017) 068
- [4] LHCb Collaboration, R. Aaij *et al.*, *Search for excited  $B_c^+$  states*, JHEP 01 (2018) 138
- [5] Liupan An (on behalf of the LHCb Collaboration), *Measurement of the branching fraction ratio  $\mathcal{B}(B_c^+ \rightarrow \psi(2S)\pi^+)/\mathcal{B}(B_c^+ \rightarrow J/\psi\pi^+)$* , PoS BEAUTY2016 (2016) 065
- [6] Liupan An (on behalf of the LHCb Collaboration), *Measurements of soft QCD and double parton scattering at LHCb*, LHCb-PROC-2017-030